Dwarf Galaxies in the Local Universe as Probes of Stellar and Galactic Evolution

Thesis by
Mithi Alexa Caballes de los Reyes

In Partial Fulfillment of the Requirements for the
Degree of
Doctor of Philosophy

CALIFORNIA INSTITUTE OF TECHNOLOGY
Pasadena, California

2022
Defended May 9, 2022

Mithi Alexa Caballes de los Reyes
ORCID: 0000-0002-4739-046X

ACKNOWLEDGEMENTS

Thank you to Evan Kirby, the best advisor I could have ever hoped for. I simply would not have made it this far without you and your unflagging support (and also the boba you brought for observing runs). Despite being your whiniest student, I have always valued your optimism, and I am forever grateful for your guidance. You are the kind of mentor I hope to become one day.

I would like to thank the members of my thesis and candidacy committee—Mansi Kasliwal, Phil Hopkins, Chuck Steidel, and Vikram Ravi—for their support and advice.

Beyond gratitude, this thesis was written for many people.

This is for Evan Kirby and for all my other mentors, past and present, including but not limited to: John Kolena, JoAnn Cohen, Janice Lee, and Rob Kennicutt.

This is for Sarah, Nitika, and Aida—I love you so much bbs. This is for the other members of the Kirby research group. Nicha, Gina, Ivanna, and Brent: thank you for being role models and for making me feel welcome in the group. Zhuyun and Evan: thank you for the many boba runs and long talks, and for inspiring me with your determination and optimism. This is for the Planet Haus crew: Aida, Shreyas, Austin, Ben, and (of course) Izzy. This is for all the other wonderful current and former graduate students who have made my time at Caltech less miserable: Devin, Ryan, Yuping, Sam, Ivey, Chris, and Kathryn, to name a few. This is for Jackie, who deserved far better from Caltech.

This is for the many friends I have made outside Caltech, through Cambridge (especially Jeannie, Blake, Alexis, and my friends from 64 Storey's Way) and conferences and Astrobites and Twitter, whose encouragement and commiseration have gotten me through tough times. This is for my students and mentees, who have taught me so much and reminded me that there can be joy in exploring the universe. This is for Dave and Jannie, who have always made their home a place of comfort for me. This is for Erin-Kate and Sofie, who helped me navigate difficult situations. This is for Erin at the Writing Center and Cassandra at the CTLO and their invaluable advice. This is for Ernie, who warmed my heart with his daily call of "mija" and warmed my stomach with nopales tacos. This is for Gita, Judy, JoAnn, Joy, Nam, and Mika, whose logistical prowess have helped me manage everything from reimbursements to reservations. This is for Grisela and Mauricio, who always

made time to chat with me even as they did the undervalued work of maintaining Cahill so that I and others could do astronomy research. This is for the cashier at AU79 (RIP to the AU79 on Colorado) who got me through writing my qual report, and for the workers at Twinkle Tea on Lake who have gotten me through writing this thesis. This is for the folks at Hangar 18 and at The Aerial House (especially my teachers Anna and Nicole, and all the lovely people I've taken classes with), who have done more for my mental health than they will ever know.

This is for Pinoy astronomers past, present, and future. May there be many more of us!

This is for those who have come before me, upon whose bodies and lands modern astronomy has been built. My work is the direct material product of a long history of settler-colonialism: throughout this degree, I have lived as a settler on the traditional and unceded territory of the Tongva peoples, and the astronomical observations described in this thesis were only possible because of the dispossession of Maunakea from Kānaka Maoli. This thesis is for them, and for all those who work to dismantle systems of oppression inside and outside astronomy.

This is for Janosz, my favorite person. Thank you for never giving up on me.

Finally, this thesis is and has always been for my family. This is for Tatay, whose example is one of the reasons I convinced myself I could get a PhD—maraming salamat po for all the conversations during our long walks, and for the reminder to "do good science and the rest will follow." This is for Nanay, whose efficiency I try to live up to every day—maraming salamat po for teaching me to read and write, and for being my first ever reviewer (for my second-grade "research articles" about Saturn's moons). This is for Yon-Soo, the strongest woman I have ever met—고마워 언니 for always supporting me, and for reminding me that life is far more than the world of academia. This is for Miguel, who is proof that kind men exist in the world—thanks for all the academia-related memes. And this is for Mireya-baby, whose creativity inspires me every day—thanks for reminding me that things will always work out.

Mahal na mahal ko kayong lahat.

ABSTRACT

Low-mass "dwarf" galaxies are numerous, diverse, and relatively simple, making them excellent laboratories for understanding both stellar and galactic evolution. Dwarf galaxies (galaxies with stellar masses $10^7 - 10^9\ M_\odot$) in the nearby universe (out to distances of $\sim$ 10 Mpc from our own Milky Way, or redshifts $z \lesssim 0.01$), are a particularly interesting population due to their proximity, which allows us to study them in detail on both spatially-resolved and global scales. In this thesis, I present a variety of observational studies investigating star formation and chemical enrichment within nearby dwarf galaxies.

I first use the chemical abundances of individual stars within Local Group dwarf spheroidal galaxies (dSphs) to understand how past stars lived and died. I use this "galactic archaeology" approach to test theoretical models of Type Ia supernovae by investigating the nucleosynthetic products of these supernovae. For example, using medium-resolution spectra from DEIMOS, I measure manganese abundances that place observational constraints on the masses of Type Ia progenitors. I also describe a novel method to measure the delay-time distribution of Type Ia SNe in an individual dSph, which probes the number of white dwarfs involved in Type Ia SNe. Finally, I show how galactic archaeology can also be used to trace star formation using a simple chemical evolution model.

For more distant galaxies, in which individual stars cannot be resolved, galaxy properties can be measured on larger scales. Using the integral field spectrograph KCWI, I produce spatially-resolved maps of dwarf galaxies located in extremely under-dense regions called cosmic voids. The dynamical properties of these galaxies provide insight into the formation of dwarf galaxies in the absence of large-scale environmental effects. On even larger spatial scales, I use photometry to measure the global properties of galaxies and understand the physical processes that drive star formation on galaxy-wide scales.

These studies pave the way for future work with ongoing and upcoming surveys that will map out our local universe—and the dwarf galaxies around us—in unprecedented detail.

PUBLISHED CONTENT AND CONTRIBUTIONS

de los Reyes, M. A. C. et al. (2022). "Simultaneous Constraints on the Star Formation History and Nucleosynthesis of Sculptor dSph." *ApJ* 925.1, 66, p. 66. DOI: 10.3847/1538-4357/ac332b.
MAdlR participated in the conception of the project, analyzed the data, and wrote the bulk of the manuscript.

de los Reyes, M. A. C. et al. (2020). "Manganese Indicates a Transition from Sub- to Near-Chandrasekhar Type Ia Supernovae in Dwarf Galaxies." *ApJ* 891.1, p. 85. DOI: 10.3847/1538-4357/ab736f.
MAdlR participated in the conception of the project, obtained and analyzed the data, and wrote the bulk of the manuscript.

de los Reyes, M. A. C. and R. C. Kennicutt (2019). "Revisiting the Integrated Star Formation Law. I. Non-starbursting Galaxies." *ApJ* 872.1, p. 16. DOI: 10.3847/1538-4357/aafa82.
MAdlR analyzed the data and wrote the bulk of the manuscript.

CONTENTS

LIST OF FIGURES

LIST OF TABLES

Chapter 1

INTRODUCTION

Low-mass "dwarf" galaxies[1] are excellent laboratories for conducting experiments in galaxy evolution. Not only are they the most numerous type of galaxy in the universe—outnumbering Milky Way-mass galaxies by a factor of ∼1000—dwarf galaxies also have a wide variety of properties (e.g., stellar masses, star formation rates, metallicities; McConnachie 2012). This diversity is useful for testing how star formation and chemical evolution vary across a wide range of galactic environments. Additionally, dwarf galaxies also tend to have fairly simple evolutionary histories (Weisz et al. 2014), making them easier to physically interpret than more massive galaxies with complex accretion or merger histories (e.g., Kruijssen et al. 2019). Indeed, the ΛCDM paradigm implies that more massive galaxies formed from smaller systems (White and Frenk 1991), so understanding the formation and evolution of dwarf galaxies is prerequisite to understanding the evolution of galaxies like our own Milky Way.

A useful framework for galaxy evolution, illustrated in Figure 1.1, can be developed by considering the baryonic matter (i.e., non-dark matter) within a galaxy. Inside all star-forming galaxies, baryonic matter is constantly cycling between two phases of matter: stars and the interstellar medium (ISM). The ISM, which is predominantly gas, contains the raw material that forms stars; stars produce heavy elements throughout their lifetimes, then release them back into the ISM when they die. This cycle is not closed—stars can also produce outflows that remove gas from a galaxy (Larson 1974; Mathews and Baker 1971), and inflows of gas can add metal-poor material to a galaxy (Dekel et al. 2009; Larson 1972). It is also not the only physical process driving galaxy evolution—environmental effects such as galaxy mergers (e.g., Tinsley and Larson 1979) and ram pressure stripping (e.g., Lin and Faber 1983), and activity driven by supermassive black holes (Fabian 2012) may have dramatic impacts on a galaxy's history. Yet this cycle of star formation and chemical enrichment underpins the evolution of every galaxy.

This thesis comprises a number of observational studies of local dwarf galaxies. As

[1]The definition of "dwarf" galaxies can vary significantly; throughout this thesis, I consider "classical" dwarf galaxies with stellar masses $< 10^9\ M_\odot$.

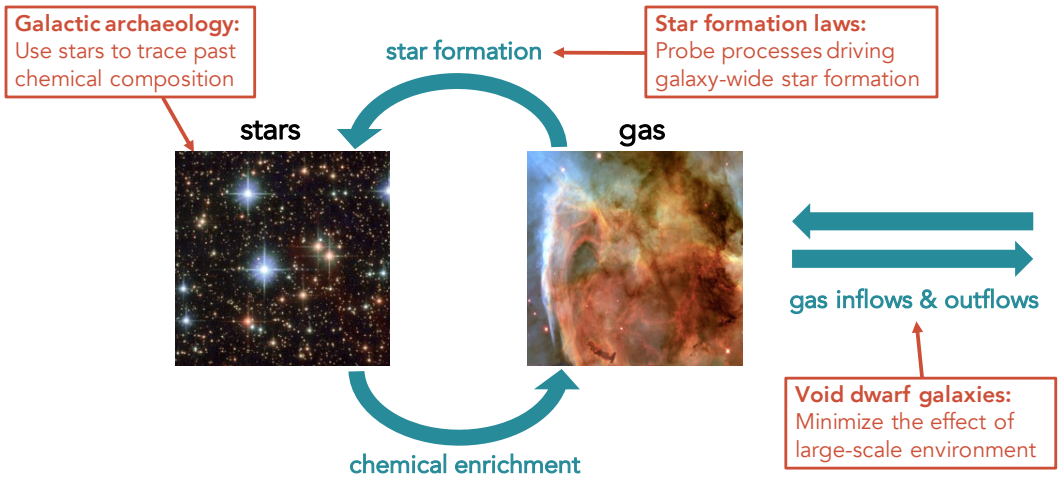

Figure 1.1: The cycle of star formation and chemical enrichment in a galaxy, through which baryons shift between stars and the ISM. This is not a closed-box cycle: gas inflows and outflows add and remove baryonic material from the galaxy. Red labels indicate the different topics of this thesis and show how they are connected to this cycle. Public domain images used with credit to ESA/NASA and Hubble.

shown in Figure 1.1, these studies are all connected with this cycle of baryonic matter in dwarf galaxies, either aiming to: (1) use this cycle as a tool for investigating how *stellar evolution* contributes to a galaxy's history, and/or (2) understand the *galactic evolution* processes that drive the cycle itself. In the following sections, I introduce the astrophysical context for each of these studies.

1.1 Galactic archaeology

First, we can use the cycle of chemical enrichment to do "galactic archaeology." This method is, in many ways, directly analogous to archaeology on Earth: as generations of humans live, they create items; when they die, they leave their creations for the next generations. Archaeologists aim to identify these items—buildings, art, remains, and other artifacts—and piece together how past humans lived and died. Similarly, as generations of stars live, they produce heavy elements (or "metals," to use the historical astronomical term for elements more massive than helium); when they die, they release these metals into the ISM to be incorporated in the next generation of stars. As a result, the stars that we observe today carry the chemical imprint of the stars that came before them, allowing galactic archaeologists to identify the metals produced by past stars in order to study how they lived and died.

This thesis involves two distinct galactic archaeology studies, both of which use the chemical abundance patterns within individual Local Group dwarf galaxies. First,

I address a major open question in *stellar evolution*: what is the primary physical mechanism of Type Ia supernovae? Second, I use chemical abundances to constrain a galaxy's overall *galactic evolution* by measuring its star formation history.

1.1.1 Type Ia supernovae

Type Ia supernovae (Ia SNe) have long been understood to be the thermonuclear explosions of white dwarfs. Their ability to be empirically normalized to the same peak luminosity (e.g., Phillips 1993) has made them indispensible astrophysical tools as "standardizable candles" for measuring cosmological distances. Indeed, Type Ia SNe were used in the Nobel Prize-winning discovery of the accelerating expansion of the Universe (Perlmutter et al. 1999; Riess et al. 1998).

Although Type Ia SNe are largely consistent with white dwarf explosions driven by carbon ignition in an electron-degenerate gas, the fundamental physics governing Type Ia SNe—particularly the actual explosion mechanism—are still poorly constrained. The traditional paradigm of Type Ia SNe suggests that a thermonuclear supernova occurs when a single white dwarf (WD) accretes material from a non-degenerate companion star and undergoes runaway thermonuclear burning near the Chandrasekhar mass of $M_{\rm Ch} \approx 1.4\ M_{\odot}$.

Several problems persist with this paradigm. Simulated detonations of a $M_{\rm Ch}$ white dwarf tend to underproduce intermediate-mass elements (IMEs) such as silicon and sulfur that dominate observed Type Ia SNe light curves (e.g., Arnett et al. 1971). Near-Chandrasekhar mass white dwarfs also appear to be rare (e.g., Giammichele et al. 2012; Tremblay et al. 2016), and the accretion rate must be finely tuned to significantly increase the mass of an accreting white dwarf without igniting the accreting hydrogen (which may cause mass loss; e.g., Maoz et al. 2014; Shen and Bildsten 2007). Finally, this physical mechanism requires accretion from a companion star, but multiple nearby Type Ia SNe have been observed without companions. For example, low radio and X-ray fluxes from SN2011fe in M101 strongly disfavor the existence of a non-degenerate companion star (Margutti et al. 2012; Pérez-Torres et al. 2014), since strong emission in these wavelengths might be expected from the supernova shock interacting with a surviving companion star. Similarly, a non-degenerate companion might produce emission from stripped hydrogen, yet most Type Ia SNe show little to no Hα emission (e.g., Leonard 2007; Lundqvist et al. 2013; Shappee et al. 2018; Shappee et al. 2013).

Various models have attempted to resolve some of these discrepancies, largely by

tweaking the assumptions of a *prompt detonation* of a *single* white dwarf at the *Chandrasekhar* limit. For example, if a $M_{\rm Ch}$ white dwarf expands before detonation instead of promptly detonating, the expansion will produce low-density regions. These regions then provide ideal conditions for the nucleosynthesis of the missing IMEs (Seitenzahl and Townsley 2017). One way to achieve this scenario is by prolonging the explosion with the so-called "deflagration-to-detonation transition (DDT)" (Khokhlov 1991).

Alternatively, the rarity of $> 1\ {\rm M}_{\odot}$ white dwarfs suggests that many, if not most, Type Ia SNe are produced by the explosions of lower-mass WDs. One of the most favored models for exploding a single sub-$M_{\rm Ch}$ white dwarf is the "double detonation" model, in which the WD accretes helium from a He-rich companion, such as a non-degenerate He-star. The helium shell may detonate when it becomes massive enough, sending shocks through the white dwarf that explode it (Livne 1990; Nomoto 1982; Woosley et al. 1986). This model can successfully reproduce most observations of typical Type Ia SNe, including the nucleosynthesis of IMEs (e.g., Woosley and Kasen 2011).

Finally, a sub-$M_{\rm Ch}$ white dwarf can also explode if it has a second white dwarf companion. This "double degenerate" channel may account not only for the rarity of massive white dwarfs and the expected nucleosynthesis of IMEs, but also for the missing companion stars near some observed Type Ia SNe. Physically, a double degenerate explosion may be similar to the double detonation model described above, in which the primary WD accretes from a secondary He WD (e.g., Shen et al. 2018a). This model has been invoked to explain the discovery of hypervelocity white dwarfs, which are thought to be surviving donor companions of these "dynamically driven double-degenerate double-detonation" explosions (Shen et al. 2018b). Alternatively, binary sub-$M_{\rm Ch}$ white dwarfs can merge, form a super-$M_{\rm Ch}$ remnant, and undergo a deflagration-to-detonation transition (Iben and Tutukov 1984; Webbink 1984).

The abundances of heavy elements can be used to distinguish between these physical models. For example, the production of iron-peak elements (such as manganese) by a Type Ia SN is a strong function of the core density of the white dwarf progenitor (e.g., Seitenzahl and Townsley 2017). In Chapter 2, I use the nucleosynthetic yield of manganese from Type Ia SNe to identify whether near-$M_{\rm Ch}$ or sub-$M_{\rm Ch}$ are the dominant progenitors of these supernovae.

Another way to distinguish among different Type Ia SN models is to measure the Type Ia delay-time distribution (DTD) $\Psi(\tau)$, which describes the expected rate

of Type Ia SNe as a function of the delay-time after a δ-function burst of star formation. The form of the DTD, which can be traced by measuring the rate of Type Ia SNe, depends strongly on the number of white dwarfs involved in the explosion. Most measurements of Type Ia rates rely on large samples of galaxies, but galactic archaeology methods allow us to measure the Type Ia rate—and thus, the Type Ia DTD—in a single dSph galaxy. I present this new method in Chapter 3.

1.1.2 Chemical evolution models

We can also use galactic archaeology techniques to trace the cycle of chemical enrichment itself, by measuring how star formation rates change over time in a galaxy—the galaxy's star formation history (SFH). There are a number of methods for measuring galaxy SFHs. First, galaxy SFHs may be estimated by fitting integrated spectral energy distributions (SEDs) with models derived from stellar population synthesis (for reviews, see Conroy 2013; Walcher et al. 2011). The SEDs may be composed of broadband photometry (e.g., Smith and Hayward 2015) or a continuous spectrum of the integrated light of the galaxy's stars and ionized gas (e.g., Magris C. et al. 2015). Although this method is useful for obtaining SFHs of distant, unresolved galaxies, it depends strongly on prior assumptions about the model SFHs (Carnall et al. 2019; Leja et al. 2019), as well as the stellar initial mass function (Conroy and Van Dokkum 2012, among others).

For nearby galaxies that can be resolved photometrically, SFHs can be more robustly derived by fitting isochrones, which depend on stellar ages and metallicities, to observed color-magnitude diagrams (CMDs). This method has been used to measure SFHs of many of the galaxies in the Local Group (e.g., Weisz et al. 2014). However, this method struggles to obtain precise SFHs for galaxies with predominantly old or metal-poor populations, because isochrones are roughly logarithmically spaced in age and metallicity. For example, the difference between otherwise identical isochrones at 11 Gyr compared to 13 Gyr (i.e., 10-20% accuracy and precision) is only a few hundredths of a magnitude in commonly used broadband filters—smaller than the discrepancies between sets of isochrones modeled by different stellar evolution codes with the same parameters. Metal-poor isochrones ([Fe/H] $\lesssim -2$) similarly bunch together in the CMD. One mitigation strategy is to obtain spectroscopic abundances for individual stars. These abundances can be used to fix the metallicities (and sometimes detailed abundance ratios) of the isochrones so that the problem is reduced to measuring age alone rather than age and metallicity simultaneously. This technique works either by measuring the ages of individual stars

with known spectroscopic metallicities (Kirby et al. 2017) or by using a spectroscopic metallicity distribution of a representative subset of the stars being fit in the CMD (e.g., Brown et al. 2014).

Galactic chemical evolution (GCE) models represent a complementary approach to measuring SFHs. By modeling nucleosynthetic events that occur throughout a galaxy's history, GCE models predict stellar abundance trends that can then be compared with abundances measured from observed stellar spectra. Stellar abundance trends are sensitive to the SFH because different types of nucleosynthetic events occur at different delay times after a burst of star formation (e.g., Gilmore and Wyse 1991; Tinsley 1979). For example, core-collapse supernovae (CCSNe) explode on short timescales of tens of millions of years after a burst of star formation. The α-elements (e.g., Mg, Ca, Si, Ti) that are predominantly produced in CCSNe are therefore indicators of the chemical enrichment that most immediately follows an episode of star formation. Iron-peak elements, on the other hand, are largely produced by Type Ia SNe. Since nucleosynthetic yields from Type Ia SNe dominate at late times ($\gtrsim$ 100 Myr after star formation; see, e.g., Maoz and Mannucci 2012), iron-peak elements trace the most delayed times in a galaxy's SFH.

As I demonstrate in Chapter 4, useful constraints on the SFH can be obtained by modeling chemical abundances produced by a variety of nucleosynthetic events.

1.2 Dwarf galaxies in cosmic voids

As we have seen in the previous section, galactic archaeology is conceptually possible because of the cycle of star formation and chemical enrichment within a galaxy. In the next sections, I describe other studies that, rather than using this cycle as a tool, aim to learn about the cycle and its role in galaxy evolution.

As shown in Figure 1.1, a primary feature of the flow of baryonic matter in a galaxy is that it is not a closed cycle. Galaxies affect their surroundings—through, e.g., outflows of gas—and are in turn affected by their environments. This is especially true for dwarf galaxies, which are particularly susceptible to environmental influences. Due to their small gravitational potential wells, they tend to be more strongly influenced by outflows of metal-enriched gas (or inflows of pristine gas) and are therefore more metal-poor than massive galaxies (Tremonti et al. 2004). We see detailed examples of this environmental dependence in our own Local Group, where more isolated dwarf galaxies tend to be gas-rich star-forming dwarf irregular galaxies (dIrrs), while Milky Way satellite galaxies are typically gas-poor dwarf

spheroidals (dSphs) (e.g., Grcevich and Putman 2009; Spekkens et al. 2014).

However, the exact role of environment in dwarf galaxy evolution remains unclear. Wheeler et al. (2017) found that the kinematic distinction between Local Group dSphs and dIrrs is not as pronounced as previously thought, suggesting that the differences between the two populations are not necessarily due to the direct environmental effect of tidal interactions (often referred to as "tidal stirring," e.g., Mayer et al. 2001). Furthermore, recent surveys have suggested that the Local Group may be an outlier galaxy ecosystem; for example, the SAGA survey (Geha et al. 2017) has recently found some evidence that the majority of satellite galaxies around Milky Way analogs may be star-forming despite their proximity to $M^\star$ galaxies (Mao et al. 2021)—though see also, e.g., Font et al. (2022), who suggest that the discrepancy observed by SAGA may be a selection effect.

One way to disentangle the effect of environment in galaxy evolution is to study systems in which potential environmental effects are minimized. This requires looking beyond our own neighborhood: even the handful of currently-known Local Group dwarf galaxies that are relatively isolated (i.e., not clearly associated with either the Milky Way or M31) are still within $\sim$ 1 Mpc of the nearest $L^\star$ galaxy (McConnachie et al. 2021). Even the most distant dwarf galaxies in the Local Group could be "backsplash galaxies" that may have interacted with an $L^\star$ host in the past (Teyssier et al. 2012). We instead search for dwarf galaxies in the lowest-density environments in the universe: cosmic voids. The vast majority of the matter in the universe resides in filaments in the so-called "cosmic web" (Bond et al. 1996), but galaxies can still be found in the large ($\gtrsim$ 10 Mpc) and underdense ($\rho_{\rm void} \sim 0.1\rho_{\rm avg}$) voids between filaments. By definition, dwarf galaxies in cosmic voids may be $\gtrsim$ 5 Mpc from other galaxies—perhaps as far removed from the external influences of other galaxies as possible in the local universe—making them an ideal population for observing how galaxies evolve in near-total isolation.

Even void dwarf galaxies that are not perfectly isolated systems may still be valuable for understanding galaxy formation. The ΛCDM cosmological model predicts that galaxies in such low-density environments will evolve more slowly due to longer timescales between galaxy-galaxy interactions (Goldberg and Vogeley 2004). At least superficially, most void dwarf galaxies appear to be optically blue, compact, and actively star forming, suggesting that they are indeed less evolved than their field counterparts (e.g., Grogin and Geller 1999, 2000; Kreckel et al. 2012). This implies that these galaxies might be direct physical analogues to the high-redshift

galaxies that are the building blocks for Milky Way-like galaxies.

There is significant motivation to study void dwarf galaxies in order to understand galaxy formation and evolution. I have led an observational program to obtain integral field spectroscopy for a sample of local void dwarf galaxies, and I present the first results from this dataset in Chapter 5.

1.3 Star formation laws

Another important component of the cycle of baryonic matter is the process of star formation. The timescales for chemical enrichment are largely set by the lifetimes of stars, which are well-described by stellar physics and are largely a function of stellar mass. The rate of star formation on galaxy-wide scales therefore drives the overall rate of this cycle.

Although the global star formation rate (SFR) of a galaxy is likely set by a balance of complex physical processes, the nature of the overall relationship between SFR and the ISM can be parameterized by simple empirical scaling laws. One such law is the relationship between gas density and star formation rate density, known as the star formation law or Schmidt law (Schmidt 1959). The Schmidt law was originally posed as a power law relationship between volume densities, but Schmidt (1963) recast it as a relation between surface densities Σ:

$$\Sigma_{\rm SFR} = A(\Sigma_{\rm gas})^n, \tag{1.1}$$

where both quantities are integrated measurements of global galaxy properties.

Kennicutt (1998) found that quiescent spiral galaxies, infrared-luminous starbursts, and circumnuclear starbursts[2] obeyed a tight relationship defined by Equation 6.1 with power-law index $n = 1.4 \pm 0.15$. This Schmidt law may imply either that the local density of gas drives star formation efficiency $\epsilon \equiv \Sigma_{\rm SFR}/\Sigma_{\rm gas}$ in a "bottom-up" formulation, or that star formation is driven by "top-down" dynamical processes (Kennicutt and Evans 2012). Regardless of its physical interpretation, this law has been widely applied as a recipe for star formation in cosmological simulations, many of which lack the spatial resolution needed to model complex sub-grid physics.

Since 1998, investigations of the global star formation law have raised additional questions about the nature of star formation. For instance, low surface brightness

[2]Throughout this thesis, I define "starburst" as a system with an SFR much higher than the long-term average SFR of the system; in comparison, a "quiescent" galaxy has an SFR roughly consistent with an equilibrium system.

galaxies show evidence for a turnover in the star formation law at low gas surface densities (Wyder et al. 2009). At the high-density end, infrared-luminous starburst galaxies may define a star formation law that bifurcates from that for normal disk galaxies (Daddi et al. 2010; Genzel et al. 2010), though this may depend on the treatment of the CO-to-H_2 conversion factor $X(\mathrm{CO})$ (Narayanan et al. 2012). Other scaling laws have also been proposed, including relationships between SFR and *dense* gas mass (Gao and Solomon 2004) or between SFR and a combination of gas and stellar surface densities (e.g., Kim and Ostriker 2015; Shi et al. 2011).

These developments motivate a fresh investigation of the global star formation law, and improvements in available multi-wavelength data now make it possible to carry out a more comprehensive analysis. I undertake this updated study in Chapter 6. Not only do I revisit the Milky Way-like spiral galaxies originally studied by Kennicutt (1998) with a larger sample and more accurate data, but I also measure the global star formation law in a consistent way for dwarf galaxies. Such a comparison can determine whether the physical processes that drive star formation on galaxy-wide scales differ among different galaxy populations.

1.4 Thesis outline

The structure of this thesis is as follows. The first section of this thesis focuses on galactic archaeology in Local Group dwarf spheroidal galaxies using the chemical compositions of *individual stars*. I place observational constraints on the physics of Type Ia SNe by measuring the nucleosynthetic yields of manganese (Chapter 2) and the Type Ia delay-time distribution (Chapter 3). In Chapter 4, I use a chemical evolution model to reproduce the abundance trends of an unprecedentedly large number of elements in Sculptor dSph, leading to a precise measurement of Sculptor's star formation history.

The second section of this thesis aims to study more distant galaxies on a larger spatial scale, using integrated field spectroscopy to produce *spatially-resolved maps* of galactic properties. In Chapter 5, I obtain spatially-resolved measurements of stellar kinematics of dwarf galaxies located in underdense cosmic voids. These measurements provide a point of direct comparison with simulations, enabling me to test hypotheses about how stellar structures form in dwarf galaxies.

The final section of this thesis zooms out even further to study *global properties* of galaxies in the local universe. In Chapter 6, I use multi-wavelength photometric measurements to re-measure the global star formation law for Milky Way-like spiral

galaxies and to extend the star formation law to a sample of local dwarf galaxies.

Finally, in Chapter 7, I summarize my main results and describe possible next steps for each of the projects outlined in this thesis. I end by discussing future prospects for studying dwarf galaxies in the local universe, with a particular focus on how ongoing and upcoming surveys will further our understanding of these useful systems in the next decade.

Chapter 2

USING MANGANESE TO PROBE THE MASS OF TYPE IA SUPERNOVA PROGENITORS

de los Reyes, M. A. C. et al. (2020). "Manganese Indicates a Transition from Sub- to Near-Chandrasekhar Type Ia Supernovae in Dwarf Galaxies." *ApJ* 891.1, p. 85. DOI: 10.3847/1538-4357/ab736f.

Mithi A. C. de los Reyes[1], Evan N. Kirby[1,2], Ivo R. Seitenzahl[3], Ken J. Shen[4]

[1]Department of Astronomy, California Institute of Technology, 1200 E California Blvd, Pasadena, CA, 91125, USA

[2]Department of Physics, University of Notre Dame, Notre Dame, IN, 46556, USA

[3]School of Science, University of New South Wales, Australian Defence Force Academy, Canberra, ACT 2600, Australia

[4]Department of Astronomy and Theoretical Astrophysics Center, University of California Berkeley, CA 94720, USA

Abstract

Manganese (Mn) abundances are sensitive probes of the progenitors of Type Ia supernovae (SNe). In this work, we present a catalog of manganese abundances in dwarf spheroidal satellites of the Milky Way, measured using medium-resolution spectroscopy. Using a simple chemical evolution model, we infer the manganese yield of Type Ia SNe in the Sculptor dwarf spheroidal galaxy (dSph) and compare to theoretical yields. The sub-solar yield from Type Ia SNe ($[\mathrm{Mn/Fe}]_{\mathrm{Ia}} = -0.30^{+0.03}_{-0.03}$ at [Fe/H] = −1.5 dex, with negligible dependence on metallicity) implies that sub-Chandrasekhar-mass (sub-M_{Ch}) white dwarf progenitors are the dominant channel of Type Ia SNe at early times in this galaxy, although some fraction ($\gtrsim$ 20%) of M_{Ch} Type Ia or Type Iax SNe are still needed to produce the observed yield. First-order corrections for deviations from local thermodynamic equilibrium increase the inferred $[\mathrm{Mn/Fe}]_{\mathrm{Ia}}$ by as much as $\sim$ 0.3 dex. However, our results also suggest that the nucleosynthetic source of Type Ia supernovae may depend on environment. In particular, we find that dSph galaxies with extended star formation histories (Leo I, Fornax dSphs) appear to have higher [Mn/Fe] at a given metallicity than galaxies with early bursts of star formation (Sculptor dSph), suggesting that M_{Ch} progenitors may become the dominant channel of Type Ia SNe at later times in a galaxy's chemical evolution.

2.1 Introduction

As described in Chapter 1, the nucleosynthetic yields of elements produced by Type Ia SNe can be used to constrain the panoply of theoretical Type Ia SN models. While these abundances can be measured directly in spectra of supernovae or supernova remnants, these direct observations are inherently limited by the rarity of Type Ia SNe, and many abundances are difficult to determine from direct spectroscopy. The focus of this paper is to instead indirectly infer nucleosynthetic yields from ancient stars, because the abundances of these stars are linked to the chemical evolution of a galaxy.

2.1.1 Measuring nucleosynthesis with dwarf galaxies

The chemical evolution of a galaxy is largely driven by enrichment from supernovae. Core-collapse supernovae are driven by the deaths of the most massive stars in a galaxy, which begin very early in a galaxy's history. Type Ia supernovae, on the other hand, can only begin to explode much later, after lower-mass stars die and create white dwarfs.

Both Type Ia and core-collapse SNe produce iron. Throughout the lifetime of a galaxy, SNe will therefore produce an increase in the overall abundance of iron, [Fe/H][1]. However, because Type Ia and core-collapse SNe have different nucleosynthetic products, the abundance of other elements relative to iron will change once Type Ia SNe begin to explode. In particular, since dwarf spheroidal (dSph) galaxies have low star formation rates, their chemical evolution is dominated at late times by Type Ia SNe rather than by core-collapse SNe. As [Fe/H] increases over time, the relative abundance of an element relative to iron will approach the Type Ia yield. The yields of various elements can then be used to infer properties of Type Ia SNe alone (McWilliam et al. 2018).

Furthermore, the abundance contributions specifically from Type Ia SNe ($f_{\rm Ia}$) can be computed using the well-constrained theoretical yields of various elements from core-collapse SNe. Once the Type Ia SNe yields are disentangled from core-collapse SNe yields, measurements of different elemental abundances can be used to infer properties of Type Ia SNe alone. Kirby et al. (2019) originally performed this analysis for several iron-peak elements (Cr, Co, Ni), fitting a simple chemical decomposition model to determine $f_{\rm Ia}$ and measure the absolute Type Ia yields of these elements.

[1]Throughout this paper, we use bracket abundances referenced to solar (e.g., [Fe/H] = $\log_{10}(n_{\rm Fe}/n_{\rm H})_* - \log_{10}(n_{\rm Fe}/n_{\rm H})_\odot$), where $n_{\rm X}$ is the atomic number density of X. Solar abundances are adopted from Asplund et al. (2009).

These yields suggested that sub-$M_{\rm Ch}$ white dwarfs are the dominant progenitors of Type Ia SNe in dwarf galaxies at early times. Kirby et al. (2019) also found that galaxies with star formation lasting for several Gyr have higher [Ni/Fe] abundances than galaxies with an early burst of star formation, potentially indicating that the dominant Type Ia supernova channel depends on star formation history.

2.1.2 Manganese

In this work, we aim to extend the analysis of Kirby et al. (2019) to manganese (Mn), which is a particularly sensitive probe of the physics of Type Ia SNe (Seitenzahl et al. 2009, 2013a, 2015). Like the other iron-peak elements, the production of Mn is dominated by Type Ia rather than core-collapse SNe. Furthermore, the only stable isotope of manganese, ^{55}Mn, is produced via nucleosynthetic pathways that are strongly dependent on the density of the progenitor white dwarf.

Nearly all ^{55}Mn is produced as its radioactive parent nucleus ^{55}Co, which can be produced in low entropy ("normal") freeze-out from nuclear statistical equilibrium at densities $\rho \gtrsim 2 \times 10^8$ g cm^{-3} (Seitenzahl and Townsley 2017). Higher yields of ^{55}Co and therefore ^{55}Mn can be achieved if silicon does not completely burn, while lower yields can be achieved at high entropy and low density, where the presence of protons during "alpha-rich" freeze-out ultimately destroys ^{55}Co via the reaction ^{55}Co(p,γ)^{56}Ni (Seitenzahl et al. 2013a). In white dwarfs well below $M_{\rm Ch}$, ^{55}Co is generally produced at densities below nuclear statistical equilibrium, producing lower yields of ^{55}Mn.

In other words, stable Mn is more likely to be synthesized in near-$M_{\rm Ch}$ white dwarfs than in sub-$M_{\rm Ch}$ progenitors. The observed yield of Mn from Type Ia SNe is therefore physically significant—higher yields suggest $M_{\rm Ch}$ explosions, while lower yields may indicate sub-$M_{\rm Ch}$ models. To that end, there is significant interest in measuring stellar manganese abundances.

Previous works have presented conflicting results of Mn measurements in nearby dSphs. North et al. (2012) compiled literature Mn abundances and used high-resolution spectroscopy to measure additional Mn abundances for stars in Sculptor ($N = 50$) and Fornax ($N = 60$) dSphs. They concluded that the Mn abundances imply sub-solar [Mn/Fe] ratios, and that the specific trend of [Mn/Fe] vs [Fe/H] implies a metallicity-dependent Mn yield from Type Ia SNe. However, the North et al. (2012) measurements used high-resolution spectroscopy and were largely limited to higher-metallicity stars ([Fe/H] $\gtrsim -1.75$), making it difficult to precisely

constrain the trend of [Mn/Fe] over a large range of [Fe/H].

On the other hand, Kobayashi et al. (2015) used a different sample to suggest that high Mn abundances point to dense Type Ia SNe, and that a special class of near-$M_{\rm Ch}$ "Type Iax" SNe are needed to produce enough Mn to match observations. Cescutti and Kobayashi (2017) made a similar argument for a combination of "normal" and "Iax" SNe using Mn abundances for $N = 20$ stars in the dSph Ursa Minor. In both studies, the observations are too incomplete to draw any significant conclusions.

In this paper, we increase the sample size and parameter space of these literature Mn abundances by using medium-resolution spectra to extend to fainter and more metal-poor stars in dSph galaxies. We then use these measurements to distinguish between different Type Ia SNe models. Our observations are described in Section 2.2. In Section 2.3, we describe our pipeline for measuring Mn abundances, validate our measurement technique using globular clusters, and present Mn abundances for stars in classical dSph galaxies. We use a simple chemical evolution model to infer Mn yields from Type Ia SNe in Section 2.4 before discussing the implications for Type Ia SN physics in Section 2.5. Finally, we summarize our conclusions in Section 2.6.

2.2 Observations

Unlike literature catalogs, which generally use high-resolution spectra to measure abundances, this work aims to use medium-resolution spectra to measure Mn abundances. Medium-resolution spectroscopy was performed using the DEep Imaging Multi-Object Spectrograph (DEIMOS; Faber et al. 2003) on the Keck II telescope. Spectra were obtained for red giant branch (RGB) stars in several globular clusters and classical dSphs. Table 2.1 lists the observations of the globular clusters and dSphs used in this work.

Our target selection prioritizes globular clusters and dSphs previously observed with the red 1200G grating on DEIMOS. We used a combination of old and newly designed slitmasks. Kirby et al. (2009, 2010, 2016) presented 1200G observations of bscl5, bfor7, n5024b (previously called ng5024), 7078l1, and 7089l1. The masks LeoIb, CVnIa, and bumia are very similar to other masks observed by Kirby et al. (2010), but previous observations allowed us to determine membership for some stars. We designed the new masks to have fewer non-members and more confirmed members. We did the same for UMaIIb, where Simon and Geha (2007) observed the previous slitmasks for Ursa Major II.

The previous references describe the membership selection, which we adopt here.

In general, members were selected to have radial velocities within $3\sigma_v$ of the mean velocity. They were also required to have colors and magnitudes consistent with the red giant branches of their respective galaxies.

In this work, we used the 1200B grating, which was commissioned in September 2017. The grating has a groove spacing of 1200 mm^{-1} and a blaze wavelength of 4500 Å. It provides a dispersion of 0.34 Å pixel^{-1} for first-order light. The FWHM of the line spread function is about 1.1 Å. The corresponding resolving power at 5000 Å is $R = \lambda/\Delta\lambda = 4500$. In contrast to DEIMOS's previous complement of gratings, 1200B provides higher resolution than 900ZD and higher throughput at $\lambda < 6000$ Å than 1200G.

We used a central wavelength of 5200 Å, which provided an approximate spectral range of 3900–6500 Å, but the exact spectral range for each slit depended on the location of the slit on the slitmask. The variation in the starting and ending wavelengths was as much as 250 Å. The GG400 order-blocking filter eliminated light bluer than 4000 Å so that second-order light did not contaminate our spectra.

Table 2.1 details the observations for each field. We observed one slitmask per globular cluster or dwarf galaxy. The coordinates indicate the center of the slitmasks, not necessarily the centers of the stellar systems. The distances are taken from Harris (1996) for globular clusters and McConnachie (2012) for dwarf galaxies. The number of stars represents the total number of slits, including both members and non-members of the corresponding stellar systems. We also report the average airmass and seeing (where available) for the observations.

All observations were reduced using a version of the `spec2d` pipeline (Cooper et al. 2012; Newman et al. 2013). The pipeline traces the edges of the slits with the help of a spectrally dispersed image of a quartz continuum lamp. The same spectral frame provides for flat fielding. We used separate exposures of Ne, Ar, Kr, Xe, and Hg arc lamps for wavelength calibration. We identified arc lines with the help of the NIST atomic spectra database (Kramida et al. 2014). After flat fielding and wavelength calibration, the `spec2d` pipeline performs sky subtraction in 2-D and then extracts the spectra into 1-D. We modified `spec2d` in several ways to improve the reliability of the wavelength solution for the 1200B grating. Most notably, we changed one of the subroutines that determined whether an arc line should be included in the wavelength calibration so that usable arc lines were not discarded erroneously.

Table 2.1: Spectroscopic targets for manganese abundance measurements.

Object	RA (J2000)	Dec (J2000)	Dist. (kpc)	Slitmask	$N_{\rm stars}$	Date	Airmass	Seeing (")	Exposures (s)
				Globular clusters					
M53 (NGC 5024)	$13^{\rm h}12^{\rm m}55^{\rm s}$	+18°09'59"	17.9	n5024b	182	2019 Mar 10	1.0	1.6	5×1200
						2019 Mar 11	1.0	0.9	1×404
M15 (NGC 7078)	$21^{\rm h}29^{\rm m}49^{\rm s}$	+12°10'20"	10.4	7078l1	175	2017 Sep 15	1.1	0.6	13×1200
M2 (NGC 7089)	$21^{\rm h}33^{\rm m}15^{\rm s}$	−00°48'36"	11.5	7089l1	157	2017 Oct 3	1.1	...	3×1200, 1×1800
				dSphs					
Sculptor	$00^{\rm h}59^{\rm m}57^{\rm s}$	−33°41'45"	86	bscl5	97	2018 Aug 14	1.8	0.8	3×1500
						2018 Sep 10	1.8	0.7	3×1800, 1×860
						2018 Sep 11	1.8	0.8	2×1800
Fornax	$02^{\rm h}39^{\rm m}49^{\rm s}$	−34°30'35"	147	bfor7	154	2018 Aug 14	1.8	0.9	2×1560, 1×1440
						2018 Sep 10	1.8	0.7	2×1320, 2×1620
						2018 Sep 11	2.0	0.8	2×1980
Ursa Major II	$08^{\rm h}52^{\rm m}48^{\rm s}$	+63°05'54"	32	UMaIIb	21	2019 Feb 6	1.5	...	3×1740
Leo I	$10^{\rm h}08^{\rm m}29^{\rm s}$	+12°18'56"	254	LeoIb	137	2018 Mar 19	1.3	0.8	2×1620, 1×1560
						2019 Feb 6	1.1	...	2×1860, 1×1920
						2019 Mar 12	1.2	0.8	3×1800, 2×1500
Canes Venatici I	$13^{\rm h}28^{\rm m}03^{\rm s}$	+33°32'44"	218	CVnIa	125	2018 Mar 19	1.1	0.7	3×1680, 2×1860
						2018 May 20	1.0	1.0	1×1200, 2×906
						2019 Mar 12	1.2	0.8	6×1800
Ursa Minor	$15^{\rm h}08^{\rm m}32^{\rm s}$	+67°11'03"	76	bumia	135	2019 Mar 12	1.5	1.4	4×1800, 2×2100

DEIMOS uses active flexure compensation to keep the data frames aligned within ~ 0.1 pixel in both the spatial and spectral directions. The flexure compensation allowed us to stack the 2-D images taken within the same week. However, the compensation becomes unreliable beyond about a week. Over longer timescales, the heliocentric velocity correction varies too much to stack images. Therefore, we reduced images taken within the same week into 1-D spectra. For slitmasks observed over multiple weeks, we coadded the 1-D spectra after correcting for the change in the heliocentric reference frame.

2.3 Abundance measurements

2.3.1 Description of pipeline

In this section, we describe the analysis pipeline used to obtain Mn abundances from the reduced and corrected spectra. Broadly speaking, this pipeline fits synthetic spectra with variable Mn abundances to an observed spectrum and uses least-squares fitting to determine the Mn abundance.

Inputs

The main inputs to this pipeline are a line list—a list of atomic and molecular lines in the spectral regions of interest—and estimates of stellar parameters.

To create our line list, we considered 10Å-wide spectral regions around strong Mn lines. Our list of strong Mn lines was initially produced from all Mn absorption lines within the DEIMOS spectral range (≈4500-6500Å) from the NIST Atomic Spectra Database[2]. This line list was then vetted by determining which lines were likely to be useful for distinguishing Mn abundances.

First, 10Å-wide spectral regions centered on each Mn line were synthesized and smoothed to match DEIMOS resolution. To determine which Mn lines would be sensitive to a 0.5 dex change in metallicity, we estimated the relative change in line strength for each line:

$$\Delta(f_\lambda) = \frac{f_\lambda([\mathrm{Mn/H}] = 0) - f_\lambda([\mathrm{Mn/H}] = -0.5)}{f_\lambda([\mathrm{Mn/H}] = 0)}, \tag{2.1}$$

where $f_\lambda([\mathrm{Mn/H}] = X)$ denotes the flux decrement of the synthetic spectral line at λ assuming a manganese abundance of $[\mathrm{Mn/H}] = X$. Lines were discarded from the list if $\Delta(f_\lambda)$ was smaller than a threshold value of 1%.

[2]The NIST Atomic Spectra Database is available at `https://www.nist.gov/pml/atomic-spectra-database`.

Table 2.2: Manganese spectral lines.

Wavelength Å	Excitation Potential eV
4739.1	2.914
4754.0	2.282
4761.5	2.953
4762.3	2.889
4765.8	2.941
4766.4	2.920
4783.4	2.300
4823.5	2.320
5399.5	3.850
5407.3	2.143
5420.3	2.143
5516.8	2.178
5537.7	2.187
6013.5	3.072
6016.6	3.075
6021.8	3.075
6384.7	3.772
6491.7	3.763

We further determined which Mn lines were likely to be useful by synthesizing spectra using the known Mn abundances of the Sun and of Arcturus and directly comparing each line with the observed spectra of these stars. Any manganese absorption lines for which the amplitudes or shapes of the synthetic spectral lines were strongly inconsistent with the observed spectra were discarded.

Finally, resonance lines (lines with excitation potential 0 eV) were removed from the line list. These lines have been known to yield significantly lower Mn abundances compared to those measured from higher-excitation lines (e.g., Bonifacio et al. 2009; Sneden et al. 2016). Resonance lines are also the most sensitive to deviations from local thermodynamic equilibrium ("non-LTE (NLTE) effects"; e.g., Bergemann and Gehren 2008; Bergemann et al. 2019). We discuss other potential implications of non-LTE effects in Section 2.5.3.

In total we consider 18 Mn lines, described in Table 2.2. We note that hyperfine structure (HFS) can increase the line strength at fixed abundance, producing Mn abundance corrections of up to $\sim$ 1.5 dex (North et al. 2012). To account for this,

Table 2.3: Full line list.

Wavelength Å	Species[a]	Excitation Potential eV	log gf
4729.019	26.0	4.073	-1.614
4729.040	58.1	3.708	-2.780
4729.042	23.0	2.264	-4.909
4729.046	25.1	6.139	-2.998
4729.049	68.0	1.069	-0.037
4729.128	90.0	0.966	-1.221
4729.136	42.0	2.597	-0.785
4729.168	26.0	4.473	-2.658
4729.186	20.0	5.049	-4.150
4729.200	21.0	1.428	-0.530

[a] Atomic species are denoted using the MOOG (Sneden et al. 2012) format of $Z.i$, where Z is the atomic number of the element and i is its ionization state.

Note: Only a portion of Table 2.3 is shown here; it is published in its entirety in a machine-readable format online.

we used Mn HFS lines from the database maintained by R. L. Kurucz[3].

Atomic and molecular lines from other species within the 10Å-wide spectral regions were taken from manually-vetted solar absorption line lists from Escala et al. (2019), with oscillator strengths tuned to match high-resolution spectra of the Sun, Arcturus, and metal-poor globular cluster stars. The full line list used in this work is enumerated in Table 2.3.

The other required input to the pipeline is a list of stellar parameters. Values for these stellar parameters (effective temperature $T_{\rm eff}$, surface gravity $\log(g)$, iron-to-hydrogen ratio [Fe/H], α-to iron ratio [α/Fe], and microturbulent velocity ξ) are adopted from Kirby et al. (2010) for dSph galaxies, and from Kirby et al. (2016) for globular clusters. Microturbulent velocity ξ is calculated from the surface gravity using the empirical formula from Kirby et al. (2009).

[3]The Kurucz line list database is available at `http://kurucz.harvard.edu/linelists.html`

Continuum normalization

Using the input line list and stellar parameters, the automated pipeline can fit synthetic spectra to an observed spectrum. First, the observed spectrum must be corrected for the slowly-varying global continuum. To do this, the pipeline synthesizes a spectrum with the same stellar parameters as the observed spectrum, but with a solar Mn abundance. The synthetic spectrum is linearly interpolated from pre-generated spectral grids as in Kirby et al. (2016).

The synthetic spectrum is then interpolated and smoothed using a Gaussian kernel to match the wavelength array and resolution of the observed spectrum. The observed spectrum is divided by the smoothed synthetic spectrum, masking out ±1Å regions around Mn lines and other regions with significant continuum fluctuations (e.g., ±5 pixel regions near the CCD chip gap, ±5Å regions around the Hα, Hβ, and Hγ Balmer lines, ±8Å regions around the strong Na D doublet at $\lambda\lambda$5890, 5896Å, and any pixels with negative inverse variances). A cubic spline is fit to the unmasked portions of this quotient with breakpoints every 150 pixels (66Å). The original observed spectrum is divided by the spline, which represents the global continuum, to obtain the continuum-normalized spectrum.

Spectral synthesis and fitting

Synthetic spectra can now be produced and fit to the continuum-normalized observed spectrum. Based on the input stellar parameters, stellar atmosphere models are linearly interpolated from the ATLAS9 grid of one-dimensional plane-parallel stellar atmosphere models (Kurucz 1993). Using these stellar atmosphere models and the line lists described in Section 4.4.2, synthetic spectra with varying Mn abundances are produced using the spectral synthesis code MOOG (Sneden et al. 2012). To decrease computation time, only spectral regions ±10Å around the Mn lines are synthesized.

As in the continuum normalization process, these synthetic regions are interpolated and smoothed to match the observed spectrum. The pipeline then fits the synthetic regions to the observed spectrum. To determine the best-fitting Mn abundance, a Levenberg-Marquardt least-squares fitting algorithm is used to minimize the χ^2 statistic, with Mn abundance as the free parameter. This is implemented using Python's `scipy.optimize.curve_fit` function (Jones et al. 2001–).

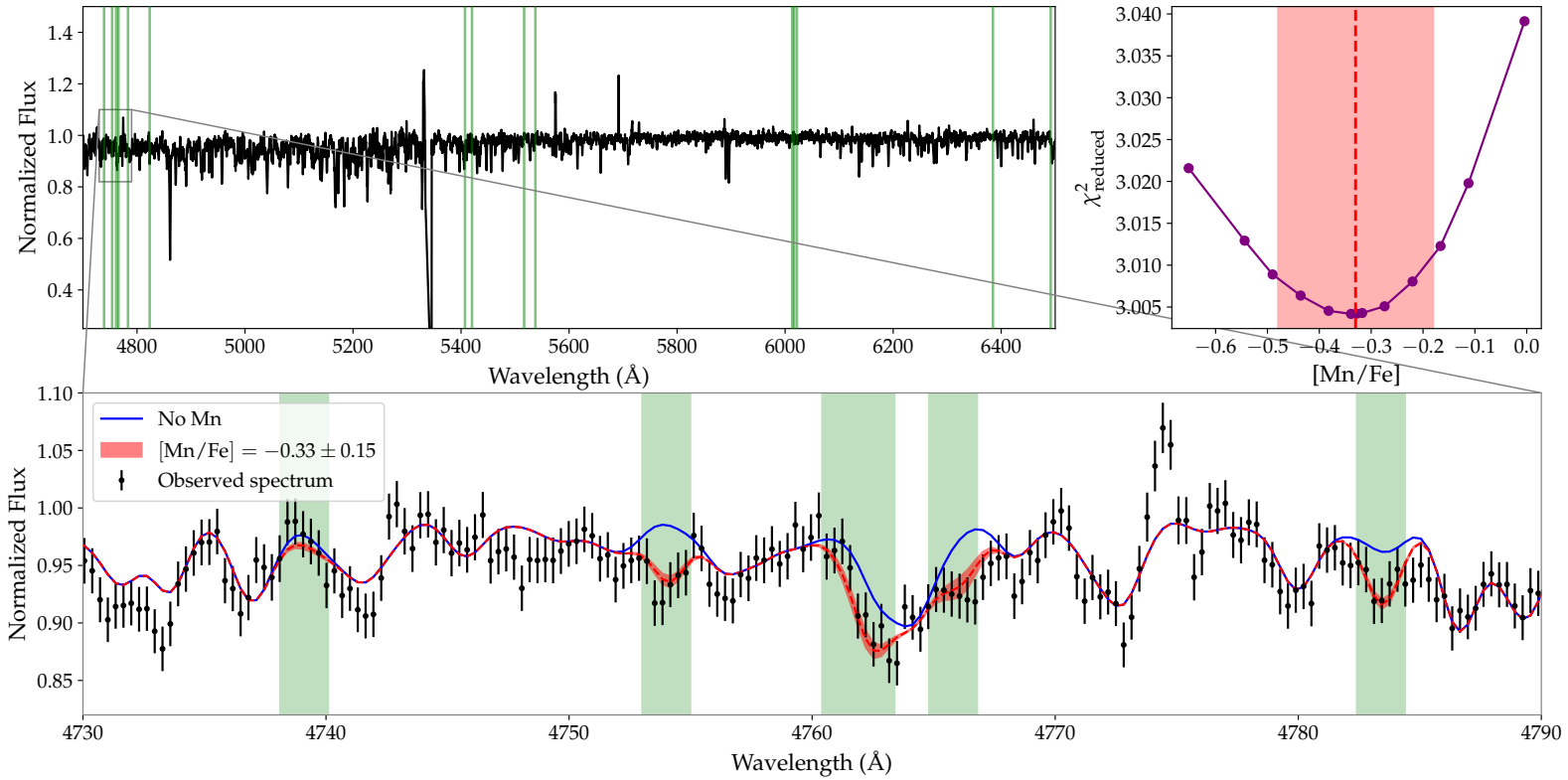

Figure 2.1: Example DEIMOS stellar spectrum with manganese abundance measurement. Top left: Full continuum-normalized observed spectrum for an example star in Sculptor dSph with a high (> 84th percentile in our sample) signal/noise ratio $S/N = 67$. Green shaded regions indicate manganese lines. Top right: Reduced χ^2 as a function of [Mn/Fe]. Shaded region indicates $\pm 1\sigma$ confidence interval. Bottom: Zoomed-in portion of the observed spectrum (black points), again with green shaded vertical bars indicating manganese lines. The median and $\pm\sigma_{\rm stat}$ best fit is indicated by the red shaded region, while the blue line indicates a fit with negligible [Mn/Fe] ([Mn/H] = −10) for comparison.

Examples of the best-fit (continuum-normalized) spectra and reduced χ^2 contour are shown for one star in Figure 2.1. The χ^2 contours of each star were manually inspected, and any stars whose χ^2 contours lacked a clear minimum were removed from analysis. Stars with a fitting error larger than 0.3 dex (a factor of ~ 2) were also removed.

2.3.2 Uncertainty analysis

In this section, we first discuss the sources of statistical and systematic uncertainty in our measurements of [Mn/Fe]. We then validate our pipeline and assumed uncertainties by comparing our measurements of [Mn/Fe] with measurements from high-resolution spectroscopy.

Statistical uncertainty

The statistical uncertainty is dominated by the spectral noise. This manifests in our [Mn/Fe] measurements when fitting synthetic spectra to the observed spectra, since the least-squares statistic is weighted by the uncertainties in the spectra. The statistical uncertainty $\sigma_{\rm stat}$ is therefore given by the square root of the diagonal values of the covariance matrix, which is generated by the `scipy.optimize.curve_fit` function. The average statistical uncertainty in our [Mn/Fe] measurements is $\langle\sigma_{\rm stat}\rangle = 0.17$ dex.

Systematic uncertainty

There are several potential sources of systematic uncertainty in our measurement pipeline. Uncertainties in the input stellar parameters, as well as our choice of line list, atmosphere models, and spectral synthesis code can all produce systematic errors in our [Mn/Fe] measurements. We consider some of these sources here.

Atmospheric parameter uncertainties

As described in Section 4.4.2, our [Mn/Fe] measurements require inputs of stellar parameters $T_{\rm eff}$, $\log g$, ξ, [Fe/H], and [α/Fe] in order to synthesize spectra. We assumed fixed values of these parameters, but variations in the atmospheric parameters ($T_{\rm eff}$, $\log g$, ξ) may affect abundance measurements ([Fe/H], [α/Fe], [Mn/Fe]).

We can estimate the effect of varying atmospheric parameters on our [Mn/Fe] measurement. Since the [Mn/Fe] measurement pipeline also requires an input value of [Fe/H], we must first consider how errors in atmospheric parameters ($T_{\rm eff}$, $\log g$) may affect [Fe/H].

Table 2.4: Effect of varying atmospheric parameters on [Mn/Fe] measurements.

Object	ID	δ[Mn/Fe]			
		$T_{\rm eff}$ ± 125 K	$T_{\rm eff}$ ± 250 K	$\log g$ ± 0.3 dex	$\log g$ ± 0.6 dex
Scl	1003702	0.02	0.04	0.02	0.05
Scl	1007989	0.01	0.03	0.01	0.01
Scl	1009387	0.00	0.01	0.02	0.03
Scl	1009510	0.01	0.03	0.02	0.02
Scl	1011529	0.02	0.04	0.04	0.05
Scl	1014514	0.02	0.03	0.02	0.03
Scl	1004020	0.02	0.04	0.02	0.02
Scl	1004084	0.03	0.05	0.01	0.01
Scl	1004448	0.01	0.04	0.04	0.07
Scl	1004645	0.03	0.04	0.01	0.02

Note: Only a portion of Table 2.4 is shown here; it is published in its entirety in a machine-readable format online.

We note that we do not consider the effect of varying atmospheric parameters on [α/Fe]. To some extent, measurements of [α/H], [Mn/H], and [Fe/H] will be similarly affected by variations in the atmospheric parameters. We therefore expect that uncertainties in atmospheric parameters will contribute less significantly to errors in abundance ratios like [α/Fe] and [Mn/Fe] than in [Fe/H].

For all stars in our sample, Kirby et al. (2010) estimated the effect of varying $T_{\rm eff}$ and $\log g$ on [Fe/H]. Using these estimates, we can directly quantify systematic errors due to uncertainties in atmospheric parameters: we change $T_{\rm eff}$ by ±125 and ±250 K, apply the resulting changes to [Fe/H] (Table 6 of Kirby et al. 2010), then run our pipeline and measure the final variation in [Mn/Fe]. We repeat this procedure for $\log g$, changing $\log g$ by ±0.3 and ±0.6 dex. When varying $\log g$, we also vary microturbulent velocity ξ using the calibration derived by Kirby et al. (2009):

$$\xi \ (\mathrm{km\ s^{-1}}) = 2.13 - 0.23 \log g. \tag{2.2}$$

We report the response of [Mn/Fe] to changes in atmospheric parameters for a representative subsample of stars in Sculptor dSph, shown in Table 2.4. The values listed in this table are the average absolute values of the changes in [Mn/Fe] caused by varying $T_{\rm eff}$ or $\log g$.

The responses of [Mn/Fe] to variations in atmospheric parameters are approximately linear within $T_{\rm eff}$ ± 250 K and $\log g$ ± 0.6 dex. On average, [Mn/Fe] changes by

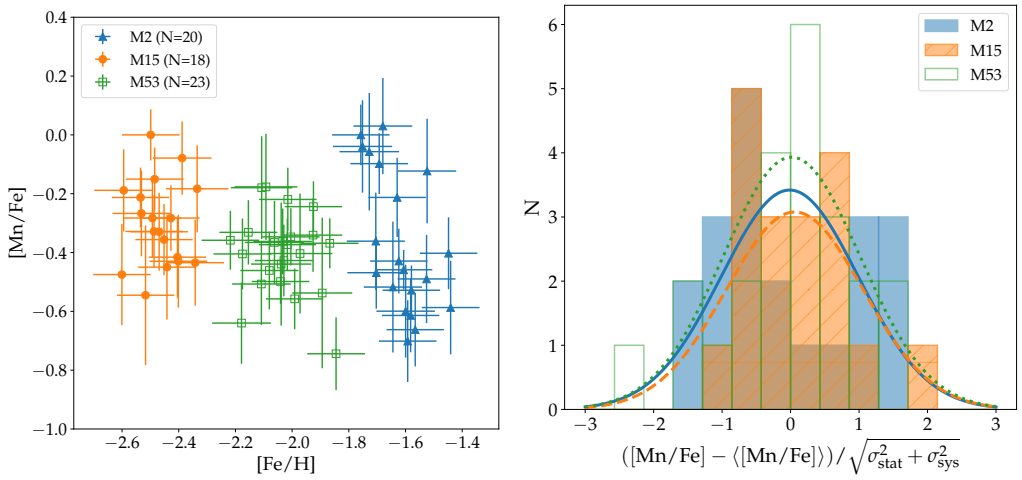

Figure 2.2: Manganese abundance measurements from globular clusters. Left: Globular cluster [Mn/Fe] abundances measured from medium-resolution spectra as a function of total metallicity [Fe/H]. Right: Distribution of deviation from the mean [Mn/Fe], in units of "total error" (including both statistical and systematic error). Lines indicate best-fit normal distributions $\mathcal{N}(0, 1)$.

± 0.014 dex per ± 100 K change in $T_{\rm eff}$. Similarly, [Mn/Fe] changes by ± 0.008 dex per ± 1 dex change in $\log g$. These responses are relatively small compared to the average statistical error ($\langle \sigma_{\rm stat} \rangle = 0.17$ dex), suggesting that any systematic errors in our [Mn/Fe] measurements due to errors in stellar parameters are negligible. As expected, varying $T_{\rm eff}$ and $\log\ g$ affects [Mn/Fe] significantly less than [Fe/H]; Kirby et al. (2010) found [Fe/H] changed by ± 0.092 dex per ± 100 K change in $T_{\rm eff}$ and ± 0.039 dex per ± 1 dex change in $\log g$.

Error floor estimation using globular clusters

Uncertainty in stellar parameters is unlikely to be the only source of systematic uncertainty. However, quantifying all individual sources of the systematic error budget is beyond the scope of this paper. We instead estimate the value of a *total* systematic error $\sigma_{\rm sys}$ by assuming globular clusters have no intrinsic dispersion in [Mn/Fe]. This $\sigma_{\rm sys}$ subsumes the error from atmospheric parameter variation discussed above, and can be added as an "error floor" to the statistical uncertainties to estimate final uncertainties.

To compute $\sigma_{\rm sys}$, we assume that globular clusters have little intrinsic dispersion in [Mn/Fe]. This assumption does not hold for all stellar abundances; for example, M2 (NGC 7089) appears to host two populations of stars with distinct C, N, Ba, and Sr abundances, suggesting that M2 has a complex star formation history (e.g.,

Lardo et al. 2013). Similarly, M15 (NGC 7078) also displays star-to-star variation in heavy elements (e.g., Sneden et al. 1997). However, since manganese is an iron-peak element and should be formed in the same sites as iron, we expect each globular cluster to display roughly zero intrinsic dispersion in [Mn/Fe] abundance.[4]

Following the procedure of Kirby et al. (2010) and Duggan et al. (2018), the assumption of no intrinsic dispersion in [Mn/Fe] suggests that our measurements of [Mn/Fe] should be distributed normally about some mean $\langle$[Mn/Fe]$\rangle$ with standard deviation equal to the combined statistical and systematic errors:

$$\text{stddev}\left(\frac{\text{[Mn/Fe]} - \langle\text{[Mn/Fe]}\rangle}{\sqrt{\sigma_{\text{stat}}^2 + \sigma_{\text{sys}}^2}}\right) = 1. \tag{2.3}$$

The value of σ_{sys} can then be computed from Equation 2.3.

This calculation yields $\sigma_{\text{sys}} = 0.19, 0.14, 0.05$ dex for M2, M15, and M53, respectively. To visualize this, the left panel of Figure 2.2 displays the measured [Mn/Fe] abundances for these globular clusters. The right panel of Figure 2.2 shows distributions of deviation from the average [Mn/Fe] (i.e., [Mn/Fe] $-$ $\langle$[Mn/Fe]$\rangle$) in units of the total error $\sqrt{\sigma_{\text{stat}}^2 + \sigma_{\text{sys}}^2}$ for each cluster. The distributions for M15 and M53 are well-fit by a Gaussian with a standard deviation $\sigma = 1$, as expected. M2, on the other hand, appears to have a bimodal distribution of [Mn/Fe]. This may be a result of poor membership selection; M2 has a low radial velocity ($|v_r| \lesssim 5$ km s^{-1}; e.g., Baumgardt and Hilker 2018), so velocity selection criteria may have falsely included foreground stars as cluster members.

Based on the intrinsic dispersions of [Mn/Fe] within globular clusters M15 and M53, we estimate an average total systematic [Mn/Fe] error of $\sigma_{\text{sys}} = 0.10$ dex. This total systematic error is comparable with the statistical error from fitting ($\langle\sigma_{\text{stat}}\rangle \sim 0.17$ dex on average). The systematic error and statistical error are added in quadrature to obtain the total error. We use the total [Mn/Fe] errors for the remainder of our analysis.

We note that one of the most significant systematic assumptions in our analysis pipeline is the assumption of local thermodynamic equilibrium (LTE). Estimating non-LTE corrections for each of the stars in our sample is beyond the scope of this work, particularly since such corrections depend on both T_{eff} and [Mn/Fe], and

[4]Some clusters do have abundance spreads in iron: ω Centauri (e.g., Johnson and Pilachowski 2010), M54 (Carretta et al. 2010), and Terzan 5 (e.g., Massari et al. 2014). However, these unusual cases are not in our sample.

Table 2.5: Literature high-resolution spectroscopy catalogs.

Reference	Object	N	Atmospheres[a]	Code[b]
		Globular clusters		
Yong et al. (2014)	M2	2	ATLAS9	MOOG
Sobeck et al. (2006)	M15	2	ATLAS9	MOOG
		dSphs		
North et al. (2012)	Sculptor, Fornax	5	MARCS	MOOG, CALRAI
Shetrone et al. (2003)	Fornax, Leo I	2	MARCS	MOOG
Frebel et al. (2010)	Ursa Major II	1	ATLAS9	MOOG

[a] ATLAS9: Castelli and Kurucz (2003), `http://kurucz.harvard.edu/grids.html`;
MARCS: Gustafsson et al. (1975, 2003, 2008), `http://marcs.astro.uu.ee`

[b] MOOG: Sneden et al. (2012); CALRAI: Spite (1967). North et al. (2012) used CALRAI for initial abundance measurements and MOOG for HFS corrections.

Note: In all literature catalogs listed here, $T_{\rm eff}$ was measured by requiring Fe I excitation equilibrium, $\log g$ was measured by requiring Fe I and Fe II ionization balance, and ξ was measured by removing abundance trends as a function of equivalent width.

are different for each Mn line. We instead estimate the overall effect of non-LTE corrections on our results by applying a statistical correction, which we discuss later in Section 2.5.3.

Validation with high-resolution spectroscopy comparison

We now validate our pipeline by comparing our [Mn/Fe] measurements, which are derived from medium-resolution spectra (MRS), with measurements from high-resolution spectra (HRS). From the literature, we find $N = 12$ stars in our sample that have HRS measurements; this small sample size is largely due to manganese's weak lines in the blue part of the optical wavelength range, which make it difficult to measure manganese from HRS. In Table 2.5, we list the literature catalogs that contain HRS measurements for these 12 stars. In Table 2.6, we list the MRS and HRS measurements of [Mn/Fe] for these stars, as well as the stellar parameters used in the HRS measurements.

Table 2.6: Comparison between DEIMOS abundances and literature high-resolution abundances.

Object	ID	Reference	HRS[b]					MRS
			$T_{\rm eff}$	$\log g$	ξ	[Fe/H]	[Mn/Fe][a]	[Mn/Fe]
M2	An08-A1045	Yong et al. (2014)	4275	0.70	1.78	−1.66	−0.41 ± 0.13	−0.49 ± 0.18
M2	An08-A13934	Yong et al. (2014)	4325	1.30	1.88	−0.97	−0.32 ± 0.16	−0.60 ± 0.19
M15	33889	Sobeck et al. (2006)	4350	0.60	1.65	−2.59	−0.06 ± 0.13	+0.00 ± 0.13
M15	41376	Sobeck et al. (2006)	4225	0.30	1.85	−2.44	−0.31 ± 0.13	−0.36 ± 0.16
Scl	1008833	North et al. (2012)	...	...	...	...	−0.27 ± 0.10	−0.18 ± 0.15
Scl	1005457	North et al. (2012)	...	...	...	...	−0.21 ± 0.12	−0.52 ± 0.15
For	37141	North et al. (2012)	...	...	...	...	−0.43 ± 0.11	−0.05 ± 0.14
For	54557[c]	North et al. (2012)	...	...	...	...	−0.23 ± 0.09	−0.24 ± 0.19
For	67094	North et al. (2012)	...	...	...	...	−0.39 ± 0.12	−0.10 ± 0.24
For	54557[c]	Shetrone et al. (2003)	4025	0.00	2.00	−1.21	−0.40 ± 0.11	−0.24 ± 0.19
LeoI	S60286	Shetrone et al. (2003)	4250	0.80	2.20	−1.52	−0.35 ± 0.11	−0.41 ± 0.18
UMaII	176_103	Frebel et al. (2010)	4550	1.00	2.20	−2.34	−0.56 ± 0.25	−0.31 ± 0.17

[a] Although the errors on HRS [Mn/Fe] measurements were computed differently in each of the literature sources, for the most part all HRS catalogs have accounted for both statistical error (i.e., uncertainty from different Mn lines) as well as systematic error (including uncertainty from stellar parameters) in their error estimates. The only exception is the North et al. (2012) catalog, which does not report errors on total [Mn/Fe] abundances; for these abundances, the errors listed are only the *statistical* errors, estimated as the standard deviation of abundances measured from different Mn lines.

[b] Sobeck et al. (2006) obtained stellar parameters from Sneden et al. (1997). The stellar parameters used by North et al. (2012) are not publicly available.

[c] The star 54557 has two separate HRS measurements from North et al. (2012) and Shetrone et al. (2003). We list them as separate entries for completeness.

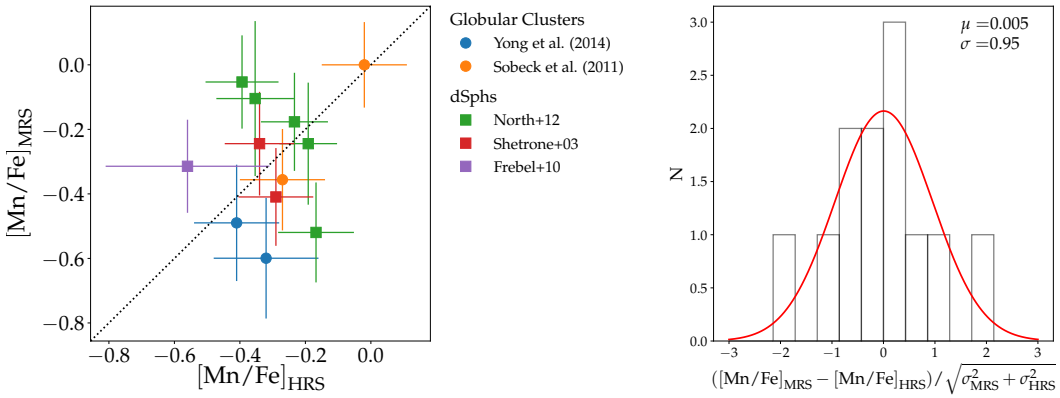

Figure 2.3: Comparison between medium-resolution and high-resolution spectroscopic measurements. Left: Comparison between our [Mn/Fe] measurements from medium-resolution spectra ($[\mathrm{Mn/Fe}]_{\mathrm{MRS}}$) and literature measurements from high-resolution spectra ($[\mathrm{Mn/Fe}]_{\mathrm{HRS}}$). The dotted line denotes the 1:1 line; circles (squares) denote stars from globular clusters (dSphs). Right: Histogram of the differences between medium-resolution and high-resolution [Mn/Fe] measurements. The red line denotes the best-fit Gaussian distribution.

The left panel of Figure 2.3 compares our MRS measurements ($[\mathrm{Mn/Fe}]_{\mathrm{MRS}}$) with the literature HRS measurements ($[\mathrm{Mn/Fe}]_{\mathrm{HRS}}$). The difference between these measurements ($[\mathrm{Mn/Fe}]_{\mathrm{MRS}} - [\mathrm{Mn/Fe}]_{\mathrm{HRS}}$) is on average -0.03 dex. This is significantly smaller than the median MRS and HRS errors reported for this comparison sample ($\sigma_{\mathrm{median,MRS}} \sim 0.10$ dex and $\sigma_{\mathrm{median,HRS}} \sim 0.16$ dex, respectively), suggesting that the MRS and HRS measurements are largely consistent. However, there is no clear correlation between the MRS and HRS measurements, likely because our comparison sample is small and covers only a narrow range of [Mn/Fe].

Assuming that both MRS and HRS measurements have accurately estimated the total (including statistical and systematic) errors, the differences between MRS and HRS measurements ($[\mathrm{Mn/Fe}]_{\mathrm{MRS}} - [\mathrm{Mn/Fe}]_{\mathrm{HRS}}$) should be distributed normally about mean zero with standard deviation equal to the combined MRS and HRS errors ($\sqrt{\sigma^2_{\mathrm{HRS}} + \sigma^2_{\mathrm{MRS}}}$).

To check this, we plot a histogram of the differences between MRS and HRS measurements in the right panel of Figure 2.3. The best-fit Gaussian distribution to this histogram (red line) has a mean of 0.005 dex and a standard deviation 0.95 dex, similar to the expected normal distribution $\mathcal{N}(0, 1)$. This suggests that the total errors in our [Mn/Fe] measurements are consistent with HRS errors.

We note that many of the HRS measurements use resonance lines, which are particu-

larly sensitive to NLTE effects (Bergemann et al. 2019); as discussed in Section 4.4.2, we remove resonance Mn lines from our line list for that reason. This may also contribute to systematic offsets between our MRS measurements and HRS literature measurements. Furthermore, the HRS measurements are not a flawless comparison set; the HRS catalogs use heterogeneous measurement techniques, which may introduce additional systematic offsets among catalogs.

2.3.3 Manganese abundance catalog

Finally, we present all manganese abundances measured from medium-resolution spectra in Table 2.7. We list here the stellar parameters $T_{\rm eff}$, $\log(g)$, [Fe/H], $[\alpha/{\rm Fe}]$, and ξ (from Kirby et al. 2010) used as inputs in the pipeline to measure [Mn/Fe], as well as the total error in [Mn/Fe] ($\sigma = \sqrt{\sigma_{\rm sys}^2 + \sigma_{\rm stat}^2}$).

The full catalog contains manganese abundance measurements of 61 stars from 3 globular clusters and 161 stars from 6 dSph galaxies. This is one of the largest self-consistent samples of dwarf galaxy manganese abundances measured to date. As previously noted, high-resolution measurements are often heterogenous in their assumptions (e.g., Table 2.6). The internal consistency of this catalog makes it particularly useful for galactic archaeology studies that require statistical samples of abundances. In the next sections, we use our sample of [Mn/Fe] abundances in dSphs for such a study.

Table 2.7: Manganese abundance catalog of GC and dSph stars.

Object	ID	$T_{\rm eff}$ (K)	$\log g$ [cm s^{-2}]	ξ (km s^{-1})	[α/Fe] (dex)	[Fe/H] (dex)	[Mn/Fe][a] (dex)
				Globular clusters			
M15	15681	5275 ± 35	+3.02 ± 0.10	1.43 ± 0.10	+0.18 ± 0.10	−2.39 ± 0.10	−0.08 ± 0.16
M15	31227	4470 ± 19	+1.06 ± 0.10	1.89 ± 0.06	+0.23 ± 0.09	−2.49 ± 0.10	−0.33 ± 0.16
M15	33889	4820 ± 25	+1.72 ± 0.10	1.73 ± 0.07	+0.44 ± 0.09	−2.50 ± 0.10	+0.00 ± 0.13
M15	36569	4409 ± 20	+0.86 ± 0.10	1.94 ± 0.06	+0.22 ± 0.09	−2.52 ± 0.10	−0.55 ± 0.26
M15	37854	4963 ± 48	+2.09 ± 0.10	1.65 ± 0.08	+0.50 ± 0.10	−2.59 ± 0.10	−0.19 ± 0.17
				dSphs			
Scl	1003702	4660 ± 54	+1.58 ± 0.10	1.77 ± 0.07	+0.31 ± 0.14	−1.95 ± 0.11	−0.52 ± 0.22
Scl	1007989	4849 ± 92	+2.12 ± 0.10	1.64 ± 0.08	+0.22 ± 0.31	−1.42 ± 0.13	−0.23 ± 0.22
Scl	1009387	4597 ± 101	+1.53 ± 0.10	1.65 ± 0.08	+0.01 ± 0.25	−1.50 ± 0.21	−0.43 ± 0.21
Scl	1009510	4677 ± 57	+1.76 ± 0.10	1.81 ± 0.07	+0.20 ± 0.13	−1.80 ± 0.11	−0.31 ± 0.21
Scl	1011529	4510 ± 54	+1.29 ± 0.10	1.72 ± 0.07	−0.02 ± 0.15	−1.48 ± 0.11	−0.41 ± 0.15

[a] The errors reported here are total errors (statistical and systematic errors added in quadrature). The statistical (fitting) errors can be obtained by removing the contribution from the systematic error, which we estimate (cf. Section 3.2.3) to be $\sigma_{\rm sys} = 0.10$ dex.

Note: Only a portion of Table 2.7 is shown here; it is published in its entirety (including coordinates) in a machine-readable format online.

2.4 Manganese yields in Sculptor

2.4.1 Inferring [Mn/Fe] yields from a simple chemical evolution model

With our measured manganese abundances, we can now estimate how much of this manganese is produced by Type Ia supernovae. Following the procedure of Kirby et al. (2019), we determined Type Ia SN yields of manganese by assuming a simple chemical evolution model. We refer readers to Kirby et al. (2019) for a more detailed discussion of this model, but summarize this procedure briefly here.

This simple model assumes that core-collapse supernovae (CCSNe) are the only nucleosynthetic sources at early times, and that CCSN yields are independent of total metallicity ([Fe/H]). The stars formed at such early times will have low [Fe/H]; furthermore, these stars will all have the same chemical abundances determined by the CCSN yields. Put another way, for any element X, [X/Fe] will be constant as a function of [Fe/H] for low-[Fe/H] stars.

After some delay-time, Type Ia supernovae will begin to explode and produce different yields of element X. Therefore, for stars with metallicities above some threshold $[\mathrm{Fe/H}]_{\mathrm{Ia}}$, [X/Fe] will begin to deviate from the original CCSN-only value ($[\mathrm{X/Fe}]_{\mathrm{CC}}$). We can model this behavior with the following parameterization:

$$[\mathrm{X/Fe}] = \begin{cases} [\mathrm{X/Fe}]_{\mathrm{CC}} & [\mathrm{Fe/H}] \leq [\mathrm{Fe/H}]_{\mathrm{Ia}} \\ [\mathrm{Fe/H}] \tan\theta + \frac{b_\perp}{\cos\theta} & [\mathrm{Fe/H}] > [\mathrm{Fe/H}]_{\mathrm{Ia}} \end{cases} \tag{2.4}$$

where continuity is enforced at $[\mathrm{Fe/H}] = [\mathrm{Fe/H}]_{\mathrm{Ia}}$. As described in Kirby et al. (2019), the sloped line in the $[\mathrm{Fe/H}] > [\mathrm{Fe/H}]_{\mathrm{Ia}}$ regime is parameterized by an angle (θ) and perpendicular offset ($b_\perp$) rather than by a slope and intercept, in order to avoid biasing the linear fit toward shallower slopes (Hogg et al. 2010).

Using this model, the free parameters $[\mathrm{Fe/H}]_{\mathrm{Ia}}$, $b_\perp$, and θ can be determined by maximizing the likelihood function L (Eqs. 3-6 in Kirby et al. 2019). To do the fitting, we used the `emcee` Python module (Foreman-Mackey et al. 2013) to minimize $-\ln L$ by implementing a Markov chain Monte Carlo (MCMC) ensemble sampler. We ran 100 ensemble members or "walkers," each with 10^5 links sampled using a Metropolis-Hastings algorithm. We discarded the first 10^4 "burn-in" links.

We assumed uniform priors[5] on $b_\perp$ and θ, but we used the values of $[\mathrm{Fe/H}]_{\mathrm{Ia}}$ previously measured by Kirby et al. (2019)[6]. As in Kirby et al. (2019), we imposed

[5] Specifically, we assumed $b_\perp \sim \mathcal{U}\{-10, 10\}$ and $\theta \sim \mathcal{U}\{-\frac{\pi}{2}, \frac{\pi}{2}\}$.

[6] Note that Kirby et al. (2019) also imposed an additional prior on $\mathrm{Mg/Fe}_{\mathrm{CC}}$, since magnesium is almost entirely produced in core-collapse supernovae.

an additional prior to avoid negative values of the linear ratio $(\mathrm{Mn/Fe})_{\mathrm{Ia}}$, which are unphysical: if any step in the MCMC chain yields $(\mathrm{Mn/Fe})_{\mathrm{Ia}} < 0$, we set the likelihood equal to zero. We further imposed a prior on $(\mathrm{Mn/Fe})_{\mathrm{CC}}$:

$$P = \frac{1}{\sqrt{2\pi\sigma_{\mathrm{Mn}}}} \exp\left(-\frac{([\mathrm{Mn/Fe}]_{\mathrm{halo}} - [\mathrm{Mn/Fe}]_{\mathrm{CC}})^2}{2\sigma_{\mathrm{Mn}}^2}\right). \tag{2.5}$$

Based on high-resolution measurements of metal-poor stars in the Milky Way halo compiled in the online database JINAbase (Abohalima and Frebel 2018), we set $[\mathrm{Mn/Fe}]_{\mathrm{halo}} = -0.3$ and $\sigma_{\mathrm{Mn}} = 0.1$. We found that this additional prior on $(\mathrm{Mn/Fe})_{\mathrm{CC}}$ does not significantly affect our results, since the enforced continuity at $[\mathrm{Fe/H}]_{\mathrm{Ia}}$ requires a low inferred value of $(\mathrm{Mn/Fe})_{\mathrm{CC}}$.

The MCMC sampled the posterior distribution of the parameters $b_\perp$ and θ. The initial values of $b_\perp$ and θ were chosen by performing a simple linear fit to the [Mn/Fe] versus [Fe/H] trend for $[\mathrm{Fe/H}] > [\mathrm{Fe/H}]_{\mathrm{Ia}}$. Unless otherwise noted, for all quantities we report the median (50th percentile) value and 68% confidence intervals about the median.

For Sculptor, we find that [Mn/Fe] is near-constant as a function of [Fe/H], with $\theta = 1.61^{+2.45}_{-1.30}$ degrees and $b_\perp = -0.26^{+0.07}_{-0.05}$ dex. The data and corresponding best fit model are shown in the left panel of Figure 2.4. There are three high-[Mn/Fe] outliers, but removing them does not significantly change our main results, again due to the enforcement of continuity in our model.

Using this best fit model, we can infer the CCSN and Type Ia yields of manganese from the parameters $b_\perp$ and θ. As described in Kirby et al. (2019), the core-collapse yield of [Mn/Fe] can be calculated as

$$[\mathrm{Mn/Fe}]_{\mathrm{CC}} = \frac{b_\perp}{\cos\theta} + [\mathrm{Fe/H}]_{\mathrm{Ia}} \tan\theta. \tag{2.6}$$

The Type Ia yield can then be determined from

$$\left(\frac{\mathrm{Mn}}{\mathrm{Fe}}\right)_{\mathrm{Ia}} = \frac{R+1}{R}\left(\frac{\mathrm{Mn}}{\mathrm{Fe}}\right)_{\star} - \frac{1}{R}\left(\frac{\mathrm{Mn}}{\mathrm{Fe}}\right)_{\mathrm{CC}} \tag{2.7}$$

where $R \equiv \frac{\mathrm{Fe_{Ia}}}{\mathrm{Fe_{CC}}}$ is the amount of iron produced by Type Ia supernovae relative to iron produced by core-collapse supernovae. Note that Equation 2.7 does not use bracket notation, as it includes linear rather than logarithmic element ratios.

Using these equations, we compute the [Mn/Fe] yields for Sculptor. These are denoted in the right panel of Figure 2.4 by the blue and red shaded regions,

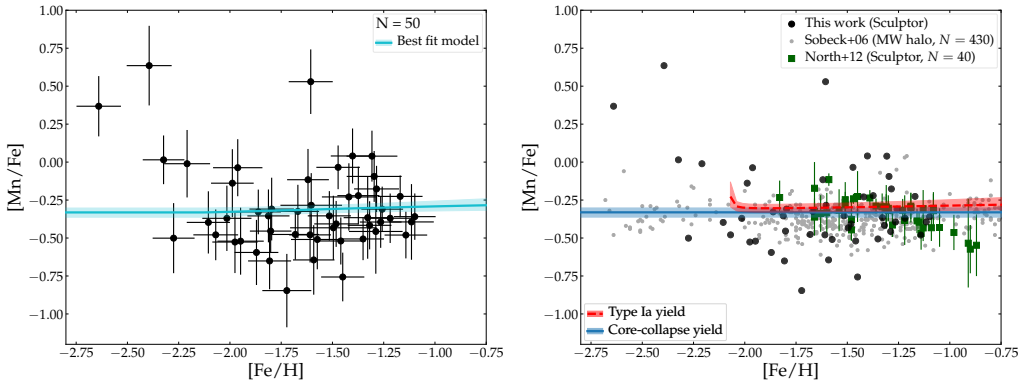

Figure 2.4: [Mn/Fe] as a function of [Fe/H] for Sculptor dSph. Left: Observed [Mn/Fe] as a function of [Fe/H] for Sculptor dSph (black points). The cyan solid line marks the median best-fit model, and the cyan shaded region denotes the 68% confidence interval about the median. Right: Same, but errorbars have been removed from black points for illustration purposes. The red dashed line and shaded region marks the Type Ia [Mn/Fe] yield, and the blue solid line and shaded region marks the core-collapse supernova [Mn/Fe] yield computed from the model. Green squares denote measurements for Sculptor dSph from North et al. (2012) (note that error bars only denote statistical rather than total errors); small gray points denote measurements of Milky Way halo globular cluster and field stars from Sobeck et al. (2006).

which represent the inferred CCSN and Type Ia SN yields, respectively. We find $[\mathrm{Mn/Fe}]_{\mathrm{CC}} = -0.33^{+0.03}_{-0.03}$ for core-collapse supernovae, and $[\mathrm{Mn/Fe}]_{\mathrm{Ia}} = -0.30^{+0.03}_{-0.03}$ at [Fe/H] = −1.5 dex for Type Ia supernovae.

Although we have manganese measurements for stars in the dSphs Ursa Minor, Ursa Major II, Canes Venatici I, Leo I, and Fornax, we do not include them in this section. In Ursa Minor, Ursa Major II, and Canes Venatici I, the samples of stars for which we were able to measure [Mn/Fe] are so small that we cannot draw meaningful conclusions. Leo I and Fornax are not well fit by our simple chemical evolution model. We discuss these other dSphs later in Section 2.5.2.

2.4.2 Comparison with prior work

We now compare our measurements with previous literature. The right panel of Figure 2.4 compares the Sculptor dSph manganese abundances from this work (black points) directly with those measured by North et al. (2012) (green squares) and Sobeck et al. (2006) (small gray points).

Our measurements imply that in Sculptor, [Mn/Fe] is roughly constant with respect to [Fe/H], suggesting that the overall manganese abundance does not change with

time—and that Type Ia supernovae and core-collapse supernovae produce roughly the same yields of manganese with respect to iron. This is consistent with North et al. (2012), who published the previously largest literature catalog of manganese abundances in Sculptor. North et al. (2012) obtained Mn abundances for ~ 40 stars from high-resolution spectroscopy. From their measurements, they found a plateau in [Mn/Fe] at metallicities $-1.75 \lesssim$ [Fe/H] $\lesssim -1.4$, which largely agrees with our finding of metallicity-independent [Mn/Fe].

However, at a given [Fe/H], our measurements indicate a larger spread in [Mn/Fe] than North et al. (2012) find. This may be because of the different line lists used. While we use the same 5407Å, 5420Å, and 5516Å Mn lines that North et al. (2012) use, we use also 15 other lines, including several in the bluer range of the optical spectrum (4700 – 5000Å). According to our line sensitivity analysis (Section 4.4.2) these blue lines are among the most sensitive to Mn abundance, so our measurements may be able to probe lower [Mn/Fe] than North et al. (2012), who discard any stars in their sample with "unreliable" Mn lines.

Furthermore, at higher metallicities North et al. (2012) reported a decreasing trend of [Mn/Fe] with respect to [Fe/H]. This trend does not appear in any of the other galaxies measured in their work, although the authors noted that a similar trend has also been observed for giants and subgiants in the globular cluster ω Centauri (Cunha et al. 2010; Pancino et al. 2011). North et al. (2012) interpreted the decreasing trend as the result of metallicity-dependent Mn yields from Type Ia supernovae. We are unable to confirm this downward trend at higher metallicities, since we do not observe stars with [Fe/H] $\gtrsim -1.1$.

On the other hand, our observed [Mn/Fe]-[Fe/H] relation is remarkably consistent with manganese abundances measured from ~ 200 Milky Way cluster and field halo stars by Sobeck et al. (2006). Sobeck et al. (2006) found an average constant value of $\langle$[Mn/Fe]$\rangle = -0.36$ for MW halo field stars, which agrees within typical uncertainties with our measured average $\langle$[Mn/Fe]$\rangle = -0.30$. We note that Feltzing et al. (2007) reported [Mn/Fe] yields for main sequence and subgiant stars in the MW thick disk that are on average 0.15 dex higher than Sobeck et al. (2006)'s measurements at [Fe/H] ~ -1. As North et al. (2012) suggested, this slight discrepancy may be due to differences in the line lists used, or differences in NLTE corrections between giants and less evolved stars (e.g., Bergemann et al. 2019). At higher metallicities ([Fe/H] $\gtrsim -1$), Feltzing et al. (2007) found that [Mn/Fe] begins to increase to super-solar abundances. This may suggest that the thick disk has a nucleosynthetic

history that is distinct from the histories of the Galactic halo and Sculptor dSph. We return to this point in Section 2.5.2, where we discuss the potential role of SFH in driving [Mn/Fe].

Cescutti and Kobayashi (2017) compiled measurements from $N \sim 20$ stars from other dSphs: Ursa Minor, Sextans, and Carina. They observed a "butterfly"-shaped distribution of [Mn/Fe] as a function of [Fe/H], i.e., large spreads in [Mn/Fe] at $-3.5 \lesssim$ [Fe/H] $\lesssim -2.0$ and $-1.75 \lesssim$ [Fe/H] $\lesssim -1.0$, with a narrow spread at an intermediate metallicity ([Fe/H] ~ -2.0). Cescutti and Kobayashi (2017) suggested that this distribution might be characteristic of a stochastic chemical evolution model with two channels: a sub-$M_{\rm Ch}$ channel and a near-$M_{\rm Ch}$ channel with relatively weak deflagrations (a "Type Iax" SN channel). We do not directly compare their results with ours, since their chemical evolution model was tuned to match the metallicity distribution function of Ursa Minor. However, we do note that the spread in our measurements ($\sigma \sim 0.29$ dex, computed as the standard deviation of all [Mn/Fe] measurements in Sculptor) is roughly consistent with the spreads predicted by these stochastic models, perhaps suggesting that the chemical evolution of Sculptor dSph is also stochastic.

Finally, we briefly discuss nucleosynthetic yields measured from X-ray emission from Type Ia SN remnants (SNRs). Yamaguchi et al. (2015) compile literature manganese-to-iron ratios for three Milky Way SNRs. Kepler's SNR, Tycho's SNR, and 3C 397 are measured to have manganese yields of [Mn/Fe] = $0.08 \pm 0.17, 0.22 \pm 0.20$, and 0.47 ± 0.14, respectively. While these super-solar abundances are much higher than our best-fit model ($[\mathrm{Mn/Fe}]_{\rm Ia} \sim -0.3$), these SNRs are also young and likely had progenitors with near-solar metallicities, so they are not directly comparable with our measurements. Their super-solar abundances may be more consistent with other measurements of high-metallicity Galactic thick disk stars (Feltzing et al. 2007).

2.5 Implications for Type Ia supernova physics

We now consider the implications of our measurements on Type Ia supernova physics. We compare our observationally-inferred Type Ia supernova yield for Sculptor with yields predicted from theoretical models (Section 2.5.1) before discussing the interpretation of [Mn/Fe] abundances in other dSph galaxies (Section 2.5.2). Finally, we consider our assumption of LTE and its impact on our results (Section 2.5.3).

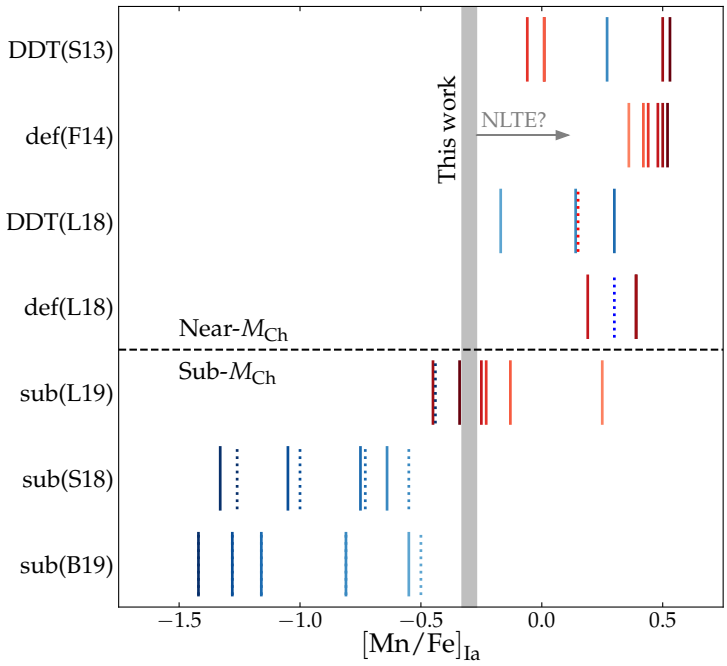

Figure 2.5: Type Ia supernova [Mn/Fe] yield (at [Fe/H] = −1.5) measured in Sculptor dSph from this work (gray shaded region, marking ±68% confidence interval about the median), compared to theoretical yields from various models (vertical lines). Models are described in more detail in Appendix 2.7. The dashed horizontal line separates near-M_{Ch}(above line) and sub-M_{Ch} models (below line). Red (blue) lines indicate theoretical yields from solar metallicity ($10^{-1.5}\,Z_{\odot}$) progenitors. Darker shading indicates more ignition sites (S13 and F14), higher initial density (L18), or higher-mass white dwarf progenitors (L20, S18, and B19). Dotted lines indicate special cases, denoted with asterisks in Tables 2.9 and 2.10. The gray arrow shows the maximal effect of applying NLTE corrections to our result (Section 2.5.3).

2.5.1 Comparison with theoretical models

Figure 2.5 compares our inferred Type Ia yield from Sculptor dSph with yields predicted from various theoretical simulations. We discuss these models and their predicted [Mn/Fe] yields in further detail in Appendix 2.7. We list the most relevant model details in Table 2.8, reproduced from Table 2 from Kirby et al. (2019).

Table 2.8: Type Ia supernova models.

Model	Reference	Description
DDT(S13)	Seitenzahl et al. (2013b)	$M_{\rm Ch}$, 3D, DDT, multiple ignition sites
def(F14)	Fink et al. (2014)	$M_{\rm Ch}$, 3D, pure deflagration, multiple ignition sites
DDT(L18)	Leung and Nomoto (2018)	$M_{\rm Ch}$, 2D, DDT, varying initial central density
def(L18)	Leung and Nomoto (2018)	$M_{\rm Ch}$, 2D, pure deflagration, varying initial central density
sub(L20)	Leung and Nomoto (2020)	sub-$M_{\rm Ch}$, 2D, double detonation with He shell
sub(S18)	Shen et al. (2018a)	sub-$M_{\rm Ch}$, 1D, detonation of bare CO WD, two choices of C/O mass ratio
sub(B19)	Bravo et al. (2019)	sub-$M_{\rm Ch}$, 1D, detonation of bare CO WD, two choices of ^{12}C + ^{16}O reaction rate

Note: Reproduced with permission from Table 2 of Kirby et al. (2019).

As discussed in Section 2.1.2, $[\mathrm{Mn/Fe}]_{\mathrm{Ia}}$ places a strong constraint on the mass of a Type Ia progenitor. This is shown in Figure 2.5; nearly all of the near-M_{Ch} models (above the horizontal dashed line) produce solar or super-solar $[\mathrm{Mn/Fe}]_{\mathrm{Ia}}$, while the sub-$M_{\mathrm{Ch}}$ models can produce sub-solar $[\mathrm{Mn/Fe}]_{\mathrm{Ia}}$. We note that when possible, we consider near-M_{Ch} models with $\sim 1/3 Z_{\odot}$ to account for core convective burning in these progenitors; we describe this "simmering" process further in Appendix 2.7. We also note that the pure deflagration models def(F14) and def(L18) may represent near-M_{Ch} Type Iax supernovae. Of the near-M_{Ch} models, our measured $[\mathrm{Mn/Fe}]_{\mathrm{Ia}}$ is most consistent with the low-density DDT model by L18, which is the only near-M_{Ch} model to have a sub-solar [Mn/Fe] yield.[7] This model has a low central density of 1×10^9 g cm^{-2}, producing a larger detonation region which produces a very low [Mn/Fe] yield at low metallicity. However, this central density may be unphysically low for single-degenerate Type Ia SNe (e.g., Figure 4 in Lesaffre et al. 2006).

Of the sub-M_{Ch} models, our measured Type Ia SN yield of $[\mathrm{Mn/Fe}]_{\mathrm{Ia}} = -0.30^{+0.03}_{-0.03}$ is most consistent with L20's solar metallicity models between $1.05 - 1.20\ M_{\odot}$. However, this is not a straightforward comparison, since we measure $[\mathrm{Mn/Fe}]_{\mathrm{Ia}}$ at $[\mathrm{Fe/H}] = -1.5$ rather than at solar metallicity. Of the remaining models, our measured $[\mathrm{Mn/Fe}]_{\mathrm{Ia}}$ is most consistent with the sub-M_{Ch} models of S18 and B19, requiring white dwarf masses $< 0.9\ M_{\odot}$. This mass constraint is lower than estimated by Kirby et al. (2019), who found that their measured yields of nickel matched Type Ia models from $\sim 1.00 - 1.15\ M_{\odot}$. This discrepancy may simply be due to uncertainties in the theoretical yields; as Figure 2.5 shows, various sub-M_{Ch} models produce a wide range of $[\mathrm{Mn/Fe}]_{\mathrm{Ia}}$ yields due to varying physical assumptions made in the models. Alternatively, our observationally-inferred yield may be incorrect. The largest uncertainty in our measurement is the assumption of LTE, and we address the effect of non-LTE corrections in Section 2.5.3.

If we take the theoretical yields and our observationally-inferred yield at face value, then the difference between Type Ia SN models best fit by $[\mathrm{Mn/Fe}]_{\mathrm{Ia}}$ and $[\mathrm{Ni/Fe}]_{\mathrm{Ia}}$ yields must have a physical explanation. Perhaps the most plausible explanation is that our measured yield is a combination of yields from both sub-M_{Ch} and near-M_{Ch} Type Ia or Type Iax SNe.

[7] The gravitationally confined detonation of a near-M_{Ch} white dwarf may also have a similar sub-solar [Mn/Fe] yield; e.g., Seitenzahl et al. (2016) find [Mn/Fe] = −0.13 for one such model. However, the other observables (particularly spectral features of other IMEs) predicted by this model do not match typical Type Ia SNe, and this model is therefore not expected to be a dominant channel of Type Ia SNe.

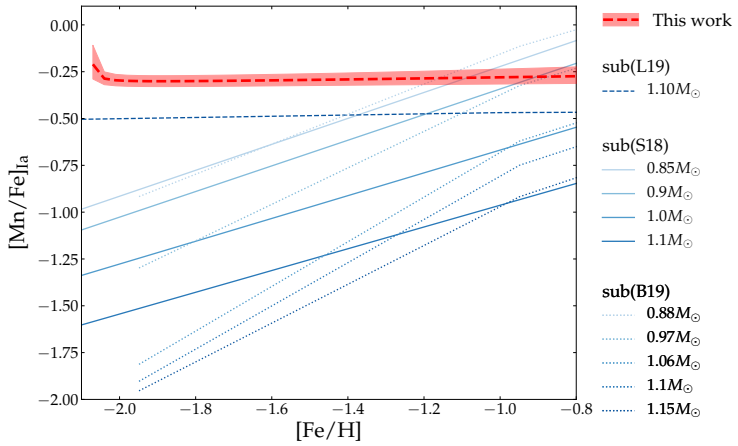

Figure 2.6: Type Ia SN yield of manganese $[\mathrm{Mn/Fe}]_{\mathrm{Ia}}$ as a function of [Fe/H]. The red dashed line and shaded region represent our inferred yield from Sculptor dSph, as shown in Figure 2.4. Other lines denote yields from various sub-M_{Ch} theoretical models.

We further explore this hypothesis by considering the metallicity dependence of our measured $[\mathrm{Mn/Fe}]_{\mathrm{Ia}}$. In Figure 2.6, we plot $[\mathrm{Mn/Fe}]_{\mathrm{Ia}}$ as a function of [Fe/H] and compare against theoretical predictions. Our observationally-inferred $[\mathrm{Mn/Fe}]_{\mathrm{Ia}}$ is near-constant as a function of metallicity across the range $-2 \lesssim \mathrm{[Fe/H]} \lesssim -1$. However, the theoretical sub-M_{Ch} models generally predict much larger increases in $[\mathrm{Mn/Fe}]_{\mathrm{Ia}}$ with metallicity. This discrepancy may indicate that the combination of sub-M_{Ch} and near-M_{Ch} Type Ia SNe depends on metallicity.[8]

We can roughly estimate the fractions of sub-M_{Ch} and near-M_{Ch} Type Ia SNe required to produce our inferred $[\mathrm{Mn/Fe}]_{\mathrm{Ia}}$. For example, at low [Fe/H], we infer a higher $[\mathrm{Mn/Fe}]_{\mathrm{Ia}}$ than sub-M_{Ch} SNe—particularly low-metallicity sub-M_{Ch} SNe—can produce. As a conservative estimate, we consider the low-metallicity sub-M_{Ch} model that is least discrepant with our observed $[\mathrm{Mn/Fe}]_{\mathrm{Ia}}$: the L20 1.1 $M_\odot$ model. At [Fe/H] ~ -2, this model has a yield of $[\mathrm{Mn/Fe}]_{\mathrm{Ia}} \sim -0.50$, nearly ~ 0.3 dex lower than our best-fit model. Therefore, assuming an average near-M_{Ch} yield from the S13 N100 model, at least $\sim 20\%$ of SNe must be near-M_{Ch} SNe to reproduce our best-fit model.

If we instead compare our observationally-inferred yield with a more strongly metallicity-dependent model like those of S18, we can estimate the fraction of

[8]This discrepancy may also be exacerbated by the dependence of [Mn/Fe] yields on the mass of sub-M_{Ch} Type Ia SNe. More massive sub-M_{Ch} WDs produce lower [Mn/Fe] yields, and younger stellar populations should preferentially host these more massive sub-M_{Ch} WD explosions. We therefore expect $[\mathrm{Mn/Fe}]_{\mathrm{Ia}}$ to be even lower at low [Fe/H].

near-$M_{\rm Ch}$ Type Ia or Type Iax SNe over a range of metallicities. Assuming $\sim 1\ M_{\odot}$ white dwarf progenitors as predicted by Kirby et al. (2019), we find that using S18's models, $\sim$ 33% of Type Ia SNe at [Fe/H] ~ -1 and $\sim$ 36% of Type Ia SNe at [Fe/H] ~ -2 must be near-$M_{\rm Ch}$. These estimates are somewhat higher than the fractions inferred from Kirby et al. (2019)'s [Ni/Fe] measurements; using the S18 $1\ M_{\odot}$ model yields for [Ni/Fe], only $\sim$ 22% of Type Ia SNe must be near-$M_{\rm Ch}$.

We emphasize that these fractions are only rough estimates, subject to uncertainties in both the observational and theoretical yields. However, our data suggest that some non-negligible fraction of Type Ia SNe must have near-$M_{\rm Ch}$ progenitors over the metallicity range $-2 \lesssim$ [Fe/H] $\lesssim -1$. Furthermore, the near-$M_{\rm Ch}$ fraction does not appear to change significantly across the metallicity range probed by our observations. This may change at higher metallicities ([Fe/H] $\gtrsim -1$), where near-$M_{\rm Ch}$ Type Ia SNe may begin to dominate, producing super-solar yields of [Mn/Fe] that are seen in, e.g., the Milky Way thick disk (Feltzing et al. 2007).

As pointed out by Kirby et al. (2019), our conclusions are valid only for Type Ia SNe that occurred while Sculptor was forming stars. Sculptor formed the middle two thirds of its stars in 1 Gyr (Weisz et al. 2014). Our measurements are therefore sensitive to models of Type Ia SNe that have "standard" delay-times < 0.6 Gyr (e.g., Maoz et al. 2014). However, our conclusions do not account for Type Ia SNe that are delayed by more than 1 Gyr. Measurements of other dSphs with different star formation histories may be required to sample different varieties of Type Ia SNe, which may have longer delay-times. We discuss this further in the next section.

2.5.2 Other dSph galaxies

As described in Section 2.4.1, we are unable to fit our simple chemical evolution model to several dSphs. Ursa Minor, Ursa Major II, and Canes Venatici have small sample sizes; Leo I and Fornax dSphs have larger sample sizes ($N = 50$ and $N = 45$, respectively), but are not well fit by the model. For completeness, we illustrate the manganese abundances as a function of metallicity for all dSphs in the left panel of Figure 2.7.

The right panel of Figure 2.7 zooms in on [Mn/Fe] as a function of [Fe/H] for the galaxies with sample sizes $N > 20$: Sculptor, Leo I, and Fornax. This illustrates that at a given [Fe/H], stars in Leo I and Fornax have higher [Mn/Fe] abundances than stars in Sculptor by $\gtrsim 0.2$ dex on average.

The most obvious differences among these galaxies that might explain this dis-

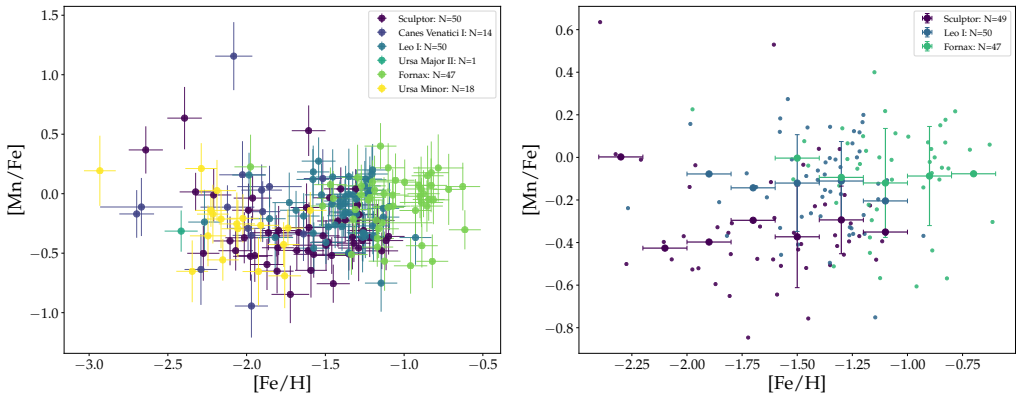

Figure 2.7: [Mn/Fe] abundances for multiple dSph galaxies. Left: [Mn/Fe] as a function of [Fe/H] for all dSph galaxies in our sample. Right: Same, but zoomed in to show only stars from Sculptor, Leo I, and Fornax dSphs. Small points denote the measured abundances (errorbars have been removed for ease of visualization), and large points with errorbars denote the weighted averages in each 0.2 dex metallicity bin (only bins with > 1 stars are plotted, and error bars indicate combined errors of averages).

crepancy are the galaxies' star formation histories (SFHs). Leo I and Fornax have extended star formation histories, while Sculptor's SFH is characterized by a burst of early star formation followed by a long period of low star formation rates. This may explain the difference in [Mn/Fe] between these galaxies. Here, we consider two potential reasons why SFH might be linked with [Mn/Fe] abundance.

First, differences in [Mn/Fe] at a given [Fe/H] may result from a combination of star formation timescales and metallicity-dependent Type Ia supernova yields. Star formation timescales are relevant because this work uses *stellar* abundances, which trace the level of chemical enrichment at the time of star formation rather than the current level of enrichment. Thus, a star with [Fe/H] ~ -1.50 may actually be sampling yields produced by Type Ia SNe with [Fe/H] < -1.50 progenitors. This "lag" in metallicity would be larger in Leo I and Fornax than in Sculptor, because of their extended SFHs. If [Mn/Fe] yields from sub-$M_{\rm Ch}$ Type Ia supernovae were metallicity-dependent—more specifically, if [Mn/Fe] yields were to increase as progenitor [Fe/H] increases—then the difference in [Mn/Fe] at a given [Fe/H] between Sculptor and Fornax/Leo I might simply be a result of the difference in "lag metallicity."

Although a full test of this hypothesis is beyond the scope of this work, to first order we can estimate the effect of this "lag" by computing the average delay-time for Type Ia supernovae in each dSph. We do this by assuming a power-law delay-time

distribution (Maoz et al. 2012):

$$\Psi = 10^{-3} \left(\frac{t}{\mathrm{Gyr}} \right)^{-1.1} \ \mathrm{SNe\ Gyr^{-1}}\ M_{\odot}^{-1}. \tag{2.8}$$

We assume that this delay-time distribution is valid only for times later than some minimum time $t_{\mathrm{min}} \sim 0.1$ Gyr. We can then compute the average delay-time for Type Ia supernovae between t_{min} and some typical star formation time t_*:

$$t_{\mathrm{delay}} = \frac{\int_{t_{\mathrm{min}}}^{t_*} t \Psi \mathrm{d}t}{\int_{t_{\mathrm{min}}}^{t_*} \Psi \mathrm{d}t}. \tag{2.9}$$

Weisz et al. (2014) find that Sculptor formed most of its stars in $\sim$ 1 Gyr, while Leo I and Fornax have been forming stars steadily over at least $\sim$ 10 Gyr. We therefore assume an average star formation time of $t_* \sim 0.5$ Gyr for Sculptor and $t_* \sim 5$ Gyr for Leo I and Fornax, which yield estimates of $t_{\mathrm{delay}} \sim 0.24$ Gyr and $t_{\mathrm{delay}} \sim 1.12$ Gyr, respectively. Using the age-metallicity relation for Sculptor (de Boer et al. 2012), we find that this average delay-time corresponds to a metallicity lag of Δ[Fe/H] ~ 0.05 dex; similarly, the age-metallicity relation for Fornax (Letarte et al. 2010) yields a metallicity lag of Δ[Fe/H] ~ 0.15 dex. Therefore, the difference in metallicity lags between Sculptor and Fornax is ~ 0.1 dex. For the S18 1 $M_{\odot}$ Type Ia SNe model, a ~ 0.1 dex difference in metallicity lags produces a difference in [Mn/Fe] of Δ[Mn/Fe] ~ 0.09 dex. This is not enough to explain the $\gtrsim 0.2$ dex difference in [Mn/Fe] between Sculptor and Fornax.

Alternatively, the discrepancy in [Mn/Fe] may result from a change over time in the underlying physical mechanism behind Type Ia supernovae. Both Leo I and Fornax have stars with significantly supersolar [Mn/Fe] abundances ([Mn/Fe] $\gtrsim 0.2$ dex); as Figure 2.5 shows, low-metallicity sub-M_{Ch} Type Ia progenitors do not produce such high [Mn/Fe] yields. This suggests that near-M_{Ch} white dwarf explosions may become the dominant channel for Type Ia supernovae at late times in a galaxy's star formation history.

Such a scenario—where near-M_{Ch} Type Ia or Type Iax supernovae explode later than sub-M_{Ch} Type Ia SNe—has been proposed by, e.g., Kobayashi and Nomoto (2009), who argue that near-M_{Ch} Type Ia SNe are suppressed at low metallicities due to metallicity-dependent white dwarf winds. This scenario may also be consistent with near-M_{Ch} explosions requiring mass growth by hydrogen accretion, which may require a longer delay-time or higher metallicity progenitors than sub-M_{Ch} double

degenerate mergers (e.g., Ruiter et al. 2011). As noted in Section 2.4.2 this also agrees with observations in the Milky Way, which show that stars in the Galactic halo have sub-solar [Mn/Fe] at [Fe/H] $\lesssim -1.0$, compared to stars in the higher-metallicity thick disk, which have have super-solar [Mn/Fe] (Feltzing et al. 2007). Like Sculptor, the Milky Way halo formed most of its stars in a short early burst, while the thick disk has a more extended SFH.

2.5.3 Non-LTE effects

Throughout our analysis, we have used [Mn/Fe] abundance measurements that rely on the assumption of local thermodynamic equilibrium (LTE). In LTE, opacity is only a function of temperature and density. However, this is only valid at high densities, when the radiation field is strongly coupled to the matter. Previous works find that accounting for non-LTE (NLTE) effects may systematically increase Mn abundances by as much as $0.5 - 0.7$ dex using 1D NLTE models (e.g., Bergemann and Gehren 2008), or up to ~ 0.4 dex using 3D NLTE models (e.g., Bergemann et al. 2019). We must therefore consider the effect of NLTE corrections on our results.

We estimate this by using the corrections determined by Bergemann and Gehren (2008), who compared Mn abundances measured using 1D LTE models and 1D NLTE models over a range of metallicities. From Figure 9 of Bergemann et al. (2019), we find that for a typical RGB star ($T_{\rm eff} = 6000$ K, $\log g = 1.5$), 1D NLTE corrections ($\Delta_{\rm NLTE} = [{\rm Mn/Fe}]_{\rm NLTE} - [{\rm Mn/Fe}]_{\rm LTE}$) determined from optical lines used in this work range from $\Delta_{\rm NLTE} \lesssim 0.462$ dex at [Fe/H] $= -3$ to $\Delta_{\rm NLTE} \gtrsim 0.173$ dex at [Fe/H] $= 0$. By linearly interpolating between these bounds, we can determine a maximum "statistical" NLTE correction as a function of [Fe/H][9]:

$$\Delta_{\rm NLTE}([{\rm Fe/H}]) = -0.10[{\rm Fe/H}] + 0.17. \tag{2.10}$$

Figure 2.8 shows the results of applying this maximum correction to our [Mn/Fe] measurements for stars in Sculptor dSph. The 1D NLTE corrections have a very slight metallicity dependence, but their primary effect is to increase all of the [Mn/Fe] yields by a factor of ~ 0.33 dex on average. This naturally increases the

[9]We note that, although we consider primarily NLTE effects on Mn I lines, NLTE conditions can also affect Fe I lines. Predictions for NLTE Fe I corrections can be quite large (up to 0.5 dex; see, e.g., Bergemann et al. 2012, 2017; Mashonkina et al. 2019). However, these large corrections are generally applicable for metal-poor stars with [Fe/H] $\lesssim -2.0$. For cool giant stars with metallicities comparable to the bulk of our sample ([Fe/H] > -2.0), Mashonkina et al. (2019) predict NLTE corrections $\lesssim 0.1$ dex (cf. their Fig 8). This change is smaller than the average NLTE corrections predicted by Equation 2.10.

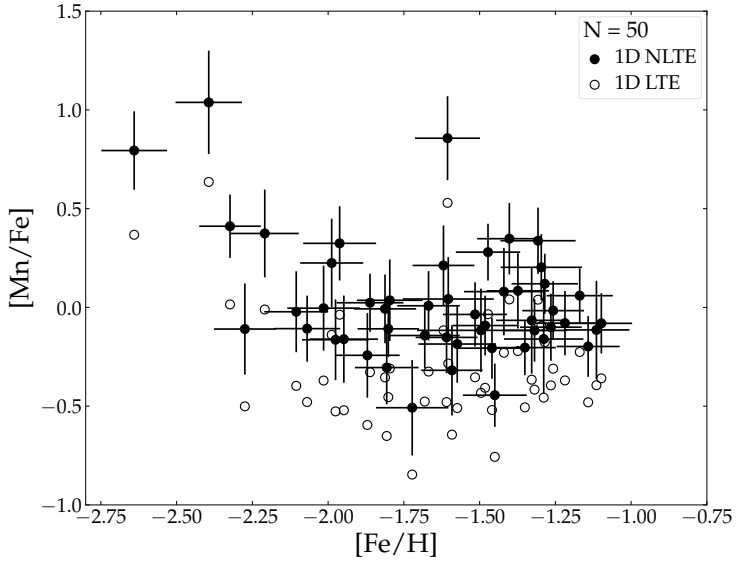

Figure 2.8: [Mn/Fe] as a function of [Fe/H] in Sculptor dSph. Filled points indicate the measurements with a statistical correction for 1D NLTE effects; empty points indicate the original 1D LTE measurements.

[Mn/Fe] yields inferred from Sculptor dSph: $[\mathrm{Mn/Fe}]_{\mathrm{CC,NLTE}} = 0.00^{+0.03}_{-0.03}$ for core-collapse supernovae, and $[\mathrm{Mn/Fe}]_{\mathrm{Ia,NLTE}} = +0.03^{+0.03}_{-0.03}$ at [Fe/H] = −1.5 dex for Type Ia supernovae. This near-solar Type Ia yield is consistent with M_{Ch} theoretical models (cf. Figure 2.5), a significant departure from our finding in Section 2.5.1 that the sub-M_{Ch} channel dominates in Sculptor dSph. Furthermore, Bergemann et al. (2019) suggest that three-dimensional effects, such as convection, may further increase [Mn/Fe] abundances in RGB stars by another ~ 0.2 dex, producing an even higher $[\mathrm{Mn/Fe}]_{\mathrm{Ia}}$ yield.

This is an interesting difference with respect to our LTE estimates. However, we will leave this complex analysis including detailed NLTE to a future study[10], since Kirby et al. (2018) found that applying 1D NLTE corrections instead increased the dispersion of iron-peak abundances ([Co/Fe] and [Cr/Fe]) in globular clusters. Kirby et al. (2018) suggested that this behavior is due to the method which the atmospheric parameters were determined (1D LTE modelling of spectra with a micro-turbulence relationship calibrated on LTE results).

In any case, the NLTE corrections do not appear to strongly affect the metallicity dependence of [Mn/Fe]; as in the LTE case, we observe a nearly-flat trend of [Mn/Fe] vs [Fe/H] across the metallicity range $-2.25 < [\mathrm{Fe/H}] < -1.0$ in Sculptor.

[10]This requires a complete reanalysis of stellar parameters of our targets using NLTE models.

Furthermore, our comparison between Sculptor and other dSph galaxies (Leo I, Fornax) depends primarily on relative differences between [Mn/Fe] abundances at a given [Fe/H]. Effective temperature might also affect the magnitude of NLTE corrections, but $T_{\rm eff}$ at a given [Fe/H] in Sculptor, Leo I, and Fornax are offset by 200 – 300 K at most; the resulting difference in NLTE corrections is $\lesssim 0.05$ dex, not enough to explain the discrepancy in [Mn/Fe] at a given [Fe/H] between these galaxies. NLTE corrections are therefore unlikely to affect our interpretation of [Mn/Fe] abundances as a function of SFH (Section 2.5.2).

2.6 Summary and conclusions

We have presented the results of medium-resolution spectra from the new 1200B grating on Keck DEIMOS. Using a pipeline that generates synthetic stellar spectra, we have measured manganese abundances for $N = 161$ stars in six classical dSph galaxies. These manganese abundance measurements were validated using the internal dispersions of globular clusters and comparison with high-resolution spectroscopy.

By fitting a simple chemical evolution model to measurements of [Mn/Fe] as a function of [Fe/H], we have inferred the manganese yields of core-collapse and early Type Ia supernovae in Sculptor dSph: $[\mathrm{Mn/Fe}]_{\rm CC} = -0.33^{+0.03}_{-0.03}$ and $[\mathrm{Mn/Fe}]_{\rm Ia} = -0.30^{+0.03}_{-0.03}$ (at [Fe/H] = −1.5), respectively. Since only sub-$M_{\rm Ch}$ Type Ia SN models are able to produce significantly sub-solar values of $[\mathrm{Mn/Fe}]_{\rm Ia}$, we conclude that the dominant explosion mechanism of Type Ia SNe that occurred before the end of star formation in Sculptor is the detonation of a sub-$M_{\rm Ch}$ WD. However, in order to reproduce our observationally-inferred $[\mathrm{Mn/Fe}]_{\rm Ia}$, we find that a fraction ($\gtrsim 20\%$) of all Type Ia SNe in our metallicity range $-2 < [\mathrm{Fe/H}] < -1$ must have near-$M_{\rm Ch}$ progenitors.

This conclusion may not hold for other environments. In particular, the Milky Way thick disk and dSphs with extended SFHs display different trends of [Mn/Fe] as a function of metallicity. We find that at a given metallicity, dSphs with extended SFHs like Fornax and Leo I have $\gtrsim 0.2$ dex higher average [Mn/Fe] abundances than Sculptor, which has an ancient SFH. This discrepancy is large enough to imply a physical change in the nucleosynthetic source of Mn—perhaps the dominant channel of Type Ia SNe evolves over time, and near-$M_{\rm Ch}$ white dwarf detonations become the dominant channel at longer delay-times.

Finally, we consider the effect of non-LTE corrections on our results. Including a

statistical NLTE correction increases the [Mn/Fe] yields from both core-collapse and Type Ia supernovae by $\sim$ 0.3 dex. The resulting $[\mathrm{Mn/Fe}]_{\mathrm{Ia}}$ is approximately solar at [Fe/H] ~ -1.5, more consistent with yields from near-M_{Ch} models. The detailed treatment of NLTE effects, however, requires a full re-analysis of stellar parameters of our targets with NLTE synthetic spectral models. This will be the subject of the future work.

We also hope to test the results of this work using more data in dSphs. Other dSphs with ancient SFHs similar to Sculptor (e.g., Draco, Canes Venatici II) could be used to confirm whether sub-M_{Ch} explosions dominate at early times in dwarf galaxies. Dwarf spheroidal galaxies with diverse star formation histories, such as Carina (e.g., Hernandez et al. 2000), may also be particularly intriguing environments in which to test our conclusions about the SFH dependence of Type Ia supernovae.

2.7 Appendix: Theoretical yield tables

In this section, we briefly describe the theoretical models of Type Ia supernovae. These models are discussed in further detail in Section 4.1 of Kirby et al. (2019). Table 2.9 and Table 2.10 list the theoretical [Mn/Fe] yields predicted by the M_{Ch} and sub-M_{Ch} models, respectively. Here we discuss the details of [Mn/Fe] predictions from these models.

2.7.1 Deflagration-to-detonation (DDT)

We consider two sets of near-M_{Ch} deflagration-to-detonation transition (DDT) models. Since the burning front is highly textured, we chose only multi-dimensional simulations.

DDT(S13): Seitenzahl et al. (2013b) (hereafter S13) produced 3D models of CO white dwarfs with varying numbers of off-center ignition sites, which are specified in the model names; e.g., N10 has 10 ignition sites. More ignition sites correspond to stronger deflagration phases where ^{55}Mn (or rather, its parent nucleus ^{55}Co) is produced, producing higher [Mn/Fe] yields.

DDT(L18): Leung and Nomoto (2018) (hereafter L18) computed 2D models with single central ignition points and a variety of central densities. As described in Section 2.1.2, manganese yields increase with density in near-M_{Ch} white dwarfs. We also consider L18's model "WDD2," the classic DDT model of Iwamoto et al. (1999) updated with new electron capture rates.

We note that both S13 and L18 ran solar-metallicity and low-metallicity models.

However, their low-metallicity models do not include "simmering," pre-explosion convective burning in the cores of near-$M_{\rm Ch}$ progenitors. "Simmering" may increase the neutron excess (e.g., Chamulak et al. 2008; Piro and Bildsten 2008), effectively making the initial metallicity of a $M_{\rm Ch}$ Type Ia SN irrelevant below a threshold of $\sim 1/3 - 2/3 Z_{\odot}$ (Martínez-Rodríguez et al. 2016; Piro and Bildsten 2008). Since our most metal-rich stars are well below this threshold metallicity, when possible we interpolate the DDT models to a threshold metallicity of $\sim 1/3 Z_{\odot}$.

2.7.2 Pure deflagration

We consider two sets of pure deflagrations of near-$M_{\rm Ch}$ WDs. These may represent Type Iax SNe (e.g., Kromer et al. 2015), so their nucleosynthetic yields may not be applicable to "normal" Type Ia SNe.

def(F14): Fink et al. (2014) (hereafter F14) produced 3D models that closely paralleled the DDT models of S13 and varied the number of off-center sites of ignition. As with S13, the number of ignition sites increases with the strength of the deflagration, increasing the [Mn/Fe] yields.

def(L18): L18 computed pure deflagrations that paralleled the initial central densities as their DDT models. As with the DDT models, manganese yields increase with density. L18 also updated the pure-deflagration "W7" model of Iwamoto et al. (1999).

2.7.3 Sub-$M_{\rm Ch}$

We consider three sets of sub-$M_{\rm Ch}$ models. Each set considers a range of sub-$M_{\rm Ch}$ WD masses, and within each set the [Mn/Fe] yield tends to decrease with increasing WD mass. This is because, as mentioned in Section 2.1.2, in low-mass WDs ($\lesssim 1.2\ M_{\odot}$) ^{55}Co is produced at densities below nuclear statistical equilibrium. As a result, the ^{55}Co yield (and therefore the ^{55}Mn yield) does not change drastically as a function of mass. Meanwhile, the ^{56}Ni mass does increase with mass; since ^{56}Ni is the parent nucleus of most stable iron, the overall [Mn/Fe] ratio decreases with mass.

sub(L19): Leung and Nomoto (2020) (hereafter L20) used the same 2D code as their earlier work in L18. All L20 models were computed at solar metallicity, except for the 1.10 $M_{\odot}$ ("benchmark") model, which we consider at [Fe/H] ~ -1.5 for ease of comparison with the observationally-inferred yields.

sub(S18): Shen et al. (2018a) (hereafter S18) simulated 1D detonations of CO

sub-$M_{\rm Ch}$ WDs. We again consider only models interpolated to a metallicity of [Fe/H] ~ -1.5 to better compare against our observations. They simulated C/O mass ratios of both 50/50 and 30/70, which is more physically representative of the C/O ratio in actual WDs.

sub(B19): Bravo et al. (2019) (hereafter B19) also simulated 1D detonations starting at the centers of sub-$M_{\rm Ch}$ WDs. They explored the effect of reducing the reaction rate of ^{12}C+^{16}O by a factor of 10; these reduced reaction rate models are represented by $\xi_{\rm CO} = 0.9$ in Table 2.10, while models with the "standard" reaction rate have $\xi_{\rm CO} = 0.0$.

Table 2.9: Theoretical yields for $M_{\rm Ch}$ models.

Model	$\log(Z/Z_\odot)$	[Mn/Fe]
DDT(S13)		
N1	0.0	+0.01
N3	0.0	−0.06
N10	0.0	+0.01
N100	−0.5	+0.27
N200	0.0	+0.50
N1600	0.0	+0.53
def(F14)		
N1def	0.0	+0.36
N3def	0.0	+0.42
N10def	0.0	+0.44
N100def	0.0	+0.48
N200def	0.0	+0.50
N1600def	0.0	+0.52
DDT(L18)		
*WDD2	0.0	+0.15
DDT 1×10^9 g cm^{-3}	−0.5	−0.17
DDT 3×10^9 g cm^{-3}	−0.5	+0.14
DDT 5×10^9 g cm^{-3}	−0.5	+0.30
def(L18)		
*W7	−0.5	+0.30
def 1×10^9 g cm^{-3}	0.0	+0.19
def 3×10^9 g cm^{-3}	0.0	+0.39
def 5×10^9 g cm^{-3}	0.0	+0.39

Note: Models marked with asterisks (*) are "special cases" denoted with dashed lines in Figure 2.5.

Table 2.10: Theoretical yields for sub-$M_{\rm Ch}$ models.

Model	$\log(Z/Z_\odot)$	[Mn/Fe]
sub(L20)		
0.90 $M_\odot$, $M_{\rm He}$ = 0.15 $M_\odot$	0.0	+0.25
0.95 $M_\odot$, $M_{\rm He}$ = 0.15 $M_\odot$	0.0	−0.13
1.00 $M_\odot$, $M_{\rm He}$ = 0.10 $M_\odot$	0.0	−0.23
1.05 $M_\odot$, $M_{\rm He}$ = 0.10 $M_\odot$	0.0	−0.25
*1.10 $M_\odot$, $M_{\rm He}$ = 0.10 $M_\odot$	−1.5	−0.44
1.15 $M_\odot$, $M_{\rm He}$ = 0.10 $M_\odot$	0.0	−0.45
1.20 $M_\odot$, $M_{\rm He}$ = 0.05 $M_\odot$	0.0	−0.34
sub(S18)		
0.85 $M_\odot$, C/O = 50/50	−1.5	−0.64
0.90 $M_\odot$, C/O = 50/50	−1.5	−0.75
1.00 $M_\odot$, C/O = 50/50	−1.5	−1.05
1.10 $M_\odot$, C/O = 50/50	−1.5	−1.33
*0.85 $M_\odot$, C/O = 30/70	−1.5	−0.55
*0.90 $M_\odot$, C/O = 30/70	−1.5	−0.73
*1.00 $M_\odot$, C/O = 30/70	−1.5	−1.00
*1.10 $M_\odot$, C/O = 30/70	−1.5	−1.26
sub(B19)		
0.88 $M_\odot$, $\xi_{\rm CO}$ = 0.9	−1.5	−0.55
0.97 $M_\odot$, $\xi_{\rm CO}$ = 0.9	−1.5	−0.81
1.06 $M_\odot$, $\xi_{\rm CO}$ = 0.9	−1.5	−1.16
1.10 $M_\odot$, $\xi_{\rm CO}$ = 0.9	−1.5	−1.28
1.15 $M_\odot$, $\xi_{\rm CO}$ = 0.9	−1.5	−1.42
*0.88 $M_\odot$, $\xi_{\rm CO}$ = 0.0	−1.5	−0.50
*0.97 $M_\odot$, $\xi_{\rm CO}$ = 0.0	−1.5	−0.81
*1.06 $M_\odot$, $\xi_{\rm CO}$ = 0.0	−1.5	−1.16
*1.10 $M_\odot$, $\xi_{\rm CO}$ = 0.0	−1.5	−1.28
*1.15 $M_\odot$, $\xi_{\rm CO}$ = 0.0	−1.5	−1.42

Note: Models marked with asterisks (*) are "special cases" denoted with dashed lines in Figure 2.5.

Chapter 3

MEASURING THE TYPE IA DELAY-TIME DISTRIBUTION WITH GALACTIC ARCHAEOLOGY

Abstract

The delay-time distribution (DTD) of Type Ia supernovae (SNe) is sensitive to the physical mechanism behind Type Ia SNe, particularly the number of white dwarfs involved in the explosion. Most previous measurements of the Type Ia DTD implicitly assume that the DTD is "universal" (i.e., constant across all galaxies) in some population of host galaxies. Here, I present a new method for measuring the rate of Type Ia SNe—and therefore the Type Ia delay-time distribution—in a single Local Group dwarf spheroidal galaxy using galactic archaeology. I first demonstrate the validity of this method using Sculptor dSph as a test case before applying it to other dSphs. In both Draco and Leo II dSphs, the observed Type Ia rates are inconsistent with DTDs with long minimum delay-times $\tau_{\rm min} \sim 1$ Gyr and DTDs with abrupt cutoffs after $\tau = 1$ Gyr, ruling out a number of single-degenerate models. More importantly, I find that the observed Type Ia rates in Draco and Leo II are best fit by different DTDs, suggesting that the Type Ia DTD is not universal. There are some indications that the Type Ia rate in Draco is consistent with a single-degenerate model, perhaps hinting at a transition from single- to double-degenerate Type Ia SNe over time, though further data are needed to substantiate this interpretation.

3.1 Introduction

As discussed in the previous chapter, the physical mechanism for Type Ia supernovae is uncertain. Although it is generally well-accepted that Type Ia SNe are the thermonuclear explosions of white dwarfs, theoretical models span a range of parameters: the physical explosion mechanism (prompt vs. delayed detonation), the number of white dwarfs involved ("single-degenerate" vs. "double-degenerate"), and/or the masses of the exploding white dwarf (Chandrasekhar mass [$M_{\rm Ch}$] vs. sub-Chandrasekhar mass [sub-$M_{\rm Ch}$]).

The previous chapter described how the nucleosynthetic products of Type Ia SNe—particularly manganese—can be used to distinguish among theoretical supernova models with different white dwarf progenitor masses. Another way to distinguish among Type Ia SN models is to measure the Type Ia delay-time distribution (DTD).

As described by Maoz and Mannucci (2012), the DTD $\Psi(\tau)$ represents the expected rate of Type Ia SNe as a function of τ, where τ is the delay-time after a δ-function burst of star formation. When convolved with the star formation history (SFH) of a galaxy $S(t)$, the DTD provides the rate of Type Ia supernova as a function of time $R_{\rm Ia}(t)$:

$$R_{\rm Ia}(t) = \int_0^t S(t-\tau)\Psi(\tau)\mathrm{d}\tau. \tag{3.1}$$

The form of the DTD itself depends only on the internal physics of Type Ia SNe (for a review, see Maoz et al. 2014). For Type Ia models in which the explosion is driven by gravitational wave radiation from the inspiral of a binary system, the DTD is set by the merger timescale (assuming a uniform distribution of binary white dwarf separations), leading to a power law DTD $\Psi(\tau) \propto \tau^{-1}$ extending to Hubble timescales. This DTD describes most double-degenerate scenarios, in which two white dwarfs accrete onto or merge with each other. For Type Ia models in which the explosion is driven by mass accretion—this includes single-degenerate models, in which a white dwarf accretes matter from a non-degenerate companion star—there is no clear consensus on the DTD. However, a number of mass accretion models suggest that the DTD may drop off sharply after a few Gyr. After this point, the remaining white dwarfs and their binary companions have masses so low that the white dwarfs cannot accrete enough material to explode within a Hubble time.

Observational constraints on the DTD therefore provide useful constraints on the physics of Type Ia SNe. Previous measurements of the Type Ia DTD are roughly consistent with a τ^{-1} power law, in agreement with inspiral-driven double-degenerate models (e.g., Maoz and Mannucci 2012). However, these measurements are difficult to make—the DTD cannot be measured directly, and must instead be inferred from the rates of Type Ia SNe in systems with known SFHs (i.e., by solving for $\Psi(\tau)$ given $R_{\rm Ia}(t)$ and $S(t)$ in Equation 3.1).

In the literature, supernova rates have typically been measured by counting supernovae in populations of host galaxies with known or assumed SFHs as a function of redshift (e.g., Graur et al. 2011; Mannucci et al. 2005; Maoz et al. 2010, 2011). For example, cluster galaxies are thought to form the majority of their stars in a short $\sim$ 100 Myr burst, so $R_{\rm Ia}$ in a cluster is the total number of Type Ia SNe normalized by the 100 Myr star formation period. This rate can then be measured in clusters at different redshifts to obtain $R_{\rm Ia}$ as a function of time (Maoz et al. 2010). A similar approach can be taken with supernovae in volumetric samples of field galaxies, where assumptions are either made about the cosmic SFH or individual galaxy SFHs

(e.g., Brandt et al. 2010; Mannucci et al. 2005; Maoz et al. 2011). These methods implicitly assume that the DTD is universal in the host galaxy population under consideration. This may be an invalid assumption, as recent studies have shown that the dominant Type Ia SN channel could vary among galaxies (de los Reyes et al. 2020).

To date, only one method has been able to measure the DTD within an individual galaxy. By counting supernova remnants and comparing to SFHs of spatially-resolved stellar populations, Maoz and Badenes (2010) were able to measure the Type Ia DTD in the Magellanic Clouds. This approach has its own limitations: for example, old supernova remnants cannot be classified as core-collapse or Type Ia, so no meaningful measurement of the Type Ia DTD at short delay-times can be made. Of the remaining younger supernova remnants, only a few (~ 10) are Type Ia SN remnants; this small sample size produces large statistical errors and prevents significant measurements of the Type Ia DTD beyond a single delay-time bin.

In this paper, I propose a new method to measure the Type Ia DTD in a dwarf spheroidal galaxy (dSph) using galactic archaeology. This method not only allows me to infer the Type Ia DTD in individual galaxies rather than a population of galaxies, it also allows me to measure the Type Ia DTD with greater time resolution than available from the Magellanic Cloud measurements.

I describe this method in Section 3.2. In Section 3.3, I test our method on a few Local Group dSphs and discuss implications for Type Ia SN physics. I summarize our conclusions in Section 3.4.

3.2 A method for measuring the Type Ia DTD in an individual galaxy

Here I present a method for measuring the time-resolved Type Ia DTD within an individual galaxy. An overview of this method is illustrated in Figure 3.1. Broadly, I use stellar abundances to measure the rate of Type Ia supernovae. I then compare this *observed* rate with an *expected* Type Ia supernova rate, obtained by assuming a DTD from a theoretical model. By comparing the difference between the observed and expected Type Ia rates, I am able to determine the best-fit model Type Ia DTD. Further details are described in the following subsections.

3.2.1 The observed rate of Type Ia SNe

To estimate the observed rate of Type Ia SNe, I first use the stellar metallicity distribution function (MDF) of the galaxy to measure the cumulative number of

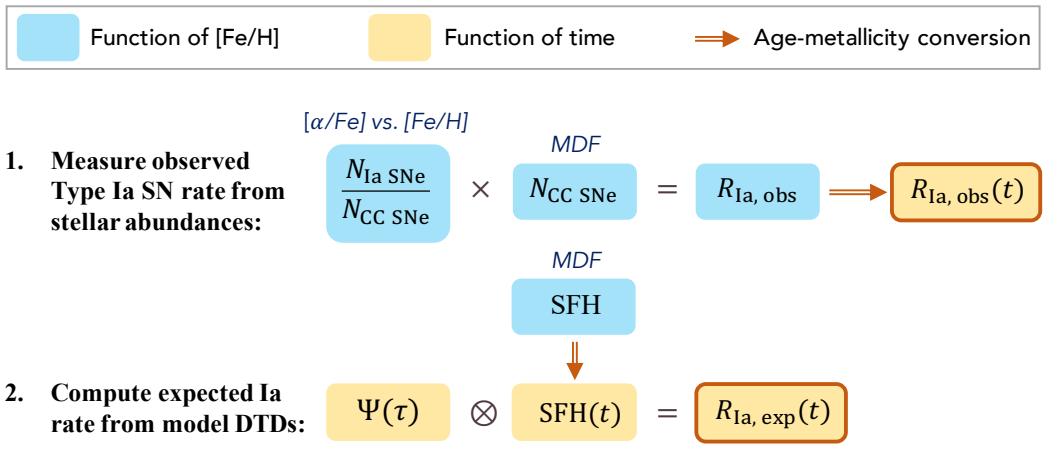

Figure 3.1: A schematic outlining the method used to compute the Type Ia DTD in a single galaxy. Observed quantities from stellar abundances (italic labels) are converted from functions of stellar metallicity (blue boxes) to functions of time (yellow boxes) using the age-metallicity relation (orange arrows) in order to compute "observed" and "expected" rates of Type Ia supernovae (yellow boxes with orange outlines).

core-collapse SNe as a function of metallicity.[1] The MDF records the number of stars produced (effectively, the star formation history) as a function of [Fe/H]. By assuming a stellar initial mass function, which determines the fraction of high-mass stars formed in a burst of star formation, the cumulative MDF can then be converted to the cumulative number of core-collapse SNe as a function of metallicity: $N_{\text{CC}}([\text{Fe/H}])$.

I then measure the cumulative ratio of core-collapse to Type Ia SNe as a function of metallicity using the stellar [Mg/Fe] abundance ratio. Mg is predominantly produced in core-collapse SNe, while iron is produced in both core-collapse and Type Ia SNe. As a result, the ratio [Mg/Fe] probes the relative nucleosynthetic contribution of both types of supernovae, since CCSNe yield ejecta with a high ratio of Mg to Fe whereas Type Ia SNe yield negligible amounts of Mg.

Kirby et al. (2019) showed that a simple model can be used to more precisely quantify these metallicity contributions. This model assumes that CCSNe are the only nucleosynthetic sources at early times, and that CCSN yields are metallicity-independent—the ratio [Mg/Fe] will therefore be constant as a function of [Fe/H]

[1] Throughout this chapter, "metallicity" refers exclusively to observed stellar metallicity, traced by [Fe/H]. I use bracket abundances referenced to solar (e.g., $[\text{Fe/H}] = \log_{10}(n_{\text{Fe}}/n_{\text{H}})_* - \log_{10}(n_{\text{Fe}}/n_{\text{H}})_\odot$), where n_{X} is the atomic number density of X. Solar abundances are adopted from Asplund et al. (2009).

for old, metal-poor stars. After some delay-time, Type Ia SNe will begin to explode and produce iron, diluting [Mg/Fe] over time. As a result, above some threshold metallicity, [Mg/Fe] will decrease as a function of [Fe/H]. Kirby et al. (2019) showed that in several dSph systems, this decrease can be modeled as a linear trend. As shown in Equation 13 of Kirby et al. (2019), this model can be used to estimate the mass ratio of iron produced by Type Ia SNe compared to iron produced by CCSNe: $R = \frac{M_{\mathrm{Fe,Ia}}}{M_{\mathrm{Fe,CC}}}$. Using theoretical yields of iron for these two types of supernovae, R can be converted to the cumulative number ratio of core-collapse to Type Ia SNe as a function of metallicity: $N_{\mathrm{CC}}/N_{\mathrm{Ia}}([\mathrm{Fe/H}])$.

Finally, I can compute the cumulative number of Type Ia SNe as a function of metallicity:

$$N_{\mathrm{Ia}}([\mathrm{Fe/H}]) = \frac{N_{\mathrm{CC}}([\mathrm{Fe/H}])}{\frac{N_{\mathrm{CC}}}{N_{\mathrm{Ia}}}([\mathrm{Fe/H}])}. \tag{3.2}$$

The first derivative of this cumulative distribution is then the *observed* instantaneous rate of Type Ia SNe as a function of metallicity: $R_{\mathrm{Ia,obs}}([\mathrm{Fe/H}])$.

To meaningfully compare with an expected rate of Type Ia SNe, $R_{\mathrm{Ia,obs}}([\mathrm{Fe/H}])$ must be converted to a function of time using the age-metallicity relation. This conversion implicitly assumes that the age-metallicity relation is a strictly monotonic (i.e., one-to-one) function. Although this assumption is fortunately true for most dSphs (see Section 3.3), the intrinsic functional form of the age-metallicity relation is unknown; converting a function of metallicity to a function of age is therefore more complicated than a simple change of variables. I circumvent this with a numerical approach, by considering that $R_{\mathrm{Ia,obs}}([\mathrm{Fe/H}])$ is a discrete, binned function. The edges of each metallicity bin are first converted to time. The value in each bin represents the number of Type Ia SNe per bin—to convert this to Type Ia SNe per *time* bin, I simply divide by the size of each time bin Δt, which yields the rate of Type Ia SNe as a function of time: $R_{\mathrm{Ia,obs}}([\mathrm{Fe/H}])$.

3.2.2 Comparing with the expected rate of Type Ia SNe

The Type Ia supernova rate can be independently computed by convolving the DTD with the star formation history (SFH) of the galaxy (Equation 3.1). I use this method to estimate an *expected* rate of Type Ia supernovae.

As I describe below, the SFH can be measured directly (from, e.g., photometry or a chemical evolution model). It can also be inferred indirectly from the stellar MDF, which is then converted to a function of time following the same procedure described

in the previous section (i.e., dividing by the time bin size Δt). I then convolve the SFH with a model DTD $\Psi(\tau)$ to obtain the expected rate of Type Ia SNe $R_{\rm Ia,exp}(t)$. Figure 3.2 shows a number of theoretical DTDs from binary population synthesis models for different types of Type Ia SNe. As expected (see Section 3.1), nearly all double-degenerate models (top panel) produce DTDs that roughly scale as τ^{-1} after a minimum delay-time, consistent with the delay-time primarily being set by a merger timescale. Single-degenerate Type Ia models (bottom panel), on the other hand, produce far more diverse DTDs, though there are some common features: for example, the DTDs are largely concentrated within the range $\tau \sim 0.1-2$ Gyr. This is because companion stars within a narrow mass range are needed to donate material to a white dwarf at suitable accretion rates without causing unstable hydrogen burning.

I can test each of these theoretical models by computing $R_{\rm Ia,exp}(t)$ from each predicted DTD, then comparing $R_{\rm Ia,exp}(t)$ and $R_{\rm Ia,obs}(t)$. To account for errors in these rates, I "bootstrap" our calculations by computing the observed and expected rates in 10^5 bootstrap iterations. In each iteration, I randomly perturb the [Fe/H] of each star, assuming that the true values are distributed normally with standard deviations equal to the measurement errors, then compute a new MDF from the perturbed metallicities; the new MDF is then used to compute $R_{\rm Ia,exp}(t)$ and $R_{\rm Ia,obs}(t)$.

I then compute the mean absolute deviation (MAD; i.e., the mean of the absolute value of $R_{\rm Ia,exp} - R_{\rm Ia,obs}$) as a measure of the goodness-of-fit. I use the MAD rather than the more commonly-used root-mean-square error (RMSE); RMSE is not necessarily an ideal statistic for this application due to its sensitivity to large deviations (e.g., Chai and Draxler 2014).

3.3 The Type Ia DTD in dSphs

I now apply the method described in the previous section on dwarf spheroidals in the Local Group: Sculptor, Leo II, and Draco dSphs. The evolution of each of these galaxies appears to be mostly consistent with simple SFHs (dominated by a single burst of star formation, rather than multiple bursts over time; e.g., Weisz et al. 2014), making them ideal systems in which to use my method to compute Type Ia rates, and consequently the Type Ia DTD.

3.3.1 Data

To compute the Type Ia DTD in these dSphs, I rely on quantities derived from abundances of red giant branch stars within the galaxy. In this work, I use literature abundances measured from medium-resolution spectra obtained with the DEep

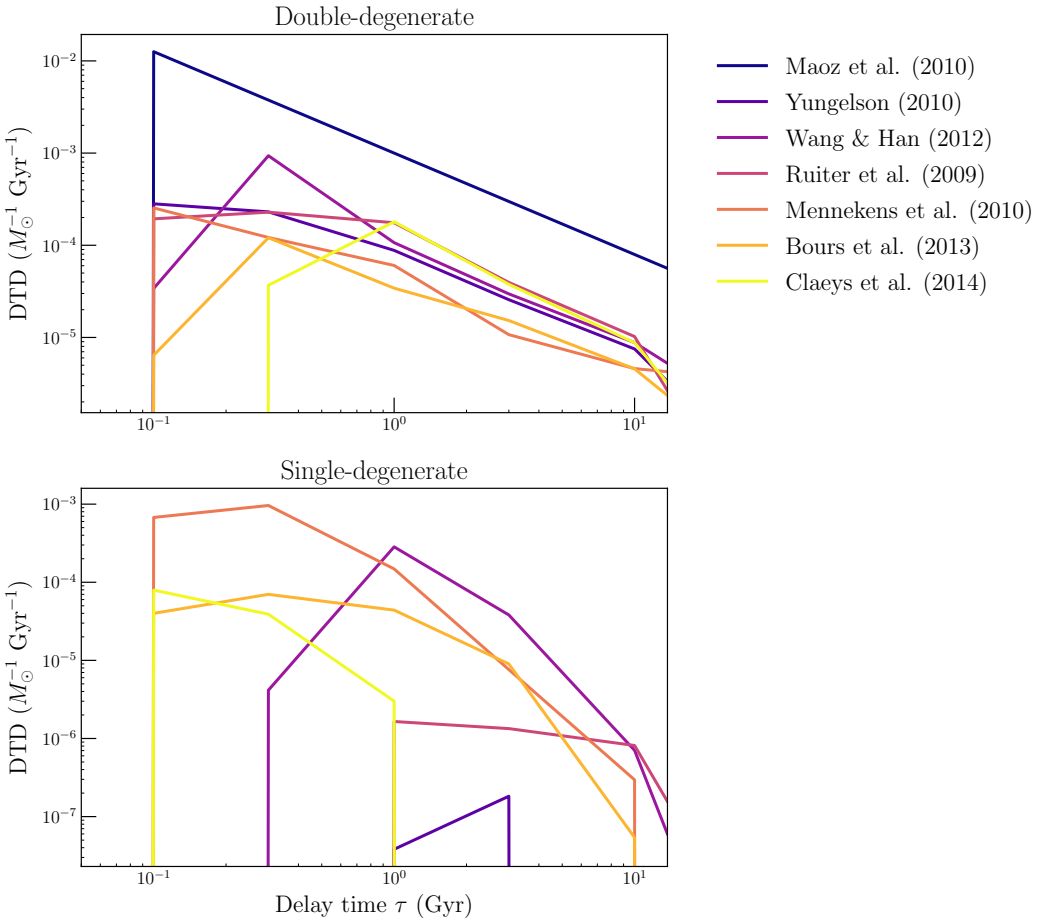

Figure 3.2: Theoretical and observed Type Ia DTDs. The top curve in the left panel is an approximation to the DTD observed by Maoz et al. (2010) and parameterized by Kirby et al. (2011) (see their Equation 9). All other curves are theoretical predictions of Type Ia DTDs compiled from binary population synthesis models by Nelemans et al. (2013) and reproduced by Maoz et al. (2014). All models have been adjusted to use the same input parameters.

Imaging Multi-Object Spectrograph (DEIMOS; Faber et al. 2003) on the Keck II telescope.

As described in Section 3.2, my calculation requires the stellar MDF and the ratio $R = \frac{M_{\mathrm{Fe,Ia}}}{M_{\mathrm{Fe,CC}}}$, which can be derived from the trend of [α/Fe] as a function of [Fe/H]. I use MDFs measured by Kirby et al. (2013) and Rs measured by Kirby et al. (2019).

In order to convert MDFs and Rs to useful quantities for our calculation, I need to assume a stellar initial mass function (IMF) and nucleosynthetic yields of iron for Type Ia SNe and CCSNe. To compute N_{CC}([Fe/H]) from the stellar MDF, I assume a Kroupa (2000) IMF. To compute $N_{\mathrm{CC}}/N_{\mathrm{Ia}}$([Fe/H]) from the ratio R, I assume an

Table 3.1: dSph galaxies used to compute Type Ia DTDs.

Object	RA (J2000)	Dec (J2000)	Distance (kpc)	Log($M_\star$) [$M_\odot$]
Sculptor	$01^h00^m04^s$	−33°41'45"	84	6.08
Draco	$17^h20^m16^s$	57°55'07"	76	5.96
Leo II	$11^h13^m27^s$	22°09'10"	233	6.16

Note: Coordinates and distances taken from the Milky Way satellite census by Drlica-Wagner et al. (2020). Stellar masses taken from Woo et al. (2008).

iron yield of $M_{\rm Fe} = 0.074\ M_\odot$ per CCSN (Maoz and Graur 2017). The iron yield from a Type Ia SN is particularly sensitive to the mass and initial metallicity of the progenitor white dwarf. Previous measurements have shown that sub-$M_{\rm Ch}$ Type Ia SNe dominate at early times in dSphs (e.g., Kirby et al. 2019); in particular, de los Reyes et al. (2020) found that the iron-peak yields of a 1.1 $M_\odot$ model by Leung and Nomoto (2020) were consistent with observations of [Mn/Fe] in Sculptor dSph. I therefore assume a yield from Leung and Nomoto (2020)'s Type Ia model with $M_{\rm WD} = 1.1\ M_\odot$ and $Z_{\rm WD} = 0.02\ Z_\odot$: $M_{\rm Fe} = 0.639\ M_\odot$ per Type Ia SN.

Finally, I also require an age-metallicity relation for each galaxy. The age-metallicity relation can be computed from the MDF (which provides the number of stars formed at each metallicity) and the star formation history (SFH, which provides the number of stars formed at each age). For Leo II and Draco, I use an SFH derived from deep Hubble photometry by Weisz et al. (2014). Sculptor, on the other hand, is comprised of particularly ancient and metal-poor stars. Fitting isochrones to photometric measurements of such a stellar population can lead to an imprecise SFH; isochrones are approximately logarithmically-spaced in age and metallicity, so old and metal-poor isochrones are "bunched together" in color-magnitude space. I therefore use an SFH for Sculptor derived from a galactic chemical evolution (GCE) model by de los Reyes et al. (2022).

The SFHs, MDFs, and age-metallicity relations for the three dSphs in our sample are plotted in Figure 3.3. I also present additional relevant data (coordinates and stellar masses) for these dSphs in Table 3.1.

3.3.2 Sculptor dSph: A proof-of-concept

As a test case, I consider Sculptor dSph. One of the earliest "classical" dwarf galaxies to be identified (Shapley 1938), this spheroidal galaxy has a simple SFH consisting

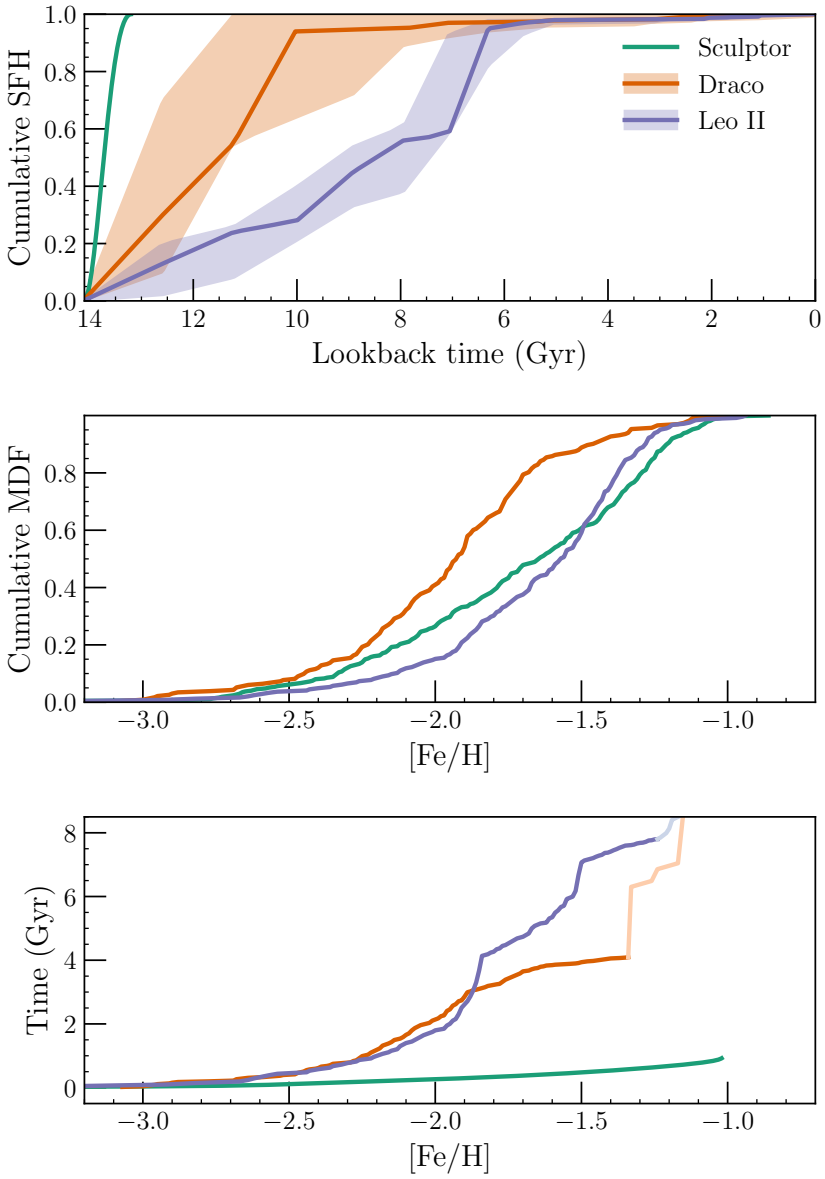

Figure 3.3: Properties of Sculptor, Draco, and Leo II dSphs. Top: The normalized cumulative star formation histories for the three dSphs in our sample. For Sculptor, the SFH is taken from a GCE model (de los Reyes et al. 2022); for Draco and Leo II, the SFHs are photometrically measured (Weisz et al. 2014). Middle: The normalized cumulative metallicity distribution functions of the galaxies in our sample, taken from Kirby et al. (2010). Bottom: The age-metallicity relations of the galaxies in my sample, computed by combining the SFHs and MDFs in the above panels. Light-colored lines indicate the age-metallicity relations produced when forming the last 5% of stellar mass in each galaxy.

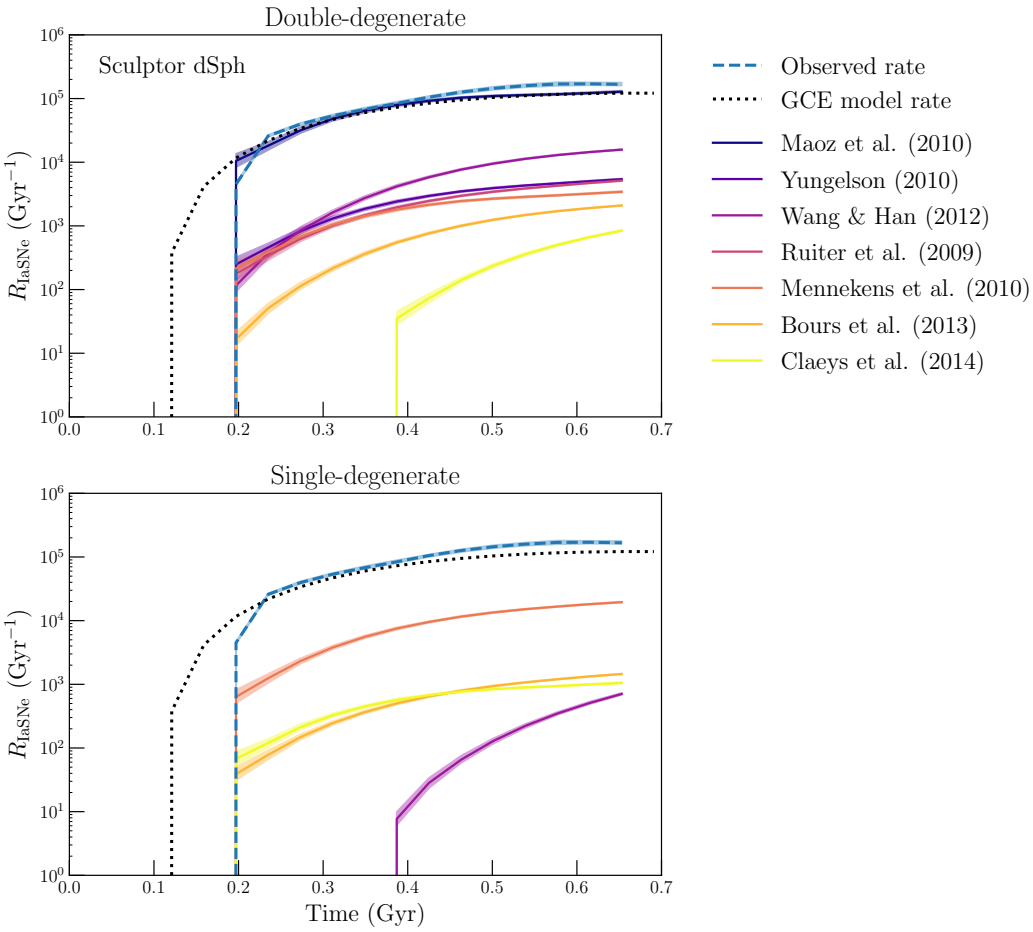

Figure 3.4: The observed rate of Type Ia SNe in Sculptor dSph (dashed blue line), compared to the Type Ia rate measured by the GCE model (black dotted line) and the expected rates computed from various model DTDs (solid lines). As expected for Sculptor, $R_{\mathrm{Ia,obs}}(t)$ is consistent with both the GCE rate and the $R_{\mathrm{Ia,exp}}(t)$ corresponding to the Maoz et al. (2010) DTD. Shaded regions indicate the 16th and 84th percentiles computed from 10^5 bootstrap iterations.

of one burst of star formation with a relatively short duration (e.g., Weisz et al. 2014), making it an ideal test for our DTD method. Unfortunately, because Sculptor's SFH is extremely ancient, the most precise SFH available for Sculptor is obtained from a GCE model. This model itself requires a Type Ia DTD as an input, so I must assume a DTD in order to obtain an SFH—and an age-metallicity relation, which I derive from the SFH—and therefore to compute the observed Type Ia rate $R_{\mathrm{Ia,obs}}(t)$. Fortunately, in some ways this circular logic provides a useful check for our method: since I know what DTD went into the GCE model, the $R_{\mathrm{Ia,exp}}(t)$ computed from this DTD should be consistent with $R_{\mathrm{Ia,obs}}(t)$. As an additional check, I can compare both of these rates with the Type Ia rate recorded in the GCE model.

Table 3.2: Mean absolute deviations for Type Ia rates computed from model DTDs.

Model	Sculptor dSph	Draco dSph	Leo II dSph
Maoz et al. (2010)	**15855**	8460	3074
Double-degenerate models			
Yungelson (2010)	67566	2017	**683**
Wang and Han (2012)	64902	1936	709
Ruiter et al. (2009)	67799	1904	685
Mennekens et al. (2010)	68175	2149	701
Bours et al. (2013)	68902	2250	710
Claeys et al. (2014)	69357	2027	687
Single-degenerate models			
Yungelson (2010)	69508	2440	779
Wang and Han (2012)	69402	**1888**	700
Ruiter et al. (2009)	69508	2436	777
Mennekens et al. (2010)	62921	1996	736
Bours et al. (2013)	69044	2272	719
Claeys et al. (2014)	69093	2378	762

Note: The minimum MAD values for each galaxy are bolded.

I present the results of this test in Figure 3.4 and Table 3.2. Here, I also plot the Type Ia yield measured from a best-fit GCE model (described in Chapter 4 de los Reyes et al. 2022), in which I assumed a DTD from Maoz et al. (2010) (and adapted by Kirby et al. 2011, top curve in the top panel of Figure 3.2). The observed Type Ia rate $R_{\mathrm{Ia,obs}}(t)$ (dashed blue line in Figure 3.4) has a minimum delay-time of $\tau_{\mathrm{min}} = 0.2 \pm 0.1$ Gyr, where the errors are intrinsic to the binning method used to compute this Type Ia rate from discrete measurements. This τ_{min} is consistent with most of the theoretical models compiled from Maoz et al. (2014), which have minimum delay-times on the order of 0.1 Gyr. Models with later minimum delay-times—the double-degenerate model of Claeys et al. (2014), or the single-degenerate models of Wang and Han (2012), Ruiter et al. (2009), and Yungelson (2010)—are poor fits, yielding the highest mean absolute deviations from the observed rate (Table 3.2).

The shape of the observed Type Ia rate is consistent with many of the models, including both the double-degenerate and single-degenerate models. This is perhaps unsurprising, since Sculptor's short SFH limits the time range over which I can

measure the Type Ia rates, and many of the double- and single-degenerate DTDs have similar shapes at such early times ($t < 0.7$ Gyr). However, the normalization of the Type Ia rates computed from the model DTDs significantly varies. Figure 3.4 clearly shows that the observed Type Ia rate is in greatest agreement with the rate expected from the Maoz et al. (2010) DTD (dark purple line in the top panel). This is further confirmed by the mean absolute deviations, which are listed in Table 3.2: the Maoz et al. (2010) DTD produces the lowest MAD, indicating that this model is the best fit to the observations. Additionally, as expected, both the observed rate and the expected rate from the Maoz et al. (2010) DTD are qualitatively consistent with the GCE model (dotted black line).

Taken together, these suggest that our method of measuring Type Ia rates is able to self-consistently identify the correct model when the input DTD is known.

3.3.3 The Type Ia DTD as a function of SFH

Having tested our method's ability to recover a DTD model, I can now apply it to other Local Group dSphs. Figures 3.5 and 3.6 show the results for Draco and Leo II dSphs, and Table 3.2 lists the mean absolute deviation (MAD) values for the DTD models. Both of these galaxies have relatively extended SFHs compared to Sculptor, so their SFHs can be reasonably well measured from photometry (Weisz et al. 2014) and do not require a chemical evolution model with an input Type Ia DTD.

I first consider Draco dSph. As Figure 3.5 illustrates, the observed Type Ia rate (dashed blue line) has a highly uncertain minimum delay-time $\tau_{\rm min} \sim 0.3 - 1$ Gyr, primarily due to the stochastic effect of binning a small number of low-metallicity stars over multiple iterations. This rules out a few of the single-degenerate models with late $\tau_{\rm min} \sim 1$ Gyr (Ruiter et al. 2009; Yungelson 2010, which again have among the highest MAD values).

After $t \sim 1$ Gyr, the observed Type Ia rate is an increasing function of time. This is in contrast with the double-degenerate models, which largely produce Type Ia rates that are close to constant (on a logarithmic scale) as a function of time after $t \sim 0.5$ Gyr. Some of the single-degenerate models are better at matching the observed shape. In particular, the model with the lowest MAD is the single-degenerate model of Wang and Han (2012); this model is able to reproduce both the shape and normalization of the observed Type Ia rate, particularly before $t \sim 3$ Gyr.

Given the ability of the Wang and Han (2012) single-degenerate model to reproduce the early Type Ia rate, I tentatively conclude that the single-degenerate channel is

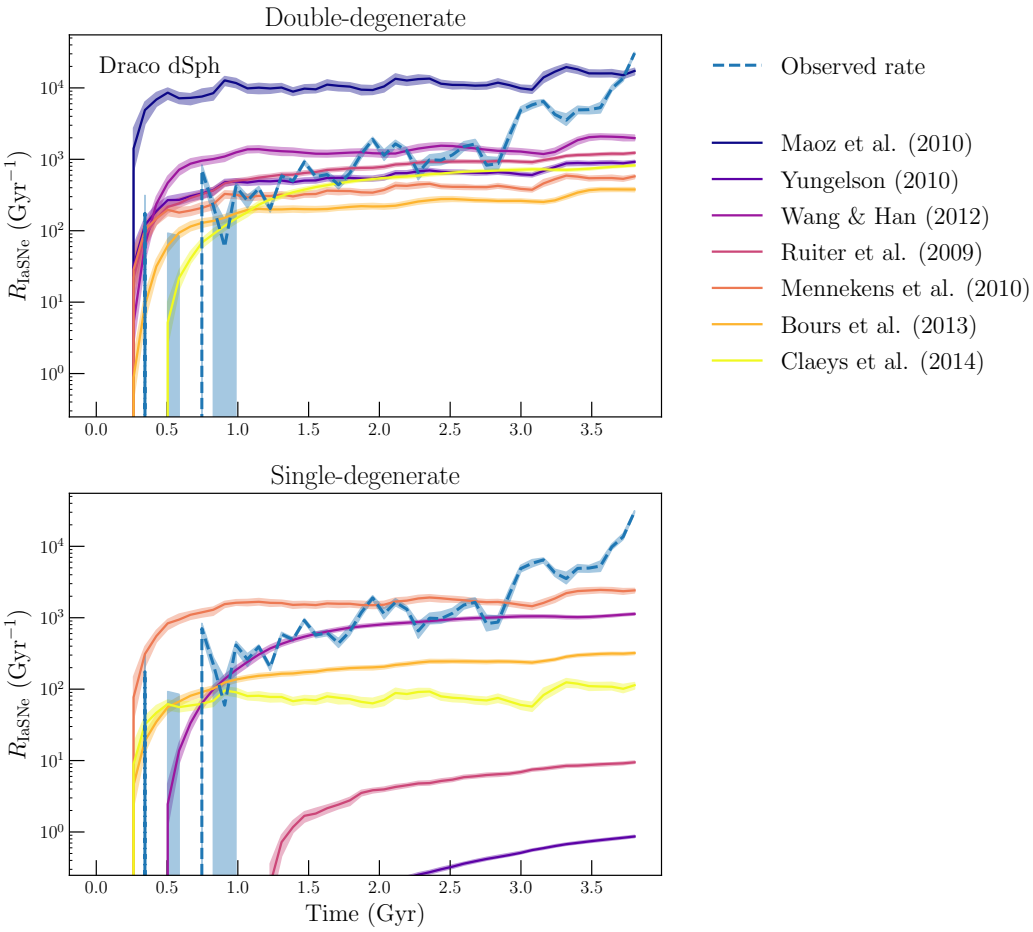

Figure 3.5: Same as Figure 3.4, but for Draco dSph.

the dominant channel of Type Ia SNe in Draco until at least $t \sim 3$ Gyr. At later times the observed rate increases even further, but none of the model DTDs listed in this work are able to reproduce this late-time increase in Type Ia SNe.

I now apply our method to Leo II, as shown in Figure 3.6. In this galaxy, the minimum delay-time of the observed Type Ia rate (dashed blue line), $\tau_{\rm min} \sim 1-2$ Gyr, is once again inconsistent with the late-$\tau_{\rm min}$ single-degenerate models of Ruiter et al. (2009) and Yungelson (2010). As before, this is supported by the high MAD values for these models.

Interpreting the shape of the Type Ia rate in Leo II, however, is less straightforward. Leo II has an even more extended SFH than Draco. Because the Weisz et al. (2014) SFHs are reported with relatively coarse time resolution, such an extended SFH produces discontinuous "kinks" in the SFH at lookback times of ~ 10 and ~ 7 Gyr (see purple line in the top panel of Figure 3.3). These create similar "kinks" in the

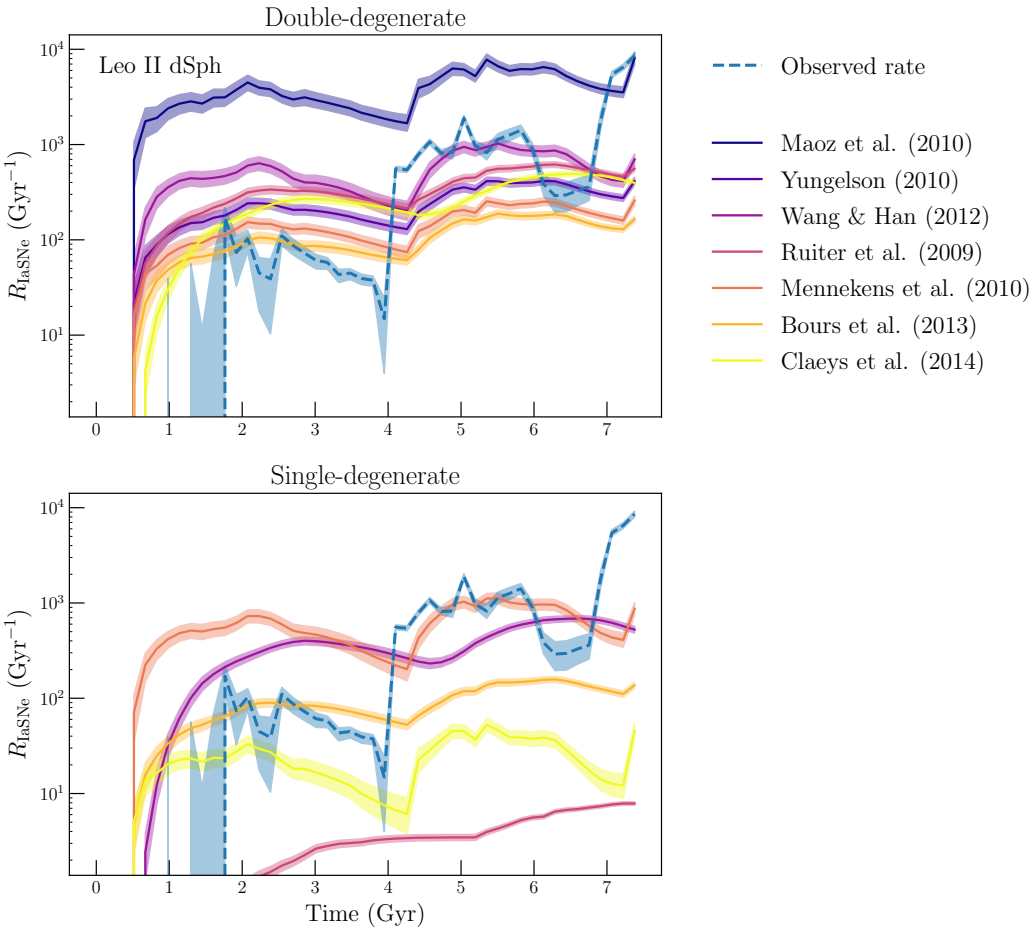

Figure 3.6: Same as Figure 3.4, but for Leo II dSph.

age-metallicity relation (bottom panel of Figure 3.3), which translate to spikes seen in the observed Type Ia SN rate at $t \sim 4$ and ~ 7 Gyr (dashed blue lin in Figure 3.6). Although many of the expected Type Ia rates (solid lines in Figure 3.6) have dips that correspond to spikes in the observed rate, none of the models is able to reproduce the amplitude of the spikes in the observed rate.

The model with the lowest MAD is the Yungelson (2010) double-degenerate model, and in general the double-degenerate models have lower MAD values than the single-degenerate models. However, Figure 3.6 clearly shows that none of the models—including the double-degenerate models—produces Type Ia rates that are clearly consistent with the observed rates. This may suggest that a DTD other than the ones listed in Figure 3.2 is required to match the observed stellar abundances in Leo II.

3.3.4 Implications for Type Ia supernova physics

The Type Ia rates measured in Draco and Leo II place several observational constraints on theoretical models. First, the "turn-on" times for Type Ia SNe in both galaxies are inconsistent with long minimum delay-times, ruling out single-degenerate models with $\tau_{\rm min} \sim 1$ Gyr. Of the DTD models I consider, these include the single-degenerate models from Ruiter et al. (2009) and Yungelson (2010). In both Draco and Leo II, the single-degenerate model of Claeys et al. (2014) has the next lowest MAD value after these late-$\tau_{\rm min}$ models. This suggests that this model, which drops off sharply after $\tau = 1$ Gyr, is also not a good fit for the observations in either galaxy.

Beyond these common features, the Type Ia rates observed in Draco and Leo II show very different behavior. In Draco, the observations are most consistent with the single-degenerate model from Wang and Han (2012), while in Leo II the observations slightly favor the double-degenerate models. This implies that the Type Ia DTD may vary depending on the host galaxy, which may have major implications for DTD measurements, since previous observations of the Type Ia DTD have typically assumed that the DTD is universal in large samples of galaxies (e.g., Maoz and Mannucci 2012).

The Type Ia DTD varying in different host galaxies also suggests that the primary physical channel of Type Ia SNe depends on the properties of its host galaxy. This is consistent with other galactic archaeology studies: using stellar abundances of iron-peak elements, Kirby et al. (2019) and de los Reyes et al. (2020) found that sub-Chandrasekhar-mass (sub-$M_{\rm Ch}$) white dwarf progenitors are the dominant channel of Type Ia SNe at early times in dSphs with ancient SFHs like Sculptor. Yet dSphs with more extended SFHs, including Leo II, have systematically higher [Ni/Fe] and [Mn/Fe] abundances, as would be expected if the dominant channel of Type Ia SNe transitions from sub-$M_{\rm Ch}$ to near-$M_{\rm Ch}$ over time.

By measuring the Type Ia DTD in individual dSphs, I can search for a similar transition in the DTD. This is difficult with only two data points (Draco and Leo II), particularly since in Leo II the observed Type Ia rate is not well-described by any of the theoretical models considered in this work. I can make some tentative interpretations if I make the significant assumption that double-degenerate models are in fact better fits to the observed Type Ia rates in Leo II. For example, Leo II has a more extended SFH than Draco, which could suggest a transition from single-degenerate to double-degenerate Type Ia SNe over the course of a dSph's

chemical evolution. This may in turn suggest some connection with the sub-$M_{\rm Ch}$ to near-$M_{\rm Ch}$ transition measured from iron-peak abundances, perhaps indicating that sub-$M_{\rm Ch}$ supernovae are typically single-degenerate while more massive white dwarf explosions result from interactions of binary white dwarfs. Alternatively, Draco has a lower stellar mass than Leo II, potentially suggesting that double-degenerate (and possibly near-$M_{\rm Ch}$) Type Ia SNe only dominate in dSphs above a certain stellar mass or metallicity.

These may hint at counterintuitive results, particularly because of the implied correlation between near-$M_{\rm Ch}$ progenitors and double-degenerate explosions; double-degenerate Type Ia SNe are frequently thought to result from sub-$M_{\rm Ch}$ white dwarf progenitors (e.g., Shen et al. 2018a). Some double-degenerate models do predict that binary sub-$M_{\rm Ch}$ white dwarfs can merge into a remnant before exploding as a near- or super-$M_{\rm Ch}$ supernova, but these have been disfavored by recent hydrodynamical models (see Section 2.2 of Maoz et al. 2014, and references therein). A connection between near-$M_{\rm Ch}$ progenitors and double-degenerate supernovae would therefore be a strong constraint on theoretical models. However, this result is tentative at best. Given the substantial uncertainties in the best-fit Type Ia DTD in Leo II, more data—more precise SFHs, as well as abundance data for more dSphs—are required to make solid physical interpretations about the Type Ia DTD as a function of galaxy properties.

3.4 Conclusions

I have demonstrated a new method for measuring the rate of Type Ia SNe—and therefore the Type Ia delay-time distribution—in a single Local Group dwarf galaxy. Based on galactic archaeology, this procedure uses stellar metallicities [Fe/H] to trace overall star formation and alpha-element abundances [α/Fe] to trace the ratio of core-collapse SNe to Type Ia SNe. I use these data, measured from medium-resolution stellar spectroscopy with DEIMOS, to measure an "observed" rate of Type Ia SNe. This observed rate is then compared with "expected" rates of Type Ia SNe, which are computed from theoretical model DTDs. To my knowledge, this is the first method to measure the time-resolved DTD in an individual galaxy.

By testing my method on Sculptor dSph, using a known DTD as input into a chemical evolution model, I showed that this method can successfully recover Type Ia rates consistent with the input DTD. I then applied our method to Draco and Leo II dSphs. In both galaxies, the first Type Ia SNe turn on at relatively early times, so DTDs with

long minimum delay-times $\tau_{\rm min} \sim 1$ Gyr (primarily from single-degenerate models) are poor fits to the data. Additionally, single-degenerate model DTDs with abrupt cutoffs after $\tau = 1$ Gyr produce Type Ia rates with much lower normalizations than the observed rates.

The observed Type Ia rates in Draco and Leo II are best fit by different DTDs, suggesting that the Type Ia DTD—and therefore the dominant physical channel of Type Ia SNe—is not universal among all galaxies. Tentative results indicate that the best-fit Type Ia DTD in Draco, which is less massive and has a more abbreviated SFH, is from a single-degenerate model. In Leo II, which is more massive and has an extremely extended SFH, none of the model DTDs considered in this work are particularly good fits, although the double-degenerate models are slightly better fits to the data than the single-degenerate models. Further data are needed to confirm these results, particularly for Leo II, and to understand if there is a transition in the Type Ia DTD—and whether this transition is related to the transition in the masses of white dwarf progenitors described in Chapter 2.

Chapter 4

A SIMPLE CHEMICAL EVOLUTION MODEL FOR SCULPTOR DSPH

de los Reyes, M. A. C. et al. (2022). "Simultaneous Constraints on the Star Formation History and Nucleosynthesis of Sculptor dSph." *ApJ* 925.1, 66, p. 66. DOI: 10.3847/1538-4357/ac332b.

Mithi A. C. de los Reyes[1], Evan N. Kirby[1,2], Alexander P. Ji[2], Evan H. Nuñez[1]

[1]Department of Astronomy, California Institute of Technology, 1200 E California Blvd, Pasadena, CA, 91125, USA

[2]Department of Physics, University of Notre Dame, Notre Dame, IN, 46556, USA

[3]The Observatories of the Carnegie Institution for Science, 813 Santa Barbara St, Pasadena, CA, 91106, USA

[4]Department of Astronomy & Astrophysics, University of Chicago, 5640 S. Ellis Avenue, Chicago, IL, 60637, USA

[5]Kavli Institute for Cosmological Physics, University of Chicago, Chicago, IL, 60637, USA

Abstract

We demonstrate that using up to seven stellar abundance ratios can place observational constraints on the star formation histories (SFHs) of Local Group dSphs, using the Sculptor dSph as a test case. We use a one-zone chemical evolution model to fit the overall abundance patterns of α elements (which probe the core-collapse supernovae that occur shortly after star formation), *s*-process elements (which probe AGB nucleosynthesis at intermediate delay times), and iron-peak elements (which probe delayed Type Ia supernovae). Our best-fit model indicates that Sculptor dSph has an ancient SFH, consistent with previous estimates from deep photometry. However, we derive a total star formation duration of ~ 0.9 Gyr, which is shorter than photometrically derived SFHs. We explore the effect of various model assumptions on our measurement and find that modifications to these assumptions still produce relatively short SFHs of duration $\lesssim 1.4$ Gyr. Our model is also able to compare sets of predicted nucleosynthetic yields for supernovae and AGB stars, and can provide insight into the nucleosynthesis of individual elements in Sculptor dSph. We find that observed [Mn/Fe] and [Ni/Fe] trends are most consistent with sub-$M_{\rm Ch}$ Type Ia supernova models, and that a combination of "prompt" (delay times similar to core-collapse supernovae) and "delayed" (minimum delay times $\gtrsim 50$ Myr) *r*-process events may be required to reproduce observed [Ba/Mg] and [Eu/Mg] trends.

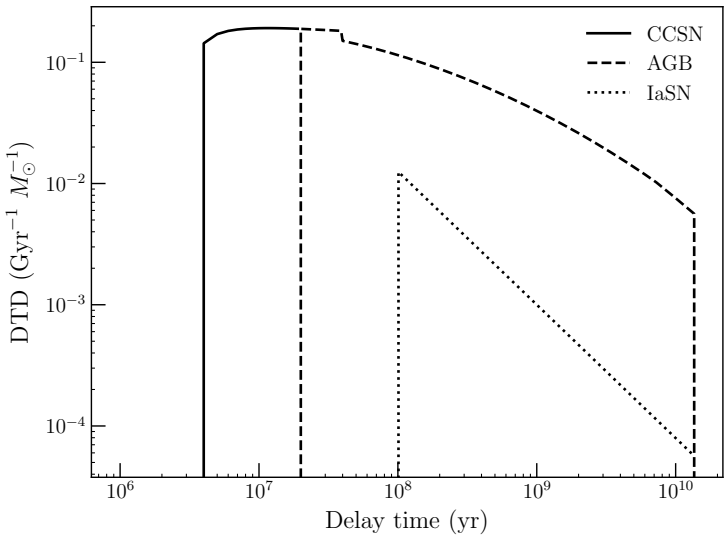

Figure 4.1: Delay-time distributions (DTDs) of core-collapse supernovae, AGB stars, and Type Ia supernovae, illustrating the different timescales that these events probe. The slight discontinuity in the AGB DTD arises from the different equations used to describe stellar lifetimes for stars with masses above and below 6.6 $M_\odot$ (Equations 4.8 and 4.9).

4.1 Introduction

Stellar abundance trends in galaxies are sensitive to measure galaxy star formation histories (SFHs). This is because, as shown in Figure 4.1, different types of nucleosynthetic events occur at different delay-times after a burst of star formation. Because classes of nucleosynthetic events each produce a characteristic yield of elements, the abundances of various elements can be used to trace a range of delay-times after star formation. We illustrate this in Figure 4.2, which shows the masses of different elements produced in response to an instantaneous burst of star formation.

Galactic chemical evolution (GCE) models can be used to place constraints on SFHs by modeling the observed trends in chemical abundances. Pagel (2006) and Matteucci (2012) describe the ingredients of a GCE model. The first such models can be traced back to Tinsley (1968); since then, a veritable cornucopia of chemical evolution models have been developed, particularly for Local Group dwarf galaxies (for a more detailed review of chemical evolution models of dwarf galaxies before the last decade, we refer the reader to Tolstoy et al. 2009). Local Group dSphs are, in many ways, ideal systems to study using chemical evolution models. Many Local Group dSphs have simple SFHs—typically one or a few bursts of star formation, followed by relatively low levels of star formation (e.g., Weisz et al. 2014). Most

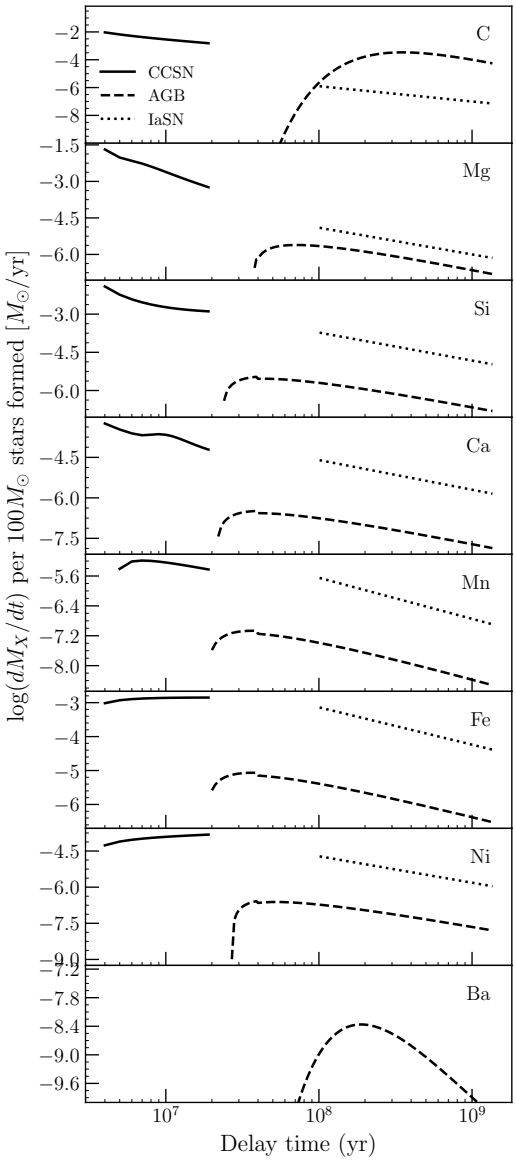

Figure 4.2: The "impulse response" of elemental yields to an instantaneous $100M_\odot$ burst of star formation—that is, the rate at which individual elements are produced as a function of delay time after $100M_\odot$ of stars are formed at $t = 0$. The yields from different nucleosynthetic events (core-collapse SNe, AGB stars, and Type Ia SNe) are plotted as a function of delay time after star formation. We assume a Type Ia delay-time distribution, stellar lifetimes, a stellar IMF, and parameterized stellar yields as described in Section 4.2. For simplicity, we also assume here that all nucleosynthetic events have a single metallicity of $Z = 0.001Z_\odot$.

dwarf galaxies are also well-mixed (Escala et al. 2018) and can be reasonably well described by one-zone GCE models. Finally, recent stellar spectroscopic surveys (e.g., Hill et al. 2019; Kirby et al. 2010; Majewski et al. 2017) have obtained a large

number of dSph stellar spectra, and upcoming surveys and instruments—Subaru PFS (Tamura et al. 2018), VLT/MOONS (Taylor et al. 2018), and MSE (McConnachie et al. 2016), among others—promise to obtain many more.

Several of these dwarf galaxy models are relatively simple one-zone chemical evolution models that have attempted to match elemental abundance patterns in Local Group dSphs (e.g., Carigi et al. 2002; Côté et al. 2017; Fenner et al. 2006; Homma et al. 2015; Kirby et al. 2011; Kobayashi et al. 2015; Lanfranchi and Matteucci 2003, 2004; Ural et al. 2015; Vincenzo et al. 2014) or disrupted dwarf galaxies (e.g., the Gaia-Enceladus-Sausage; Vincenzo et al. 2019). Many of these simple models have been extremely successful; in fact, Vincenzo et al. (2016) showed that the outputs from such a one-zone model can reproduce many of the observed *photometric* features on a dSph's CMD. More recently, some one-zone chemical evolution models have attempted to match *isotopic* abundance patterns (Pandey and West 2021). Other models use input parameters from semianalytic models of galaxy formation (e.g., Calura and Menci 2009; Romano and Starkenburg 2013) or are chemodynamical (and hydrodynamical), tracking both the kinematics and abundances in dwarf galaxies (e.g., Escala et al. 2018; Hirai et al. 2017; Kawata et al. 2006; Marcolini et al. 2006; Recchi et al. 2001; Revaz and Jablonka 2012; Revaz et al. 2016; Revaz et al. 2009).

However, many chemical evolution models of Local Group dSphs require assumptions about the SFH. One-zone models in particular typically use the SFHs determined from photometric studies as inputs. For example, the majority of previous one-zone models of Sculptor dSph (Côté et al. 2017; Fenner et al. 2006; Homma et al. 2015; Lanfranchi and Matteucci 2003, 2004; Pandey and West 2021; Vincenzo et al. 2014) have assumed SFHs from CMD studies (de Boer et al. 2012; Dolphin 2002). The old, metal-poor stellar populations that dominate dSphs make it difficult to obtain photometrically derived SFHs with fine time resolution. In this paper, we instead use a one-zone GCE model to independently derive the SFHs of dSphs in the Local Group, expanding upon previous work by, e.g., Kirby et al. (2011) and Vincenzo et al. (2016).

This work demonstrates how simultaneously fitting a wide variety of stellar abundances can place useful constraints on the SFHs of Local Group dSphs, using Sculptor dSph as a test case. We use a one-zone chemical evolution model that, like previous dSph models, is able to fit the overall abundance patterns of α elements and iron-peak elements in these galaxies. Unlike most previous one-zone models,

we also use our model to fit the abundances of carbon and barium, elements predominantly produced by asymptotic giant branch (AGB) stars. Medium-resolution spectroscopy has enabled large homogeneous catalogs of abundances of C and Ba in dSphs. These elements probe *intermediate* delay times (dashed lines in Figures 4.1 and 4.2) after a burst of star formation and are therefore crucial to constraining a galaxy's full SFH.

Additionally, like other GCE models, our model can provide insights into chemical evolution in Sculptor dSph. A major hurdle for GCE models is disentangling the contributions from multiple nucleosynthetic channels; as shown in Figure 4.2, a single element may be produced by multiple nucleosynthetic sources. This is further complicated by significant uncertainties in additional nucleosynthetic processes, such as the r-process and i-process. We aim to build on the results of previous analyses of abundance trends (e.g., de los Reyes et al. 2020; Duggan et al. 2018; Hill et al. 2019; Kirby et al. 2011, 2019; Skúladóttir et al. 2019) and one-zone GCE models (e.g., Côté et al. 2017) of Sculptor dSph, not only by simultaneously fitting several types of elements—particularly elements produced by AGB stars, which have not typically been included in GCE models of dSphs—but also by varying the input yields from supernovae and AGB stars. This will allow us to directly compare theoretical yield sets. We can also compare our model to the observed abundance trends of elements that were not used to fit our model but that may be sensitive to particular nucleosynthetic channels: for example, manganese and nickel are sensitive to the density of Type Ia supernova progenitors (e.g., Seitenzahl et al. 2013a), while barium and europium are produced by the r-process.

The structure of this paper is as follows. We describe the observed chemical abundances and the simple GCE model used to fit these abundances in Section 4.2 before presenting the measured SFH of Sculptor dSph in Section 4.3. In Section 4.4 we compare our measured SFH to previous literature measurements and discuss the effects of our model assumptions. Our simple GCE model alsec:gceintroso allows us to probe the nucleosynthesis of different individual elements, and we discuss these additional implications in Section 4.5. We summarize our conclusions in Section 4.6. Throughout this paper, we assume a flat ΛCDM cosmology with Planck 2018 parameters ($H_0 = 67.4$ km s^{-1}Mpc^{-1}, $\Omega_m = 0.315$; Aghanim et al. 2020).

4.2 Methods

4.2.1 Abundance measurements

In this work, we primarily use literature abundances derived from medium-resolution spectroscopy with the DEep Imaging Multi-Object Spectrograph (DEIMOS; Faber et al. 2003) on the Keck II telescope. A number of previous works have obtained spectra of red giant branch stars in several globular clusters and classical dSphs. We compile several abundance ratios[1] from these catalogs: [Fe/H] and [α/Fe] ([Mg/Fe], [Si/Fe], and [Ca/Fe]) abundances from Kirby et al. (2010), [C/Fe] from Kirby et al. (2015), [Ni/Fe] from Kirby et al. (2018), [Mn/Fe] from de los Reyes et al. (2020), and [Ba/Fe] from Duggan et al. (2018). We also use supplemental data from the DART survey (Tolstoy et al. 2006), which used ESO VLT/FLAMES to obtain high-resolution ($R \gtrsim 20,000$) spectra of RGB stars in dSphs. The DART abundance ratios for Sculptor dSph are presented in North et al. (2012), who measured [Mn/Fe], and Hill et al. (2019), who measured all the other abundances used in this work.

In particular, we use the DART data to modify the [Ba/Fe] abundances for our analysis. Although the majority of barium is produced in the *s*-process in AGB stars (see, e.g., Table 10 of Simmerer et al. 2004), *r*-process nucleosynthesis also contributes to the production of barium—particularly at low metallicities—and the sites and yields of *r*-process nucleosynthesis are poorly constrained (Cowan et al. 2021). For this reason, we opt not to include the *r*-process in our GCE model. To accommodate this choice, we remove the *r*-process contributions to the barium yields by using measurements of europium (Eu), which is almost entirely produced by the *r*-process (Simmerer et al. 2004). We use the available Eu measurements from the DART survey (Hill et al. 2019) to compute [Ba/Eu], which is an indicator of the ratio of *s*-process to *r*-process contributions. We follow the procedure outlined in Duggan et al. (2018) to convert [Ba/Eu] to the fraction of barium produced from the *r*-process:

$$f_r = \frac{\frac{N_s(\mathrm{Eu})}{N_s(\mathrm{Ba})} - 10^{[\mathrm{Ba/Eu}]_\odot - [\mathrm{Ba/Eu}]}}{\frac{N_s(\mathrm{Eu})}{N_s(\mathrm{Ba})} - \frac{N_r(\mathrm{Eu})}{N_r(\mathrm{Ba})}} \tag{4.1}$$

where $N_s(\mathrm{X})$ and $N_r(\mathrm{X})$ are the solar *s*-process and *r*-process number abundances of element X, obtained from Table 10 of Simmerer et al. (2004).

Since the number of available Eu measurements is relatively small, we compute a simple statistical correction by fitting a line to [Ba/Eu] as a function of metal-

[1] Throughout this paper, we use bracket abundances referenced to solar (e.g., [Fe/H] = $\log_{10}(n_{\mathrm{Fe}}/n_{\mathrm{H}})_* - \log_{10}(n_{\mathrm{Fe}}/n_{\mathrm{H}})_\odot$), where n_{X} is the atomic number density of X. Solar abundances are adopted from Asplund et al. (2009).

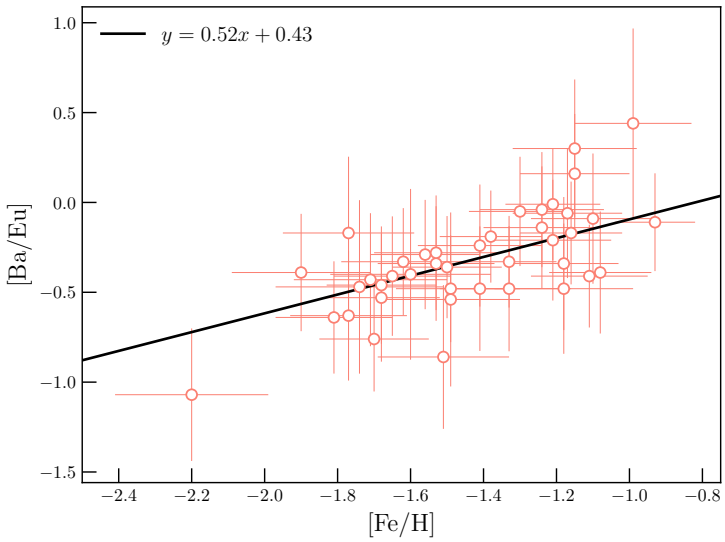

Figure 4.3: Observed [Ba/Eu] as a function of [Fe/H] from the DART dataset (orange empty points) and the line of best fit, used as a statistical correction to remove *r*-process contributions from [Ba/Fe].

licity. This is shown in Figure 4.3, where we derive the best-fit line[2] [Ba/Eu] = 0.52[Fe/H] + 0.42, which can be used to determine the [Ba/Eu] ratio for all stars with metallicity measurements. The *s*-process-only barium yield, $[\mathrm{Ba/Fe}]_s$, can then be computed using the fraction f_r (Equation 4.1):

$$[\mathrm{Ba/Fe}]_s = [\mathrm{Ba/Fe}] + \log(1 - f_r). \tag{4.2}$$

Table 4.1 lists the full catalog of all abundances, including the original [Ba/Fe] abundances as well as *s*-process-only $[\mathrm{Ba/Fe}]_\mathrm{s}$. The estimated uncertainties include both statistical and systematic uncertainties, as reported in the original catalog papers. We note that we use [C/Fe] abundances that Kirby et al. (2015) have corrected for astration (the depletion of carbon by stars moving up the red giant branch; Carbon et al. 1982; Smith and Briley 2006; Suntzeff 1981) using the corrections proposed by Placco et al. (2014).

[2]Since measurement uncertainties exist in both the *x*- and *y*-directions, we do this fit by computing 10^5 bootstrap samples. In each sample, we randomly perturb each data point in both the *x*- and *y*-directions, assuming that the true values are distributed normally with standard deviations equal to the measurement errors. We perform unweighted linear regression on all samples, and we report the 50th percentile coefficients as the best fit.

Table 4.1: Abundance catalog of Sculptor dSph stars.

ID	[Fe/H] (dex)	[Mg/Fe] (dex)	[Si/Fe] (dex)	[Ca/Fe] (dex)	[C/Fe] (dex)	[Mn/Fe] (dex)	[Ni/Fe] (dex)	$[Ba/Fe]_s$[a] (dex)
				DEIMOS[b]				
1002473	-2.30 ± 0.18	0.65 ± 0.93	0.59 ± 0.20	0.64 ± 0.28	...	...	...	...
1002447	-2.04 ± 0.16	0.36 ± 0.29	0.47 ± 0.16	0.33 ± 0.19	-0.23 ± 0.34	...	-0.19 ± 0.29	-0.67 ± 0.38
1002888	-1.97 ± 0.16	...	0.30 ± 0.18	0.47 ± 0.24	...	...	-0.18 ± 0.33	...
1003386	-1.30 ± 0.15	-0.50 ± 0.45	0.21 ± 0.25	0.14 ± 0.19	-0.25 ± 0.33	...	-0.27 ± 0.29	-0.50 ± 0.39
1003505	-1.82 ± 0.15	0.26 ± 0.20	0.20 ± 0.17	0.20 ± 0.18	-0.37 ± 0.33	...	-0.21 ± 0.29	-0.47 ± 0.35
				DART[c]				
ET0009	-1.68 ± 0.16	0.57 ± 0.22	...	0.20 ± 0.07	...	-0.32 ± 0.12	-0.02 ± 0.15	-0.62 ± 0.22
ET0013	-1.68 ± 0.21	0.53 ± 0.27	...	0.28 ± 0.10	...	-0.13 ± 0.17	...	-0.69 ± 0.32
ET0024	-1.24 ± 0.10	...	...	0.00 ± 0.14	...	-0.28 ± 0.07	-0.39 ± 0.13	...
ET0026	-1.80 ± 0.16	0.44 ± 0.19	...	0.07 ± 0.06	...	...	-0.07 ± 0.19	-0.75 ± 0.21
ET0027	-1.50 ± 0.13	0.12 ± 0.15	...	-0.06 ± 0.04	...	-0.41 ± 0.07	-0.18 ± 0.10	-0.48 ± 0.19

[a] The *s*-process contribution to [Ba/Fe] is estimated using Equation 4.1 as described in the text.

[b] The DEIMOS abundances are compiled from a number of sources: the [Fe/H], [Mg/Fe], [Si/Fe], and [Ca/Fe] measurements from Kirby et al. (2010); the [C/Fe] measurements from Kirby et al. (2015); the [Ni/Fe] measurements from Kirby et al. (2018); the [Mn/Fe] measurements from de los Reyes et al. (2020); and the [Ba/Fe] measurements from Duggan et al. (2018).

[c] All DART abundances are from Hill et al. (2019), except the [Mn/Fe] abundances, which are from North et al. (2012).

Note: The errors reported here are total errors (statistical and systematic errors added in quadrature). Only a portion of Table 4.1 is shown here; it is published in its entirety in a machine-readable format online.

4.2.2 A fast, simple galactic chemical evolution model

We now consider the simple GCE model used to fit the data described above. Conceptually this model is similar to that used by Kirby et al. (2011), and we refer the reader to that work for more details about the individual equations.

The model treats each dwarf galaxy as a chemically homogeneous, open-box system. In this system, the gas-phase abundance of each element is tracked over a discrete grid of time steps ($\Delta t = 1$ Myr). Gas inflows and ejecta from CCSNe, Type Ia SNe, and AGB stars can contribute to the gas-phase abundance of each element, while gas outflows and star formation remove gas-phase elements. The full model is therefore described by

$$\begin{aligned} \xi_j(t) &= \int_0^t \Big(-\dot{\xi}_{j,\mathrm{SF}} + \dot{\xi}_{j,\mathrm{II}} + \dot{\xi}_{j,\mathrm{Ia}} + \dot{\xi}_{j,\mathrm{AGB}} \\ &\quad + \dot{\xi}_{j,\mathrm{in}} - \dot{\xi}_{j,\mathrm{out}}\Big) \end{aligned} \tag{4.3}$$

where $\xi_j(t)$ is the gas-phase abundance of element j.

The other terms in Equation 4.3 describe the processes that contribute or remove gas-phase elements. Star formation is described by a Schmidt-like power law (Kennicutt 1998; Schmidt 1959):

$$\dot{\xi}_{j,\mathrm{SF}}(t) = A_\star \left(\frac{M_{j,\mathrm{gas}}(t)}{10^6\ M_\odot}\right)^\alpha . \tag{4.4}$$

Following Kirby et al. (2011), the rate of pristine gas inflows is parameterized with a fast increase and slow decline (e.g., Lynden-Bell 1975):

$$\dot{\xi}_{j,\mathrm{in}}(t) = A_{\mathrm{in}} \frac{M_{j,\mathrm{gas}}(0)}{M_{\mathrm{gas}}(0)} \left(\frac{t}{\mathrm{Gyr}}\right) \exp\left(\frac{-t}{\tau_{\mathrm{in}}}\right) \tag{4.5}$$

where $\frac{M_{j,\mathrm{gas}}(0)}{M_{\mathrm{gas}}(0)}$ is the initial mass fraction of element j, indicating that the inflows are primordial.[3] We assume that gas outflows are predominantly caused by supernovae, so the outflow is assumed to be linearly proportional to the supernova rate:

$$\dot{\xi}_{j,\mathrm{out}}(t) = A_{\mathrm{out}} \frac{M_{j,\mathrm{gas}}(t)}{M_{\mathrm{gas}}(t)} \left(\dot{N}_{\mathrm{II}} + \dot{N}_{\mathrm{Ia}}\right). \tag{4.6}$$

From Equations 4.4, 4.5, and 4.6, we define the variables $\{A_\star, \alpha, A_{\mathrm{in}}, \tau_{\mathrm{in}}, A_{\mathrm{out}}\}$ as free parameters in the model.

The ejecta from SNe and AGB stars at a given time step ($\dot{\xi}_{j,\mathrm{II}}$, $\dot{\xi}_{j,\mathrm{Ia}}$, $\dot{\xi}_{j,\mathrm{AGB}}$) depend on the numbers of SNe/AGB stars occurring at that time, which are determined by

[3] We assume that the initial mass fractions of H and He are 0.7514 and 0.2486, respectively, from Big Bang nucleosynthesis. All other primordial mass fractions are set to zero.

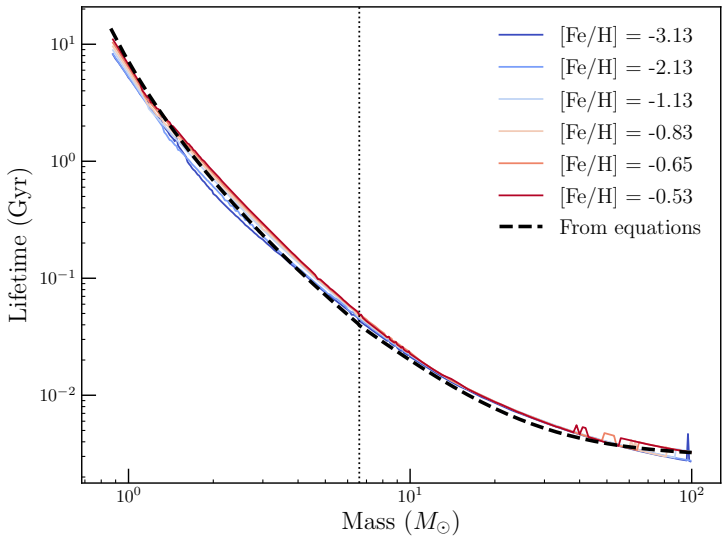

Figure 4.4: Stellar lifetimes as a function of stellar mass from Equations 4.8 and 4.9 (black dashed line). The vertical dotted line indicates the domain border of the two equations at $M = 6.6\ M_\odot$. Numerical results from the BPASS stellar evolution code are shown for comparison; bluer (redder) colors represent lower (higher) stellar metallicity.

convolving the past SFH with a DTD. For a given type of astrophysical event, the DTD describes the expected event rate as a function of τ, where τ is the delay time after a δ-function burst of star formation. The DTD for Type Ia SNe is observed to be a power law with index ~ -1 (e.g., Maoz et al. 2010):

$$\Psi_{\rm Ia} = \begin{cases} 0 & t_{\rm delay} < 0.1\ {\rm Gyr} \\ (10^{-3}\ {\rm Gyr}^{-1}\ M_\odot^{-1}) \left(\frac{t_{\rm delay}}{\rm Gyr}\right)^{-1.1} & t_{\rm delay} \geq 0.1\ {\rm Gyr}. \end{cases} \tag{4.7}$$

The exact parameterization of the Type Ia DTD is still an open question, and we discuss the effects of modifying the values in Equation 4.7 on our results later in Section 4.4.2.

For CCSNe and AGB stars, the DTD is primarily set by the stellar IMF, since stellar lifetimes depend strongly on stellar mass. For ease of comparison with Kirby et al. (2011), we use a Kroupa et al. (1993) IMF; we consider the effect of changing the IMF in Section 4.4.2. We further assume that all stars with birth masses between 10 and 100 $M_\odot$ explode as CCSNe at the end of their lifetimes, and that all stars with birth masses $\leq 10\ M_\odot$ eject mass through AGB winds within the final 1 Myr time step of their lifetimes (Marigo and Girardi 2007). Stellar lifetimes are then parameterized as a function of mass using the following equations (Padovani and

Matteucci 1993):

$$\tau_\star(M) = (1.2(M/M_\odot)^{-1.85} + 0.003)\ \text{Gyr} \tag{4.8}$$

for stars with $M > 6.6\ M_\odot$, and

$$\tau_\star(M) = 10^{\frac{0.334-\sqrt{1.790-0.2232(7.764-\log_{10}(M/M_\odot))}}{0.1116}}\ \text{Gyr} \tag{4.9}$$

for stars with $M \leq 6.6\ M_\odot$. Figure 4.4 compares these equations (black dashed line) with numerical results from the Binary Population and Spectral Synthesis (BPASS) code (Eldridge et al. 2017; Stanway and Eldridge 2018), showing that Equations 4.8 and 4.9 are consistent with stellar evolution models.

To determine the number of SNe/AGB stars at each time step, Kirby et al. (2011) computed the full convolution of the *past* SFH with the DTD (see their Equations 7, 10, and 13). In this work, we instead track the elemental abundances in a *forward-looking* array; at each time step, we compute the number of stars that will produce SNe or AGB winds in the future, and we add the nucleosynthetic yields from these SNe/AGB stars (see next section) to the appropriate future times in the array. This approach, similar to that of the One-zone Model for the Evolution of GAlaxies code (OMEGA; Côté et al. 2017), eliminates most numerical integration from the model. Consequently, the computation of the GCE code is approximately an order of magnitude faster, making it possible to run it many times for a Markov Chain Monte Carlo sampler (see Section 4.3.1).

4.2.3 Input nucleosynthetic yields

A key component of our GCE model is the set of nucleosynthetic yields from supernovae and AGB stars. A number of models have predicted yield sets, and we summarize a subset of these models in Table 4.2. The physical assumptions and computational limitations inherent in these models can produce significant uncertainties in their predicted yields (see Figures 4.12-4.14 in Appendix 4.7).

Table 4.2: Supernova and AGB models.

Reference	Description
	Core-collapse supernova models
Nomoto et al. (2013)	Thermal bomb explosions with fixed SN energy (10^{51} erg); include mass loss, but not rotation; all progenitors explode
Limongi and Chieffi (2018)	Thermal bomb explosions with variable SN energy; include mass loss, rotation; only progenitors $\leq 25\ M_{\odot}$ explode
	AGB models
FRUITY[a]	Produce ^{13}C pocket with time-dependent convective overshoot; Reimers (1975) pre-AGB mass loss, Straniero et al. (2006) AGB mass loss
Stromlo[b]	Parameterize ^{13}C pocket with proton abundance profile; no pre-AGB mass loss, Vassiliadis et al. (1993) AGB mass loss
	Type Ia supernova models
Leung and Nomoto (2018)	Near-$M_{\rm Ch}$ deflagration-to-detonation transition, 2D
Leung and Nomoto (2018)	Near-$M_{\rm Ch}$ pure deflagration, 2D
Leung and Nomoto (2020)	Sub-$M_{\rm Ch}$ (1.1 $M_{\odot}$) double detonation with He shell, 2D
Shen et al. (2018a)	Sub-$M_{\rm Ch}$ (1.1 $M_{\odot}$) detonation of bare CO WD, 1D

[a] This set of yields, described in Cristallo et al. (2011) and Cristallo et al. (2015), is available at `http://fruity.oa-teramo.inaf.it/modelli.pl`.

[b] This set of yields is described in Lugaro et al. (2012), Karakas and Lugaro (2016), and Karakas et al. (2018).

Rather than selecting uncertain yield sets, we instead choose to parameterize the yields with representative analytic expressions, which we will allow to vary in our final fit. First, we fit analytic functions of mass and metallicity to the yields plotted in Figures 4.12, 4.13, and 4.14. For each nucleosynthetic source (CCSNe, AGB stars, and Type Ia SNe), we then vary the input yield sets in the GCE model to determine which elemental abundances are the most sensitive to variations in the yields. For example, for CCSNe, we run the GCE model twice using the same set of fiducial parameters $\{A_{\rm in}, \tau_{\rm in}, A_{\rm out}, A_\star, \alpha\}$ (for simplicity, we use the parameters measured by Kirby et al. 2011), varying only the input CCSN yields—either those from Nomoto et al. (2013) or those from Limongi and Chieffi (2018). We find that the abundances of C, Mg, and Ca predicted by the GCE model are sensitive to the input CCSN yields—that is, the predicted [X/Fe] abundances change by > 0.2 dex at the peak of the metallicity distribution function (MDF) ($-1.5 <$ [Fe/H] < -1.0). We therefore define parameters in our analytic functions for C, Mg, and Ca that can be varied to match all of the input yield sets.

Appendix 4.7 describes the final analytic functions and parameters in more detail. We obtain seven parameters that represent variations in the nucleosynthetic yields: the Fe yield from Type Ia SNe ($\rm Fe_{Ia}$), the exponent of the C yields from CCSNe ($\rm expC_{II}$), the normalization of Mg and Ca yields from CCSNe ($\rm normMg_{II}$, $\rm normCa_{II}$), the normalization of the C yield from AGB stars ($\rm normC_{AGB}$), and the normalization and peak of the Ba yield from AGB stars ($\rm normBa_{AGB}$, $\rm meanBa_{AGB}$). These parameters are then allowed to vary in the GCE model.

4.3 Results: Dwarf galaxy star formation histories

4.3.1 Fitting the GCE model

We use the chemical evolution model described in the previous section to simultaneously match the MDF as well as the abundance trends of [Mg/Fe], [Si/Fe], [Ca/Fe], [C/Fe], and *s*-process-only $\rm [Ba/Fe]_s$ (see Section 4.2) as a function of [Fe/H]. We choose not to include [Mn/Fe] and [Ni/Fe] in the model fitting. Manganese and nickel are iron-peak elements that are produced in the same nucleosynthetic events as iron. However, unlike iron, these elements—particularly manganese—are likely more sensitive to the physics of Type Ia supernova than to the SFH (e.g., Seitenzahl et al. 2013a; Seitenzahl and Townsley 2017). Rather than use [Mn/Fe] and [Ni/Fe] to fit the model, we instead use these abundances to validate our model and probe additional physics in Section 4.5.2.

Following Kirby et al. (2011), we treat the chemical evolution model as tracing a path $\epsilon_j(t)$ in the six-dimensional {[Fe/H], [Mg/Fe], [Si/Fe], [Ca/Fe], [C/Fe], [Ba/Fe]$_s$}-space. The probability of a star forming at any time t is given by $dP/dt = \dot{M}_\star(t)/M_\star$, where $M_\star$ is the final stellar mass. The likelihood of a star i forming along the path defined by the chemical evolution model is therefore given by the line integral of dP/dt along the path ϵ_j for the total duration of the model $t_{\rm final}$:

$$L_i = \int_0^{t_{\rm final}} \left(\prod_j \frac{1}{\sqrt{2\pi}\sigma_{i,j}} \exp \frac{-(\epsilon_{i,j} - \epsilon_j(t))^2}{2(\sigma_{i,j})^2} \right) \frac{\dot{M}_\star(t)}{M_\star} dt \tag{4.10}$$

where $\epsilon_{i,j}$ is the jth observed elemental abundance ratio for star i, and $\sigma_{i,j}$ is the corresponding uncertainty. The final time step, $t_{\rm final}$ is not a free parameter. Rather, it is the last time step before the galaxy runs out of gas.

The total likelihood for a model is therefore proportional to the product of L_i for all N stars:

$$\begin{aligned} L \;=\; & \prod_i^N L_i \times \left(\frac{1}{\sqrt{2\pi}\delta M_{\star,\rm obs}} \exp \frac{-(M_{\star,\rm obs} - M_{\star,\rm model})^2}{2(\delta M_{\star,\rm obs})^2} \right. \\ & \left. \times \frac{1}{\sqrt{2\pi}\delta M_{\rm gas,model}} \exp \frac{-(M_{\rm gas,model})}{2(\delta M_{\rm gas,obs})} \right)^{0.1N} . \end{aligned} \tag{4.11}$$

Here, the additional terms require that the final stellar and gas masses of the model ($M_{\star,\rm model}$ and $M_{\rm gas,model}$) match the observed masses ($M_{\star,\rm obs}$ and $M_{\rm gas,obs}$) within the observational uncertainties. The exponent $0.1N$ is chosen to weight these terms relative to the abundance distributions, to prevent them from dominating the likelihood while ensuring that the models end up with approximately the correct stellar and gas masses. We use observed stellar masses and uncertainties from Woo et al. (2008). We assume the observed gas mass $M_{\rm gas,obs}$ is zero for all dSphs, and we choose an arbitrary uncertainty of $\delta M_{\rm gas,obs} = 10^3\ M_\odot$ to ensure the model converges. This is similar to observed upper limits on gas measurements (e.g., Putman et al. 2021, who find an upper limit of $(3.2 \pm 0.4) \times 10^3\ M_\odot$ on Sculptor's HI mass).

To estimate the values of the 12 free parameters {$A_{\rm in}$, $\tau_{\rm in}$, $A_{\rm out}$, $A_\star$, α, $\mathrm{Fe_{Ia}}$, $\mathrm{expC_{II}}$, $\mathrm{normMg_{II}}$, $\mathrm{normCa_{II}}$, $\mathrm{normC_{AGB}}$, $\mathrm{normBa_{AGB}}$, $\mathrm{meanBa_{AGB}}$} that minimize the negative log-likelihood ($-\ln L$), we used the `emcee` Python module (Foreman-Mackey et al. 2013) to implement a Markov Chain Monte Carlo (MCMC) ensemble sampler. Table 4.3 describes the inputs and outputs of this MCMC sampling: the priors, initial values from linear optimization, and the best-fit values for each parameter.

For all free parameters except meanBa$_{\rm AGB}$, we assumed uniform priors with lower limits at 0 to avoid unphysical negative values and upper limits chosen based on the range of parameters determined by Kirby et al. (2011). For the parameter meanBa$_{\rm AGB}$, which dictates the mass of the AGB stars that produce the most barium, we assume a normal prior with a mean of 2 $M_\odot$ and standard deviation 0.5 $M_\odot$. This is because meanBa$_{\rm AGB}$ describes when the *s*-process begins to contribute meaningfully to the abundance of barium: low meanBa$_{\rm AGB}$ means that lower-mass AGB stars produce most of the *s*-process barium, so [Ba/Fe]$_s$ begins to increase at later times and higher [Fe/H]. As a result, any measurements of [Ba/Fe]$_s$ at low [Fe/H] will have outsized leverage on the value of meanBa$_{\rm AGB}$. We therefore enforce a Gaussian prior to keep this parameter within physically reasonable limits. Initial values of the parameters were chosen by performing a simple linear optimization of $-\ln L$. We sampled 10^6 steps using 32 ensemble members or "walkers" initialized about these values, discarded the first 10^4 "burn-in" steps, and used the remaining steps to sample the posterior distribution of the parameters.

Table 4.3: MCMC free parameters in chemical evolution model.

Parameter	Description	Prior	Initial value	Best-fit result
$A_{\rm in}$	Normalization of gas infall rate ($10^9\ M_\odot\ {\rm Gyr}^{-1}$)	$\mathcal{U}(0,5)$	1.07	$0.53^{+0.09}_{-0.08}$
$\tau_{\rm in}$	Gas infall time constant (Gyr)	$\mathcal{U}(0,1)$	0.16	$0.27^{+0.03}_{-0.02}$
$A_{\rm out}$	Gas lost per supernova ($M_\odot\ {\rm SN}^{-1}$)	$\mathcal{U}(0,20)$	4.01	$4.79^{+0.19}_{-0.19}$
$A_\star$	Normalization of star formation law ($10^6\ M_\odot\ {\rm Gyr}^{-1}$)	$\mathcal{U}(0,10)$	0.89	$0.79^{+0.14}_{-0.13}$
α	Power-law index of star formation law	$\mathcal{U}(0,2)$	0.82	$0.72^{+0.09}_{-0.07}$
$\mathrm{Fe_{Ia}}$	Fe yield from Type Ia SNe	$\mathcal{U}(0,0.9)$	0.80	$0.58^{+0.03}_{-0.03}$
$\mathrm{expC_{II}}$	Exponent of C yield from CCSNe	$\mathcal{U}(0,2)$	1.0	$1.32^{+0.03}_{-0.03}$
$\mathrm{normMg_{II}}$	Normalization of Mg yield from CCSNe	$\mathcal{U}(0,2)$	1.0	$1.41^{+0.10}_{-0.09}$
$\mathrm{normCa_{II}}$	Normalization of Ca yield from CCSNe	$\mathcal{U}(0,0.5)$	0.01	$0.24^{+0.05}_{-0.05}$
$\mathrm{normC_{AGB}}$	Normalization of C yield from AGB stars	$\mathcal{U}(0.4,5)$	0.60	$1.98^{+0.44}_{-0.36}$
$\mathrm{normBa_{AGB}}$	Normalization of Ba yield from AGB stars	$\mathcal{U}(0,1)$	0.33	$1.08^{+0.31}_{-0.21}$
$\mathrm{meanBa_{AGB}}$	Mass of peak Ba yield from AGB stars ($M_\odot$)	$\mathcal{N}(2,0.25)$	2.0	$2.80^{+0.16}_{-0.16}$

Note: For all parameters, the best-fit values are reported as the median (50th percentile) values, with uncertainties based on the 16th and 84th percentiles.

4.3.2 The star formation history of Sculptor dSph

We use the GCE model described in the previous section to fit the stellar abundances of Sculptor dSph. For Mg, Si, Ca, and C, we simultaneously fit our model to both the medium-resolution abundances from DEIMOS (Table 4.1) and the high-resolution DART abundances (Hill et al. 2019; North et al. 2012) (filled blue and empty orange points, respectively, in Figure 4.5). When fitting [Fe/H], we use only the DEIMOS yields because the DART sample is significantly smaller than the DEIMOS sample ($N_{\rm DART}$ = 89 compared to $N_{\rm DEIMOS}$ = 376). When fitting *s*-process Ba abundances, we use only the DART yields because the statistical correction used to remove the *r*-process contribution (Section 4.5.3) was based on the DART yields of Eu and Ba.

Figure 4.5 shows the best-fit abundance trends from the GCE model, illustrating that the model fits the stellar abundances reasonably well. We also plot the outputs from the best-fit GCE model, showing how the components of the galaxy change over time, in Figure 4.6. We note that while the rates of Type Ia SNe (dotted line in bottom panel) appear relatively low—particularly when compared to AGB stars at late times—this is because the average yield per Type Ia SN is much larger (typically by at least two orders of magnitude; see Figures 4.12 and 4.14) than the average yield per AGB wind. Despite their small numbers, Type Ia SNe dominate galactic chemical evolution at late times.

The corresponding cumulative SFH from this best-fit model is shown in Figure 4.7 as a thick black line; to give a rough sense of the uncertainty in this model, thin black lines represent random realizations of the posterior distribution. We find that Sculptor has an ancient stellar population: the best-fit SFH is a single burst of star formation with a relatively short duration of $\sim$ 0.92 Gyr. We note that chemical evolution models measure relative rather than absolute ages, so the exact location of our measured SFH on the time axis is uncertain. Bromm and Yoshida (2011) point out that the halos thought to be the hosts of the first galaxies are predicted to form $\sim$ 500 Myr after the Big Bang; we therefore assume our SFH begins when the universe is 500 Myr old.

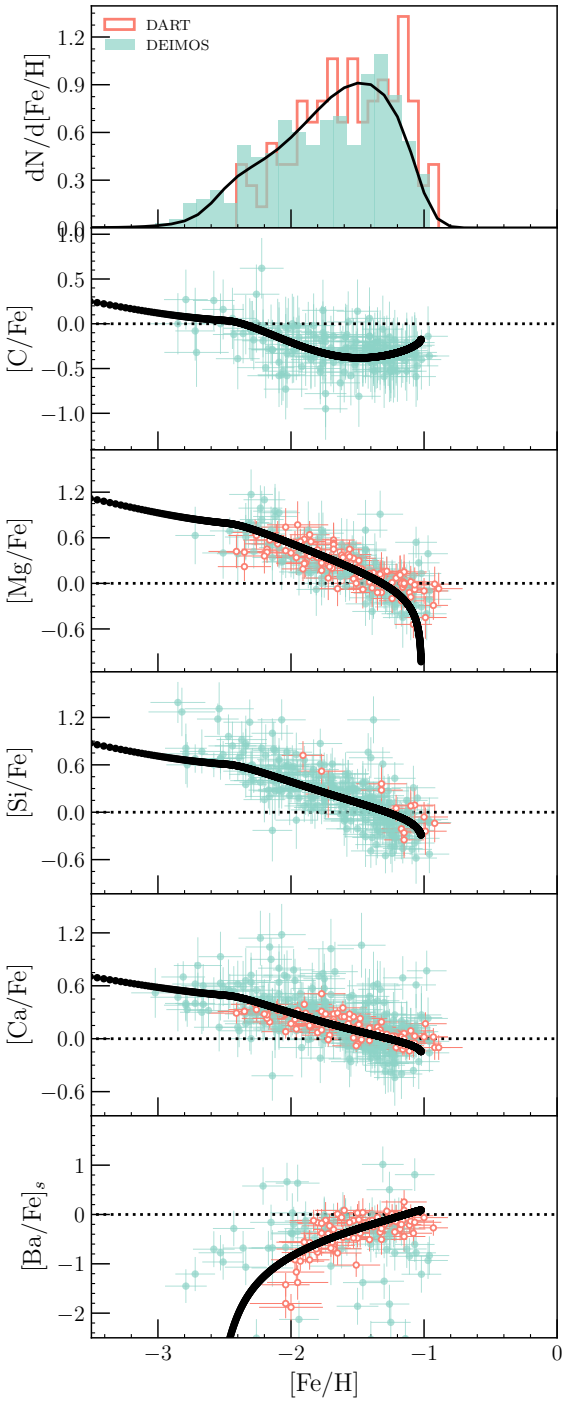

Figure 4.5: Metallicity distribution function (top panel) and abundance trends as a function of [Fe/H] from the best-fit GCE model for Sculptor dSph (black lines). Filled blue (empty orange) histogram and points represent the observed data from DEIMOS (DART). Note that [Fe/H] from DART and [Ba/Fe] from DEIMOS were excluded from fitting and are shown here for illustration.

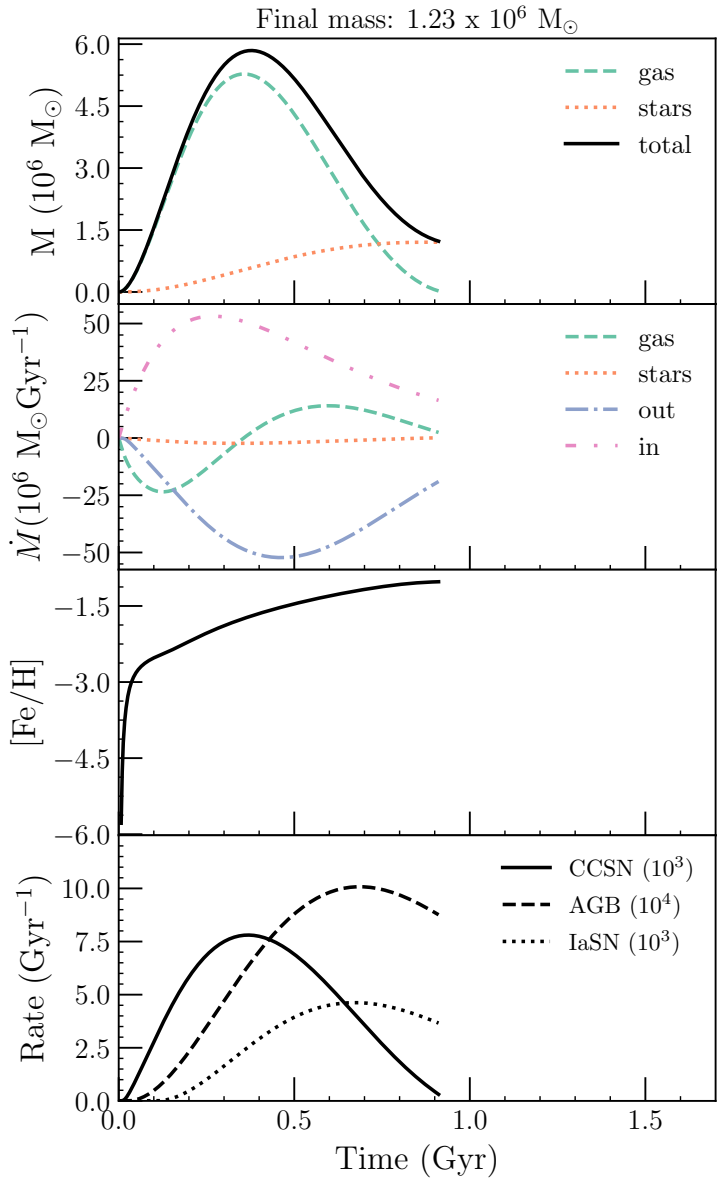

Figure 4.6: Outputs from the best-fit GCE model as a function of time. Top: the total masses of the different components. Second from top: the changes in mass. Third from top: the overall stellar metallicity. Bottom: the rates of nucleosynthetic events.

4.4 Discussion

4.4.1 Comparison to previous literature

As shown in Figure 4.7, we also compare our results to previous measurements of dSph SFHs. Nearly all measurements of Sculptor's SFH have been based on CMD fitting. Da Costa (1984) and Monkiewicz et al. (1999) fit a few model isochrones of varying ages and metallicities to CMDs and found that most of the stars in Sculptor must be relatively ancient ($\sim$ 13 $\pm$ 2 Gyr old). Dolphin (2002) reanalyzed the data

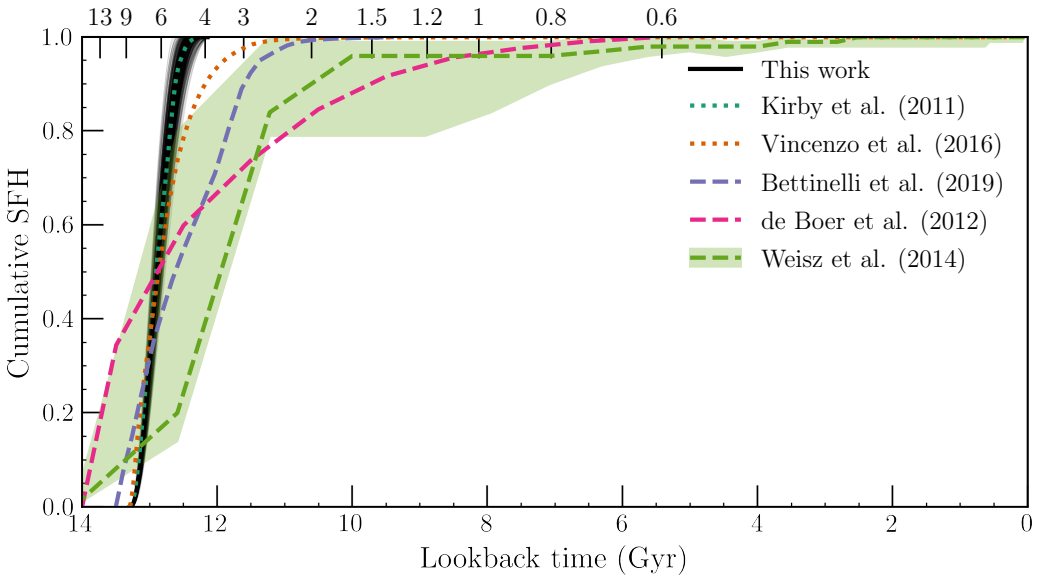

Figure 4.7: Cumulative star formation history from the best-fit GCE model for Sculptor dSph (black solid lines). Photometrically derived SFHs from the literature are plotted as dashed lines and shaded regions, while SFHs derived from GCEs and stellar abundances are plotted as dotted lines.

from Monkiewicz et al. (1999) by interpolating over a grid of synthetic CMDs to get a "true model CMD" rather than fitting discrete isochrones, coming to the same conclusion that Sculptor must be "entirely ancient." On the other hand, de Boer et al. (2012) argued that Sculptor has a much more extended SFH than these previous measurements would indicate. Using a new technique to simultaneously fit the CMD and the MDF, de Boer et al. (2012) found that Sculptor had a continuous period of star formation with a duration of $\sim 6-7$ Gyr (dashed pink line in Figure 4.7). Savino et al. (2018) extended this technique to include horizontal branch stars in fitting the CMD and MDF, finding an extended SFH with a prominent tail of star formation at younger ages.

However, these results were based on relatively shallow photometry that did not reach significantly below the main-sequence turnoff (MSTO). Other measurements from deeper photometry appear to confirm the original picture of Sculptor as an ancient galaxy that formed all of its stars in a short burst. Weisz et al. (2014) measured CMDs using the Hubble Space Telescope, obtaining photometry with $\sim$ 30% completeness at $\sim$ 2 mag below the MSTO. From these, they determined that Sculptor formed $\sim$ 90% of its stars $>$ 10 Gyr ago (dashed green line and shaded region in Figure 4.7). Similarly, Bettinelli et al. (2019) used DECam to obtain a

CMD down to $\sim$ 2 mag below the MSTO and found that Sculptor had a single burst of star formation with a full width at half maximum of $\sim$ 2.2 Gyr (dashed purple line in Figure 4.7).

As Figure 4.7 shows, SFHs measured from GCE models are also ancient, in qualitative agreement with the results from deep photometry. Yet GCE models tend to produce shorter absolute star formation durations (dotted lines) than the photometrically derived SFHs (dashed lines). This discrepancy likely arises from the limitations of photometric methods; although photometry is excellent at determining absolute ages, as discussed in Section 4.2 the age resolution of CMD fitting degrades for old and metal-poor populations. Abundance-derived estimates of the star formation duration may therefore better resolve the *relative* spread in ages within the ancient population of Sculptor.

Our results are largely consistent with previous SFH measurements using GCE models. The SFH we derive in this work (solid black line in Figure 4.7) has a duration of 0.92 Gyr. This is slightly shorter than the SFH found by Vincenzo et al. (2016), who used a one-zone model and found that 99% of the stars in Sculptor dSph formed within the first 2.16 Gyr of its evolution (dotted orange line in Figure 4.7). However, their model only aimed to fit the stellar metallicity distribution function and did not include information about individual abundances. Kirby et al. (2011), on the other hand, used similar methods to our work and traced both the stellar MDF and several abundance ratios. They found that Sculptor finished forming stars within 1.1 Gyr; as Figure 4.7 shows, this SFH (dotted blue line) is entirely consistent with the random realizations of the posterior distributions from our model (black lines).

This work expands on that of Kirby et al. (2011) by using more data—they used only DEIMOS abundances and did not use any [C/Fe] or [Ba/Fe] abundance information. Our model incorporates *s*-process abundances, as well as additional abundances measured from the VLT DART survey. It also has additional free parameters beyond those used in Kirby et al. (2011), which we use to fit the analytic functions describing nucleosynthetic yields. The consistency between our results and those of Kirby et al. (2011) suggests that including these additional parameters in our model does not significantly impact our main results; instead, as we will discuss later in Section 4.5.1, these parameters provide additional useful information about predicted nucleosynthetic yield sets.

4.4.2 Model assumptions

In this section, we discuss the simplifying assumptions on which our chemical evolution model depends, and their potential impact on our results. These assumptions can broadly be classified into three categories: assumptions inherent to the construction of the model, assumptions in the model inputs, and other potential sources of systematic errors. In Figures 4.8 and 4.9, we illustrate some of the effects of changing these assumptions.

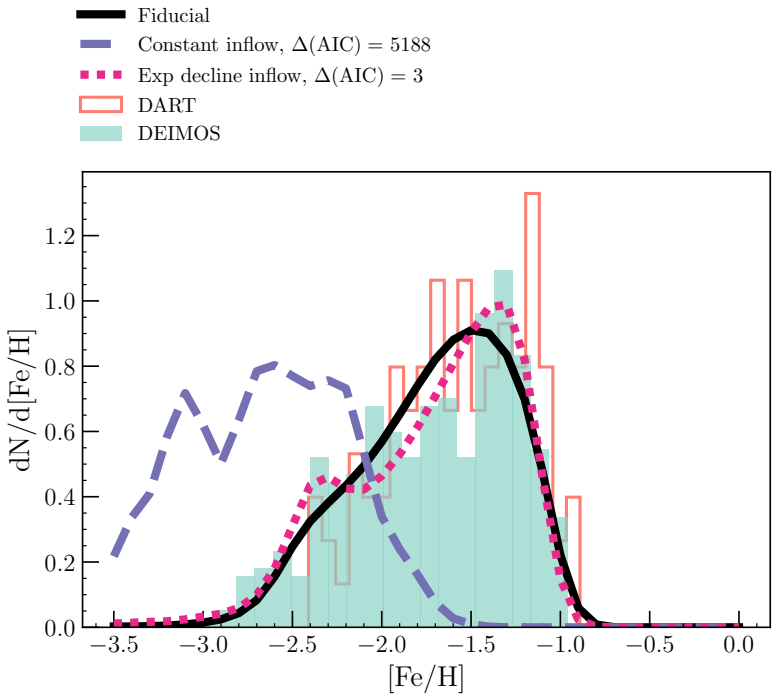

Figure 4.8: Comparisons between the MDFs of Sculptor from the fiducial GCE model (black solid line) and from models with other gas inflow parameterizations. The assumed parameterization of gas inflow significantly influences the shape of the MDF.

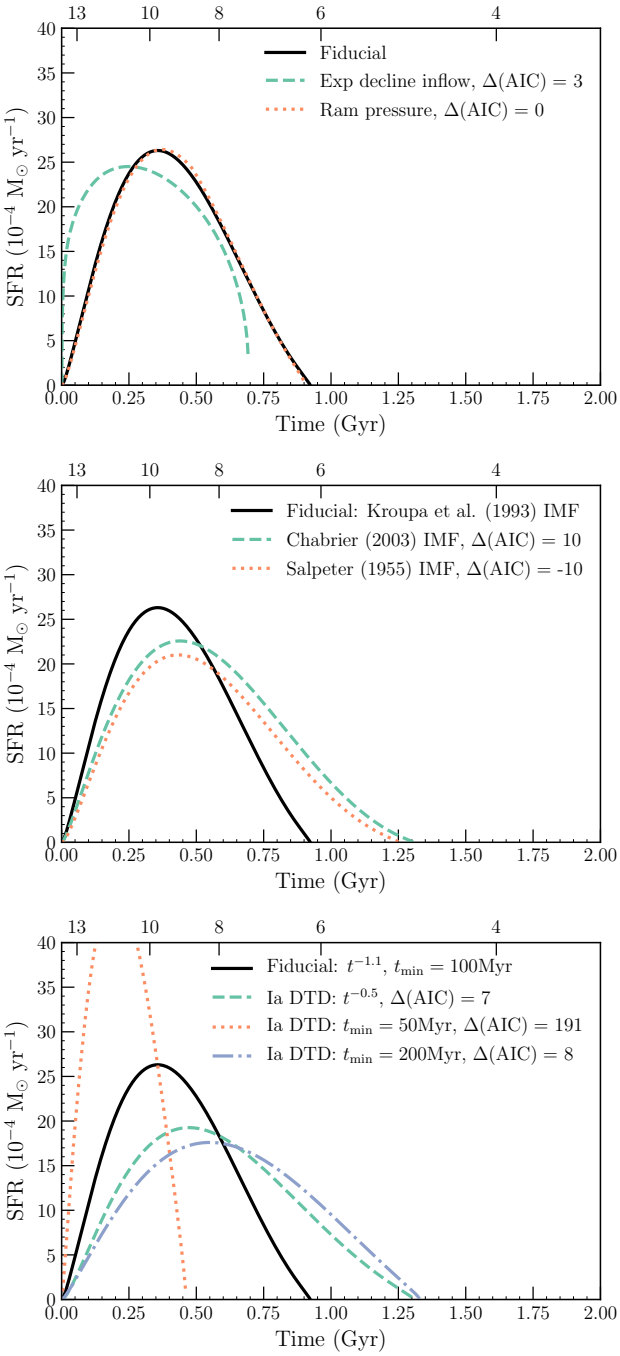

Figure 4.9: Comparisons between the SFHs of Sculptor from the fiducial GCE model (black solid line) and from other test models as described in the text. Top: results from varying assumptions in model construction: using an exponentially declining gas inflow (green dashed line) and adding ram pressure stripping (orange dotted line). Middle: results from varying the stellar IMF: Chabrier (2003) IMF (green dashed line) and Salpeter (1955) IMF (orange dotted line). Bottom: results from varying Type Ia DTD: decreasing the power law index to −0.5 (green dashed line), decreasing the minimum delay time to 50 Myr (orange dotted line), and increasing the minimum delay time to 200 Myr (purple dot-dashed line).

Model construction

In constructing our simple one-zone model, we have made a number of inherent assumptions. For example, the primary assumption in our model is the "one-zone" assumption of instantaneous mixing. This approximation is reasonably well-founded for dSphs; Escala et al. (2018) found that in simulated dwarf galaxies, a well-mixed ISM due to turbulent metal diffusion successfully reproduces observed abundance distributions of dSphs.

Other model assumptions may have greater impacts on the measured SFH. For example, the parameterization of gas inflow (Equation 4.5) strongly influences the shape of the SFH because star formation depends on the gas mass, which is in turn predominantly set by the gas inflow. Fortunately, the inflow parameterization is constrained by the metallicity distribution function. This is shown in Figure 4.8, which illustrates the output MDFs of models using other common inflow parameterizations. To compare the goodness-of-fit of these models, we compute the Akaike information criterion (AIC); a lower AIC implies less information loss, so a given model is a "better" fit than our fiducial model if $\Delta(\mathrm{AIC}) = \mathrm{AIC}_{\mathrm{model}} - \mathrm{AIC}_{\mathrm{fiducial}}$ is positive. A constant gas inflow, given by the equation

$$\dot{\xi}_{j,\mathrm{in}}(t) = A_{\mathrm{in}} \frac{M_{j,\mathrm{gas}}(0)}{M_{\mathrm{gas}}(0)} \tag{4.12}$$

where A_{in} is a free parameter, is entirely unable to match the MDF of Sculptor dSph ($\Delta(\mathrm{AIC}) \gg 0$).

An exponentially declining inflow,

$$\dot{\xi}_{j,\mathrm{in}}(t) = A_{\mathrm{in}} \frac{M_{j,\mathrm{gas}}(0)}{M_{\mathrm{gas}}(0)} \exp\left(\frac{-t}{\tau_{\mathrm{in}}}\right) \tag{4.13}$$

with free parameters A_{in} and τ_{in}, performs better than the constant inflow model, but not as well as our fiducial model ($\Delta(\mathrm{AIC}) = 3$). As shown in the top panel of Figure 4.9, using the exponentially declining inflow produces a single burst of star formation that ends after 0.69 Gyr (green dashed line). This is shorter than our fiducial model SFH (total duration of 0.92 Gyr) by a factor of $\sim 25\%$, likely because higher gas inflow at early times accelerates star formation and more quickly depletes gas. While this demonstrates that the parameterization of the gas inflow may have a significant effect on the predicted shape and duration of the SFH, more complex parameterizations of the gas inflow are somewhat disfavored for Sculptor dSph. As noted by de Boer et al. (2012) and Escala et al. (2018), among others, a bursty SFH

might produce a wider spread in [α/Fe] at fixed [Fe/H] than observed in Sculptor (although see, e.g., Marcolini et al. 2008).

Our model also ignores environmental effects like tidal or ram pressure stripping, which may cut off gas inflows and/or contribute to the removal of gas. Simulations (e.g., Kazantzidis et al. 2017) have shown that these environmental effects can, depending on galaxy orbital parameters, contribute significantly to gas loss in dSphs. To test this, we apply a simple model of ram pressure stripping by adding a constant to the gas outflow (Equation 4.6). This parameterization is similar to that used in the analytic model of Kirby et al. (2013), who found that ram pressure stripping successfully reproduced the metallicity distribution function of Sculptor dSph. Following this parameterization, we apply an additional constant outflow starting at [Fe/H] = −1.5 (based on the best-fit parameterization found by Kirby et al. 2013, who found that ram pressure stripping in Sculptor began at [Fe/H] < −1.41):

$$\dot{\xi}_{j,\mathrm{out}}(t) = \frac{M_{j,\mathrm{gas}}(t)}{M_{\mathrm{gas}}(t)} \left[A_{\mathrm{out}} \left(\dot{N}_{\mathrm{II}} + \dot{N}_{\mathrm{Ia}} \right) + C_{\mathrm{ram}} \right]. \tag{4.14}$$

Here, we allow C_{ram} to be a free parameter setting the removal of gas due to ram pressure stripping. We fit it along with the other parameters in our GCE model,[4] finding a best-fit value of $C_{\mathrm{ram}} = 2.76^{+1.53}_{-1.77}\ M_{\odot}\ \mathrm{yr}^{-1}$. The resulting SFH is shown as a orange dotted line in the top panel of Figure 4.9, which is almost exactly the same as the fiducial model; the overall star-forming duration of 0.90 Gyr is $\sim 2\%$ different from that predicted by the fiducial model and has almost the same goodness-of-fit (as measured by the AIC).

There are a number of other model assumptions that may affect our measurement of the SFH. For example, we do not account for reionization, which may heat infalling gas and delay star formation. Furthermore, our parameterization of the outflow rate as linearly proportional to the supernova rate (Equation 4.6) assumes that supernovae are the only factors in determining outflow rates and that all supernovae (both Type Ia and core-collapse) contribute equally to outflows. However, recent hydrodynamic simulations indicate that other factors, such as a galaxy's gas fraction (e.g., M. Orr et al., in preparation) and the clustering of supernovae (e.g., Fielding et al. 2018), can strongly affect whether supernovae are able to produce galactic outflows. Equation 4.6 also assumes that the galactic gravitational potential remains constant, but dark matter accretion, environmental effects, and stellar feedback might all affect

[4]When fitting C_{ram}, we assume a uniform prior of $\mathcal{U}(0, 5)$ and an initial value of 0.

the underlying gravitational potential of a galaxy. Fully addressing these assumptions would require a more sophisticated model, which we defer to future work.

Model inputs

We now consider the effects of different inputs in our GCE model. First, we consider the assumed forms of the supernova and AGB DTDs. For CCSNe and AGB stars, these are set by a combination of the stellar IMF and stellar lifetimes. Our initial model assumes a Kroupa et al. (1993) IMF. The middle panel of Figure 4.9 shows the effect of using a Chabrier (2003) or Salpeter (1955) IMF on the output SFH. Both these IMFs are slightly steeper than our fiducial model, producing more low-mass stars and fewer high-mass stars. The dearth of massive stars means it takes longer for stellar feedback to remove gas from the galaxy, leading to longer predicted SFHs. Adopting a Chabrier (2003) IMF leads to a total star formation duration of 1.30 Gyr (a 41% increase from the fiducial duration of 0.92 Gyr), while the Salpeter (1955) IMF predicts a star formation duration of 1.25 Gyr (a 36% increase).

Finally, perhaps the most uncertain input in our model is the Type Ia DTD. Although it appears that many observational studies have reached a consensus on the power law index of the Type Ia DTD of ~ -1 (see, e.g., the review by Maoz and Mannucci 2012), for completeness we consider the effect of changing the DTD index. We find that a shallower DTD power law ($\propto t^{-0.5}$) provides a fit that is only slightly worse than our fiducial model ($\Delta(\mathrm{AIC}) = 7$). This shallower DTD flattens the rate of Type Ia SNe as a function of time, so that it takes longer for Type Ia SNe to remove gas from the galaxy. As a result, the best-fit SFH from this shallower DTD (green dashed line in the bottom panel of Figure 4.9) is longer than the fiducial SFH by 42% (an increase from 0.92 to 1.31 Gyr).

We next consider the minimum delay time t_{min}. This parameter, which sets the time at which Type Ia SNe first "turn on," is currently poorly constrained by observations (e.g., Maoz and Mannucci 2012). A number of studies (e.g., Castrillo et al. 2021; Greggio 2005; Wiseman et al. 2021) suggest t_{min} should be as short as ~ 0.04 Gyr, which is approximately the main-sequence lifetime of the most massive secondary in the binary system that produces a Type Ia SN (i.e., an 8 $M_{\odot}$ progenitor). Our fiducial GCE model (Section 4.3) assumes a minimum delay time of $t_{\mathrm{min}} \sim 0.1$ Gyr, which corresponds to the formation of a carbon-oxygen white dwarf from a $4-5$ $M_{\odot}$ progenitor. We test the effect of making Type Ia SNe more prompt by decreasing t_{min} to 0.05 Gyr. As shown by the orange dotted line in the bottom panel of Figure 4.9,

this decreases the duration of the SFH by 50% and provides a significantly worse fit to the data (Δ(AIC) = 191).

We also consider a later minimum delay time, which may imply a lower-mass progenitor. Increasing $t_{\rm min}$ to 0.2 Gyr flattens the rate of Type Ia SNe; similar to the shallower $t^{-0.5}$ power law, this increases the duration of the SFH by 50% (purple dotted-dashed line in the bottom panel of Figure 4.9). The fit to the data is only slightly worse than the fiducial model (Δ(AIC) = 9). Kirby et al. (2011) also experimented with increasing the delay time to 0.3 Gyr. With this change, they found a much longer SFH duration of 3.7 Gyr for Sculptor. Our result is different because we have the benefit of AGB products (C and Ba) to better constrain the SFH.

We conclude that changing the Type Ia DTD to reduce the number of Type Ia SNe may produce models that can also fit the observed data reasonably well. These models may produce SFHs that are more extended than our fiducial model by up to $\sim$ 50%. We note, however, that full constraints on the form of the Type Ia DTD are beyond the scope of this paper, and we defer this to a later work (M. de los Reyes et al., in preparation).

Additional systematics

Another potential source of systematic error is the selection effect of the observed stellar population. The DEIMOS spectroscopic sample was centrally concentrated to maximize the number of member stars per slit mask. However, evidence suggests that there are two distinct stellar populations in Sculptor: a kinematically cold, relatively metal-rich centrally concentrated population, and a warm, metal-poor spatially extended population (e.g., Battaglia et al. 2008). Indeed, although they do not agree on absolute ages in Sculptor's SFH, previous studies that measure the SFH in different regions of Sculptor find that the duration of star formation is longer in its more central regions.

Both de Boer et al. (2012) and Bettinelli et al. (2019) define a "central" region of $\sim 10''$ in which the SFH duration is longest. This region has roughly the same radial extent as our spectroscopic sample (both the DEIMOS and DART samples are concentrated in the inner $\sim 12''$ of Sculptor dSph, as shown in Figure 2 of Hill et al. 2019), so we expect our measurements to probe the younger, more metal-rich stars. In this case, the duration of star formation for the overall stellar population in Sculptor may be even shorter than the $\sim$ 1 Gyr duration of star formation that we measure. We also note that the existence of a bimodal population suggests multiple

bursts of star formation, but no measurement of Sculptor's SFH—including our own—finds evidence of more than one burst of star formation.

4.5 Implications for nucleosynthetic yields

Not only does our GCE model result in a robust measurement of the SFH, it can also probe the nucleosynthetic production of different elements. The free parameters used to describe nucleosynthetic yields can be used to compare different sets of theoretical yields. Furthermore, even though we do not fit [Mn/Fe], [Ni/Fe], total [Ba/Fe], and [Eu/Fe] in our initial GCE model, our best-fit model can still be used to provide insight into their nucleosynthesis.

4.5.1 Comparing CCSN and AGB yield sets

As described in Section 4.2.3, the nucleosynthetic yields from CCSN and AGB models can vary widely. We aimed to work around these uncertainties by parameterizing the yields with analytic functions (Appendix 4.7). For a number of these yields we defined free parameters, allowing the model to vary the yields in order to best match the observed abundance trends. By examining the behavior of these free parameters, we can determine whether certain yield sets are preferred over others.

Among the CCSN yields, we varied the yields for C, Mg, and Ca. The best-fit yields, shown as blue lines in Figure 4.13, are a better match to the yields compiled by Nomoto et al. (2013) rather than those from the models of Limongi and Chieffi (2018). There are a number of differences between these two yield sets that could contribute to this discrepancy. At least one major difference is in the assumed explosion "landscape" (i.e., what masses of progenitor stars explode): Limongi and Chieffi (2018) assumed that all stars with initial masses above 25 $M_\odot$ implode, so that no yields are produced from explosive nucleosynthesis. As a result, many of their predicted CCSN yields (the dotted lines in Figure 4.13) are zero for high-mass progenitors. Our model, which finds nonzero yields at masses $> 25\ M_\odot$ (i.e., extremely prompt nucleosynthesis) for the parameterized elements C, Mg, and Ca, is therefore more consistent with the Nomoto et al. (2013) yields, which assume that all massive progenitor stars explode. This may suggest that an explosion landscape different from the simple one assumed by Limongi and Chieffi (2018) is needed to match observations (see, e.g., Griffith et al. 2021).

Our GCE model also exhibits other features—high Mg yields and relatively low Ca yields at low progenitor masses—in the best-fit yields that appear to be consistent with the Nomoto et al. (2013) yields. These features could result from a number of

model assumptions. For example, Limongi and Chieffi (2018) evolve massive stars from pre-main sequence to pre-supernova, fix the explosion energy such that all exploding models produce exactly 0.1 $M_\odot$ of Fe, and include the effects of rotation. Nomoto et al. (2013), on the other hand, evolve massive stars from pre-supernova to explosion, assume fixed supernova energy $E_{\rm SN} = 10^{51}$ erg, and do not include rotation. Determining the exact reasons why our model appears to agree with the C, Mg, and Ca yields of Nomoto et al. (2013) is beyond the scope of this paper. We also note that our result differs slightly from the result of Nuñez et al. (2022), who independently infer CCSN nucleosynthetic yields for a number of elements using damped Lyα systems. They find that while the C yields from Nomoto et al. (2013)[5] are consistent with the observed [C/Fe] ratio, the Limongi and Chieffi (2018) yields are typically more consistent with other observed abundance ratios, including [C/O].

For the AGB yields, we varied the yields of C and Ba, shown in Figure 4.14. The best-fit yields (blue lines) are more consistent with the Stromlo AGB yields from Karakas and Lugaro (2016) and Karakas et al. (2018), which predict enhanced C and Ba values at low progenitor masses. The AGB yields predicted by the FRUITY models (Cristallo et al. 2015) do not predict such a large enhancement. The large C and Ba yields may result from the Stromlo models including a deeper third dredge-up mixing, which brings more He-shell material to the stellar surface. This mixing predominantly affects elements made by neutron capture such as barium, along with the products of partial He-shell burning such as carbon.

4.5.2 Probing Type Ia SNe using Mn and Ni

Manganese and nickel are both iron-peak elements predominantly produced in Type Ia SNe. As discussed in Section 4.3.1, Mn is particularly sensitive to the physics of Type Ia SNe. The production of the only stable isotope of manganese, ^{55}Mn, depends strongly on the density—and therefore the mass—of the progenitor white dwarf (Seitenzahl et al. 2013a; Seitenzahl and Townsley 2017). White dwarfs near the Chandrasekhar mass ($M_{\rm Ch} \approx 1.4\ M_\odot$) are expected to produce solar or supersolar [Mn/Fe] and [Ni/Fe], while sub-$M_{\rm Ch}$ models tend to produce subsolar [Mn/Fe] and [Ni/Fe] (see, e.g., Figure 4.12).

Kirby et al. (2019) and de los Reyes et al. (2020) found that in Sculptor dSph, subsolar [Ni/Fe] and [Mn/Fe] abundances indicate that sub-$M_{\rm Ch}$ Type Ia SNe likely dominate. Both found that the Ni and Mn yields in Sculptor were most consistent

[5]Specifically, Nuñez et al. (2022) consider the yields from Kobayashi et al. (2006) and Nomoto et al. (2006), from which Nomoto et al. (2013) built their yield catalog.

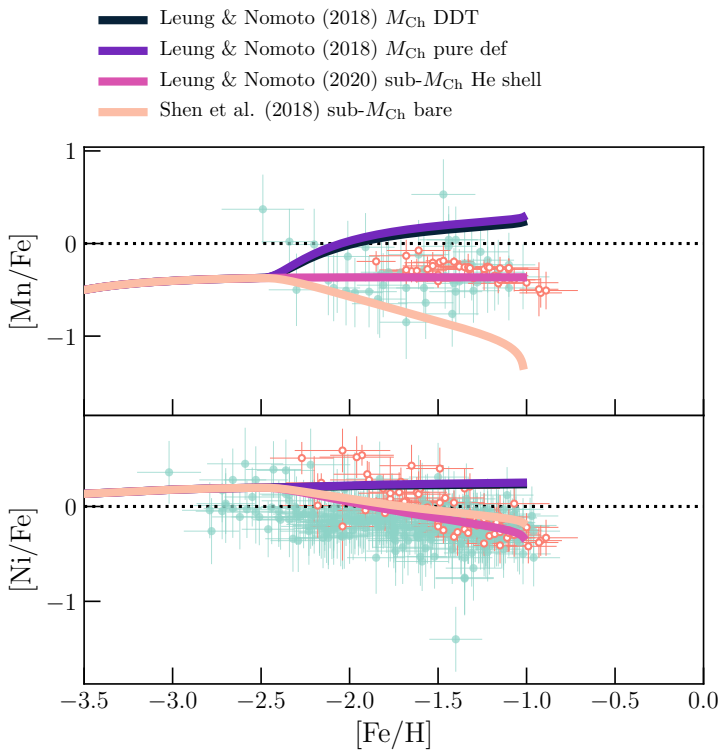

Figure 4.10: Comparisons among different Type Ia yields in the best-fit GCE model (solid lines) for manganese (top) and nickel (bottom). Points denote observations from DEIMOS (filled blue points) and DART (empty orange points).

with $\sim$ 1 $M_\odot$ sub-$M_{\rm Ch}$ models from Leung and Nomoto (2020). However, these comparisons were based on an analytic model that made a number of simplifying assumptions (e.g., that CCSNe are the only nucleosynthetic sources at early times, that CCSN yields are metallicity-independent, that the only contributions to stellar abundances are from supernovae). Our GCE model can be used to make more sophisticated comparisons.

In Figure 4.10, we use the best-fit parameters from Table 4.3 and vary the Type Ia yields of Mn and Ni. We find that the observed [Mn/Fe] and [Ni/Fe] trends are consistent with sub-$M_{\rm Ch}$ models, supporting the hypothesis that sub-$M_{\rm Ch}$ Type Ia SNe likely dominate in Sculptor dSph. In particular, the Leung and Nomoto (2020) model of a $\sim$ 1 $M_\odot$ CO white dwarf with a helium shell appears to best fit our data. This is in broad agreement with the findings of Kobayashi et al. (2020), who used a one-zone chemical evolution model to study dSphs and found that a significant fraction of sub-$M_{\rm Ch}$ Type Ia SNe are needed to reproduce the observed iron-peak abundances. Similar results have also been obtained in the Milky Way (see, e.g.,

Palla 2021, and references therein).

Although we have attempted to pick a representative subset of Type Ia models, there are many other yield sets that we do not consider here. For the models that we have used in our comparison, we have included the effect of metallicity-dependent yields; however, our GCE model does not make any assumptions about the masses of Type Ia SNe that explode, so we are unable to include mass-dependent yields. For simplicity, we also do not consider the effects of multiple simultaneous channels of Type Ia SNe. In contrast, see, e.g., Kobayashi et al. (2020) who found that Type Iax SNe, potentially the pure deflagrations of hybrid C+O+Ne white dwarfs, are required to match the observed [Mn/Fe] abundances. Furthermore, we do not attempt to correct the observed Mn or Ni abundances for the effects of stellar atmospheres not being in local thermodynamic equilibrium (LTE). These non-LTE effects may be especially significant for manganese (e.g., Bergemann et al. 2019).

4.5.3 Probing *r*-process nucleosynthesis using Ba and Eu

As shown in Figure 4.5, our simple GCE model is largely able to capture the behavior of the barium abundances produced by the slow neutron-capture process $[\mathrm{Ba/Fe}]_s$. However, as discussed in Section 4.2, the rapid neutron-capture process (*r*-process) produces a non-negligible amount of barium. It also produces the majority of europium. Because our initial model does not include any *r*-process contribution, it significantly underpredicts the total Ba and Eu abundances (solid cyan lines in Figure 4.11).

Despite recent work identifying neutron star mergers (NSMs) as a key site of the *r*-process (see, e.g., Rosswog et al. 2018; Shibata and Hotokezaka 2019, and references therein), the details of *r*-process nucleosynthesis are still uncertain. A full analysis of *r*-process nucleosynthesis is beyond the scope of this work, but our GCE model can place some constraints on *r*-process timescales and yields. In particular, we can constrain the rough timescale of *r*-process nucleosynthesis: does the *r*-process primarily occur in prompt events (such as high-mass or rapidly-rotating CCSNe), or relatively more delayed events (such as NSMs)?

To test this, we use our best-fit GCE model (parameters from Table 4.3) and modify the input yields to simulate prompt or delayed *r*-process events. To model prompt *r*-process events, we add a contribution to the CCSN yields for Ba and Eu. We use Ba yields predicted by Li et al. (2014) (see Appendix 4.7 for details) and assume a universal *r*-process ratio of $[\mathrm{Ba/Eu}] \sim -0.7$ (Sneden et al. 2008) to compute

Eu yields. To model delayed r-process events, we assume a relatively steep NSM DTD in the form of a $t^{-1.5}$ power law (e.g., Côté et al. 2019; Simonetti et al. 2019). Specifically, we initially adopt the following NSM DTD from Simonetti et al. (2019):

$$\Psi_{\rm Ia} = \begin{cases} 0 & t_{\rm delay} < 0.01 \text{ Gyr} \\ (10^{-4} \text{ Gyr}^{-1}\ M_\odot^{-1}) \left(\frac{t_{\rm delay}}{\rm Gyr}\right)^{-1.5} & t_{\rm delay} \geq 0.01 \text{ Gyr}. \end{cases} \tag{4.15}$$

We assume that each NSM produces the same amount of r-process elements: $M_{\rm Ba} = 2.3 \times 10^{-6}\ M_\odot$ and $M_{\rm Eu} = 2.3 \times 10^{-7}\ M_\odot$, from Li et al. (2014).

In the left panels of Figure 4.11, we plot the results of this test, showing the model predictions for [Ba/Mg] and [Eu/Mg] as a function of [Fe/H] assuming different r-process parameterizations: no r-process contributions (solid cyan line), contributions from either prompt or delayed channels (solid blue and purple lines, respectively), and contributions from both channels (solid black line). We plot [X/Mg] rather than [X/Fe] because Type Ia SNe contribute significantly to Fe at late times and could complicate our interpretation. Observations from both DEIMOS and DART are plotted for comparison. A successful model should be consistent with the observed trends: subsolar [Ba/Mg] below [Fe/H] $\lesssim -1.5$ that increases to near-solar at higher metallicities, and near-solar [Eu/Mg] that is roughly constant as a function of metallicity.

We first consider whether prompt r-process events alone can reproduce these observed trends. Our initial test (left panels of Figure 4.11) finds that the prompt r-process channel (solid blue line) appears to significantly underpredict both [Ba/Mg] and [Eu/Mg]. This may suggest that our assumed CCSN yields of Ba and Eu (respectively, from Cescutti et al. 2006; Li et al. 2014) are too low. We therefore attempt to produce better consistency with observations by increasing the CCSN yields of Ba and Eu, as shown by the dotted lines in the right panels of Figure 4.11. In order to better match the Ba abundances, the r-process yields from typical CCSN-like events must be drastically increased by a factor of 20. This may correspond physically to some combination of increasing the rate of CCSN-like r-process events and increasing the Ba and Eu yields expected from these events. This enhancement of prompt r-process contributions is able to increase the predicted [Ba/Mg] trend at low metallicity, making it consistent with observations at $-2.5 \lesssim$ [Fe/H] $\lesssim -2$ (blue dotted line in the upper right panel of Figure 4.11), but it underpredicts the observed [Ba/Mg] at $-2 \lesssim$ [Fe/H] $\lesssim -1.5$.

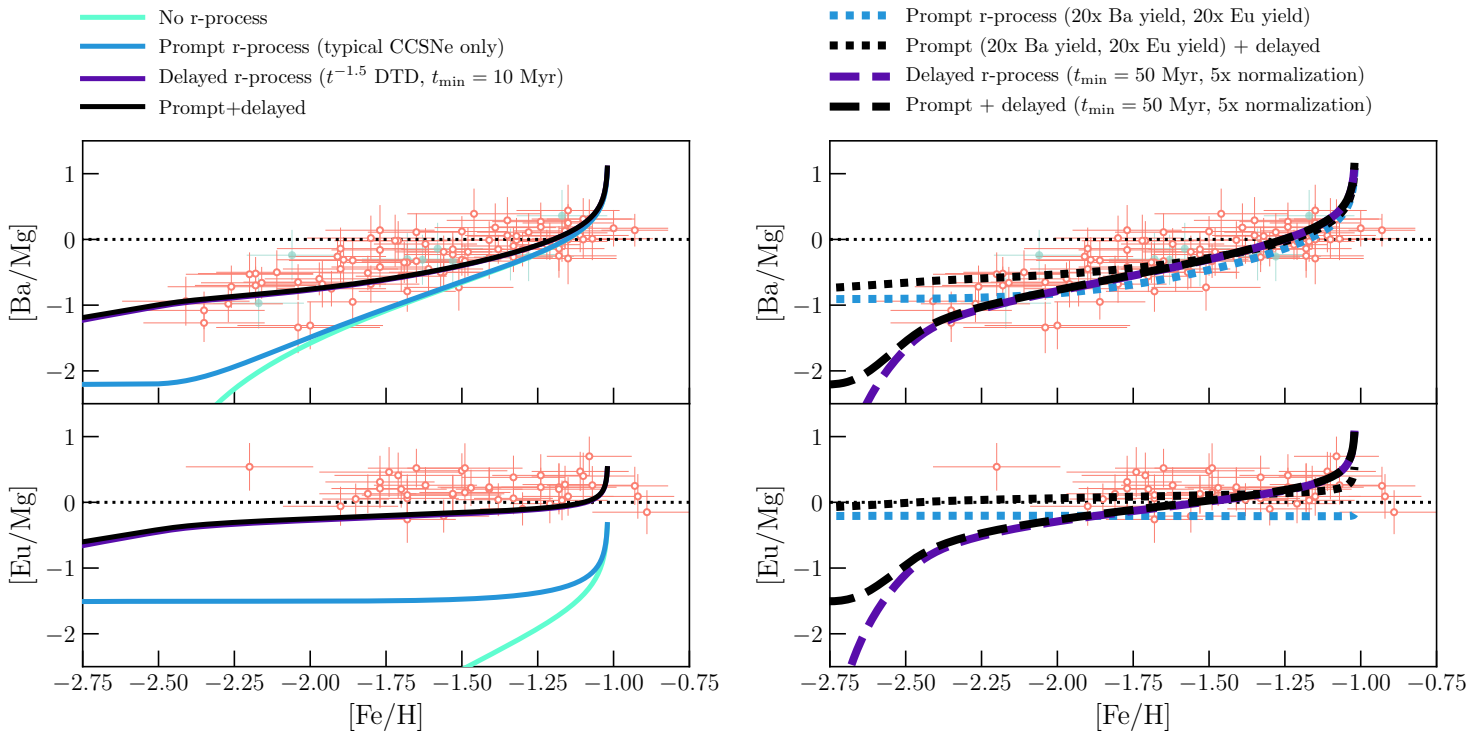

Figure 4.11: Comparisons among different parameterizations of the *r*-process in the best-fit GCE model (solid lines) for barium (top) and europium (bottom). Left: Best-fit GCE models without any r-process production (cyan), with only prompt CCSN-like r-process events (blue), with only delayed r-process events based on the Simonetti et al. (2019) DTD for neutron star mergers (purple), and with both prompt and delayed r-process events (black). Right: GCE models where the *r*-process channels have been modified to better match the observations. The dotted lines indicate the prompt and prompt+delayed channels when the prompt *r*-process yields have been enhanced, while the dashed lines indicate the delayed and prompt+delayed channels when the DTD has been modified. Points denote observations from DEIMOS (filled blue points) and DART (empty orange points).

Additionally, Frebel et al. (2010) measured abundances in the most metal-poor star in Sculptor and found abundance ratios of [Fe/H] ~ -3.8 and [Ba/Mg] $\lesssim -1.58$. This is well below the [Ba/Mg] ~ -1 at low metallicities predicted by the prompt r-process channel with enhanced yields. Since r-process events are likely rare (e.g., Ji et al. 2016), it is possible that this star simply formed before any prompt CCSN-like events could produce barium. However, the prompt channel alone also underestimates the observed [Eu/Mg] trend (blue dotted line in the lower right panel of Figure 4.11), despite the drastic enhancement in r-process yields. We therefore tentatively conclude that prompt CCSN-like r-process events alone may not be able to explain the observed trends, and at least some contribution from a delayed NSM-like process is likely needed.

We now consider the delayed r-process channel. The left panels of Figure 4.11 show that the delayed r-process channel (solid purple lines) is more consistent with observations than the prompt r-process channel (solid blue lines). The delayed channel also appears to dominate r-process nucleosynthesis; prompt r-process events do not contribute significantly to the combined prompt+delayed model (solid black lines). Yet this delayed r-process model, based on the Simonetti et al. (2019) NSM DTD (Equation 4.15), underpredicts the observed [Eu/Mg] trend. It also slightly overpredicts [Ba/Mg] at low [Fe/H] and underpredicts [Ba/Mg] at $-2 \lesssim$ [Fe/H] $\lesssim -1$.

In order to better match observations, we increase the normalization of the delayed r-process contributions by a factor of five. Physically, this can be done either by increasing the normalization of the Simonetti et al. (2019) NSM DTD, or by increasing the Ba and Eu yields expected from individual NSMs. Both of these modifications are plausible because both the NSM DTD and the nucleosynthetic yields from NSMs are relatively uncertain. We also increase the NSM $t_{\rm min}$ from 10 to 50 Myr. As shown by the dashed lines in the right panels of Figure 4.11, this allows the delayed r-process channel to begin contributing to r-process yields at later times than the CCSNe, so that [Ba/Mg] begins increasing at a higher [Fe/H]. This more-delayed NSM DTD produces a steeper [Ba/Mg] trend as a function of metallicity, which is more consistent with the observed trend. However, it also produces a steeper [Eu/Mg] trend as a function of metallicity, which is less consistent with the observed flat [Eu/Mg] trend (Skúladóttir et al. 2019). We conclude that relatively delayed (with minimum delay times $\gtrsim$ 50 Myr) r-process events alone may not be able to reproduce observed abundance trends in Sculptor, and that a combination of prompt and delayed events is needed.

Our result is consistent with previous results. Duggan et al. (2018) found that in multiple Local Group dSphs, the positive trend of [Ba/Fe] as a function of [Fe/H] appears to be steeper than the positive trend of [Mg/Fe] as a function of [Fe/H]. They argued that the primary *r*-process source of Ba must therefore be delayed relative to CCSNe (the primary source of Mg) in order to produce the [Ba/Fe] trend in dwarf galaxies. In a separate analysis of Sculptor dSph, Skúladóttir et al. (2019) use the flat [Eu/Mg] trend to argue the opposite: that the primary source of Eu must *not* be significantly delayed relative to the primary source of Mg. As our GCE model shows, both prompt and delayed *r*-process channels may be needed to reproduce the observed Ba and Eu trends in Sculptor. This agrees with investigations of the *r*-process in the Milky Way and in the universe (e.g., Cescutti et al. 2015; Côté et al. 2019; Matteucci et al. 2014; Siegel et al. 2019; Wehmeyer et al. 2015), which find that a combination of delayed NSMs and prompt CCSN-like events can successfully reproduce the observed trend and scatter of [Eu/Fe] in the Milky Way.

4.6 Conclusions

We have used a simple one-zone GCE model (Equation 4.3) to simultaneously understand the SFH and chemical evolution history of Sculptor dSph. This model is able to fit both the metallicity distribution function and the abundance patterns of seven elements. Like previous one-zone GCE models, our model fits the trends of the α elements Mg, Si, and Ca, which probe CCSNe (delay times of ~ 10 Myr after star formation), and Fe, which is predominantly produced by Type Ia supernovae (delay times of $\gtrsim 100$ Myr). Our model is also able to fit the observed abundances of C and Ba, which trace nucleosynthesis in AGB stars (delay times of $\gtrsim 10$ Myr after star formation).

Our best-fit model (Figure 4.5) indicates that Sculptor dSph had an SFH with a total star formation duration of ~ 0.92 Gyr. As shown in Figure 4.7, this is in contrast with some photometric measurements (e.g., de Boer et al. 2012; Savino et al. 2018), which found that Sculptor dSph has an extended SFH spanning $6 - 7$ Gyr, but qualitatively consistent with other recent estimates from deep photometry that find a relatively short and ancient SFH (e.g., Bettinelli et al. 2019; Weisz et al. 2014). It is also quantitatively consistent with other SFHs derived from GCE models (Kirby et al. 2011; Vincenzo et al. 2016), which predict SFH durations of $1 - 2$ Gyr. However, the star formation duration of ~ 0.92 Gyr predicted by our GCE model is shorter than the estimates from even the deepest photometric measurements, which found that the majority of star formation ended after $\sim 3 - 4$ Gyr. This discrepancy may be

partly due to various assumptions of our model—in particular, we find that changing the stellar IMF or the Type Ia DTD may increase the duration of the SFH by up to 50% (from ~ 0.92 to ~ 1.4 Gyr). Alternatively, our model's short SFH estimate may be a real result; although spectroscopic measurements cannot determine absolute ages, they may be more sensitive to age spreads in old stellar populations than photometric measurements.

Not only is our model able to probe Sculptor dSph's SFH, it can also provide insight into the nucleosynthesis of individual elements in the galaxy. In our model, we parameterized the nucleosynthetic yields from CCSNe and AGB stars using analytic functions. For the elements most sensitive to variations in the nucleosynthetic yields, we defined free parameters to vary the yields. The best-fit free parameters produce yield patterns that resemble those from the Nomoto et al. (2013) CCSN yields and the Stromlo (Karakas and Lugaro 2016; Karakas et al. 2018) AGB yields.

We also used our GCE model to test the nucleosynthesis of elements that were not used to fit the model. Mn and Ni are iron-peak elements that are sensitive to the physics of Type Ia supernovae. We found that the observed [Mn/Fe] and [Ni/Fe] trends are best reproduced by the sub-M_{Ch} (1.1 $M_{\odot}$) Type Ia supernova model from Leung and Nomoto (2020). Similarly, Ba and Eu are elements that can be used to trace r-process nucleosynthesis. We find that a combination of prompt CCSN-like events and delayed r-process events (with minimum delay times $\gtrsim$ 50 Myr) are required to reproduce the observed trends of [Ba/Mg] and [Eu/Mg].

We have shown that a simple GCE model can be used to probe both the star formation and chemical evolution of Sculptor dSph by fitting to the observed abundances of elements produced by multiple kinds of nucleosynthetic events. This method could easily be applied to other Local Group dSphs with available stellar spectroscopy. This would not only provide a complementary approach to photometrically derived SFHs but could also be used to test nucleosynthetic processes in different environments—for example, previous measurements of iron-peak elements have suggested that the dominant channel of Type Ia supernovae might depend on a galaxy's SFH (de los Reyes et al. 2020; Kirby et al. 2019). Finally, as always, this work could be extended with a larger sample size of observations, more precise spectroscopic measurements, or a more sophisticated model.

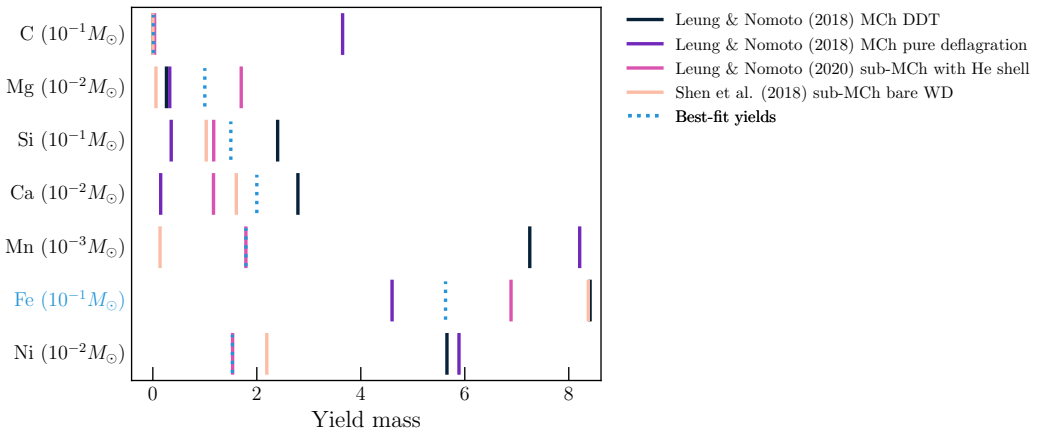

Figure 4.12: Nucleosynthetic yields from Type Ia supernovae. Colors denote different models. Yields are assumed to be independent of metallicity. Dotted blue lines show the parameterized yields, qualitatively chosen as described in Appendix 4.7. A free parameter is used to fit the yield of Fe (labeled with blue text), so the dotted blue line for Fe is the best-fit value from the fiducial GCE model (Table 4.3).

4.7 Appendix: Nucleosynthetic yield parameterizations

As described in Chapter 4, rather than select particular model yield sets for our galactic chemical evolution model, we represent the nucleosynthetic yields from supernovae and AGB stars with analytic functions. Parameters of these functions are varied in conjunction with the other model parameters.

The yields from Type Ia SNe are assumed to be independent of progenitor mass and metallicity. We plot the Type Ia SN yields from different models in Figure 4.12, as well as the yields chosen for our model (dotted blue lines). For C, Mg, Si, and Ca, the Type Ia SN yields were selected to be within the range of model yields, although the exact values do not matter because these yields do not significantly impact the final abundance trends. Manganese and nickel are not included in the GCE model fitting, so for our initial model we arbitrarily choose the yields from Leung and Nomoto (2020) for these elements (see Section 4.5.2). The yield of Fe from Type Ia SNe is a free parameter ($\mathrm{Fe_{Ia}}$); Figure 4.12 shows the best-fit value from our fiducial model (Table 4.3).

For CCSN and AGB yields, we fit the model yield sets (Table 4.2) with combinations of exponential and Gaussian functions. We chose functions that qualitatively approximate the shapes of the theoretical yields as functions of progenitor mass (M) and metallicity (Z). In particular, we fit yields that are mass-weighted by a Kroupa et al. (1993) IMF (i.e., multiplied by the IMF dN/dM). The analytic functions can

then be integrated over a range of progenitor stellar masses to compute the total yield of a given element that will be produced by stars in that mass range after an instantaneous 1 $M_{\odot}$ star formation burst. These functions are listed in Table 4.4 and illustrated as dotted blue lines in Figures 4.13 and 4.14 for CCSNe and AGB stars, respectively. The theoretical yield sets are also plotted for comparison (solid and dotted lines). For completeness, Figure 4.13 also illustrates the Li et al. (2014) r-process yields from CCSNe assumed in Section 4.5.3.

Table 4.4: Analytic functions describing IMF-weighted CCSN and AGB yields.

Element	CCSN yield ($M_\odot$)
H	$10^{-3}\left(255\left(\frac{M}{M_\odot}\right)^{-1.88}-0.1\right)$
He	$10^{-3}\left(45\left(\frac{M}{M_\odot}\right)^{-1.35}-0.2\right)$
C	$10^{-5}\left(100\left(\frac{M}{M_\odot}\right)^{-\mathrm{expC_{II}}}\right)$
Mg	$10^{-5}\left(\mathrm{normMg_{II}}+13\mathcal{G}\left(\frac{M}{M_\odot},19,6.24\right)\right)$
Si	$10^{-5}\left(2260\left(\frac{M}{M_\odot}\right)^{-2.83}+0.8\right)$
Ca	$10^{-6}\left(15.4\left(\frac{M}{M_\odot}\right)^{-1}+\mathrm{normCa_{II}}\left(40-10^4\frac{Z}{Z_\odot}\right)\mathcal{G}\left(\frac{M}{M_\odot},15,3\right)+0.06\right)$
Mn	$10^{-7}\left(30\left(\frac{M}{M_\odot}\right)^{-1.32}-0.25\right)$
Fe	$10^{-5}\left(2722\left(\frac{M}{M_\odot}\right)^{-2.77}\right)$
Ni[a]	$10^{-7}\left(8000\left(\frac{M}{M_\odot}\right)^{-3.2}\right)$
Ba[b]	$10^{-12}\left(1560\left(\frac{M}{M_\odot}\right)^{-1.80}+0.14-480\mathcal{G}\left(\frac{M}{M_\odot},5,5.5\right)\right)$
Element	**AGB yield ($M_\odot$)**
H	$10^{-1}\left(1.1\left(\frac{M}{M_\odot}\right)^{-0.9}-0.15\right)$
He	$10^{-2}\left(4\left(\frac{M}{M_\odot}\right)^{-1.07}-0.22\right)$
C	$10^{-3}\left(\mathrm{normC_{AGB}}\left(1.68-220\frac{Z}{Z_\odot}\right)\mathcal{G}\left(\frac{M}{M_\odot},2,0.6\right)\right)$
Mg	$10^{-5}\left(\left(400\frac{Z}{Z_\odot}+1.1\right)\left(\frac{M}{M_\odot}\right)^{0.08-340(Z/Z_\odot)}+\left(360\frac{Z}{Z_\odot}-1.27\right)\right)$
Si	$10^{-5}\left(\left(800\frac{Z}{Z_\odot}\right)\left(\frac{M}{M_\odot}\right)^{-0.9}-\left(80\frac{Z}{Z_\odot}+0.03\right)\right)$
Ca	$10^{-6}\left(\left(800\frac{Z}{Z_\odot}-0.1\right)\left(\frac{M}{M_\odot}\right)^{-0.96}-80\frac{Z}{Z_\odot}\right)$
Mn	$10^{-7}\left(1500\frac{Z}{Z_\odot}\left(\frac{M}{M_\odot}\right)^{-0.95}-160\frac{Z}{Z_\odot}\right)$
Fe	$10^{-5}\left(1500\frac{Z}{Z_\odot}\left(\frac{M}{M_\odot}\right)^{-0.95}-160\frac{Z}{Z_\odot}\right)$
Ni	$10^{-6}\left(840\frac{Z}{Z_\odot}\left(\frac{M}{M_\odot}\right)^{-0.92}-\left(80\frac{Z}{Z_\odot}+0.04\right)\right)$
Ba	$10^{-8}\left(\mathrm{normBa_{AGB}}\left(10^3\frac{Z}{Z_\odot}+0.2\right)\mathcal{G}\left(\frac{M}{M_\odot},\mathrm{meanBa_{AGB}},0.75-100\frac{Z}{Z_\odot}\right)\right)$
Eu	$10^{-11}\left(\left(3400\frac{Z}{Z_\odot}+0.4\right)\mathcal{G}\left(\frac{M}{M_\odot},2,0.65\right)\right)$

[a] The CCSN yield function for Ni was chosen to fit the yields from Limongi and Chieffi (2018). Since Ni is not included in fitting our GCE model (Section 4.2.2), this does not affect any of our results; however, we find that the Nomoto et al. (2013) yields significantly underpredict the observed [Ni/Fe] at low [Fe/H].

[b] Our fiducial model assumes that zero Ba and Eu are produced by CCSNe. The functions describing CCSN yields listed here are for the r-process; as described in the text, we use the Ba yields from Li et al. (2014) and scale by the universal r-process ratio [Ba/Eu] ~ -0.7 (see Sneden et al. 2008) to obtain the Eu yields.

Note: As described in the text, these yields are weighted by a Kroupa et al. (1993) IMF. In these equations, we use the notation $\mathcal{G}\left(\frac{M}{M_\odot},\mu,\sigma\right)$ to denote a normalized Gaussian function as a function of mass with mean μ and standard deviation σ.

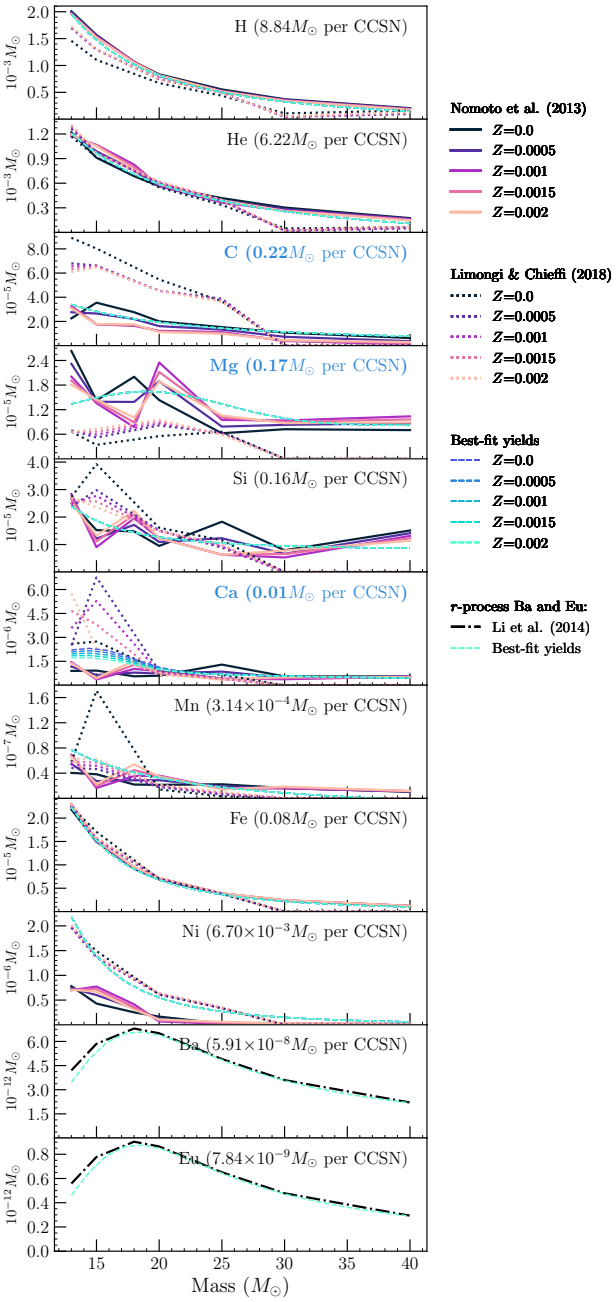

Figure 4.13: Nucleosynthetic yields from core-collapse supernovae as a function of initial stellar mass. Colors denote different metallicities; yields have been linearly interpolated to match the same metallicity range. Dashed lines show parameterized yields for illustration. For elements labeled with bold blue text, free parameters are used to fit the GCE model. As described in the text, these yields are weighted by a Kroupa et al. (1993) IMF. To aid in interpretation, we list the average $Z = 0.002$ yield per CCSN—i.e., the $Z = 0.002$ best-fit analytic function integrated over the yield sets' CCSN progenitor mass range 13 – 40 $M_\odot$ and multiplied by a factor of 500 (since roughly 1 CCSN is produced for every 500 $M_\odot$ of stars formed)—in the upper right corner of each plot.

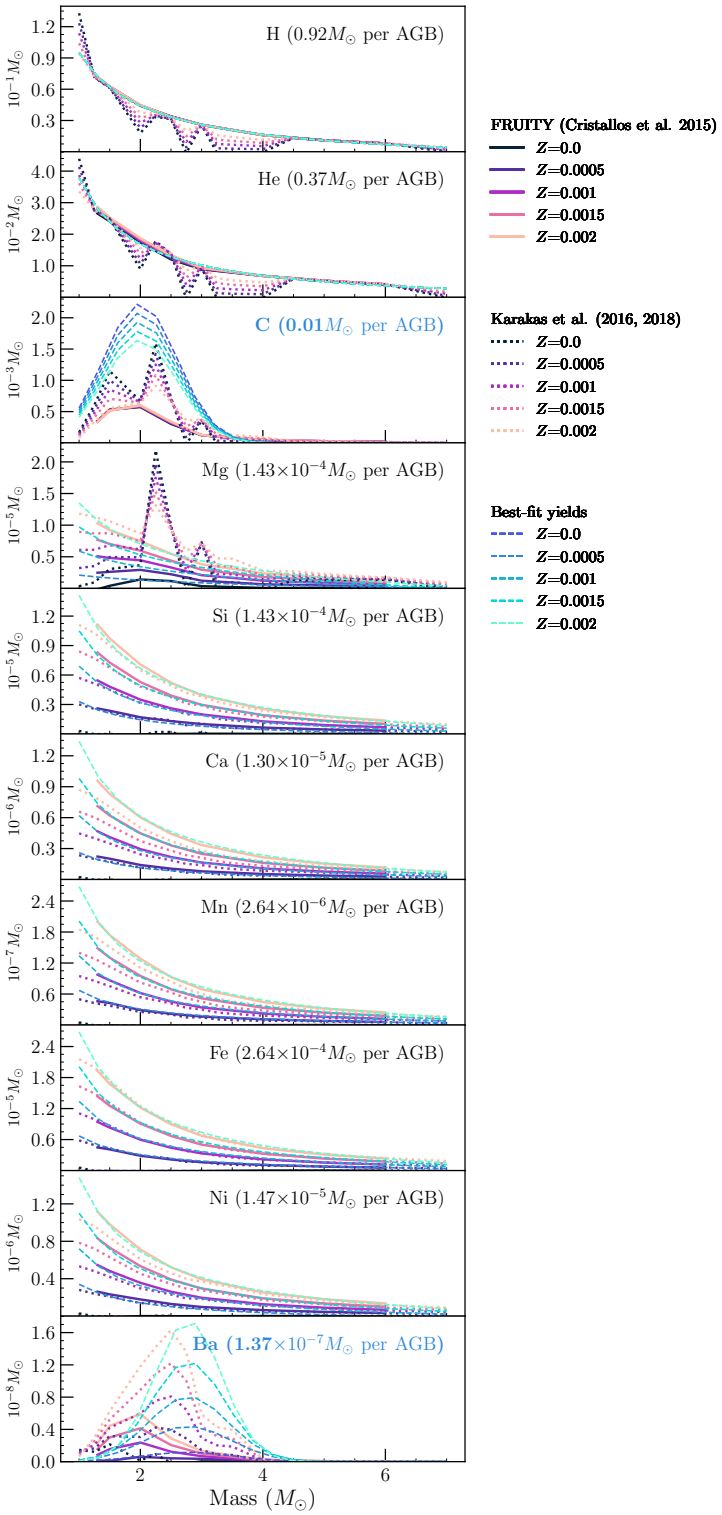

Figure 4.14: Similar to Figure 4.13, but plotting nucleosynthetic yields from AGB stars. To compute the average $Z = 0.002$ yield per AGB star, we integrate over the yield sets' AGB progenitor mass range $1 - 7\ M_\odot$ and multiply by a factor of 5.7 (since roughly 1 AGB star is produced for every 5.7 $M_\odot$ of stars formed).

Chapter 5

THE STELLAR KINEMATICS OF VOID DWARF GALAXIES USING KCWI

Abstract

Dwarf galaxies located in extremely under-dense cosmic voids are excellent testbeds for disentangling the effects of large-scale environment on galaxy formation and evolution. The stellar kinematics of these void dwarf galaxies can help shed light on secular dynamical processes in galaxies. I have obtained integrated field spectroscopy for low-mass galaxies ($M_\star = 10^7 - 10^{8.5}\ M_\odot$) located inside ($N = 21$) and outside ($N = 9$) cosmic voids using the Keck Cosmic Web Imager (KCWI). In this chapter I present these observations, along with measurements of stellar line-of-sight rotational velocity and velocity dispersion. I use these measurements to test the tidal stirring hypothesis, which posits that dwarf spheroidal galaxies are formed through tidal interactions with more massive host galaxies. My preliminary results find relatively low values of $v_{\rm rot}/\sigma_\star < 1$ for the majority of my sample, suggesting that dwarf galaxies can become dispersion-supported "puffy" systems even in the absence of large-scale environmental effects. I also find no trend between $v_{\rm rot}/\sigma_\star$ and distance from a massive galaxy $d_{L^\star}$ out to $d_{L^\star} \lesssim 3$ Mpc. Along with recent findings in Local Volume, these results suggest that tidal interactions are not responsible for formation of the majority of dispersion supported dwarf galaxies, and that isolated low-mass galaxies form as puffy systems rather than the dynamically cold disks predicted by classical galaxy formation theory. I find some indication of an upward trend between $v_{\rm rot}/\sigma_\star$ and galaxy stellar mass at higher stellar masses ($\gtrsim 10^{7.5}\ M_\odot$). This may imply the existence of a minimum stellar mass (in the range $10^{8.5} - 10^9\ M_\odot$) below which stellar disks are unable to form.

5.1 Introduction

Galaxies, particularly dwarf galaxies, are not closed-box systems. They affect and are in turn affected by their environments, and these interactions leave an imprint on their observable properties. As discussed in Chapter 1, dwarf galaxies located in cosmic voids are useful systems for disentangling environmental effects. These void dwarf galaxies can provide a number of insights into galaxy formation and evolution, having formed and evolved in the lowest-density environments in the universe.

First, by studying void dwarf galaxies we can observe how low-mass galaxies evolve in near-total isolation. Their distance from massive galaxies makes them ideal observational counterpoints for direct "apples-to-apples" comparisons with simulations of isolated dwarf galaxies. Furthermore, ΛCDM predicts that the evolution of void galaxies will be slowed relative to "field" galaxies located in cosmic filaments, potentially making them direct analogs to the high-redshift galaxies that were the building blocks for Milky Way-like galaxies. Detailed characterizations of high-z analogs in the local universe might provide complementary information to observations taken by, e.g., JWST (Gardner et al. 2006), which will be able to detect extremely high-z galaxies, but may not necessarily obtain detailed spectra of these objects.

A number of previous studies have aimed to characterize the galaxies located in voids (e.g., Beygu et al. 2016, 2017; Domínguez-Gómez et al. 2022; Douglass and Vogeley 2017; Florez et al. 2021; Kniazev et al. 2018; Kreckel et al. 2012, 2014; Penny et al. 2015; Pustilnik et al. 2016, 2011, 2019; Wegner et al. 2019, and references therein). However, the vast majority of these studies have aimed to measure integrated galaxy properties, including global colors, star formation rates, and metallicities. In this chapter, I will describe an observational program designed to measure the *spatially-resolved* properties of a sample of local void dwarf galaxies. In particular, this program aims to probe the stellar kinematics of these galaxies, which can help shed light on the dynamical processes that drive galaxy formation.

Classical galaxy formation theory suggests that all galaxies form as thin, rotationally supported disks (Fall and Efstathiou 1980; White and Rees 1978). However, it is not clear whether this picture of disk formation extends to the lowest-mass galaxies ($M_\star \lesssim 10^9\ M_\odot$). Disk-like morphologies are not as readily apparent among dwarf galaxies, particularly compared to the obvious and dramatic spiral disks common among higher-mass galaxies, leading some authors to suggest that dwarf and disk galaxies are structurally distinct systems (Schombert 2006). Detailed kinematic measurements are most readily available for the dwarf galaxies closest to us: our own Local Group. The Local Group hosts both gas-rich star-forming dwarf irregular (dIrr) galaxies and gas-poor dwarf spheroidal (dSph) galaxies (e.g., McConnachie 2012). The prevalence of these two classes is a well-known function of location: most dIrrs live outside the virial radii of the Milky Way or M31, while satellite galaxies are typically dSphs. This local "morphology-density relation" (first noted by Einasto et al. 1974) appears to be a direct consequence of environmental effects,

as tidal effects and ram-pressure stripping can remove gas from gas-rich dIrrs and turn them into gas-poor dSphs (e.g., Grcevich and Putman 2009; Putman et al. 2021; Spekkens et al. 2014).

Environmental effects have also been thought to affect the stellar kinematics of Local Group dwarf galaxies. In the "tidal stirring" model (Mayer et al. 2001), a rotationally supported dwarf galaxy with a stellar disk will experience repeated tidal shocks as it passes through the pericenter of its orbit around a massive host galaxy. These shocks may produce a tidally induced bar, which transfers angular momentum to the outer regions of the galaxy. As high-angular momentum material is stripped, the overall rotation of the galaxy decreases, transforming it into a pressure-supported, kinematically "puffy" stellar system. Simulations have had some success in showing that dSphs may be formed from dIrrs through this mechanism (e.g., Kazantzidis et al. 2017, and references therein).

Yet the kinematic distinction between dIrrs and dSphs is perhaps more ambiguous than the tidal stirring model would suggest. Stellar spectroscopy has revealed that a number of Local Group dIrrs are primarily dispersion-supported (e.g., Kirby et al. 2017; Leaman et al. 2012)—and indeed, nearly all the lowest-mass ($M_* \lesssim 10^8$ $M_\odot$) Local Group dwarf galaxies are either dispersion-supported or only weakly rotationally supported (Kirby et al. 2014; Wheeler et al. 2017). Wheeler et al. (2017) suggest that this may point to a formation scenario in which dwarf galaxies initially form as "puffy" stellar systems rather than dynamically cold disky systems, and they show that zoom-in simulations of isolated dwarf irregular galaxies are consistent with this picture. I will demonstrate in this chapter that void dwarf galaxies provide a useful test of these scenarios.

The structure of this chapter is as follows. I describe the observations and data reduction in Section 5.2. In Section 5.3, I present measurements of spatially-resolved stellar kinematics, before discussing the implications of these results in Section 5.4. I summarize my conclusions in Section 5.5.

5.2 Data

Since the stellar populations of galaxies outside the Local Group cannot be resolved, spatially-resolved spectroscopy is needed to estimate stellar kinematic properties. Integral field units (IFUs), which can obtain spectral information across the full spatial extent of an extended source, are ideal for such measurements. I use the Keck Cosmic Web Imager (KCWI; Morrissey et al. 2018) to obtain IFU observations

of dwarf galaxies inside and outside voids. In this section, I describe the sample selection, observations, and data reduction process.

5.2.1 Sample selection

I selected a sample of void dwarf galaxies from Table 1 of Douglass et al. (2018), who identified 993 void dwarf galaxies from the Sloan Digital Sky Survey Data Release 7 (SDSS DR7; Abazajian et al. 2009). To classify these galaxies as "void" galaxies, Douglass et al. (2018) used the void catalog compiled by Pan et al. (2012), which was built from the SDSS DR7 catalog using the VoidFinder algorithm (El-Ad and Piran 1997; Hoyle and Vogeley 2002). This algorithm finds geometric voids using the spatial distribution of massive galaxies in SDSS DR7 (with absolute magnitudes $M_r < -20$. Isolated galaxies (described as having the third nearest-neighbor more than $\sim$ 7 Mpc/h away) are removed, then all remaining "wall" galaxies are then placed on a three-dimensional grid. Every grid cell devoid of "wall" galaxies is potentially part of a void, so VoidFinder aims to identify the maximal sphere that can be drawn in the void: a sphere is grown from each empty grid cell, reaching its maximum size once four galaxies are present on its surface (since a sphere is uniquely defined by four non-coplanar points). Overlapping spheres are combined, and any sphere with radius > 10 Mpc is then associated with a void.

I chose 19 void dwarf galaxies, aiming to evenly span a range of stellar masses from $10^7 - 10^9$ $M_\odot$ (i.e., approximately one galaxy in each 0.1 dex stellar mass bin). Because gas-phase metallicities are a property of particular interest in void dwarf galaxies (e.g., Douglass and Vogeley 2017; Kreckel et al. 2014; Pustilnik et al. 2016), I further prioritized galaxies in each mass bin with the highest [OIII] λ4363 fluxes.[1] The stellar mass estimates (Kauffmann et al. 2003) and emission line fluxes (Tremonti et al. 2004) were both obtained from the MPA/JHU value-added catalog.

By targeting galaxies selected from geometric voids in a galaxy survey, this sample selection implicitly assumes that the relatively bright ($m_r < 17.77$) galaxies in SDSS DR7 perfectly trace the underlying dark matter distribution of the universe. This may not be the case (see Desjacques et al. 2018, for a review of this so-called galaxy "bias"), which means our void sample could be contaminated with galaxies that are not in truly low-density voids—that is, galaxies that live in regions devoid of relatively bright galaxies, but which still contain "dark" non-emitting gas, ultra low surface brightness systems, or dark matter. Additionally, selecting for [OIII] λ4363-

[1] [OIII] λ4363 is the weakest of the emission lines required to measure "direct" gas-phase metallicities.

bright galaxies might introduce additional bias, since void dwarf galaxies with high [OIII] λ4363 fluxes are likely to be among the most metal-rich of the full void dwarf galaxy population. I revisit these assumptions and discuss their implications in Section 5.4.

An additional 7 dwarf galaxies were also selected from SDSS Data Release 16 (SDSS DR16; Ahumada et al. 2020) as a control sample, with stellar masses similar to those of galaxies in the void sample. These were selected to have relatively low redshift ($z < 0.02$), visible OIII and Hβ lines in their SDSS spectra, and (as with the void galaxies) were prioritized based on their [OIII] λ4363 flux. These control galaxies were either observed or identified as galaxies in SDSS data releases after DR7, so they could not be directly checked against the SDSS DR7 void catalog of Pan et al. (2012). Given the relative rarity of void dwarf galaxies—Douglass et al. (2018) identified 993/9519 (10%) of the SDSS DR7 dwarf galaxies as "void" galaxies—the majority of the control galaxies are likely non-void galaxies. However, without further verification, I simply consider these "field" galaxies (as none of them appear to have nearby massive host galaxies) throughout the remainder of my analysis.

Finally, 3 dwarf galaxies were added to the sample as potential objects of interest. These include Pisces A and B, which are nearby dwarf galaxies that have been identified at the boundary between nearby voids and higher-density filaments. Their star formation histories have undergone a recent increase, potentially triggered by gas accretion from a more dense environment, suggesting that they are in the process of exiting the voids in which they likely formed (Tollerud et al. 2016). IFU maps of Pisces A and B will help identify how this environmental transition affects the kinematic and chemical properties of these galaxies.

The last galaxy in the sample is ID 65 from Reines et al. (2020), who recently reported discoveries of luminous compact radio sources in nearby dwarf galaxies that are consistent with radiation from accreting black holes. Several of these sources appear to be located outside their host galaxies' central regions, and Reines et al. (2020) suggest that these are evidence for so-called "wandering" (i.e., non-AGN) black holes. Optical spectroscopy has previously been employed to search for central supermassive black holes in dwarf galaxies (e.g., Moran et al. 2014; Reines et al. 2013; Sartori et al. 2015), but the IFU data here present the first opportunity for investigating ionizing radiation from an *off-nuclear* black hole candidate in a dwarf galaxy.

Table 5.1 lists the properties of the final dwarf galaxy sample.

Table 5.1: General properties of void and field dwarf galaxy sample.

ID[a]	RA (J2000)	Dec (J2000)	z[b]	g[b] (mag)	log $M_\star$[b] [$M_\odot$]	Type[c]
1180506	09 12 51.73	+31 40 51.48	0.0064	17.17	6.99	v
281238	09 45 40.99	+01 37 03.87	0.0064	18.38	7.06	v
1904061	08 48 43.52	+22 55 47.60	0.013	17.93	7.47	v
821857	10 06 42.44	+51 16 24.23	0.0162	17.49	7.47	v
1158932	09 28 44.47	+35 16 41.14	0.0151	17.42	7.53	v
866934	09 16 25.07	+43 00 19.30	0.0085	16.66	7.57	v
825059	08 13 39.49	+36 42 34.56	0.0130	16.99	8.1	v
2502521	09 13 19.89	+12 32 07.32	0.0161	18.11	7.63	v
1228631	10 13 58.42	+39 48 01.62	0.007	15.65	7.64	v
1876887	08 49 56.66	+25 41 02.61	0.008	16.67	7.65	v
1246626	11 30 11.93	+44 27 16.07	0.0172	17.06	7.68	v
1142116	08 18 19.70	+24 31 36.94	0.0073	15.56	8.06	v
955106	10 16 28.21	+45 19 17.53	0.0055	14.86	8.10	v
1063413	11 23 22.03	+45 45 16.34	0.0202	17.37	8.22	v
1074435	09 48 00.79	+09 58 15.43	0.0104	16.30	8.35	v
1785212	07 50 41.62	+50 57 40.28	0.0187	17.51	8.36	v
1280160	11 07 13.71	+06 24 42.38	0.0085	15.88	8.53	v
1782069	10 04 38.88	+67 49 22.05	0.0145	16.99	8.59	v
1126100	09 34 03.03	+11 00 21.67	0.0085	15.15	9.02	v
Pisces A	00 14 46.00	+10 48 47.01	0.0008	17.56	...	v
Pisces B	01 19 11.70	+11 07 18.22	0.0020	17.43	...	v
SDSS J0133+1342	01 33 52.56	+13 42 09.39	0.0087	17.92	6.56	f
AGC 112504	01 36 40.92	+15 05 12.14	0.0088	17.84	7.58	f
UM 240	00 25 07.43	+00 18 45.63	0.0109	17.04	7.64	f
SHOC 150	03 04 57.97	+00 57 14.09	0.0121	17.86	7.78	f
LEDA 3524	00 58 55.47	+01 00 17.44	0.0179	16.47	7.99	f
LEDA 101427	00 24 25.95	+14 04 10.65	0.0142	15.86	8.35	f
IC 0225	02 26 28.29	+01 09 37.92	0.0051	14.06	8.72	f
reines65	11 36 42.72	+26 43 37.68	0.0333	15.65	7.64	f

[a] Galaxy ID. For most void galaxies, these are the galaxy index numbers from the KIAS Value Added Galaxy Catalog (Choi et al. 2010). For most field galaxies, these are the galaxy names preferred by NASA/IPAC Extragalactic Database (NED). The galaxy "reines65" is identified as galaxy 65 from(Reines et al. 2020).

[b] Redshifts, g-band magnitudes, and stellar masses are from SDSS. The photometrically-derived stellar masses are obtained from the MPA/JHU value added catalog (Kauffmann et al. 2003).

[c] Galaxy classification as "v" for void dwarf galaxy or "f" for field dwarf galaxy. Note that Pisces A and B are classified as "void" galaxies for our purposes, although they are likely moving into a cosmic filament (see text).

Table 5.2: Observations of void and field dwarf galaxies.

Object	Exposures (s)	Position angles (°)	Date (dd-mm-yy)	Airmass
Void dwarf galaxies				
1180506	2×300	167.6, 177.6	29-12-2019	1.03
281238	2×900	139.9, 149.9	28-12-2019	1.25
1904061	3×800	44.1, 54.1, 64.1	28-12-2019	1.01
821857	2×700	97.4, 107.4	28-12-2019	1.17
1158932	2×700	47.7, 57.7	29-12-2019	1.10
866934	2×300	4.4, 14.4	29-12-2019	1.11
825059	1×600, 2×700, 1×940	20.1, 30.1	30-12-2019	1.20
2502521	2×400	18.0, 28.0	28-12-2019	1.19
	2×800	8.0, 18.0	29-12-2019	1.25
1228631	2×600	16.0	22-01-2020	1.06
1876887	2×400	145.7, 175.7	28-12-2019	1.14
1246626	2×800	49.0	22-01-2020	1.10
1142116	2×900	144.3, 154.3	28-12-2019	1.12
955106	1×600	9.0	22-01-2020	1.12
1063413	4×900	167.0, 177.0	22-01-2020	1.26
1074435	1×600, 3×840	103.0, 113.0	22-01-2020	1.28
1785212	2×400	50.0, 60.0	29-12-2019	1.20
	2×850	50.0, 60.0	30-12-2019	1.50
1280160	2×700	145.0	22-01-2020	1.09
1782069	4×750	37.1, 47.1, 57.1	29-12-2019	1.62
1126100	2×300	149.2, 159.2	29-12-2019	1.02
Pisces A	1×600, 2×1200	0.0, 10.0	28-12-2019	1.11
	2×900	0.0, 10.0	30-12-2019	1.35
Pisces B	1×600, 2×1000	140.0, 150.0	30-12-2019	1.02
Field dwarf galaxies				
SDSS J0133+1342	1×500	128.0	22-01-2020	1.11
AGC 112504	2×900	134.1, 144.1	28-12-2019	1.51
UM 240	4×1000	91.0, 101.0	22-01-2020	1.13
SHOC 150	2×600, 2×660	118.0, 128.0	22-01-2020	1.44
LEDA 3524	2×400	147.4, 157.4	28-12-2019	1.55
LEDA 101427	2×400	14.8, 24.8	30-12-2019	1.54
IC 0225	2×900	167, 177	28-12-2019	1.10
reines65	4×600	45.0, 55.0	22-01-2020	1.10

5.2.2 Observations and data reduction

IFU data were obtained for the sample over 2.5 nights using KCWI, an optical integral field spectrograph on the Nasmyth platform of the 10 m Keck II telescope (Morrissey et al. 2018). KCWI has multiple configurations; in order to match the typical angular size of the dwarf galaxies in my sample, I used the medium slicer and blue BL grating centered at $\lambda = 4500$ Å. This combination yields a $20'' \times 16.5''$ field of view, nominal spectral resolution of ~ 2.5 Å ($\sigma \sim 71$ km s^{-1}) at 4500 Å, and a usable wavelength range of $3500 - 5100$ Å.

Table 5.2 describes the observations of each galaxy. For galaxies with multiple exposures, I rotated the position angles by $\pm 10^{\circ}$ for each exposure in order to minimize spatial covariance during stacking. For each object exposure, I observed a patch of nearby sky with the same exposure time and position angle to perform sky subtraction. I processed all object exposures using the most recent version of the KCWI data reduction pipeline[2], which produces flux-calibrated data cubes. Data cubes of the same object were then aligned and stacked using a drizzling algorithm (O'Sullivan and Chen 2020)[3].

5.3 Analysis

The final stacked data cubes are then analyzed using a custom pipeline[4] whose primary goal is to produce maps of stellar kinematics—stellar velocities and stellar velocity dispersions—from IFU datacubes. Although many of the specific details are tailored for this specific application, the pipeline follows many of the same general steps as other IFS survey analysis pipelines, including the Mapping Nearby Galaxies at Apache Point Observatory (MaNGA) Data Analysis Pipeline (Westfall et al. 2019) and Pipe3D (Sánchez et al. 2016).

5.3.1 Binning and covariance correction

Some initial steps are taken to prepare the data cubes: the cubes are first corrected for Galactic reddening using the $E(B - V)$ color indices measured by (Schlafly and Finkbeiner 2011), then the observed wavelength array is divided by $(1 + z)$ to correct for redshift. Each data cube is then spatially binned to increase the continuum signal-to-noise (S/N). The S/N of an individual spaxel is often too low to reliably fit with stellar continuum templates, particularly in low surface brightness regions

[2] `https://github.com/Keck-DataReductionPipelines/KcwiDRP`

[3] `https://github.com/yuguangchen1/kcwi`

[4] The full pipeline, along with all custom code used in this paper, is available at `https://github.com/mdlreyes/void-dwarf-analysis`

like galaxy outskirts or faint dwarf galaxies. It is therefore important to spatially bin spaxels, averaging multiple adjacent spaxels to increase the S/N. To do this, I use `vorbin`, an adaptive spatial binning algorithm that produces Voronoi tessellations (Cappellari and Copin 2003).

I first define the nominal S/N of an individual spaxel, assuming that each spaxel is independent. Because I am primarily interested in measuring information from the stellar continuum in each spaxel, I use the formula for the detrended *continuum* S/N defined by Rosales-Ortega et al. (2012):

$$\left(\frac{S}{N}\right)_c = \frac{\mu_c}{\sigma_c}, \tag{5.1}$$

where μ_c is the mean of the flux in the continuum band $f(\lambda)_c$, and σ_c is the detrended standard deviation (i.e., the standard deviation in the difference between $f(\lambda)_c$ and a linear fit to $f(\lambda)_c$). I take $f(\lambda)_c$ to be the flux across the continuum range 4700 – 4750 Å, which lacks strong emission features.

The S/N values from Equation 5.1 are likely overestimates, since stacking data cubes introduces covariance between adjacent spaxels. To account for this, rather than computing full covariance matrices for each spaxel in every data cube, I use an empirical formula to estimate the ratio between the "true" noise ϵ_{true} and the noise assuming no covariance $\epsilon_{\text{no covar}}$. This ratio, denoted η, is assumed to be a function of the bin size, with the form suggested by Husemann et al. (2013):

$$\eta = \epsilon_{\text{true}}/\epsilon_{\text{no covar}} = \begin{cases} \beta(1 + \alpha \log n) & N \leq N_{\text{threshold}} \\ \beta(1 + \alpha \log N_{\text{threshold}}) & N > N_{\text{threshold}}. \end{cases} \tag{5.2}$$

Here, N is the number of spaxels in each bin, α describes the strength of the dependence of η on bin size, and β is a normalization factor. Above a certain bin size $N_{\text{threshold}}$, additional spaxels are assumed to be far enough apart that they do not add any extra covariance, so the ratio η is capped at a constant.

I estimate the value of the free parameters $\{\alpha, \beta, N_{\text{threshold}}\}$ following the procedure of Law et al. (2016) as follows. First, I create mock data cubes in which all pixels have fluxes independently drawn from a normal distribution $\mathcal{N} \sim (1, 1)$ with mean and variance both unity. These mock cubes are stacked following the same drizzling procedure as the actual data cubes from individual exposures, producing mock intensity and variance cubes. For a stacked cube, the spaxels are binned using a simple boxcar of size n^2 where n varies. The standard deviation of each bin in the mock

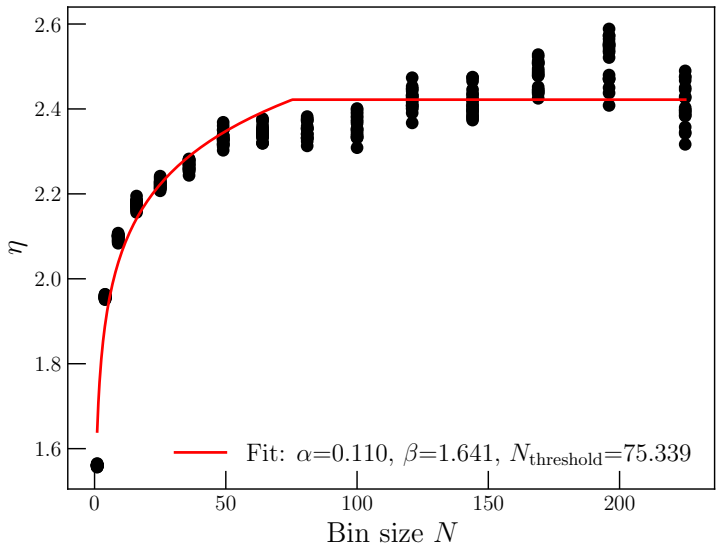

Figure 5.1: The ratio $\eta = \epsilon_{\text{true}}/\epsilon_{\text{no covar}}$ as a function of bin size for an example with 4 stacked exposures. Black points represent empirical estimates from mock data cubes, as described in the text. The red line indicates the best-fit empirical curve of the form Equation 5.2.

intensity cube is an estimate of the "true" noise ϵ_{true}, since it accounts for the effects of stacking. The stacked mock variance cube, on the other hand, is used to compute a separate noise estimate $\epsilon_{\text{no covar}}$ using simple error propagation rules, assuming that each spaxel is independent. The ratio of these two estimates can be plotted as a function of bin size N and fit with a curve of the functional form described in Equation 5.2 to determine the best-fit values of $\{\alpha, \beta, N_{\text{threshold}}\}$. Figure 5.1 demonstrates an example of this fitting for four stacked exposures, showing that Equation 5.2 is a good representation of η.

By multiplying this empirical estimate for η by the noise estimate (i.e., dividing Equation 5.1 by η), the S/N within a bin can be corrected for the effects of spatial covariance. Using covariance-corrected S/N values, the `vorbin` algorithm then creates bins with a target S/N while optimally preserving spatial resolution. The target S/N is at least 10 for all galaxies; some galaxies with longer exposures have higher overall S/N, so the target S/N per bin for these galaxies is higher (for reference, the maximum target S/N is 50 for galaxy 955106). Figure 5.2 illustrates the effect of binning without and with this covariance correction (bottom left and right panels, respectively); the unbinned white light image is shown for comparison in the top panel.

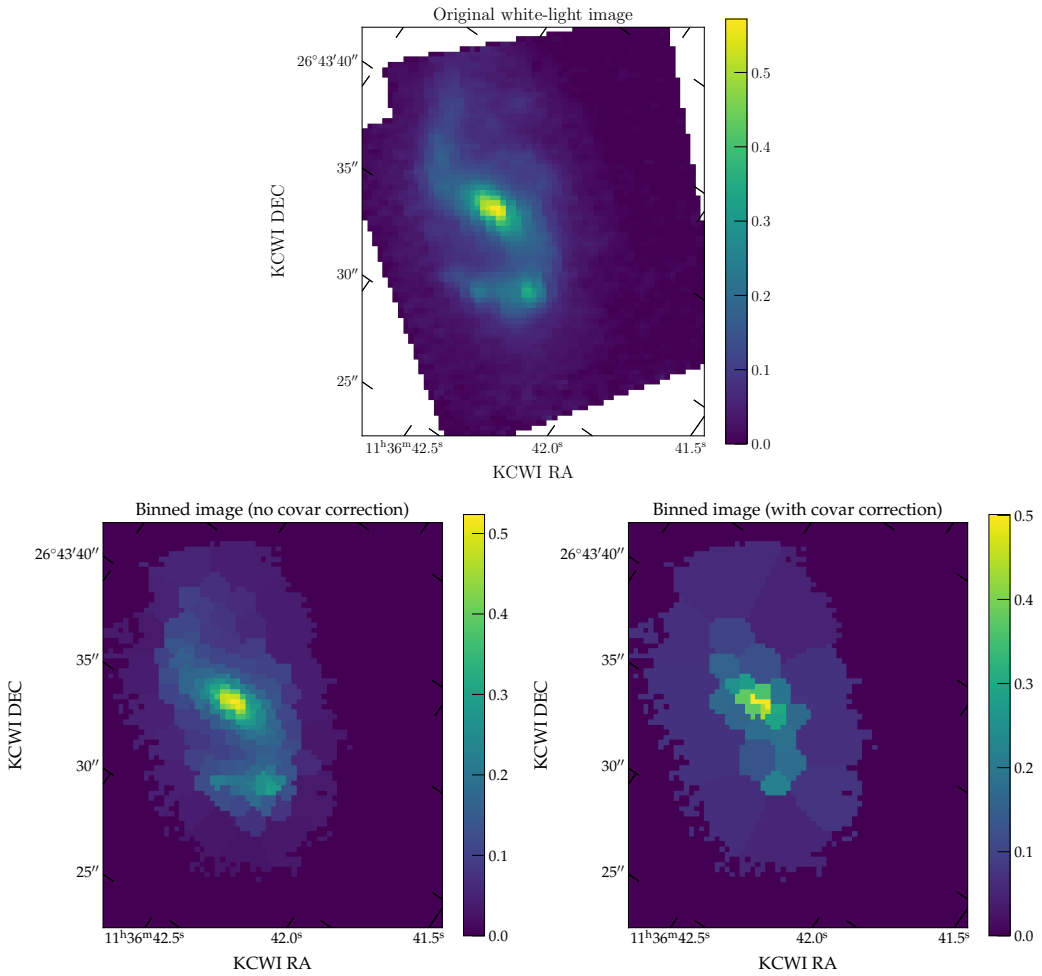

Figure 5.2: The effect of covariance correction on spatial binning of a stacked IFU data cube. Top: White-light image from stacked data cube of reines65. Bottom: Same image, but spatially binned using `vorbin` algorithm to reach a target S/N = 15 without (left) and with (right) accounting for spatial covariance. All colorbars represent the average flux (erg s^{-1} cm^{-2}) per pixel (for top figure) or per bin (bottom figures).

5.3.2 Continuum fitting and kinematics measurements

Taking the average spectrum in each bin, I now fit the stellar continuum using the full spectral-fitting algorithm `ppxf` (Cappellari 2017; Cappellari and Emsellem 2004). This algorithm attempts to determine the line-of-sight velocity distribution (LOSVD) of the stars in a galaxy by fitting a galaxy spectrum with a combination of templates. I use templates from the MILES stellar library of single stellar population models (Falcón-Barroso et al. 2011; Sánchez-Blázquez et al. 2006). The spectra in this library have wavelength range 354 – 741 nm with a constant resolution FWHM of 2.51Å, and they cover a metallicity range $-2.86 < [Fe/H] < 0.65$.

KCWI has an instrumental resolution FWHM of ~ 2.5Å (measured from arc lamps), so before using `ppxf` I smooth the observed spectra to match the resolution of the templates. I also mask strong gas emission lines from the observed spectra. For each binned spectrum, the `ppxf` algorithm expands the LOSVD $\mathcal{L}(v)$ as a Gauss-Hermite series

$$\mathcal{L}(v) = \frac{e^{-(1/2)y^2}}{\sigma\sqrt{2\pi}}\left(1 + \sum_{m=3}^{M} h_m H_m(y)\right) \tag{5.3}$$

where $y = (v - V)/\sigma$ and H_m are the Hermite polynomials. The variables V and σ are the stellar velocity and velocity dispersion, respectively. The top panels of Figure 5.3 illustrate `ppxf` fits to binned spectra with different S/N. For comparison, the bottom panel shows the integrated (i.e., variance-weighted average) spectrum.

The resulting maps of stellar (line-of-sight) velocity and velocity dispersion are shown in Appendix 5.6. (Note that any bins with S/N<1 are not plotted, and they are discarded from the following calculations.) These spatially-resolved measurements are then used to compute global measurements of *rotational* velocity $v_{\rm rot}$ and velocity dispersion $\sigma_\star$. I first compute the systemic velocity of the galaxy $v_{\rm syst}$, which I take to be the weighted average[5] of the velocities V in each bin. The rotational velocity is then assumed to be the maximum of the bin velocities with the systemic velocity removed:

$$v_{\rm rot} = \max(V - v_{\rm syst}), \tag{5.4}$$

and the global stellar velocity dispersion $\sigma_{]star}$ is the weighted average of the bin velocity dispersions (Binney 2005).

Table 5.3 describes the measured global stellar kinematics (systemic velocities, peak rotational velocities, and velocity dispersions) for the galaxies in my sample. Note that in spite of the high S/N of the integrated spectra, the velocity dispersion measurements still suffer from another issue—the observed spectra were smoothed to match the dispersion of the spectral templates, $\sigma_{\rm instrument} \sim \sigma_{\rm template} \sim 66$ km/s. Given the difficulty of measuring velocity dispersions below this resolution limit, we set $\sigma_{\rm instrument}$ as an upper limit on any measurements of $\sigma_\star$ that are less than $\sigma_{\rm instrument}$. For completeness, I list all original measurements of $\sigma_\star$ in Table 5.3. However, the values of $v_{\rm rot}/\sigma_\star$ listed in the table are computed using corrected measurements of $\sigma_\star$: if $\sigma_\star > \sigma_{\rm instrument}$, then $v_{\rm rot}/\sigma_\star = v_{\rm rot}/\sqrt{\sigma_\star^2 - \sigma_{\rm instrument}^2}$;

[5] All weighted averages are defined as $\bar{x} = \frac{\sum_i^n w_i x_i}{\sum_i^n w_i}$ for i measurements of quantity x. Unless otherwise noted, the weights w_i are the inverse variance of x_i: $w_i = \frac{1}{{\rm Var}(x_i)}$.

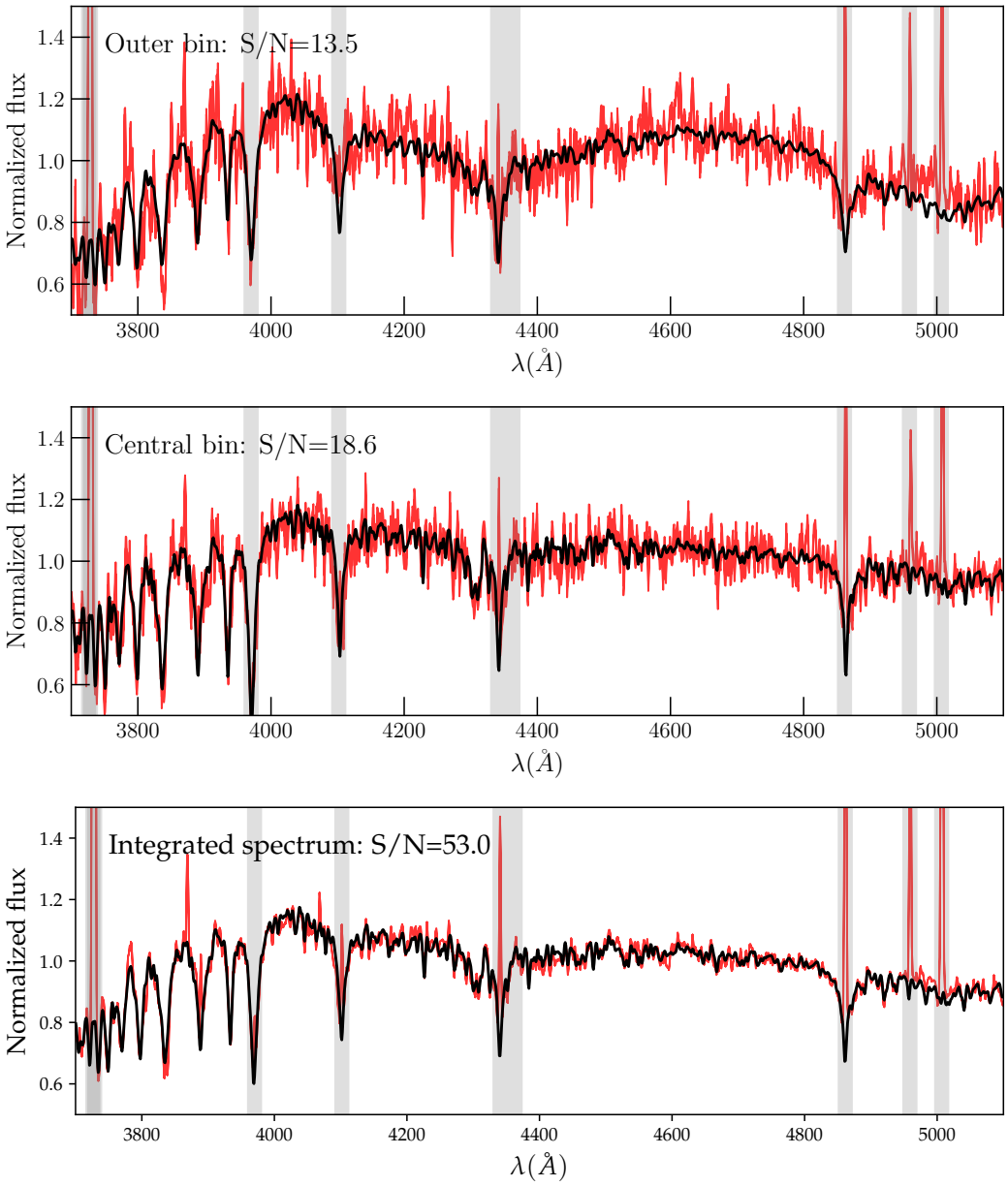

Figure 5.3: Example `ppxf` fits for binned and integrated spectra. Top: Example `ppxf` fit (black line) to observed spectrum (red line) for a bin in the outer region of reines65, with relatively low continuum S/N (Equation 5.1). Gray shaded regions indicate gas emission lines, which are masked out of the spectrum before fitting. Middle: Same, but for a bin in the center of reines65, with higher S/N. Bottom: Same, but for the integrated spectrum, which has higher S/N than any of the binned spectra.

otherwise, $\sigma_{\rm instrument}$ is taken to be an upper limit on $\sigma_\star$, so $v_{\rm rot}/\sigma_{\rm instrument}$ is reported as a lower limit.

5.4 Discussion

The stellar motions within a galaxy can be summarized using the global value of $v_{\rm rot}/\sigma_\star$ (e.g., Bender et al. 1993; Binney 2005; Ferré-Mateu et al. 2021; Illingworth 1977). Higher values of this ratio ($v_{\rm rot}/\sigma_\star \gtrsim 1$) indicate dynamically cold "disky" systems, while "puffy" systems like dSphs have $v_{\rm rot}/\sigma_\star < 1$. The dependence of $v_{\rm rot}/\sigma_\star \gtrsim 1$ on external galaxy environment and on intrinsic galaxy properties is therefore a useful metric for understanding the processes that drive galaxy formation and dynamical evolution.

Table 5.3 shows that although most of our measurements are lower limits, few (4/18 void dwarf galaxies and 1/7 field dwarf galaxies) show any evidence for rotation support, with $v_{\rm rot}/\sigma_\star > 1$. Of these, most are only weakly rotating—only 2 galaxies, the void dwarf galaxy 1785212 and the field galaxy reines65, have $v_{\rm rot}/\sigma_\star \gtrsim 2$. There are a few unambiguous detections of dispersion-supported systems in cosmic voids (the galaxies 821857 and Pisces B have $v_{\rm rot}/\sigma_\star = 0.39$ and 0.36, respectively). These measurements are consistent with those found by Wheeler et al. (2017) for Local Group dwarf galaxies, suggesting that at least some of the dwarf galaxies in my sample are kinematically similar to dwarf galaxies that are by definition located near a massive host. Finally, the values of $v_{\rm rot}/\sigma_\star$ are similar for the void galaxy sample and the "field" galaxy sample, suggesting that the large-scale environment of voids does not have a significant effect on stellar dynamics.

Figure 5.4 illustrates the relation between $v_{\rm rot}/\sigma_\star$ and $M_\star$. Wheeler et al. (2017) found no clear trend between these quantities for Local Group dwarf galaxies over the mass range $M_\star = 10^{3.5} - 10^8\ M_\odot$. The galaxies in my sample occupy a higher mass range $M_\star = 10^7 - 10^9\ M_\odot$; with the addition of my measurements, there is a tentative increase in $v_{\rm rot}/\sigma_\star$ at $M_\star \gtrsim 10^{7.5}\ M_\odot$. The lower limits in my sample are still higher than the extremely low $v_{\rm rot}/\sigma_\star$ found for many of the Local Group dSphs. Furthermore, the galaxies in my sample that show the strongest evidence of rotation support all have $M_\star > 10^{7.5}\ M_\odot$. Additional measurements of dwarf galaxies in this mass range are needed to confirm this potential trend, and to identify whether this is a gradual trend or a sharp discontinuity between dSphs/dEs and rotating disks; for example, Sánchez-Janssen et al. (2010) have proposed a critical stellar mass $M_\star = 2 \times 10^9\ M_\odot$ above which all galaxies become systematically thinner.

Table 5.3: Stellar kinematics of void and field dwarf galaxies.

Object	$v_{\rm syst}$ (km/s)	$v_{\rm rot}$ (km/s)	$\sigma_\star$ [a] (km/s)	$v_{\rm rot}/\sigma_\star$ [a]
Void dwarf galaxies				
1180506	49.32 ± 2.76	28.61 ± 10.28	32.62 ± 10.91	> 0.40
281238	80.93 ± 2.05	49.57 ± 13.14	62.65 ± 4.33	> 0.70
1904061[b]	...	...	...	...
821857	103.80 ± 2.31	86.79 ± 27.18	235.75 ± 15.12	0.39 ± 0.12
1158932	49.13 ± 2.30	34.08 ± 15.22	74.74 ± 5.87	1.46 ± 0.66
866934	83.34 ± 1.49	50.15 ± 10.38	42.71 ± 4.36	> 0.71
825059	85.00 ± 0.72	35.15 ± 10.03	41.36 ± 1.97	> 0.50
2502521[b]	...	...	...	...
1228631	53.63 ± 0.76	37.46 ± 4.78	52.28 ± 1.83	> 0.53
1876887	102.26 ± 0.79	49.86 ± 12.98	40.79 ± 2.66	> 0.70
1246626	52.29 ± 1.72	162.64 ± 38.91	108.52 ± 5.93	1.98 ± 0.49
1142116	117.67 ± 0.36	24.54 ± 5.33	49.69 ± 0.77	> 0.35
955106	88.91 ± 0.81	26.53 ± 11.52	36.49 ± 2.30	> 0.37
1063413	9.50 ± 0.61	57.31 ± 9.03	40.85 ± 1.90	> 0.81
1074435[b]	...	...	...	...
1785212	71.23 ± 1.01	197.64 ± 58.55	44.93 ± 4.17	> 2.78
1280160	70.86 ± 0.67	17.06 ± 9.77	42.50 ± 1.66	> 0.24
1782069	66.82 ± 0.47	71.03 ± 6.99	40.83 ± 1.12	> 1.00
1126100	−24.91 ± 0.43	56.55 ± 7.93	49.26 ± 0.85	> 0.80
PiscesA	105.58 ± 3.14	135.16 ± 68.63	124.36 ± 6.66	1.32 ± 0.68
PiscesB	117.42 ± 3.70	41.04 ± 16.09	134.67 ± 8.12	0.36 ± 0.14
Field dwarf galaxies				
SDSS J0133+1342[b]	...	...	...	...
AGC 112504	114.27 ± 0.95	56.66 ± 22.47	50.89 ± 2.40	> 0.80
UM 240	−129.62 ± 1.34	23.33 ± 7.18	42.97 ± 3.98	> 0.33
SHOC 150	111.34 ± 1.46	27.22 ± 11.09	36.24 ± 3.92	> 0.38
LEDA 3524	94.89 ± 1.90	44.78 ± 11.66	37.57 ± 7.11	> 0.63
LEDA 101427	108.06 ± 1.45	23.99 ± 5.34	31.05 ± 5.78	> 0.34
IC 0225	117.74 ± 0.46	32.25 ± 3.42	34.49 ± 1.37	> 0.45
reines65	117.63 ± 1.26	272.48 ± 52.91	56.68 ± 2.83	> 3.84

[a] The values of $\sigma_\star$ listed here are the raw measurements, without correcting for instrument dispersion. The values of $v_{\rm rot}/\sigma_\star$ are computed after correcting $\sigma_\star$ for instrumental dispersion as described in the text; if $\sigma_\star < \sigma_{\rm instrument}$, we report $v_{\rm rot}/\sigma_\star$ as a lower limit (denoted with a > symbol).

[b] The wavelength solutions for these galaxies are poor, so we do not consider their kinematic measurements in the rest of this paper.

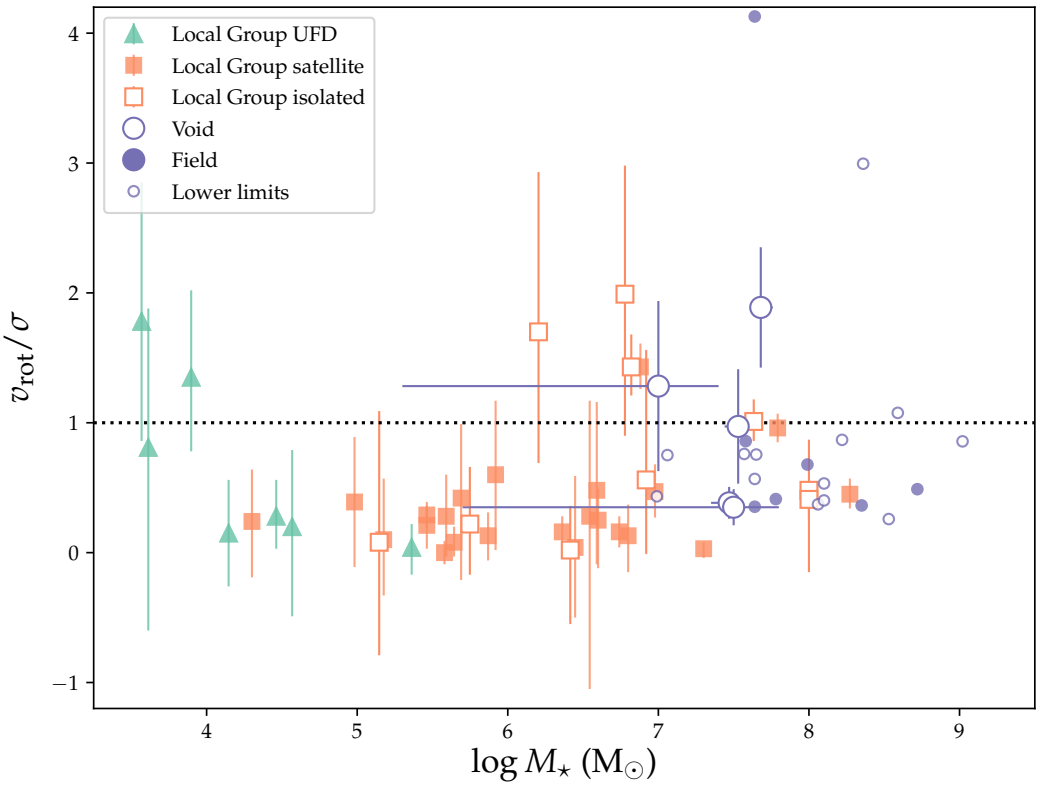

Figure 5.4: Stellar rotation support ($v_{\rm rot}/\sigma_\star$) as a function of galaxy stellar mass. Measurements for Local Group galaxies—ultra-faint dwarf galaxies (green triangles), MW and M31 satellites (filled orange squares), and isolated dwarf galaxies (open orange squares)—are taken from Wheeler et al. (2017). Measurements from this work are denoted as purple circles: filled circles denote "field" galaxies from the control sample, while open circles denote void galaxies. Small circles mark galaxies for which $\sigma_\star < \sigma_{\rm template}$, so $v_{\rm rot}/\sigma_{\rm template}$ are lower limits.

Measurements of the $v_{\rm rot}/\sigma_\star$ can also be used to directly test the predictions of the tidal stirring model. In this model, which posits that tidal interactions remove angular momentum from dwarf galaxy disks during pericentric passages, $v_{\rm rot}/\sigma_\star$ is expected to increase with increasing distance from a massive galaxy (Kazantzidis et al. 2011). Wheeler et al. (2017) did a systematic search of 40 Local Group dwarf galaxies and did not find evidence of a trend between $v_{\rm rot}/\sigma_\star$ and distance to a massive host (either the Milky Way or M31). Since the dwarf galaxies in my sample are typically extremely isolated, they can be used to extend this trend to higher distances.

I first located the closest massive neighbor to each galaxy in my sample. Using the SDSS DR16 catalog, I identified all galaxies with apparent magnitudes ($14 < g <$

20 mag) within 50" of my galaxies. I then computed three-dimensional distances using SDSS coordinates and spectroscopic redshifts[6] and identified the closest massive ($M_\star > 10^{10}\ M_\odot$) neighbor. Figure 5.5 plots $v_{\rm rot}/\sigma_\star$ as a function of the distance to the nearest massive neighbor, denoted $d_{L\star}$.

The vast majority of the galaxies in my sample are, as expected, extremely isolated, with $d_{L\star} > 3$ Mpc. Note that there are significant uncertainties in distances, since they are computed from redshifts: not only is there intrinsic scatter in the Hubble relation, but SDSS spectroscopic redshifts also have an uncertainty of $\Delta(cz) \sim 30$ km/s (Abazajian et al. 2005). Combined, these effects can correspond to distance uncertainties on the order of hundreds to thousands of kpc. These systematic x-axis uncertainties are not shown here.

Even with these uncertainties, Figure 5.5 indicates that there is no clear trend between $v_{\rm rot}/\sigma_\star$ and $d_{L\star}$. This is again consistent with the result of Wheeler et al. (2017) and inconsistent with the predictions of tidal stirring models. In particular, given the extreme isolation of many of the galaxies in my sample, it is unlikely that these galaxies would have had more than one pericentric passage around a massive galaxy. In the tidal stirring hypothesis, dIrrs typically need multiple pericentric passages within a Milky Way-like gravitational potential to complete the full conversion to dSphs (see, e.g., Table 3 of Kazantzidis et al. 2017, in which at least two pericentric passages are required even with the inclusion of baryonic feedback).

My measurements have some limitations: for example, as mentioned in the previous section, the dispersion of the stellar templates (as well as the intrinsic instrumental dispersion of KCWI itself) limits the precision of many of the $\sigma_\star$ measurements. Additionally, if a galaxy's angular momentum vector is inclined with an angle i relative to the line-of-sight, then $v_{\rm rot,obs} = v_{\rm rot,intrinsic} \sin i$, so the line-of-sight velocities I measure are lower limits to the true velocity. Inclination may also have effect on $\sigma_\star$ in rotation-supported systems—for example, $\sigma_\star$ is larger in the Milky Way viewed face-on than viewed edge-on—but since most of our objects are dispersion-supported, this is likely a smaller effect than the effect of inclination on $v_{\rm rot}$. As a result, all of my measurements of $v_{\rm rot}/\sigma_\star$ are likely lower limits, not just the measurements limited by instrumental dispersion. Higher-resolution spectroscopy could be used to obtain more precise measurements of $\sigma_\star$, while inclination can be estimated either from rough photometric estimates (i.e., elliptical isophote fitting)

[6]To convert redshifts to distances, I assumed a flat ΛCDM cosmology with Planck 2018 parameters ($H_0 = 67.4$ km s^{-1}Mpc^{-1}, $\Omega_m = 0.315$; Aghanim et al. 2020).

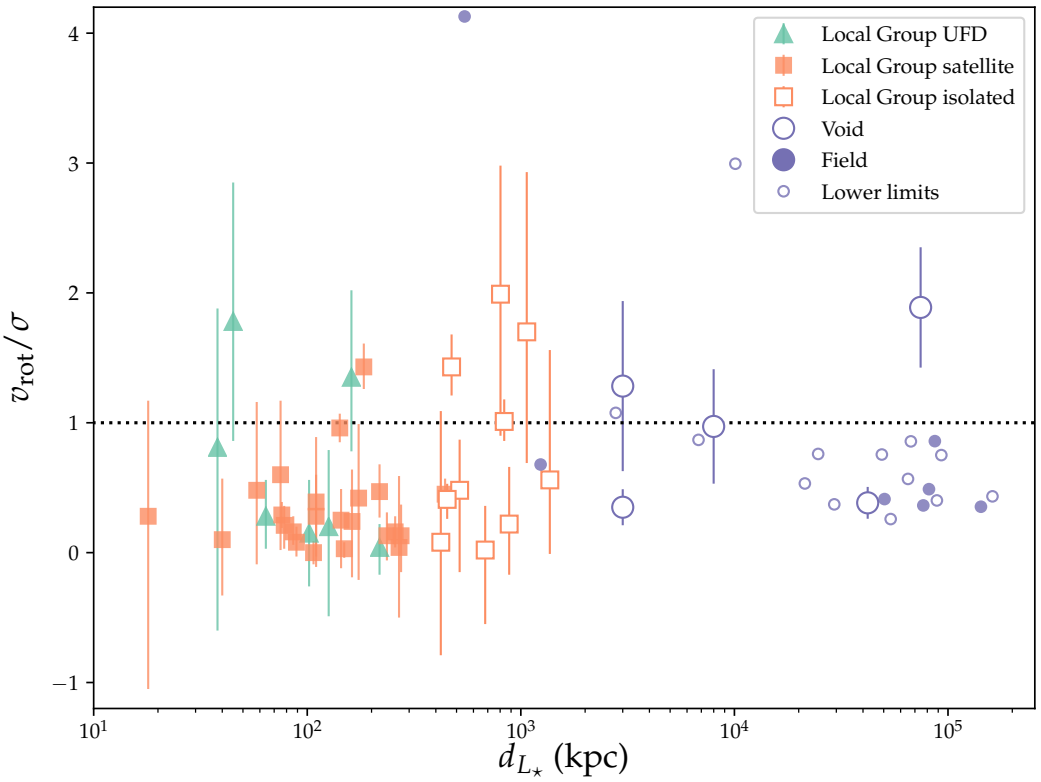

Figure 5.5: Stellar rotation support ($v_{\rm rot}/\sigma_\star$) as a function of distance from closest massive galaxy ($d_{L\star}$). Symbols and colors are the same as Figure 5.4.

or from more sophisticated modeling (i.e., Jeans modeling; Cappellari 2008).[7]

Finally, and perhaps most crucially, although my measurements have some spatial resolution, they are not actually measurements of resolved stars. Any comparisons with measurements of galaxies in the Local Group are therefore not direct "apples-to-apples" comparisons. Until it becomes possible to resolve stellar populations in dwarf galaxies outside the Local Volume, this gap can still be bridged with simulations. Simulations of dwarf galaxies are a promising tool: not only can they provide a more direct comparison to the extremely isolated dwarf galaxies in this sample, but they could also be useful for producing mock observations. Such mock observations may be able to quantify systematic differences between resolved and IFU observations (Zhuang et al. 2021).

[7]Though see El-Badry et al. (2017), who note that Jeans modeling is frequently not well-suited for low-mass galaxies that are not necessarily in dynamical equilibrium.

5.5 Conclusions

Using the Keck Cosmic Web Imager, I have obtained IFU spectroscopy for a number of dwarf galaxies (over the mass range $M_\star = 10^7 - 10^9\ M_\odot$) located inside and outside of cosmic voids. I have developed an analysis pipeline to measure spatially-resolved stellar velocities and stellar velocity dispersions from KCWI data. In order to compare the stellar dynamics of these galaxies with other galaxies, particularly in the Local Group, I have computed global values of $v_{\rm rot}/\sigma_\star$.

There is no significant difference between $v_{\rm rot}/\sigma_\star$ for the void dwarf galaxies and the "field" dwarf galaxies located outside voids; furthermore, several of the galaxies in both these subsamples have $v_{\rm rot}/\sigma_\star$ consistent with the values measured for Local Group dwarf galaxies (Wheeler et al. 2017). This suggests that the large-scale void environment does not seem to affect the dynamics of stars in dwarf galaxies.

Environmental processes in general do not appear to be primary drivers of the dynamical formation of field dwarf galaxies. I find that the majority of dwarf galaxies in my sample (80%) have $v_{\rm rot}/\sigma_\star < 1$, suggesting that they are predominantly dispersion-supported systems. Additionally, I find no correlation between $v_{\rm rot}/\sigma_\star$ and distance to the closest massive galaxy $d_{L^\star}$, even for extremely isolated dwarf galaxies (with $d_{L^\star} \sim 3000$ kpc). This again confirms the results of Wheeler et al. (2017), who find a similar lack of trend (and overall low values of $v_{\rm rot}/\sigma_\star$) among Local Group dwarf galaxies. These results are further evidence that dSphs/dEs form as "puffy" dispersion-supported systems, rather than as rotation-supported disks that are converted by tidal interactions into dispersion-supported spheroidal systems (the "tidal stirring" hypothesis).

I find some evidence that $v_{\rm rot}/\sigma_\star$ may increase with galaxy stellar mass for masses $\gtrsim 10^{7.5}\ M_\odot$. Further investigation—perhaps through a combination of high-resolution spectroscopy and resolved dwarf galaxy simulations—is needed to confirm the existence and form of this trend. If it is real, this trend could be a particularly useful clue for identifying the formation pathway of stellar disks in low-mass galaxies.

Simulations also provide a promising path forward to understand the implications of comparing observations with different spatial resolutions: i.e., stellar kinematic measurements from resolved stellar populations versus from IFU data. The advent of new instruments, such as JWST (Gardner et al. 2006), may make it possible to resolve individual stars in galaxies outside the Local Group. However, IFU data remains one of our most promising tools for obtaining detailed observations of distant galaxies. Measuring stellar kinematics is just one of the many applications

of IFU data, and I plan to continue using the KCWI dataset described in this chapter to investigate other properties of void dwarf galaxies in future work.

5.6 Appendix: Velocity and velocity dispersion maps

Spatially-resolved maps of stellar velocity (V) and stellar velocity dispersion (σ) are shown here for the galaxies in my sample.

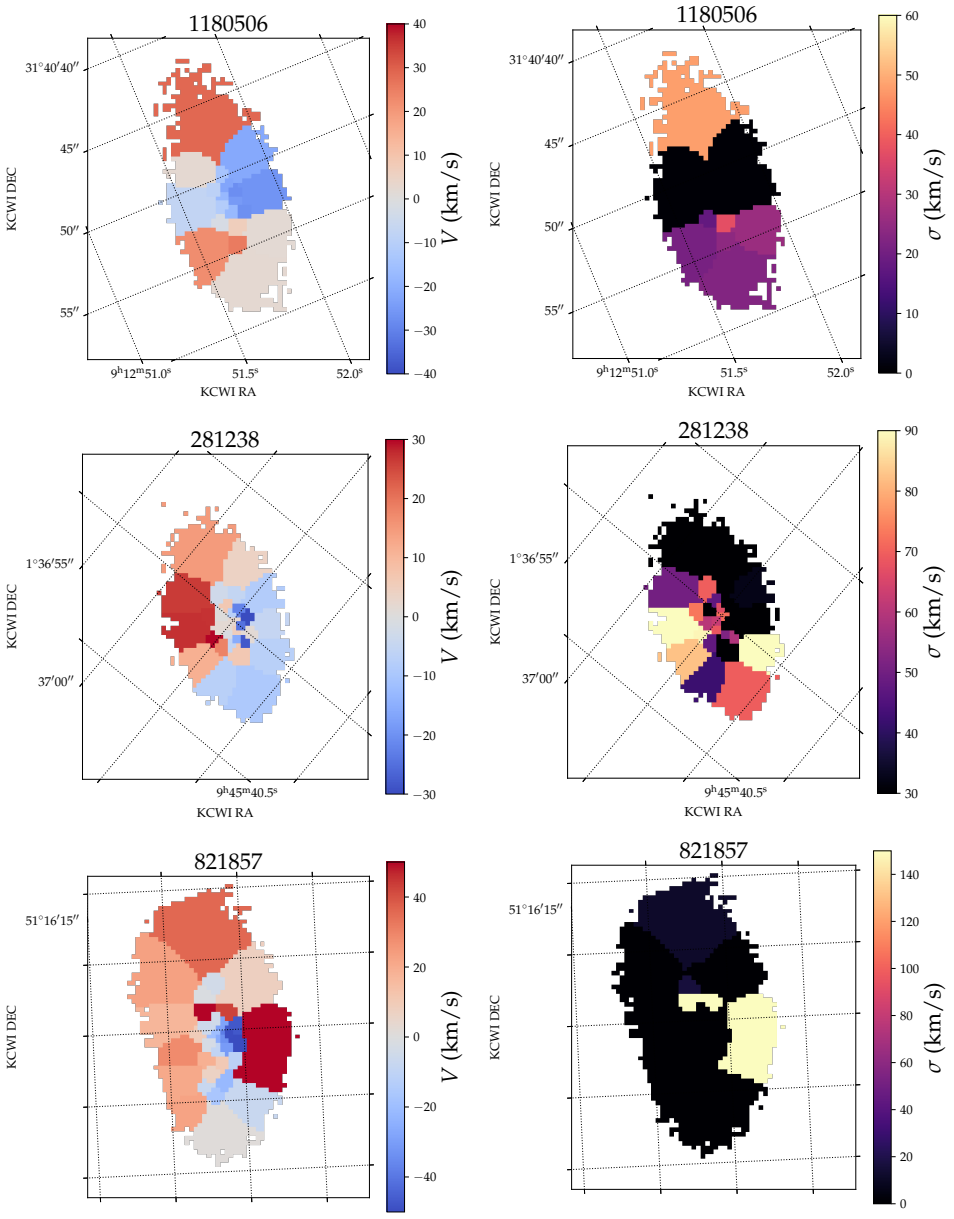

Figure 5.6: Stellar kinematic maps of dwarf galaxies. Left: Maps of (line-of-sight) stellar velocity V for dwarf galaxies. Right: Maps of stellar velocity dispersion σ.

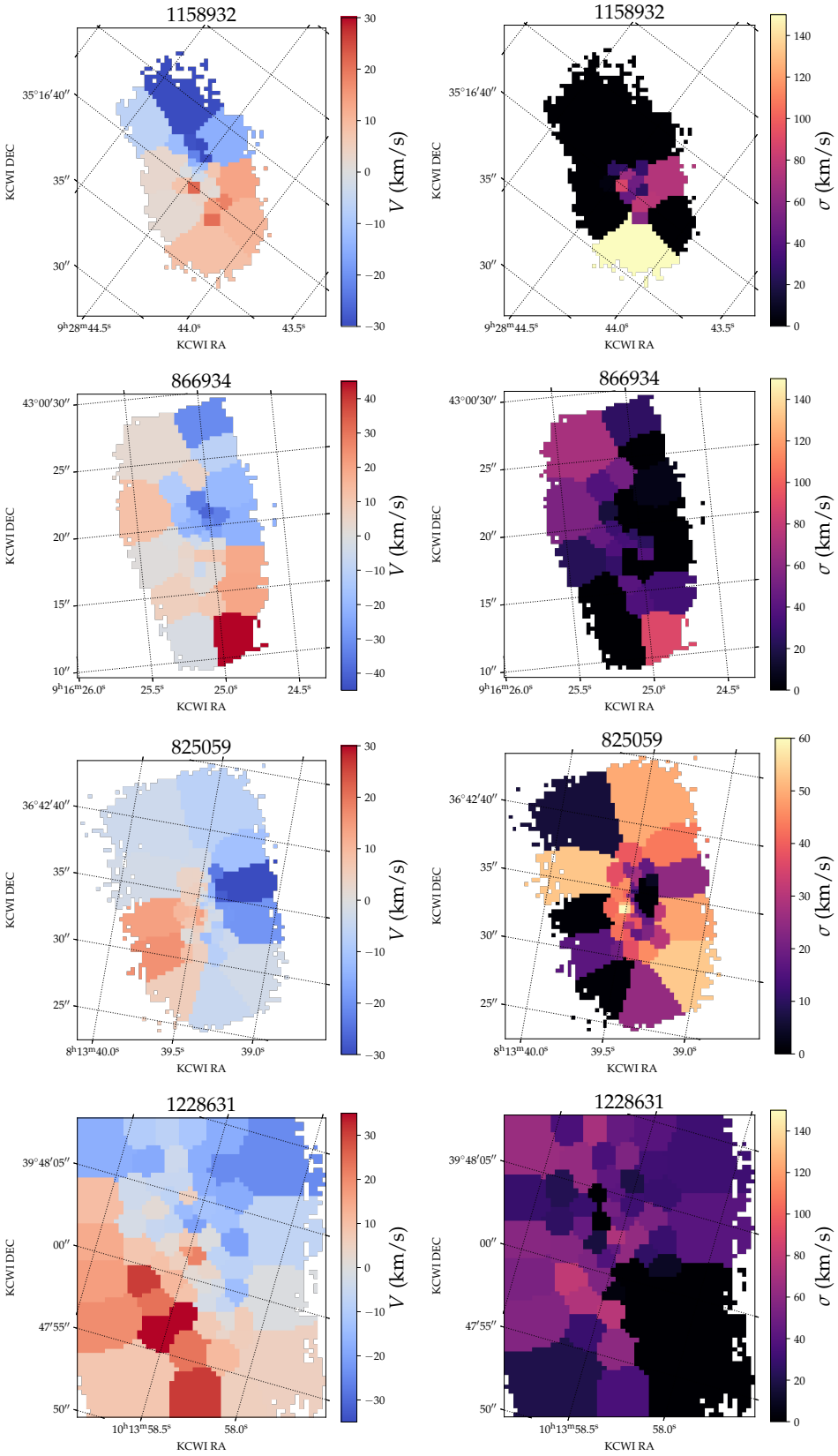

Figure 5.7: Figure 5.6 continued.

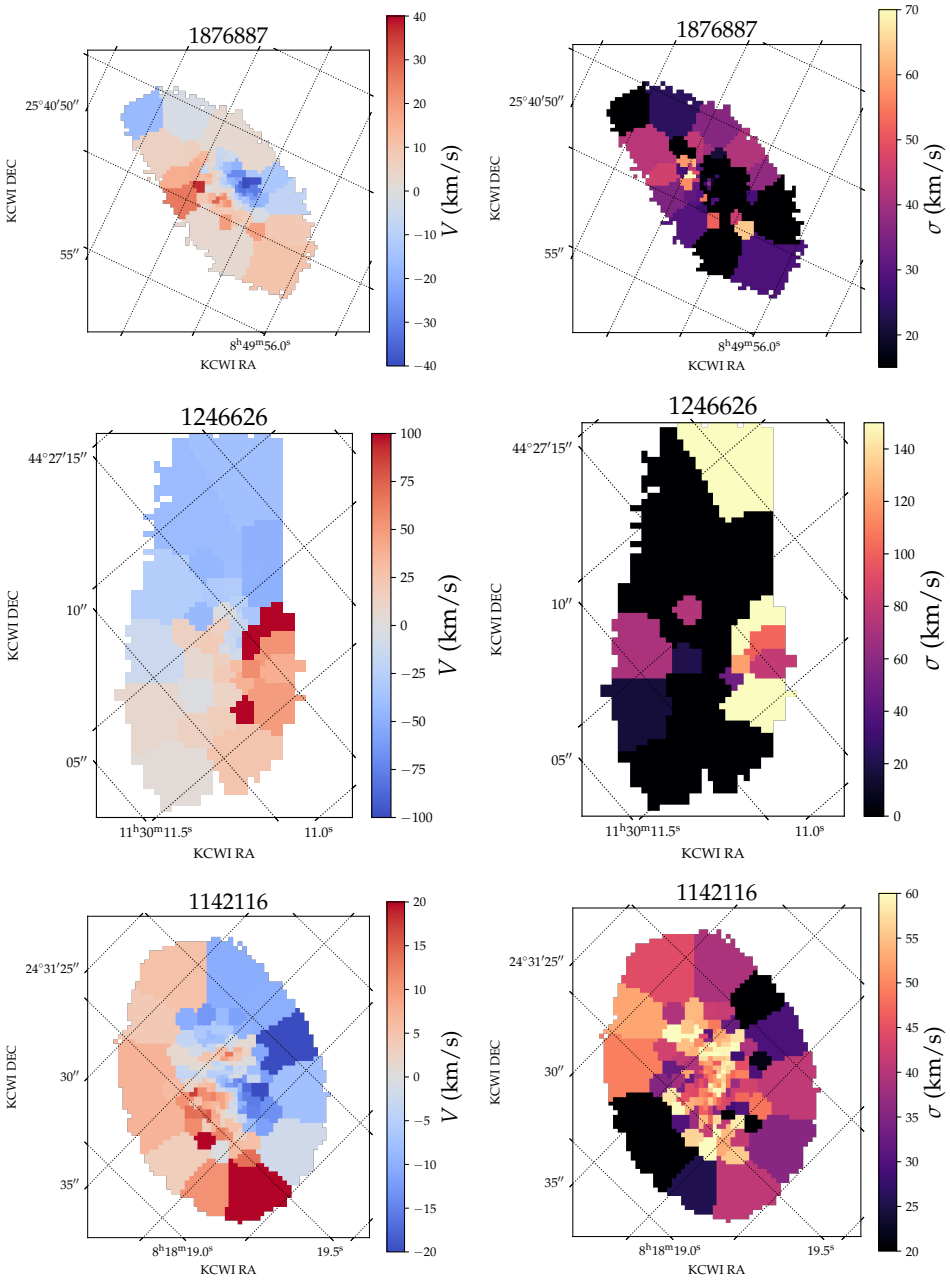

Figure 5.8: Figure 5.6 continued.

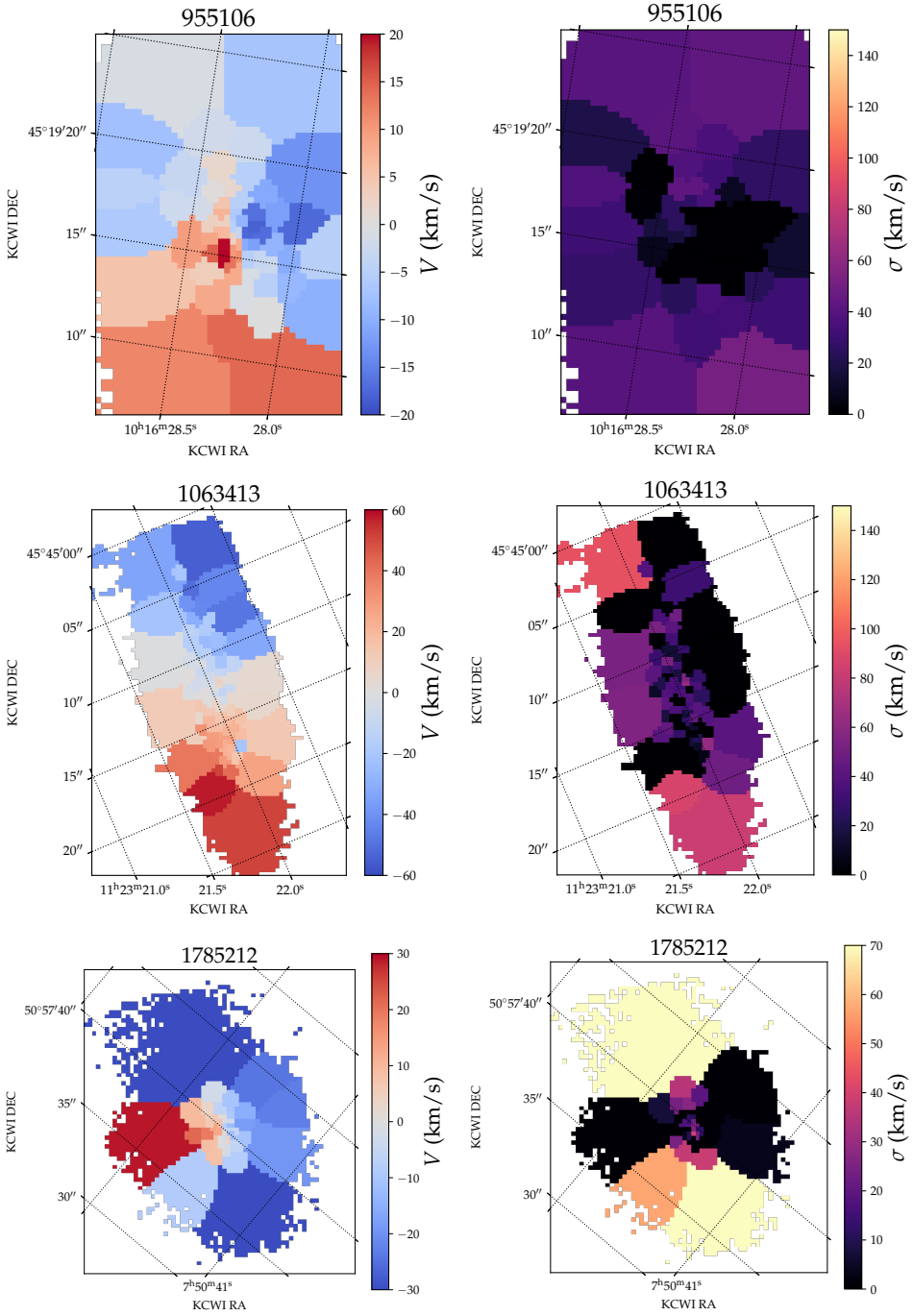

Figure 5.9: Figure 5.6 continued.

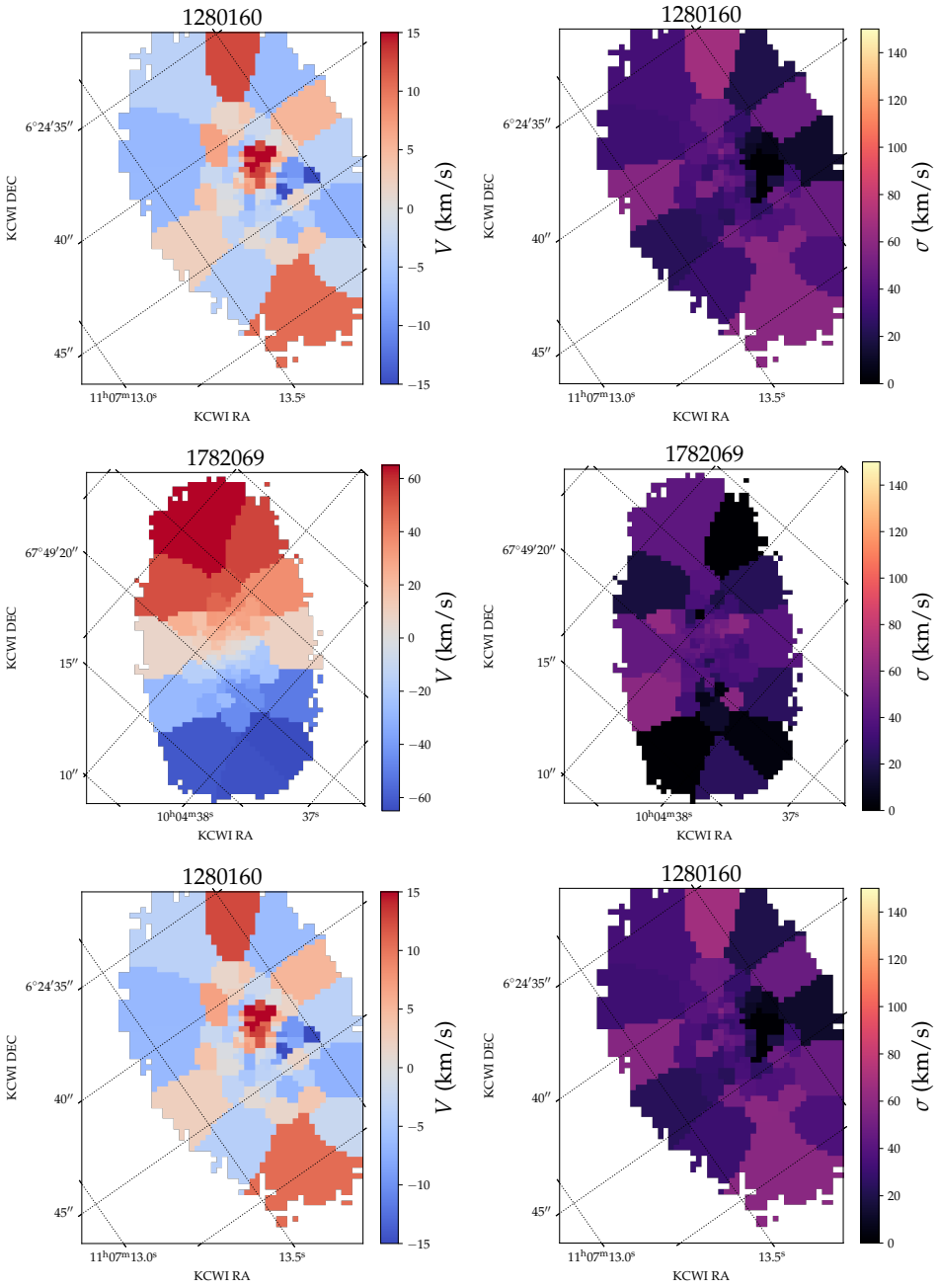

Figure 5.10: Figure 5.6 continued.

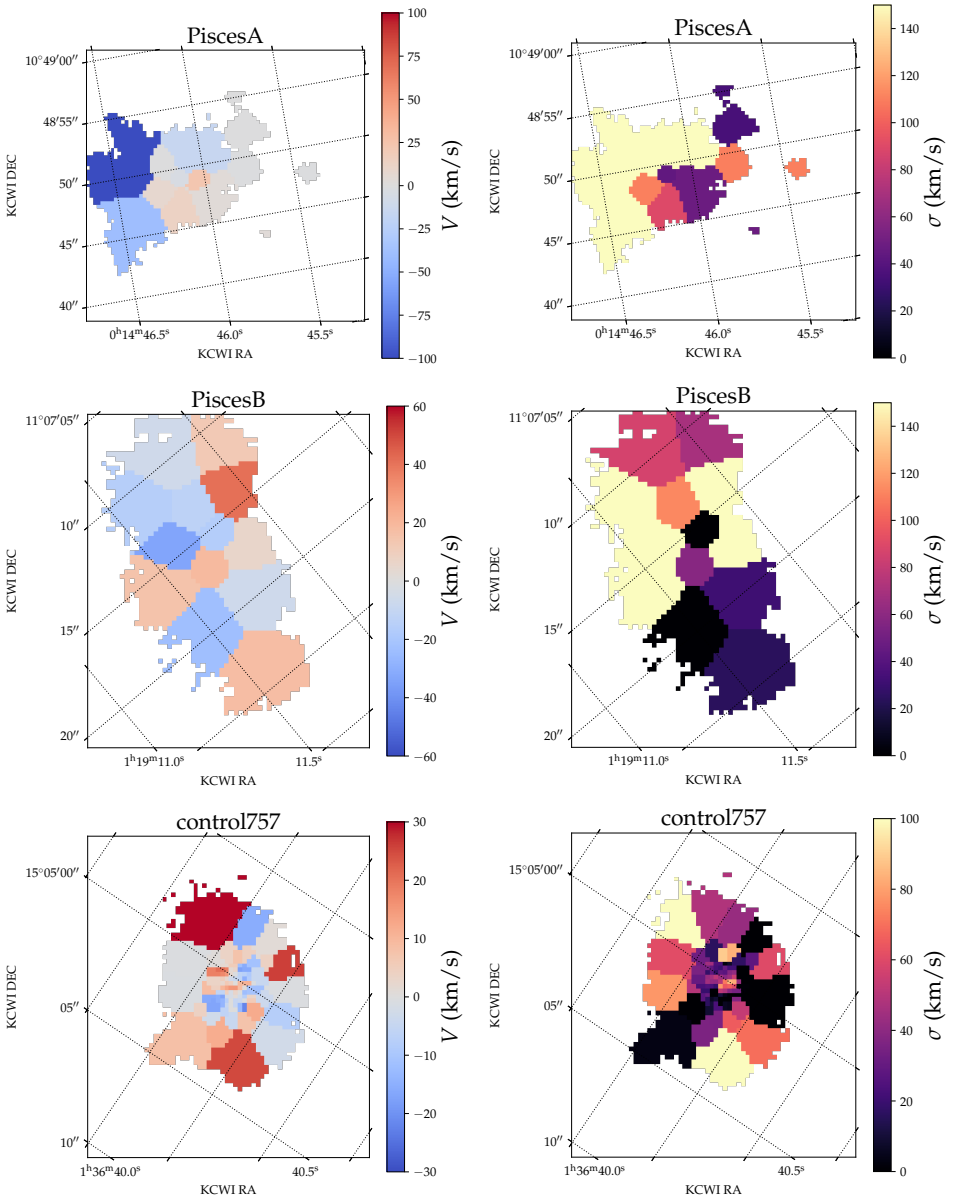

Figure 5.11: Figure 5.6 continued.

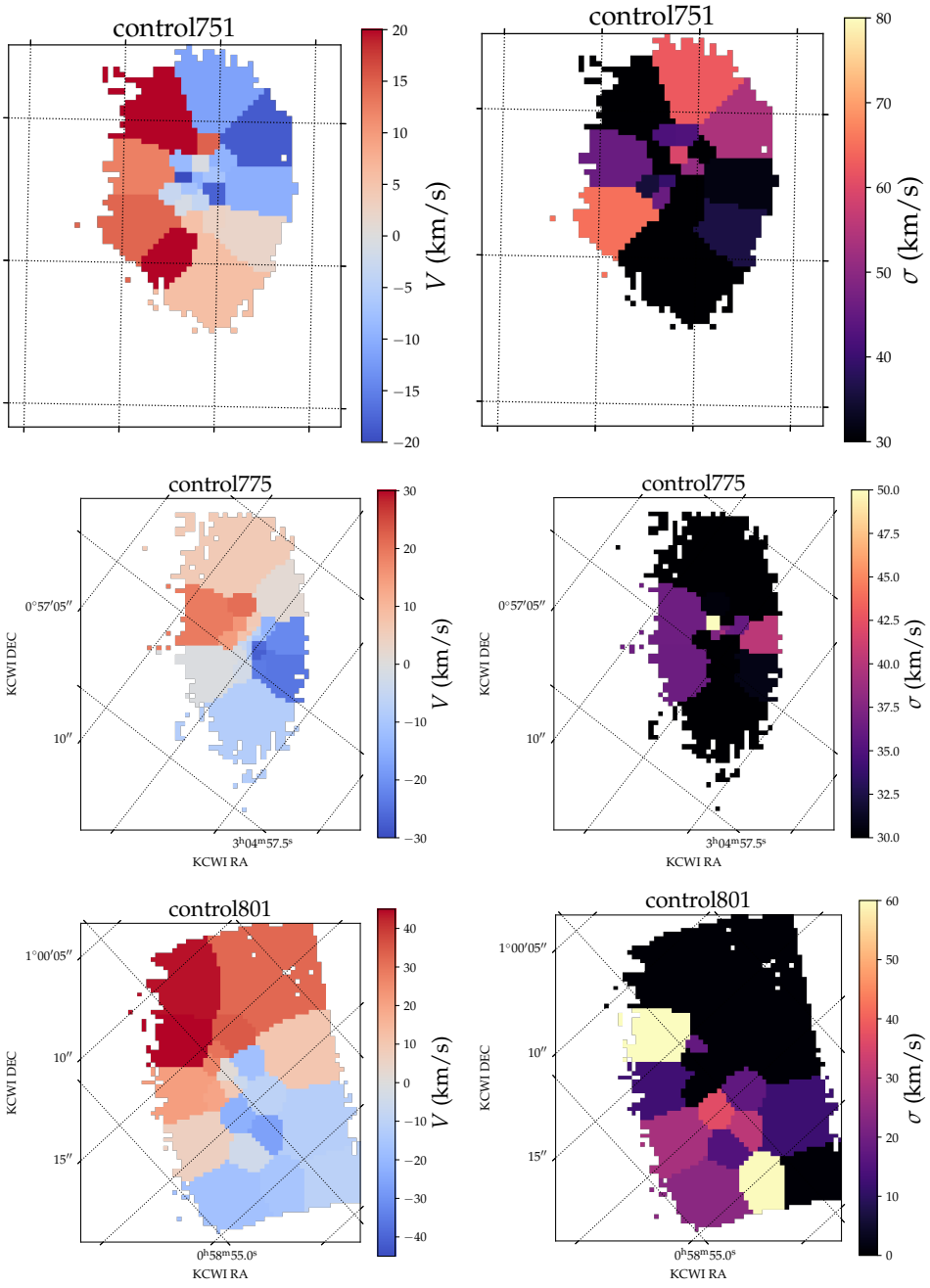

Figure 5.12: Figure 5.6 continued.

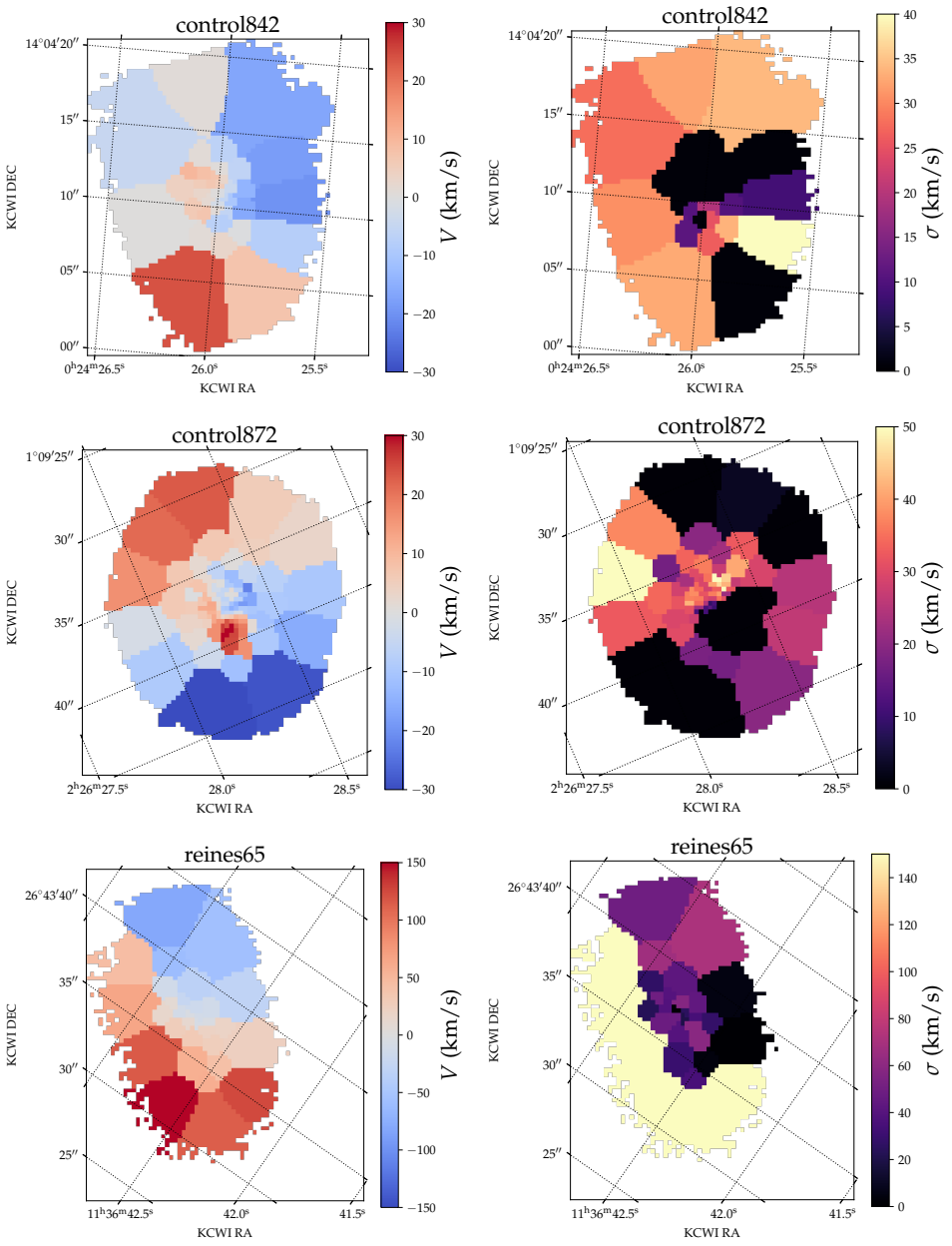

Figure 5.13: Figure 5.6 continued.

Chapter 6

GLOBAL STAR FORMATION LAWS IN LOCAL SPIRAL AND DWARF GALAXIES

de los Reyes, M. A. C. and R. C. Kennicutt (2019). "Revisiting the Integrated Star Formation Law. I. Non-starbursting Galaxies." *ApJ* 872.1, p. 16. DOI: 10.3847/1538-4357/aafa82.

Mithi A. C. de los Reyes[1], Robert C. Kennicutt, Jr.[2,3]

[1]Department of Astronomy, California Institute of Technology, 1200 E California Blvd, Pasadena, CA, 91125, USA
[2]Department of Astronomy and Steward Observatory, University of Arizona, Tucson, AZ 85721, USA
[3]Department of Physics and Astronomy, Texas A&M University, College Station, TX 77843, USA

Abstract

We use new and updated gas and dust-corrected SFR surface densities to revisit the integrated star formation law for local "quiescent" spiral, dwarf, and low-surface-brightness galaxies. Using UV-based SFRs with individual IR-based dust corrections, we find that "normal" spiral galaxies alone define a tight $\Sigma_{(\mathrm{HI}+\mathrm{H_2})}$-$\Sigma_{\mathrm{SFR}}$ relation described by a $n = 1.41^{+0.07}_{-0.07}$ power law with a dispersion of $0.28^{+0.02}_{-0.02}$ (errors reflect fitting and statistical uncertainties). The SFR surface densities are only weakly correlated with HI surface densities alone, but exhibit a stronger and roughly linear correlation with H_2 surface densities, similar to what is seen in spatially-resolved measurements of disks. However, many dwarf galaxies lie below the star formation law defined by spirals, suggesting a low-density threshold in the integrated star formation law. We consider alternative scaling laws that better describe both spirals and dwarfs. Our improved measurement precision also allows us to determine that much of the scatter in the star formation law is intrinsic, and we search for correlations between this intrinsic scatter and secondary physical parameters. We find that dwarf galaxies exhibit second-order correlations with total gas fraction, stellar mass surface density, and dynamical time that may explain much of the scatter in the star formation law. Finally, we discuss various systematic uncertainties that should be kept in mind when interpreting any study of the star formation law, particularly the $X(\mathrm{CO})$ conversion factor and the diameter chosen to define the star-forming disk in a galaxy.

6.1 Introduction

The formation of stars from the interstellar medium (ISM) is one of the driving processes in galaxy evolution. As discussed in Chapter 1, empirical scaling laws can be used to parameterize the overall relationship between star formation rate (SFR) and the ISM. Kennicutt (1998) (hereafter K98) found that quiescent spiral galaxies (i.e., Milky Way-like galaxies), infrared-luminous starbursts, and circumnuclear starbursts obey a tight relationship defined by

$$\Sigma_{\rm SFR} = A(\Sigma_{\rm gas})^n, \tag{6.1}$$

with $n = 1.4 \pm 0.15$. This relationship, called the global star formation law, has become a sub-grid recipe for star formation in a number of cosmological simulations. It is frequently thought to result from a "bottom-up" paradigm of star formation, in which the local density of gas drives star formation efficiency $\epsilon \equiv \Sigma_{\rm SFR}/\Sigma_{\rm gas}$.

K98 also found that quiescent spirals and starbursts obeyed an alternative version of the star formation law, posed by Silk (1997) and Elmegreen (1997):

$$\Sigma_{\rm SFR} = A\frac{\Sigma_{\rm gas}}{\tau_{\rm dyn}}, \tag{6.2}$$

where $\tau_{\rm dyn}$ represents the dynamical (orbital) timescale (K98). This version may imply that global dynamical features like spiral arms or bars might convert a constant fraction of gas into stars, potentially favoring a picture in which star formation is driven by "top-down" dynamical processes (Kennicutt and Evans 2012). This concept was subsequently generalized by Krumholz et al. (2012) into a universal correlation between SFR surface density and gas surface density per free fall time.

Since 1998, observational efforts have shifted to studying the star formation law on the scale of star-forming regions *within* individual galaxies. These spatially-resolved studies have presented a range of results. On global scales, K98 found that SFR correlates strongly with total gas surface density, moderately with atomic gas surface density ($\Sigma_{\rm HI}$), and only weakly with molecular gas surface density ($\Sigma_{\rm H_2}$). Most of the spatially-resolved studies, on the other hand, find that SFR correlates most strongly with $\Sigma_{\rm H_2}$ and almost not at all with $\Sigma_{\rm HI}$ (e.g., Bigiel et al. 2014, 2008; Kennicutt et al. 2007; Leroy et al. 2008).

Furthermore, many spatially-resolved studies report a shallower star formation law slope n than that found by K98. These works also suggest that the molecular gas depletion time ($\tau_{\rm depl}({\rm H_2}) \equiv \Sigma_{\rm H_2}/\Sigma_{\rm SFR}$) is constant (e.g., Bigiel et al. 2008; Leroy

et al. 2013; Schruba et al. 2011). However, studies of larger samples show that a larger range of $\tau_{\rm depl}(H_2)$ may instead depend systematically on specific SFR (SSFR≡SFR/M_*; Saintonge et al. 2011). Other studies also find a steeper $\Sigma_{\rm SFR}$-Σ_{H_2} law (Kennicutt et al. 2007), which may be a result of removing the "diffuse" local infrared and ultraviolet background (Liu et al. 2011; Momose et al. 2013; Morokuma-Matsui and Muraoka 2017).

While the spatially-resolved star formation law may shed more light on the local physical processes driving star formation, the global star formation law still plays a vital role. In many scenarios (e.g., high-redshift galaxies) only global measurements are available. Spatially-resolved SFRs are also subject to more physical uncertainty than globally averaged SFRs, due to the stochastic nature of star formation on local scales. For example, SFR tracers are generally sensitive to the high-mass end of the stellar initial mass function (IMF), but the IMF is often poorly sampled within small regions (i.e., on spatial scales of $\sim 0.1-1$ kpc in typical star-forming galaxies; Kennicutt and Evans 2012), leading to large variations in tracer luminosities for a given SFR. Indirect SFR tracers, such as Hα and infrared luminosities, can also be biased by emission from diffuse gas and dust, which may be located far from actual regions of star formation; these can affect measurements on the scale of hundreds of parsecs (Kennicutt and Evans 2012). Finally, stellar ages can fluctuate dramatically on small spatial scales (i.e., spatial scales small enough to be dominated by very young stellar clusters). This produces uncertainty since SFR is computed as the mass of recently-formed stars divided by the time over which they were formed. In part because of these complicated systematic uncertainties, it is important to understand if and how the star formation law depends on spatial scale.

Additionally, recent investigations of the global star formation law have found some discrepancies with the K98 study. Liu et al. (2015) recently re-measured the global Schmidt law using 1.4 GHz radio continuum sizes and SFR measurements. This analysis confirmed basic results from K98 but, like the spatially-resolved studies, found a significantly shallower power law slope.

To investigate the issues raised above, we revisit the global star formation law with improved multi-wavelength data. The increased availability of spatially-resolved HI maps and CO data makes it possible to measure gas surface densities of more galaxies. Similarly, the Galaxy Evolution Explorer (*GALEX*) provides ultraviolet (UV) fluxes that can be used to compute SFRs for much larger samples of galaxies. The UV measurements also allow us to extend reliable SFR measurements to dwarf

galaxies and other systems with low SFRs, where Hα rates are subject to large uncertainties introduced by stochasticity in the instantaneous SFR (e.g., Lee et al. 2009). With these spatially-resolved maps, we are able to define physically-based radii for averaging surface densities, rather than arbitrarily using optical or radio continuum isophotes. These larger samples also enable us to significantly extend the range of galaxy types and surface densities probed by the star formation law. Infrared (IR) measurements and new prescriptions for dust attenuation corrections make it possible to improve the precision of SFR measurements, allowing us to search for secondary physical parameters driving the dispersion in the relation.

We present the results in two papers. In this paper, we revisit the integrated star formation law for non-starbursting spiral, dwarf, and low surface brightness galaxies. We aim to determine if spiral galaxies alone can define a tight correlation between gas and SFR surface densities. By extending the surface density range probed to over three orders of magnitude, we also address other questions about the low-density regime of global star formation in galaxies. Paper II (Kennicutt and de los Reyes 2021) considers starbursts and high surface density systems, as well as the combined relation over all densities.

This paper is organized as follows. In Section 6.2, we present the dataset used in this sample. Our main results are outlined in Section 6.3, and we consider the possibility of second-order correlations in the star formation law in Section 6.4. We discuss the limitations of our dataset in Section 6.5 before considering literature comparisons (Section 6.6) and the physical implications of our results (Section 6.7). Finally, we summarize our findings in Section 6.8.

6.2 Data

In this section, we present the multi-wavelength data used to measure star formation rate densities[1], gas densities, and other galaxy properties.

6.2.1 Sample selection

Our base sample is composed of $N = 307$ nearby galaxies with good coverage in UV, mid-IR, and radio wavelengths. In particular, these galaxies were selected based on the availability of CO maps and spatially-resolved HI maps. Known luminous active galactic nuclei (AGN) were removed from the sample to prevent AGN radiation from being misidentified as radiation from star formation.

[1]Unless otherwise noted, we henceforth use "densities" to refer to "surface densities."

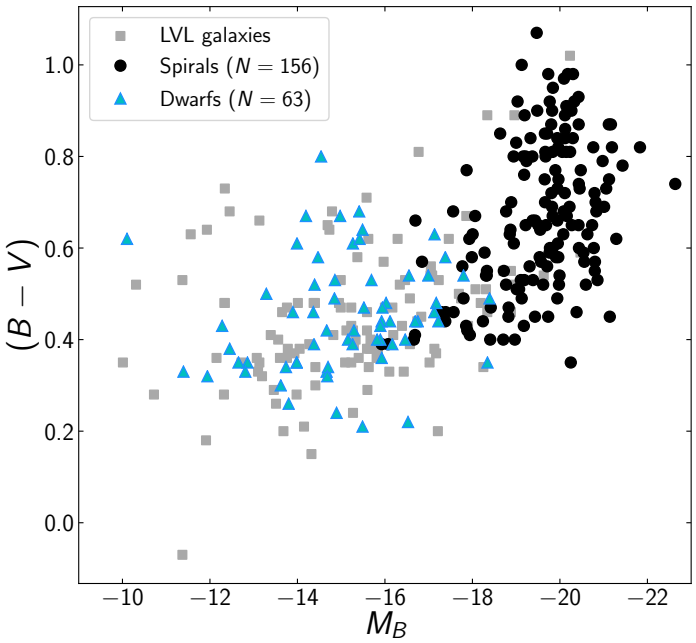

Figure 6.1: Color-magnitude diagram of the spiral (black solid points) and dwarf (cyan triangles) galaxies in our sample. Local Volume Legacy (LVL) galaxies not included in our sample are plotted as small gray points for comparison.

To characterize our sample, we plot a color-magnitude diagram of our sample in Figure 6.1. We also plot the Local Volume Legacy (LVL; Dale et al. 2009) galaxies, a volume-limited sample of galaxies within 11 Mpc of the Milky Way, on Figure 6.1 (small gray points) for comparison. The overlap between our sample and the LVL sample suggests that our galaxies form a generally representative sample of local galaxies, suitable for studying the general star formation law.

Of the $N = 307$ galaxies in the sample, 169 are typical star-forming disk or "spiral" galaxies, while the remaining 138 are "dwarf" galaxies. We initially defined dwarf galaxies as galaxies with low stellar masses ($M_* \leq 10^9\ M_\odot$) or low luminosities ($M > -17$ mag). However, the exact definition of dwarf galaxies is somewhat ambiguous, and we manually reclassified several dwarf galaxies—particularly low-luminosity disks—based on clear morphological distinctions. We also removed known blue compact dwarf (BCD) galaxies from our sample, and defer discussion of these highly-starbursting systems to Paper II. This reclassification does not significantly affect the results of any part of our analysis; as shown in Figure 6.1, the final "spiral" and "dwarf" populations are still largely distinct on a color-magnitude diagram. We note that the spirals have a relatively narrow range in physical properties, as is typical of the blue sequence.

Table 6.1: General properties of local spiral and dwarf galaxies.

NED ID[a]	RA (J2000)	Dec (J2000)	Dist[b] (Mpc)	m_B (mag)	$B-V$[c] (mag)	Type[d]	θ (deg)	$E(B-V)$[e]	D_{25}[f] (")	$D_{\mathrm{H}\alpha}$[f] (")	b/a[c]
WLM	00h01m58.16s	-15d27m39.3s	0.92	...	0.44 ± 0.04	d	4	0.04	689	154	0.35
NGC 7817	00h03m58.91s	+20d45m08.4s	26.13	12.56 ± 0.18	...	s	45	0.06	213	105	0.26
NGC 0023	00h09m53.41s	+25d55m25.6s	56.22	12.56 ± 0.14	0.82 ± 0.05	s	8	0.04	125	55	0.65
UGC 00191	00h20m05.20s	+10d52m48.0s	15.9	14.89 ± 0.26	0.44 ± 0.04	d	150	0.11	97	70	0.74
M 031	00h42m44.35s	+41d16m08.6s	0.79	4.16 ± 0.19	0.92 ± 0.02	s	35	0.58	11433	5940	0.32
IC 1574	00h43m03.82s	-22d14m48.8s	4.92	14.47 ± 0.21	0.61 ± 0.04	d	0	0.02	128	60	0.36
NGC 0253	00h47m33.12s	-25d17m17.6s	3.94	8.27 ± 0.21	0.85 ± 0.05	s	52	0.02	1653	1200	0.25
UGCA 015	00h49m49.20s	-21d00m54.0s	3.34	15.34 ± 0.21	0.43 ± 0.05	d	42	0.02	102	100	0.43
NGC 0278	00h52m04.31s	+47d33m01.8s	11.8	11.49 ± 0.22	0.64 ± 0.01	s	30	0.14	125	45	0.95
UGC 00634	01h01m25.10s	+07d37m35.0s	27.2	15 ± 0.3	0.48 ± 0.06	d	35	0.05	100	88	0.65

[a] Galaxy name preferred by the NASA/IPAC Extragalactic Database (NED). NED is operated by the Jet Propulsion Laboratory, California Institute of Technology, under contract with the National Aeronautics and Space Administration.

[b] Distances adopted from the 11 Mpc Hα UV Galaxy Survey (11HUGS; Kennicutt et al. 2008) catalog when possible or from NED otherwise.

[c] B-V colors adopted from RC3. Ratios of semi-minor to semi-major axis b/a measured from B-band isophotes by RC3.

[d] Galaxy classification as a "dwarf" (d) or "spiral" (s).

[e] Adopted from Schlegel et al. (1998) unless otherwise noted.

[f] D_{25} diameter is defined as the major axis of the RC3 B-band 25 mag arcsec^{-2} isophote. $D_{\mathrm{H}\alpha}$ diameter is defined as the semimajor axis of the region containing ~95% of the Hα flux (see Section 6.2.2).

Note: Only a portion of Table 6.1 is shown here; it is published in its entirety in a machine-readable format online.

Table 6.1 presents the basic properties of this sample. Columns 1-8 list general properties of the sample, while Columns 9-12 include data used to perform photometry (Sections 6.2.3 and 6.2.4).

6.2.2 Diameters

Since we aim to obtain SFR and gas surface densities rather than total SFRs and gas masses for the star formation law, we must define a diameter [2] by which to normalize our measured quantities. Rather than using an optically-defined size such as the D_{25} isophotal diameter, we choose to define a *star-forming region* as the region containing ∼95% of the Hα flux (Table 6.1). This is largely motivated by an attempt to remain self-consistent with our work with starburst galaxies (Paper II). In these galaxies, nearly all of the star formation is confined to circumnuclear molecular disks on the scale of 1 kpc, an order of magnitude smaller than the scale of the optical disk; the D_{25} diameter is therefore not a relevant scale for studying global star formation in these galaxies.

The Hα flux, on the other hand, is a more direct tracer of star formation than the near-IR. It is also less susceptible to dust attenuation than other star formation tracers, such as the UV continuum (see next section). Finally, Hα maps of local galaxies are readily available from the literature, including the 11HUGS survey (Kennicutt et al. 2008). However, we note that the use of Hα-based diameters may produce uncertainties for some galaxies; for example, in some cases extended UV emission can be found without obvious Hα counterparts (e.g., Goddard et al. 2010; Thilker et al. 2007). We note that the Hα-defined diameter is generally more compact than both the D_{25} diameter and a UV-defined diameter, with $D_{25} = 1.83 D_{\mathrm{H}\alpha}$ and $D_{\mathrm{UV}} = 2.24 D_{\mathrm{H}\alpha}$ on average. In Section 6.5, we consider potential systematic effects on our analysis that may arise from defining the star-forming region by Hα flux.

6.2.3 SFR surface densities

The most physically direct measure of SFR is the ultraviolet continuum produced by young stars, which traces SFR within the past ∼10 – 200 Myr. The UV continuum is less sensitive to fluctuations in the high-mass end of the stellar initial mass function

[2] Note that the choice of a single star-forming diameter is not necessarily the most physically correct choice. For a variety of reasons (e.g., extended gas distributions affecting star formation on more compact scales), it is certainly possible to define different gas and SFR diameters, or even to plot total gas masses and SFRs (i.e., total efficiencies). However, a full discussion of diameter choice is beyond the scope of this work. Here, we choose instead to consider an "idealized" case of a single star-forming region to measure both gas and SFR densities, and we defer deeper discussion to Paper II (Kennicutt and de los Reyes 2021).

(IMF) than other SFR tracers, particularly emission-line tracers such as Hα, which has been shown to be unreliable in low-SFR regions (Lee et al. 2009). We therefore use UV-based SFRs throughout our analysis.

The main disadvantage of UV light as a SFR tracer is its sensitivity to dust extinction and reddening. Since dust absorbs starlight at all wavelengths and re-emits in the infrared, IR luminosities can be used to correct for this attenuation (e.g., Hao et al. 2011).

In this section, we describe the UV and IR photometry obtained for our sample, as well as the SFR and SFR density calculations. The final SFR and SFR densities are listed in Table 6.4 at the end of the section.

UV photometry

UV data were obtained by the Galaxy Evolution Explorer (*GALEX*), a 50 cm aperture space telescope launched in 2003 by NASA. *GALEX* consisted of a 50 cm aperture space telescope that took simultaneous FUV ($\lambda_{\rm eff}$ = 1539Å) and NUV ($\lambda_{\rm eff}$ = 2316Å) observations. For this work, FUV is preferentially used; older stars contribute to the near-UV flux, so NUV-based SFR calibrations are more sensitive to the recent star formation history and the assumed stellar IMF.

When possible, we use *GALEX* FUV fluxes from various literature catalogs. In order of priority, we compiled FUV aperture fluxes from: the Gil de Paz et al. (2007) Atlas of Nearby Galaxies; the Local Volume Legacy (LVL) survey (Lee et al. 2011) (using apertures matched to the IR apertures of Dale et al. 2009); the Spitzer Infrared Nearby Galaxies Survey (SINGS; Dale et al. 2007); the LVL survey (Lee et al. 2011) (using apertures defined by the "outermost elliptical annulus where both FUV and NUV photometry can be performed"); Bai et al. (2015), the Virgo Cluster Survey (Voyer et al. 2014); and the Herschel Reference Survey (Cortese et al. 2012).

Eighty galaxies in the base N = 307 sample were not included in the above catalogs. Of these 80 galaxies, 68 had available *GALEX* imaging, and we performed aperture photometry for most of these using the deepest available *GALEX* FUV images. For 12 galaxies, FUV observations were not available, and we used the deepest available NUV images instead. The photometric procedure is described in detail in Appendix 6.9.1. As described in Appendix 6.9.2, we also performed FUV photometry for an additional 59 galaxies to check for consistency between our measurements and the catalogs. We find that most of the discrepancies between

Table 6.2: UV photometric data for local spiral and dwarf galaxies.

NED ID	$m_{\rm UV}$ (mag)	UV ref.[a]	$t_{\rm exp}$ (s)	*GALEX* tile	NUV[b]
WLM	12.8 ± 0.1	2	...	...	...
NGC 7817	15.0 ± 0.2	1	90.	AIS_144	1
NGC 0023	16.4 ± 0.4	1	3398.05	GI1_013001_NGC0023	0
UGC 00191	...	...	...	...	...
M 031	8.4 ± 0.1	6	...	...	...
IC 1574	16.9 ± 0.1	3	...	...	...
NGC 0253	11.6 ± 0.1	2	...	...	...
UGCA 015	17.1 ± 0.1	3	...	...	...
NGC 0278	11.8 ± 0.1	1	106.	AIS_43	1
UGC 00634	16.6 ± 0.5	1	197.05	AIS_264	0

[a] Table references: (1) This paper; (2) Gil de Paz et al. (2007); (3) LVL, using IR-matched apertures (Lee et al. 2011); (4) SINGS (Dale et al. 2007); (5) LVL, using "outermost elliptical aperture" (Lee et al. 2011); (6) Bai et al. (2015); (7) Virgo Cluster Survey (Voyer et al. 2014); (8) Herschel Reference Survey (Cortese et al. 2012).

[b] NUV flag: 0 if FUV flux was available, 1 if FUV unavailable and NUV used instead.

Note: Only a portion of Table 6.2 is shown here; it is published in its entirety in a machine-readable format online.

our measured fluxes and the catalog fluxes arise from differences in aperture size, since the literature catalogs report either asymptotic fluxes or aperture fluxes with different aperture sizes. Statistical aperture correction factors, tabulated in Table 6.8, were therefore applied to the catalog fluxes to correct for this aperture effect.

The final UV fluxes—either aperture-corrected catalog fluxes, or our measured photometric fluxes—are listed in Table 6.2. Table 6.2 also summarizes the observations of the 139 galaxies for which we measured photometric fluxes.

All images used for photometric measurements were preprocessed using the latest available *GALEX* pipeline (Martin et al. 2005; Morrissey et al. 2005, 2007).

IR photometry

The IR data in this work come from three instruments: the Spitzer Space Telescope's Multiband Imaging Photometer (*MIPS*), the Infrared Astronomical Satellite (*IRAS*), and the Wide-field Infrared Survey Explorer (*WISE*). Spitzer *MIPS*, launched in 2003 by NASA, contains separate detector arrays that perform imaging and spectroscopy

at 24, 70, and 160 μm bands; the 24 μm images, used in this work, were taken by a camera with a 5' square field of view (Rieke et al. 2004). *IRAS*, launched in 1983 as a joint project between the US, the UK, and the Netherlands, performed an all-sky survey at 12, 25, 60, and 100 μm (Neugebauer et al. 1984). Finally, *WISE* was a NASA space telescope launched in 2009; the data in this paper were obtained during the original *4-Band (or Full) Cryogenic survey*, which observed the entire sky in 3.4, 4.6, 12 and 22 μm bandpasses (Wright et al. 2010).

Although dust re-radiates attenuated UV light at all wavelengths in the IR (Draine 2003), complete wavelength coverage is available for few galaxies. We therefore use data from the $\approx$24 μm band, since Spitzer *MIPS*, *IRAS*, and *WISE* all have comparable bandpasses, and monochromatic dust corrections at this wavelength are only slightly less accurate than corrections using total IR (Hao et al. 2011). In Section 6.5, we discuss potential uncertainties arising from our use of a single infrared band rather than total IR.

When possible, we use mid-IR fluxes from existing catalogs. In order of priority, we compiled either Spitzer *MIPS* 24μm or *IRAS* 25μm fluxes from: the LVL survey (Dale et al. 2009); SINGS (Dale et al. 2007); the Gil de Paz et al. (2007) Atlas of Nearby Galaxies; the *MIPS* Local Galaxy Survey (*MIPS* LG; Bendo et al. 2012); and the *IRAS* Revised Bright Galaxies Sample (*IRAS* BGS; Sanders et al. 2003). As before, we also performed photometry for 46 galaxies using Spitzer *MIPS* images to check for consistency between our measurements and the catalog fluxes. These images were pre-processed by the LVL, SINGS, and *MIPS* LG surveys (Bendo et al. 2012; Dale et al. 2007, 2009); the processing steps (including instrumental correction, calibration, and background subtraction) are described in detail in the above references. We find that the catalog fluxes must be corrected to account for not only differences in aperture size, but also differences in the bandpass wavelength (24μm for Spitzer *MIPS* or 25μm for *IRAS*). Both the photometry procedure and the correction factors are described in Appendix 6.9.1.

The above catalogs do not contain 104 of the galaxies in our sample. We performed photometry for these galaxies using 22μm data from *WISE*'s AllWISE Image Atlas[3]. The AllWISE images used for photometry come from the *WISE* Image Atlas, which are co-adds of corrected *WISE* frames. As described in Appendix 6.9.1, we also performed additional photometry using AllWISE data to compare with the fluxes

[3]The AllWISE explanatory supplement can be found at `http://wise2.ipac.caltech.edu/docs/release/allwise/expsup/`

Table 6.3: IR photometric data for local spiral and dwarf galaxies.

NED ID	$f_{\rm IR}$ (Jy)	IR ref.[a]	$t_{\rm exp}$[b] (s)	Survey[c]	$n_{\rm frame}$[d]	Co-add ID[d]
WLM	$(70 \pm 9)\times10^{-3}$	3	...	...	...	...
NGC 7817	$(29 \pm 2)\times10^{-2}$	2	...	...	99	0016p212_ac51
NGC 0023	$(11 \pm 2)\times10^{-1}$	7	...	...	...	...
UGC 00191	$(4 \pm 2)\times10^{-3}$	2	...	...	124	0046p106_ac51
M 031	98 ± 23	5	...	...	...	...
IC 1574	$< 6.87 \times 10^{-4}$	2	...	...	150	0114m228_ac51
NGC 0253	139 ± 17	3	...	...	...	...
UGCA 015	$< 1 \times 10^{-3}$	2	...	...	141	0129m213_ac51
NGC 0278	$(22 \pm 5)\times10^{-1}$	7	...	...	...	...
UGC 00634	$(3 \pm 2)\times10^{-3}$	2	...	...	127	0152p075_ac51

[a] Table references: (1) This paper (using Spitzer MIPS images); (2) This paper (using AllWISE images); (3) LVL (Dale et al. 2009); (4) SINGS (Dale et al. 2007); (5) Gil de Paz et al. (2007); (6) *MIPS* LG (Bendo et al. 2012); (7) *IRAS* BGS (Sanders et al. 2003).

[b] *MIPS* LG files do not list exposure times. See Bendo et al. (2012) for more details.

[c] For Spitzer *MIPS* images, "Survey" indicates the name of the survey that pre-processed the image.

[d] For AllWISE images, $n_{\rm frame}$ is the number of frames (single-band images) and "Co-add" is the ID of the co-add (image produced by combining single-exposure frames).

Note: Only a portion of Table 6.3 is shown here; it is published in its entirety in a machine-readable format online.

we measured from Spitzer *MIPS* images. A statistical correction factor is applied to the AllWISE fluxes to correct for the difference in AllWISE 22μm and Spitzer 24μm bandpasses, as well as for variations in background subtraction methods.

The final IR fluxes—either aperture-corrected catalog fluxes, or our measured AllWISE fluxes—for our sample are listed in Table 6.3. Table 6.3 also summarizes the IR observations of the 150 galaxies for which we measured photometric fluxes.

SFRs and SFR surface densities

After converting UV and IR fluxes to luminosities using the distances reported in Table 6.1, the UV luminosity can be corrected for dust correction by using an energy

balance argument (Hao et al. 2011):

$$L(\mathrm{FUV})_{\mathrm{corr}} = L(\mathrm{FUV})_{\mathrm{obs}} + (3.89 \pm 0.20) L(24\mu\mathrm{m})_{\mathrm{obs}} \quad (6.3)$$

$$L(\mathrm{NUV})_{\mathrm{corr}} = L(\mathrm{NUV})_{\mathrm{obs}} + (2.26 \pm 0.16) L(24\mu\mathrm{m})_{\mathrm{obs}}. \quad (6.4)$$

The SFR is then calculated using the calibrations of Murphy et al. (2011), assuming a Kroupa IMF (Kroupa 2000). These calibrations are also tabulated in Kennicutt and Evans (2012):

$$\log[\mathrm{SFR}\ (\mathrm{M}_\odot\ \mathrm{yr}^{-1})] = \log[L(\mathrm{FUV})_{\mathrm{corr}}\ (\mathrm{erg\ s}^{-1})] - 43.35 \quad (6.5)$$

$$\log[\mathrm{SFR}\ (\mathrm{M}_\odot\ \mathrm{yr}^{-1})] = \log[L(\mathrm{NUV})_{\mathrm{corr}}\ (\mathrm{erg\ s}^{-1})] - 43.17. \quad (6.6)$$

These calibrations are appropriate for estimating SFRs integrated over entire galaxies; other works have considered SFR estimation on smaller spatial scales (e.g., Leroy et al. 2012).

Finally, the total SFR is converted to SFR surface density Σ_{SFR} by normalizing by the de-projected area of the star-forming region πR^2. As noted in Section 6.2.2, this star-forming region is defined as the region containing ~95% of the Hα flux, so that the physical radius R is computed from the distance to the galaxy and the semi-major axis a of the star-forming region. Table 6.1 lists these diameters, and Table 6.4 lists the SFR surface densities.

We defer a discussion of potential systematic uncertainties arising from these SFR calculations, including the choice of diameter and the recipe for dust correction, to Section 6.5.

6.2.4 Gas surface densities

Disk-averaged surface densities of HI and H_2 were compiled from published 21 cm and CO measurements in the literature, and it is the availability of these data which primarily determines the selection of galaxies for this study. Unless otherwise stated, the surface densities quoted are for hydrogen alone; densities including helium can be derived by multiplying by a factor of 1.36.

It is well known that the HI disks of galaxies extend in most cases well beyond the main star-forming disks, and the total HI masses and surface densities averaged over the entire HI disk often deviate significantly from the mean densities in the star-forming regions. Consequently, following K98 we restricted our interest to galaxies with well-resolved HI maps, usually measured from aperture synthesis arrays, in

order to measure the mean HI surface density over the same physical region as for the molecular gas and the SFR. Data were compiled from 114 papers as listed in Table 6.4, though a majority of the data come from a handful of large surveys made with the Westerbork Synthesis Radio Telescope (WSRT), the Very Large Array (VLA), or the Giant Millimetre Radio Telescope (GMRT). In most cases the primary papers present azimuthally-averaged HI surface density profiles, which were used to determine the average surface density $\Sigma_{\rm HI}$ within the radius of the star-forming region, listed in Table 6.1; otherwise, these were derived from the published contour maps. Care was taken to exclude galaxies where the beam size was too large to determine an accurate average In a handful of instances (mostly dwarf galaxies), we used a single-dish flux and star-forming radius to estimate the mean HI surface density, but only in cases where resolved maps were unavailable and the relevant beam size was comparable to the diameter of the star-forming disk. All surface densities were deprojected to face-on orientation.

Mean molecular hydrogen surface densities $\Sigma_{\rm H_2}$ were calculated from published CO(1-0) and/or CO(2-1) measurements. For the galaxies in this paper, most of these data were obtained with single-dish millimeter telescopes using single-beam (often with multiple pointings across the disks) or multi-beam arrays. In nearly all cases, the CO emission is restricted to a region of size comparable to or smaller than the star-forming disks, so in practice we adopted the published fluxes and molecular gas masses and divided the latter by the de-projected area of the star-forming region to determine the mean surface density. Care was taken to correct these values to a common CO to H_2 conversion factor (see below), assumed $\rm CO(2-1)/CO(1-0)$ ratio, and a molecular hydrogen (only) mass. When data from multiple sources were available, they were averaged. Many of these measurements consisted of a series of pointings (ususally along the major axis), and the integrated fluxes were computed from the resulting fitted radial profile of CO emission. We adopted these published values, but excluded galaxies with insufficient radial coverage for a reliable estimate of the total flux. This interpolation is often the dominant source of uncertainty in the fluxes (±30%).

Estimates of molecular hydrogen masses derived from CO rotational line measurements are notorious for their dependence on a variable $\rm CO/H_2$ conversion factor (X(CO) or α(CO); see Bolatto et al. 2013). Both the average value adopted and the prescriptions for parametrizing systematic variability in X(CO) have evolved considerably since K98. For most of the subsequent analysis we chose to adopt a

constant value:

$$X(\mathrm{CO}) = 2.0 \times 10^{20}\ \mathrm{cm}^{-2}\ (\mathrm{K\ km\ s}^{-1})^{-1}, \tag{6.7}$$

which appears to apply to the molecular disks of most quiescent spirals (Bolatto et al. 2013). However, this value almost certainly does not apply in low-mass dwarf galaxies, and when we discuss that subsample in Section 6.3, we will consider alternative formulations for $X(\mathrm{CO})$.

The uncertainties in the mean surface densities for HI and H_2 listed in Table 6.4 are dominated by the signal/noise of the maps (HI and CO), and corrections for spatial undersampling of the disks (CO). Since the surface density measurements come from a variety of sources, we assume a conservative estimate of measurement uncertainty: 0.1 dex ($\sim$ 26%) each for $\log \Sigma_{\mathrm{HI}}$ and $\log \Sigma_{\mathrm{H_2}}$. Uncertainties in the adopted radii also propagate into the SFRs, but these are relatively small for HI (which tend to have flatter radial profiles), and for H_2 any deviation will be identical to that in the mean SFR surface density. Other systematic uncertainties in the surface densities not included in Table 6.4 will be discussed in Section 6.5.

Table 6.4 lists the computed SFRs, gas masses, and SFR and gas surface densities.

Table 6.4: SFRs, gas masses, and SFR and gas surface densities.

NED ID	$\log \mathrm{SFR}_{\mathrm{uncorr}}$ $[M_\odot \mathrm{yr}^{-1}]$	$\log \mathrm{SFR}_{\mathrm{corr}}$ $[M_\odot \mathrm{yr}^{-1}]$	$\log \Sigma_{\mathrm{SFR}}$ $[M_\odot \mathrm{yr}^{-1} \mathrm{kpc}^{-2}]$	$\log \Sigma_{\mathrm{HI}}$[a] $[M_\odot \mathrm{pc}^{-2}]$	HI ref.[b]	$\log \Sigma_{\mathrm{H_2}}$[a] $[M_\odot \mathrm{pc}^{-2}]$	H_2 ref.[b]
WLM	-2.62 ± 0.04	-2.59 ± 0.04	-2.16	0.81	127	...	...
NGC 7817	-0.56 ± 0.09	-0.14 ± 0.04	-2.28	0.94	8	1.06	2
NGC 0023	-0.50 ± 0.17	0.96 ± 0.09	-1.28	0.66	106	1.70	2
UGC 00191	...	...	...	0.93	146	...	...
MESSIER 031	-1.00 ± 0.04	-0.59 ± 0.07	-3.19	0.31	102	-0.38	3,201
IC 1574	-2.80 ± 0.05	<-2.79	-2.99	0.49	149	...	...
NGC 0253	-0.89 ± 0.04	0.76 ± 0.06	-1.86	0.59	104,105	0.89	1,202,228
UGCA 015	-3.22 ± 0.05	<-3.20	-3.51	0.41	149,154	...	...
NGC 0278	0.02 ± 0.03	0.24 ± 0.04	-0.47	1.00	106	2.10	1
UGC 00634	-1.20 ± 0.19	-1.17 ± 0.18	-3.19	0.94	146	...	...

[a] As noted in the text, we assume conservative measurement uncertainties of ±0.1 dex for $\log \Sigma_{\mathrm{HI}}$ and $\log \Sigma_{\mathrm{H_2}}$.
[b] See Appendix 6.10 for references.
Note: Only a portion of Table 6.4 is shown here; it is published in its entirety in a machine-readable format online.

Table 6.5: Other properties of local spiral and dwarf galaxies.

NED ID	$\log M_*$ $[M_\odot]$	$\log M_*$ ref.[a]	Z (12 + log[O/H])	Z ref.[b]	C_{42}	$\tau_{\rm dyn}$[c] (10^8 yr)	$v_{\rm rot}$[c] (kpc/10^8 yr)
WLM	7.39	1	7.83	2	...	1.92	1.12
NGC 7817	10.55	3	...	...	2.53	1.90	21.97
NGC 0023	...	...	8.50	4	...	1.75	26.88
UGC 00191	8.82	3	...	...	2.96	...	...
MESSIER 031	...	...	...	...	...	3.18	22.48
IC 1574	7.74	1	...	...	2.40	...	...
NGC 0253	10.88	1	9.00	5	...	3.36	21.46
UGCA 015	6.79	1	...	...	2.33	...	...
NGC 0278	...	...	8.47	4	...	0.49	16.56
UGC 00634	9.03	3	...	...	2.90	...	...

[a] Stellar mass references: (1) IR fluxes from LVL (Dale et al. 2009); (2) IR fluxes from SINGS (Dale et al. 2007); (3) S4G (Muñoz-Mateos et al. 2013; Querejeta et al. 2015; Sheth et al. 2010).

[b] Metallicity references: (1) Moustakas et al. (2010); (2) Berg et al. (2012); (3) Lee et al. (2006a); (4) Calculated from spectra from Moustakas and Kennicutt (2006) using PT05 calibration; (5) Cook et al. (2014).

[c] References for dynamical time and rotational velocity are largely the same as the HI and H_2 references listed in Table 6.4.

Note: Only a portion of Table 6.5 is shown here; it is published in its entirety in a machine-readable format online.

6.2.5 Other properties

In order to investigate possible second-order correlations in the star formation law in Section 6.4, we obtain measurements of various secondary parameters.

Stellar mass

We determine approximate stellar masses from mid-IR luminosities. Several studies have found a nearly constant ratio of M_* to 3.6 μm luminosity (e.g. Cook et al. 2014; Eskew et al. 2012). Eskew et al. (2012) also use 4.5 μm luminosities; since observations from both wavelengths are available for the LVL and SINGS galaxies, we calculate stellar masses for these ($N = 130$) galaxies using the Eskew et al. (2012) prescriptions:

$$\frac{M_*}{M_\odot} = 10^{5.65} \left(\frac{F_{3.6}}{\mathrm{Jy}}\right)^{2.85} \left(\frac{F_{4.5}}{\mathrm{Jy}}\right)^{-1.85} \left(\frac{D}{0.05\mathrm{Mpc}}\right)^2 .$$

For $N = 96$ additional galaxies, we obtain 3.6 μm-based stellar masses from the Spitzer Survey of Stellar Structure in Galaxies (S4G; Muñoz-Mateos et al. 2013; Querejeta et al. 2015; Sheth et al. 2010). To check that the 4.5 μm and 3.6 μm calibration used for LVL and SINGS galaxies is consistent with the 3.6 μm calibration used in S4G, we compare the two calibrations for the LVL and SINGS galaxies where both fluxes are available. We find that the average difference between the two calibrations is < 0.005 dex.

Metallicity

We compile 71 integrated gas-phase metallicities[4] from the following literature sources: Berg et al. (2012) and Lee et al. (2006a) compiled "direct" metallicities based on electron temperature T_e, while Moustakas et al. (2010) used the Pilyugin and Thuan (2005) (PT05) "strong-line" calibration, which was empirically calibrated against direct metallicities.

For an additional 64 galaxies, we calculate metallicities from integrated optical spectra provided by Moustakas and Kennicutt (2006), using the PT05 calibration. This calibration depends on the line ratio $R_{23} = ([\mathrm{OII}]\lambda\lambda 3727, 3729 + [\mathrm{OIII}]\lambda\lambda 4959, 5007)/\mathrm{H}\beta$. Since any relation between R_{23} and Z is double-valued, the line ratio $[\mathrm{NII}]\lambda 6854/\mathrm{H}\alpha$ is used to determine which metallicity "branch" a galaxy occupies.

[4]Unless otherwise noted, we refer to $Z = 12 + \log[\mathrm{O/H}]$, or oxygen abundance relative to solar, as a proxy for total gas-phase metallicity.

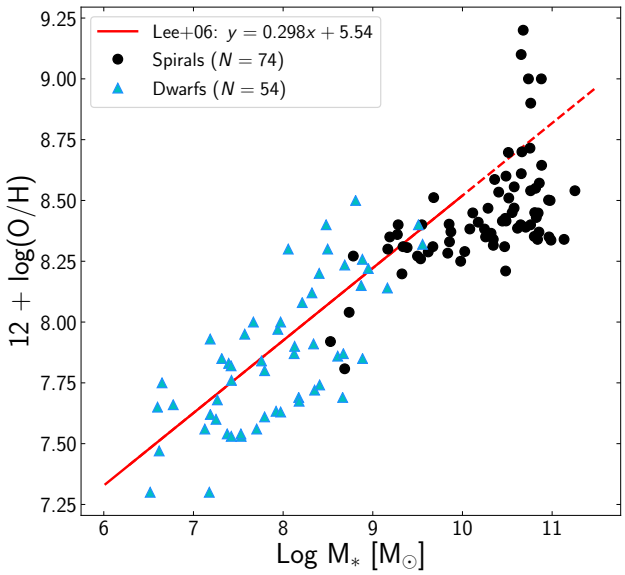

Figure 6.2: Mass-metallicity relation for our sample. The best-fit relation found for dwarf galaxies by Lee et al. (2006a) is plotted in red; the solid line illustrates the mass range over which this relation is valid, while the dashed line extrapolates this relation to the full mass range of our sample.

Finally, metallicities are obtained for a remaining 19 galaxies from Cook et al. (2014). Many of these are direct metallicities, but others were derived from inconsistent strong-line calibrations. Due to this variation in calibration methods, Cook et al. (2014) estimates potential systematic uncertainties of ~0.3 dex for these abundances.

We characterize the stellar masses and gas-phase metallicities of the total sample by plotting the mass-metallicity relation in Figure 6.2. Our sample is consistent with the mass-metallicity relation determined for dwarf galaxies by Lee et al. (2006a), which is a smooth extension of the well-studied mass-metallicity relation for star-forming galaxies (Tremonti et al. 2004).

Dynamical timescale

As described in Section 6.1, the relationship between dynamical timescale ($\tau_{\rm dyn}$) and SFR reflects a physical picture in which global perturbations convert a constant fraction of gas into stars (Silk 1997). In this work, dynamical timescale is defined as the orbital timescale of the disk: $\tau_{\rm dyn} = 2\pi R/v(R)$, where R is the radius of the star-forming region, and v is the rotational velocity. Rotational velocities were compiled from the literature, with sources in the following order of preference: (1) full rotation curves measured in Hα, HI, and/or CO, either as published in the

primary reference or measured by us from the data; (2) position-velocity relations in HI and/or CO; (3) 21 cm HI linewidths, as compiled from NED, and corrected for turbulent broadening following the prescription of Tully and Fouque (1985).

All velocities were corrected for inclination, using values usually derived from fitting the velocity fields themselves, or otherwise from photometric measurements. We excluded galaxies less than 20° from face-on orientation, or systems with irregular or disturbed velocity fields. The latter were especially problematic for some of the lowest-mass dwarf galaxies; as a result, the number of galaxies with $\tau_{\rm dyn}$ ($N = 163$) is considerably smaller than that for the gas surface density power law ($N = 244$). The rotation speed was measured at the radius of the star-forming disk, as given in Table 6.4, though for most galaxies the edge of the star-forming disk lies in the flat part of the rotation curve. This same radius was adopted to calculate the dynamical time. Readers should be aware that the scaling radius for $\tau_{\rm dyn}$ varies in the literature; the definition here is consistent with that used in K98.

Concentration index

To investigate how the star formation law might be affected by morphology, we consider the concentration index. This index, often denoted C_{42}, is defined as

$$C_{42} = 5 \log \left(\frac{r_{80}}{r_{20}} \right),$$

where r_{80} and r_{20} are the radii containing 80% and 20% of a galaxy's light, respectively (Kent 1985). This is a rough quantitative measure of galaxy morphology, since it is a proxy for the bulge-to-total luminosity ratio; elliptical (spiral) galaxies therefore have higher (lower) C_{42} (Shimasaku et al. 2001). We obtain C_{42} values for $N = 200$ galaxies from the S4G survey, which measured C_{42} at 3.6 μm (Sheth et al. 2010).

All of the secondary properties described in the previous sections are compiled in Table 6.5:

Derived properties

We note that additional important parameters can be derived from the ones listed in Tables 6.2, 6.3, 6.4, and 6.5. These derived properties include:

- Specific star formation rate, SSFR = SFR/M_*

- Molecular gas fraction, $f_{\rm mol} = M_{\rm H_2}/(M_{\rm HI} + M_{\rm H_2})$
- Stellar mass surface density, $\Sigma_* = M_*/(\pi R^2)$
- Gas fraction, $f_{\rm gas} = \frac{M_{\rm HI}+M_{\rm H_2}}{(M_*+M_{\rm HI}+M_{\rm H_2})}$
- The ratio of obscured star formation to unobscured star formation, which is roughly approximated by $L_{\rm IR}/L_{\rm UV}$

6.3 Star formation scaling laws

In this chapter, we update the global star formation law, consider alternative star formation laws, and discuss potential systematic uncertainties affecting our data.

6.3.1 The revised star formation law for spiral galaxies

We first repeat the analysis of K98 and consider the relationship between $\Sigma_{\rm SFR}$ and total gas surface density $\Sigma_{\rm gas}$ using a constant Milky Way value of $X({\rm CO})$ (Equation 6.7). In this paper, as in many studies of the star formation law, we define $\Sigma_{\rm gas} = \Sigma_{\rm HI} + \Sigma_{\rm H_2}$ and ignore contributions from helium and other species. In Figure 6.3, we present the global star formation law for "typical" spiral galaxies (black solid points) and determine lines of best fit to this relation. Although a thorough analysis of statistical methods to fit a line is beyond the scope of this paper (for a more detailed discussion, see Hogg et al. 2010), we briefly discuss the techniques used here.

We first consider a naive *unweighted* linear regression, which simply minimizes the mean squared errors of the y-residuals and weights all points equally, without accounting for any statistical uncertainties. This is clearly an inadequate model, since there are heteroscedastic measurement uncertainties in both the x and y directions. However, since the errors in $\Sigma_{\rm SFR}$ and the errors in $\Sigma_{\rm gas}$ are of roughly the same order of magnitude, this method (dashed blue line in Figure 6.3) provides a first-order approximation to compare with other fits, yielding a slope of 1.34 ± 0.07. Note that all parameter uncertainties reported in this text are 1σ fitting errors.

We then consider measurement uncertainties in both x- and y-directions by computing a *bivariate* fit using orthogonal distance regression. Note that we consider only statistical measurement uncertainties here; we discuss systematic uncertainties in Section 6.5. This method minimizes the orthogonal squared distance from the line to all points, which are weighted by the uncertainties in both the x- and y-directions. Bivariate regression was used by K98 to determine power-law indices of

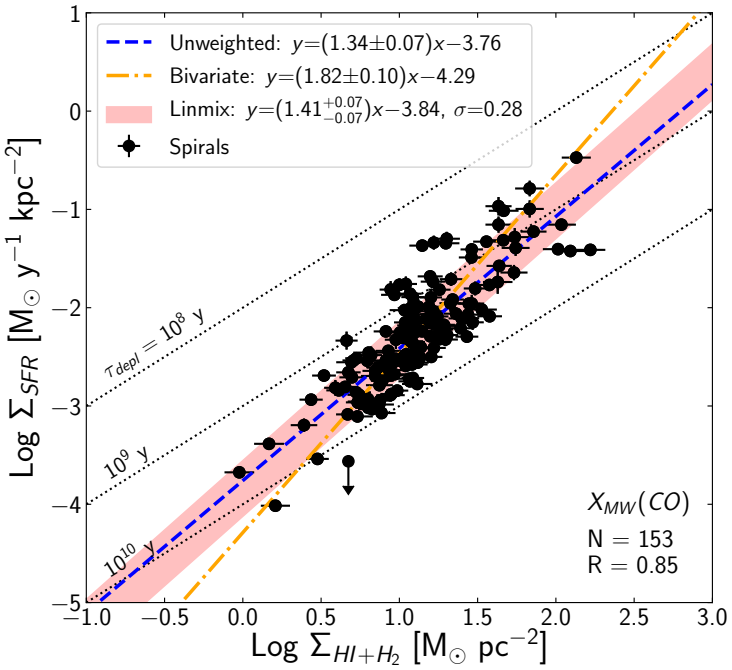

Figure 6.3: The global star formation law for spirals (black circles), using a constant Milky Way X(CO). Dashed lines represent constant depletion time $\tau_{\rm depl} = \Sigma_{\rm gas}/\Sigma_{\rm SFR}$. The lines of best fit are derived using different methods as described in the text: *unweighted* linear regression (blue dashed line), *bivariate* linear regression (orange dot-dashed line), and an MCMC model using the *linmix* algorithm (red shaded area marks the median of the posterior distributions for the linear slope, intercept, and intrinsic dispersion). Note that the correlation coefficient R shown in the bottom right is the Pearson correlation coefficient.

$n = 1.4 \pm 0.15$ for spiral and starburst galaxies and $n = 2.47 \pm 0.39$ for spiral galaxies alone. When applied to our updated sample of spiral galaxies (dot-dashed orange line in Figure 6.3), this regression yields an intermediate slope of 1.82 ± 0.10.

However, it can be shown analytically that bivariate regression becomes biased and tends to overestimate the slope when there is intrinsic dispersion in the relation between the x and y quantities (Akritas and Bershady 1996; Carroll and Ruppert 1996). To more appropriately handle both x- and y-errors as well as intrinsic dispersion in the relation, we therefore use a hierarchical Bayesian model called *linmix*, described by Kelly (2007).[5]

The linmix method first assumes that a measured data point (x, y) can be drawn from a two-dimensional Gaussian distribution P_1 with some "true" mean (ξ, η)

[5]The linmix algorithm has been ported to a Python package by J. Meyers and is available on github at `https://github.com/jmeyers314/linmix`.

and covariance matrix determined from measurement uncertainties σ_x and σ_y. The "true" value of the dependent variable η can in turn be drawn from a Gaussian distribution P_2 with mean $\beta\xi + \alpha$ and variance σ^2, where β describes the slope of the line, α the y-intercept, and σ^2 the intrinsic dispersion in the y-direction. Finally, the "true" value of the independent variable ξ is assumed to be drawn from a weighted sum of K Gaussian distributions P_3, since a large enough number of Gaussians can approximate any true distribution.[6] The distributions $\{P_1, P_2, P_3\}$ are then convolved hierarchically to compute the full likelihood of obtaining the data (x, y) given parameters $\{\beta, \alpha, \sigma^2\}$. Assuming uniform prior distributions for the parameters $\{\beta, \alpha, \sigma^2\}$, a Markov chain Monte Carlo (MCMC) algorithm is used to sample from the posterior distributions until convergence is reached. We note that for all linmix fits presented in this paper, the marginalized posterior distributions for $\{\beta, \alpha, \sigma^2\}$ are roughly Gaussian.

This linmix model (red shaded area in Figure 6.3) yields a median slope of $1.41^{+0.07}_{-0.07}$, where the parameter uncertainties given are the 16th and 84th percentiles of the marginalized distribution. This slope is much shallower than the bivariate K98 result for the spiral galaxies alone ($n = 2.47 \pm 0.39$). It is, however, remarkably consistent with the oft-cited $n \sim 1.4$ law for both spiral and starburst galaxies. We take this result to be the fiducial star formation law for spiral galaxies:

$$\log \Sigma_{\rm SFR} = \left(1.41^{+0.07}_{-0.07}\right) \log \Sigma_{\rm gas} - 3.84^{+0.08}_{-0.09}. \tag{6.8}$$

Furthermore, the linmix method estimates an intrinsic dispersion in the y-direction of $\sigma = 0.28^{+0.02}_{-0.02}$ dex in the y-direction, which is larger than the typical measurement uncertainty in SFR ($\sigma_{\rm SFR} \lesssim 0.10$ dex).

The linmix model also estimates the intercept of the star formation law to be $-3.84^{+0.08}_{-0.09}$, which corresponds to a coefficient $A = 1.5^{+0.3}_{-0.3} \times 10^{-4}$ in Equation 6.1. This is slightly smaller than the value $A = 2.5 \pm 0.7$ measured in K98. This discrepancy may result from a number of factors. In particular, the composite FUV and 24μm calibrations used in this work yield SFRs ∼0.2 dex lower than those in K98, primarily due to differences in the assumed IMF and updated stellar population models (Kennicutt and Evans 2012). The individual 24μm dust corrections used to compute SFRs may also play a role; we correct the UV luminosities for internal extinction by a factor of ∼2.4 on average, compared to the factor of 2.8 assumed by

[6]Following the procedure of Kelly (2007), we use $K = 2$ Gaussians to estimate posteriors. The addition of more Gaussians has a negligible effect on our results.

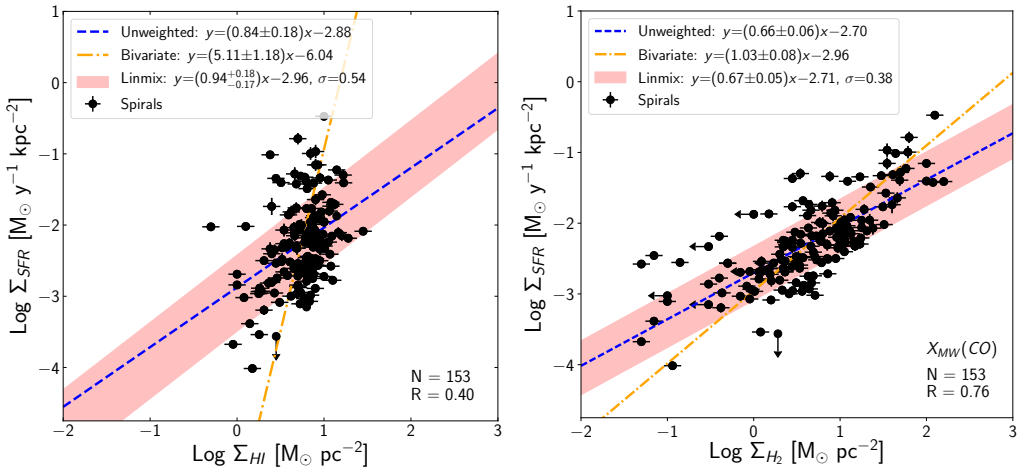

Figure 6.4: The relationships between SFR surface density and atomic gas surface density (left) and between SFR surface density and molecular gas surface density (right) for spiral galaxies (black circles). Downward arrows represent upper limits on $\Sigma_{\rm SFR}$. Linear fits are marked by lines and shaded regions as described in Figure 6.3.

K98. Some combination of these explanations likely produces the discrepancy in measured star formation law intercepts.

We note that upper limits are excluded when applying all three fitting methods. In our sample of spiral galaxies, there is only a single point with an upper limit in $\Sigma_{\rm SFR}$ (see Figure 6.3), so we do not expect its exclusion to significantly affect the fit. For completeness, we check this using the linmix method, which is capable of handling upper limits in the y-direction (Kelly 2007). We find that including this upper limit does not significantly affect the model parameters.

6.3.2 Separate atomic and molecular gas components in spiral galaxies

As in K98, we now separately consider the atomic and molecular hydrogen gas components. Star formation is thought to occur in molecular clouds; indeed, results from spatially-resolved studies of the star formation law have found moderate correlation between $\Sigma_{\rm SFR}$ and $\Sigma_{\rm H_2}$ but little to no correlation between Σ_{SFR} and $\Sigma_{\rm HI}$ (Bigiel et al. 2008; Kennicutt et al. 2007; Leroy et al. 2008; Schruba et al. 2011). Several of these studies have proposed that star formation is a two-step process: a baryonic reservoir of atomic gas is converted to molecular gas, and dense clumps of molecular gas are then converted into stars.

On the global scale, K98 found that the correlation between SFR density and atomic gas density was almost as strongly correlated as the $\Sigma_{\rm SFR}$-$\Sigma_{\rm HI+H_2}$ relation, with a

Pearson correlation coefficient[7] of $R = 0.66$ (compared to $R = 0.68$ for the total gas relation). The correlation between SFR density and molecular gas density was much weaker, and it was suggested that this was perhaps in part due to variations in the CO-to-H_2 conversion factor $X(\mathrm{CO})$. We investigate the tension between these conflicting results with our updated sample.

The left panel of Figure 6.4 illustrates the relationship between Σ_{SFR} and Σ_{HI} for spiral galaxies. The correlation between the SFR and atomic gas surface density is weaker than that found by K98, with a correlation coefficient $R = 0.40$ compared to the K98 value of $R = 0.66$. The large difference between the slopes estimated using various regression methods ($n = 5.10 \pm 1.20$, $n = 0.94^{+0.18}_{-0.17}$ and $n = 0.84 \pm 0.18$ for bivariate, linmix, and unweighted regressions, respectively) also suggests a weak Σ_{SFR}-Σ_{HI} correlation, as does the large intrinsic dispersion $\sigma = 0.54^{+0.03}_{-0.03}$ estimated by linmix. These inconsistencies suggest that a simple power law fit is a poor representation of the observed relation. Instead we suspect that the nearly vertical relation is strongly influenced by the conversion of atomic hydrogen to molecular gas above a surface density of $\sim$10 $\mathrm{M_\odot\ pc^{-2}}$ (column density of $\sim 10^{21}$ $\mathrm{cm^{-2}}$), as discussed previously for spatially-resolved studies by Kennicutt et al. (2007) and Bigiel et al. (2008).

We now consider the Σ_{SFR}-$\Sigma_{\mathrm{H_2}}$ relation for spiral galaxies in the right panel of Figure 6.4. As noted in Section 6.2.4, the molecular gas surface density depends on the assumed $X(\mathrm{CO})$ conversion factor from CO luminosity to H_2 gas mass; we initially assume a constant $X(\mathrm{CO})$ that is roughly reliable for non-starbursting spiral galaxies (Equation 6.7). The correlation between Σ_{SFR} and molecular gas density $\Sigma_{\mathrm{H_2}}$ is stronger than the star formation law based on atomic gas density, with a correlation coefficient of $R = 0.79$. Although the various regression methods find inconsistent slopes, again suggesting some amount of intrinsic scatter in the relation, all methods yield approximately linear slopes $n \sim 1$.

Both the weak $\Sigma_{\mathrm{SFR}} - \Sigma_{\mathrm{HI}}$ correlation and tighter, roughly linear $\Sigma_{\mathrm{SFR}} - \Sigma_{\mathrm{H_2}}$ correlation are consistent with the results found by spatially-resolved studies (e.g., Bigiel et al. 2008). These are the opposite of the global results reported by K98, suggesting that the K98 results were strongly influenced by a smaller sample size and/or a narrower parameter space. However, both the atomic gas and the molecular gas star formation laws have weaker correlations than the total gas star formation law in Figure 6.3 ($R = 0.85$); the linmix method also finds that the atomic gas and molecular

[7] In this analysis, all correlation coefficients are Pearson product-moment correlation coefficients.

gas star formation laws have larger intrinsic dispersions by ≥ 0.1 dex. This appears to confirm the K98 finding that $\Sigma_{\mathrm{HI+H_2}}$ is a strong predictor of SFR surface density.

6.3.3 Molecular gas conversion factors

Before extending the star formation law to include low-Σ_{SFR} dwarf galaxies, we must consider the effect of varying $X(\mathrm{CO})$. $X(\mathrm{CO})$ is likely dependent on environmental factors; in particular, metallicity is correlated with the presence of dust, which can help shield CO from photodissociation. As a result, in low-mass and low-metallicity environments such as dwarf galaxies, CO will under-predict the true amount of H_2, and $X(\mathrm{CO})$ should be higher than the Milky Way value (see Bolatto et al. 2013, and references therein). We therefore consider the effect of using metallicity-dependent prescriptions of $X(\mathrm{CO})$.

First, we consider the prescription recommended by Bolatto et al. (2013), who used a simple analytical model to approximate a correction factor f such that $X(\mathrm{CO}) = fX_{\mathrm{MW}}(\mathrm{CO})$:

$$f = 0.67 \exp\left(\frac{0.4}{Z'\Sigma_{100,\mathrm{GMC}}}\right). \tag{6.9}$$

Here, $Z' = Z/Z_\odot$ is metallicity relative to solar (note that $12+\log(\mathrm{O}_\odot/\mathrm{H}_\odot) = 8.69$; Asplund et al. 2009), and $\Sigma_{100,\mathrm{GMC}} = 1.0$ is the assumed characteristic surface density of molecular clouds in units of 100 $\mathrm{M}_\odot$ pc^{-2}. This factor accounts for the H_2 mass in outer regions of clouds, where CO is more likely to be photodissociated.

Glover and Mac Low (2010) developed a more extreme $X(\mathrm{CO})$ prescription by simulating a more complex dynamical model for individual giant molecular clouds. We use the Bolatto et al. (2013) adaptation of Equation 16 in Glover and Mac Low (2010), which assumes that mean extinction (i.e., dust abundance) scales linearly with metal abundance. This yields the following correction factor f:

$$f = \begin{cases} 1 & \text{for } Z'\overline{A}_{V,MW} > 3.5 \\ (\frac{Z'\overline{A}_{V,MW}}{3.5})^{-3.5} & \text{for } Z'\overline{A}_{V,MW} < 3.5, \end{cases}$$

where Z' is again metallicity relative to solar, and $\overline{A}_{V,MW} = 5$ is the assumed mean extinction through a molecular cloud with surface density $\Sigma^{100}_{GMC} = 1.0$.

We note that even spiral galaxies are affected by changing $X(\mathrm{CO})$. Although the relationship between star formation rate and *molecular* gas surface density for spirals does not change significantly, using metallicity-dependent $X(\mathrm{CO})$ prescriptions rather than a constant Milky Way value can decrease the slope of the *total* gas star formation laws by ~ 0.12 dex, from 1.41 to 1.29.

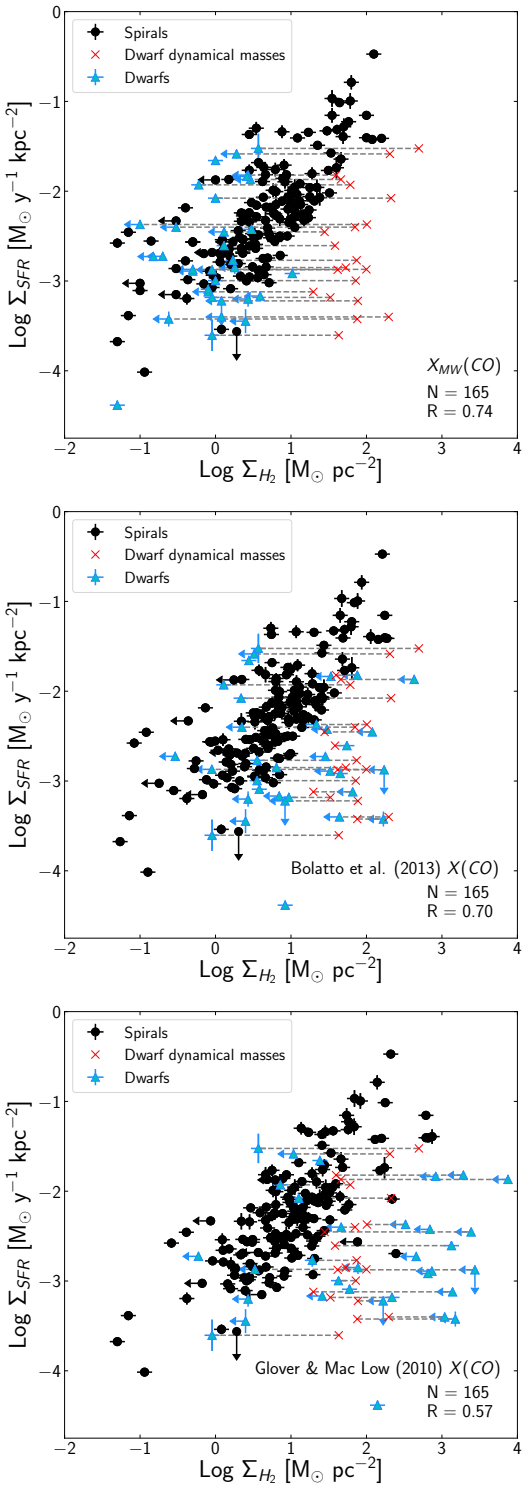

Figure 6.5: The effect of using various X(CO) prescriptions (described in the text) on the relationship between SFR surface density and molecular gas surface density for spirals (black circles) and dwarfs (cyan triangles). For each dwarf galaxy with an available dynamical mass, the dynamical mass surface density $\Sigma_{\rm dyn}$ is plotted as a connected red X. Arrows represent upper limits on either $\Sigma_{\rm H_2}$ (downward) or $\Sigma_{\rm SFR}$ (leftward).

This effect can become particularly extreme for dwarf galaxies. In Figure 6.5 we plot the relationship between $\Sigma_{\rm SFR}$ and $\Sigma_{\rm H_2}$ for these different X(CO) calibrations. To check how realistic these prescriptions are, we compare the molecular gas surface densities $\Sigma_{\rm H_2}$ with dynamical mass surface densities $\Sigma_{\rm dyn}$, which are computed from dynamical mass $M_{\rm dyn} = v^2 R/G$. Here v is the circular velocity at the star formation radius R, computed from 21cm lines; see Section 6.2.5. For dwarf galaxies, $\Sigma_{\rm dyn}$ are plotted as red Xs in Figure 6.5.

Figure 6.5 shows that applying either the Bolatto et al. (2013) or the Glover and Mac Low (2010) metallicity-dependent X(CO) prescription shifts the low-metallicity galaxies—which are mostly dwarf galaxies—to higher $\Sigma_{\rm H_2}$. Many of the shifted galaxies only have upper limits on $\Sigma_{\rm H_2}$, so increasing these limits does not constrain the star formation law. However, the Glover and Mac Low (2010) X(CO) formula has particularly extreme effects, shifting several dwarf galaxies without upper limits on $\Sigma_{\rm H_2}$ to molecular gas surface densities greater than the dynamical mass surface densities. This unrealistic result is likely not because of any intrinsic flaw in the Glover and Mac Low (2010) prescription, but rather because their result is based on individual giant molecular clouds and is not applicable to entire galaxies. As with the star formation rate calibrations (Section 6.2.3), we emphasize the importance of exercising caution when applying small-scale prescriptions to galaxy-scale problems. We therefore use the Bolatto et al. (2013) X(CO) prescription in all following analyses.

6.3.4 The star formation law for both spiral and dwarf galaxies

Having determined which X(CO) prescription is the least unrealistic for our sample, we can now extend the total gas star formation law to include low-$\Sigma_{\rm SFR}$ dwarf galaxies (cyan triangles). In the left panel of Figure 6.6, we plot all galaxies with HI, CO, and SFR measurements, showing a clear correlation between $\Sigma_{\rm SFR}$ and $\Sigma_{\rm gas}$ (correlation coefficient $R = 0.81$).

Various linear regression methods produce a larger range of star formation indices. The unweighted method yields a slope of $n = 1.21 \pm 0.08$, the bivariate method yields a slope of $n = 1.94 \pm 0.17$, and the linmix model estimates a slope $n = 1.26^{+0.08}_{-0.08}$. As described in Section 6.3.1, the linmix regression method is more appropriate in fitting relations with some intrinsic scatter (e.g., Hogg et al. 2010). We therefore take the linmix result to be the fiducial star formation law for the combined sample

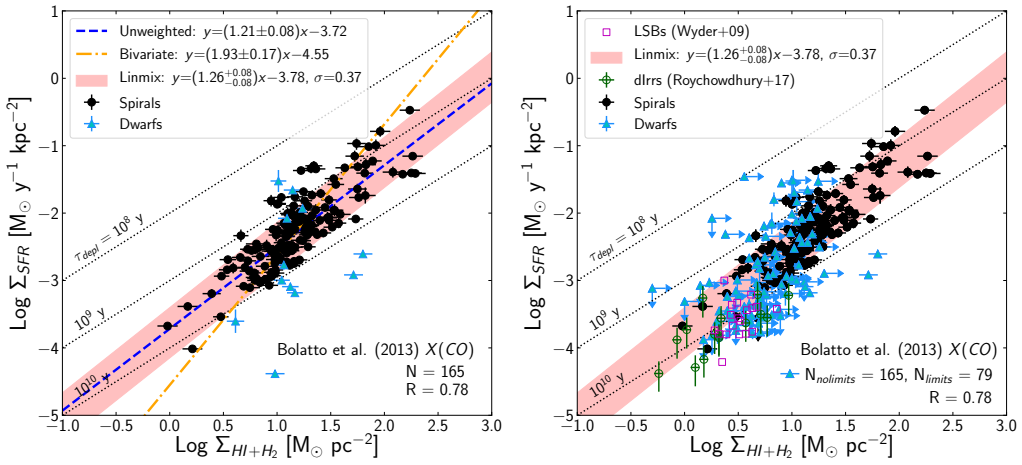

Figure 6.6: Same as Figure 6.3, but including dwarf galaxies (cyan triangles). The left panel only includes galaxies with CO and SFR detections, as well as unweighted (blue dashed line) and bivariate (yellow dot-dashed line) fits. The red shaded area marks the median fit and intrinsic dispersion determined using the linmix MCMC method. The right panel has the same linmix fit, but also plots galaxies with only HI measurements (rightward arrows) or upper limits on SFR measurements (downward arrows); the numbers of galaxies with and without these limits are given by $N_{\rm limits}$ and $N_{\rm nolimits}$, respectively. For comparison, low-surface brightness galaxies from Wyder et al. (2009) (purple unfilled triangles) and dwarf irregular galaxies from Roychowdhury et al. (2017) (green unfilled circles) are also shown.

of spirals and dwarf galaxies:

$$\log \Sigma_{\rm SFR} = \left(1.26^{+0.08}_{-0.08}\right) \log \Sigma_{\rm gas} - 3.78^{+0.10}_{-0.10}. \tag{6.10}$$

The linmix model also estimates an intrinsic dispersion of $\sigma = 0.37^{+0.02}_{-0.02}$ dex, which we discuss in further detail in Section 6.4.

For visualization purposes, in the right panel of Figure 6.6 we plot galaxies with measurement limits: galaxies with upper limits on SFR, or galaxies with upper limits or non-detections of H_2 (and therefore lower limits on the total $\Sigma_{\rm gas}$). We note that in our analyses, we exclude these points when determining the correlation coefficient and linear fit [8]. We instead plot the linmix linear fits from Figure 6.6 to compare these measurement limits to the derived slope of $n = 1.26^{+0.08}_{-0.08}$. We also plot low-surface brightness galaxies (LSBs; purple triangles) from Wyder et al. (2009) and

[8]The linmix method is capable of handling upper limits in the y-direction; however, as in Section 6.3.1, only one of our points has *only* an upper limit in the y-direction. All other points with upper limits in the y-direction also have lower limits in the x-direction. Properly treating such points is a complex problem beyond the scope of this statistical analysis, particularly since the lower x-limits are primarily dominated by systematic uncertainties in X(CO) anyway (see Section 6.5 for further discussion of this systematic effect).

dwarf irregular galaxies (dIrrs; green diamonds) from Roychowdhury et al. (2017) for comparison.

Figure 6.6 indicates that dwarf galaxies tend to increase the intrinsic scatter in the star formation law. Indeed, the linmix regression method suggests that σ (the intrinsic dispersion in the y-direction) increases by ~ 0.1 dex when dwarf galaxies with reliable measurements are included in the fit. The inclusion of dwarf galaxies also decreases the slope in the star formation law from $n \sim 1.41$ (for spiral galaxies alone) to $n \sim 1.26$ (for both spirals and dwarfs). Furthermore, Figure 6.6 shows that the majority of dwarf galaxies—including LSBs, dwarf irregular galaxies, and dwarf galaxies with lower limits on $\Sigma_{\rm gas}$—lie at lower $\Sigma_{\rm SFR}$ than the star formation law defined by spiral galaxies. Those dwarf galaxies that lie above the main locus of spiral galaxies tend to have non-detections of CO (rightward arrows); a "dark" (i.e., not traced by CO) molecular component could shift these galaxies to higher $\Sigma_{\rm gas}$, into agreement with the other dwarf galaxies. Note that the choice of X(CO) does not affect this qualitative result, because adding a correction for undetected molecular gas only drives these galaxies towards higher $\Sigma_{\rm gas}$ (without changing $\Sigma_{\rm SFR}$), and thus further below the star formation law for spiral galaxies.

This may be consistent with a low-density threshold in the star formation law. Such a threshold—below which the star formation law steepens or even breaks down—has been well-measured on spatially-resolved scales within galaxies (e.g., Bigiel et al. 2008; Kennicutt 1989; Skillman et al. 1987). As shown in Figure 6.6, this threshold does appear to exist on integrated scales, although it is much less distinct than that observed on spatially-resolved scales. We discuss potential interpretations of this threshold in Section 6.7.

6.3.5 Alternative star formation laws

The original Schmidt law is not the only star formation scaling law. Equation 6.2 describes an alternative version of the star formation law, in which the dynamical timescale $\tau_{\rm dyn}$ is taken to be the characteristic time of star formation (Elmegreen 1997; Silk 1997). In this relationship, hereafter referred to as the Silk-Elmegreen relation, star formation efficiency $\epsilon = \Sigma_{\rm SFR}/\Sigma_{\rm gas}$ depends linearly on $\tau_{\rm dyn}$ rather than on local gas density $\Sigma_{\rm gas}$.

We plot the Silk-Elmegreen relation for both our spiral and dwarf galaxies in Figure 6.7. As in K98, the local dynamical timescale $\tau_{\rm dyn}$ is taken to be the orbital period at the star-forming radius (Section 6.2.5). The slope of this relation estimated from

the linmix algorithm is sub-linear ($n = 0.78 \pm 0.05$), inconsistent with the predicted linear slope (dotted purple line). The shallower slope appears to be driven by spiral galaxies with high SFR surface densities that have higher $\Sigma_{\rm gas}/\tau_{\rm dyn}$ than expected, suggesting that the fraction of gas converted into stars is not entirely constant for quiescent star-forming galaxies.

However, the relationship between $\Sigma_{\rm SFR}$ and $\Sigma_{\rm gas}/\tau_{\rm dyn}$ is at least as tight as the star formation law for our updated sample of spiral and dwarf galaxies, with a correlation coefficient $R = 0.80$ close to $R = 0.78$ for the Schmidt law (Figure 6.6). The intrinsic dispersion in the relationship also indicates a tight relation; the linmix estimate of intrinsic scatter is $0.33^{+0.02}_{-0.02}$ dex, slightly smaller than the dispersion estimate for the Schmidt law (intrinsic scatter $0.37^{+0.02}_{-0.02}$ dex). Yet unlike the Schmidt law, the Silk-Elmegreen law does not have a clear turnover at low gas densities. This may imply that gas density (the main driving factor in the star formation law) may not be the most important (or only) driver of star formation across different galaxy types. However, we note that many of the points at low $\Sigma_{\rm gas}/\tau_{\rm dyn}$ are dwarf galaxies with lower limits in $\Sigma_{\rm gas}$, so these points may move to the right and produce a turnover at low gas densities.

We investigate this further by investigating another alternative star formation scaling law: the "extended Schmidt law" proposed by Dopita (1985) assumes that star formation is affected not only by gas density, but also by the density of existing stars. This relationship was originally formulated as

$$\Sigma_{\rm SFR} = A(\Sigma_{\rm gas})^n(\Sigma_*)^m, \tag{6.11}$$

with stellar mass surface density Σ_*. Various studies have since found different values of power law indices n and m; Dopita and Ryder (1994) initially suggested that $n = 1/3$ and $m = 5/3$. More recently, Shi et al. (2011) and Roychowdhury et al. (2017) found values near $n = 1$ and $m = 0.5$ and showed that with these indices, Equation 6.11 described a tighter correlation than the Schmidt law. Furthermore, on spatially-resolved scales, this extended Schmidt law did not exhibit a threshold and appeared to hold for low surface brightness regions.

To determine if this result still holds for our sample, we plot the relation between $\Sigma_{\rm SFR}$ and $\Sigma_{\rm gas}\Sigma_*^{0.5}$ in Figure 6.8. With a correlation coefficient of $R = 0.82$, this extended Schmidt law is a slightly stronger correlation than the global star formation law ($R = 0.80$). The linmix estimator yields a slightly sublinear slope of $0.83^{+0.05}_{-0.05}$, but the bivariate slope of 1.08 ± 0.08 is consistent with a linear slope as predicted if

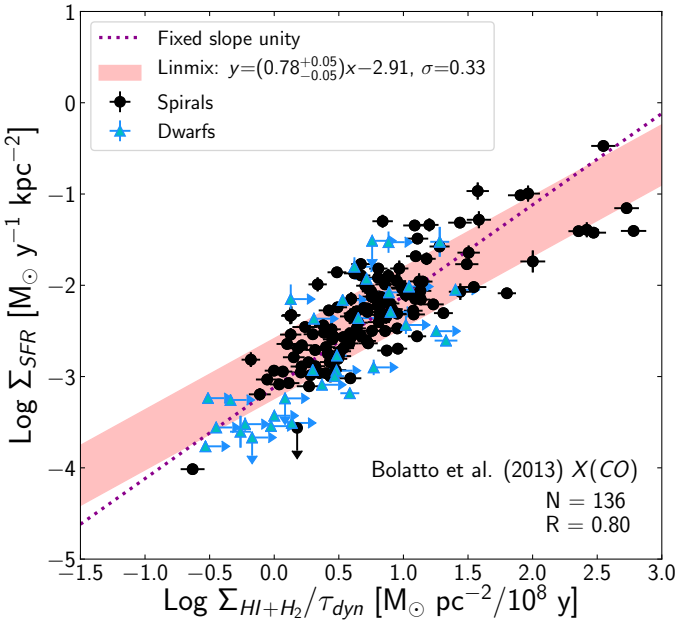

Figure 6.7: The Silk-Elmegreen relation for spirals (black circles) and dwarfs (cyan triangles), including galaxies with only HI measurements (rightward arrows) and upper limits on SFR measurements (downward arrows). The metallicity-dependent X(CO) prescription from Bolatto et al. (2013) is used. Red shaded area marks the median fit and intrinsic dispersion computed using the linmix MCMC. The dotted purple line indicates a line of slope unity.

$n = 1$ and $m = 0.5$. However, the extended Schmidt law does not appear to show a turnover at low densities, suggesting that stellar surface densities Σ_* may be an important parameter in driving star formation in low-$\Sigma_{\rm gas}$ systems. Again, we note that many of the points at the low-density end are dwarf galaxies with lower limits in $\Sigma_{\rm gas}$, so there may indeed be a low-density threshold.

We return to the importance of Σ_* later, when we discuss the physical implications of the extended Schmidt law in Section 6.7.

6.4 Second-order correlations

The updated SFRs used in this paper are more precise than those used in K98, with measurement uncertainties $\lesssim 0.1$ dex smaller than the uncertainties of $(+0.3, -0.5)$ dex assumed by K98. However, the scatter in the star formation law (Figure 6.6) is nearly identical (0.28 dex in this study, compared to 0.3 dex). This suggests that much of the dispersion in the global star formation law is likely intrinsic, an effect further exacerbated when dwarf galaxies are included. A correlation between this intrinsic dispersion and a second-order parameter may indicate a more physically "fundamen-

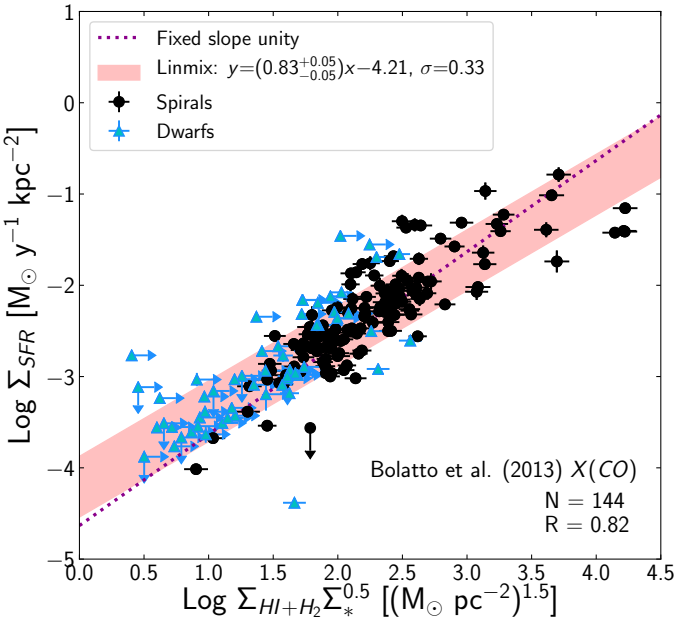

Figure 6.8: The extended Schmidt relation for spirals (black circles) and dwarfs (cyan triangles), including galaxies with only HI measurements (rightward arrows) and upper limits on SFR measurements (downward arrows). The metallicity-dependent X(CO) prescription from Bolatto et al. (2013) is used. Red shaded area marks the median linear fit and intrinsic dispersion computed using the linmix MCMC method. The dotted purple line indicates a line of slope unity.

tal" relationship. Indeed, Section 6.3.5 considers alternative star formation scaling laws that may describe the data better than the canonical star formation law. In particular, the "extended Schmidt law" suggests that gas density is not the sole driver of star formation, and that stellar density may play a role for dwarf galaxies. Other secondary parameters could have similarly important implications for the physics of star formation. We therefore present here a rudimentary test for second-order correlations in the global star formation law.

We consider the various secondary physical properties described in Section 6.2.5. Plotting the scatter in the star formation law as a function of these physical parameters is a simple way to examine which properties show second-order correlations with the star formation law. We define the scatter in the star formation law as the residuals in the law for the composite dwarf and spiral sample (Eq. 6.10):

$$\begin{aligned}\Delta \log \Sigma_{\rm SFR} &= \log \Sigma_{\rm SFR_{observed}} - \log \Sigma_{\rm SFR_{predicted}} \\ &= \log \Sigma_{\rm SFR} - (1.26 \log \Sigma_{\rm (HI+H_2)} - 3.78).\end{aligned} \tag{6.12}$$

Figure 6.9 shows plots of these residuals as functions of physical parameters, as

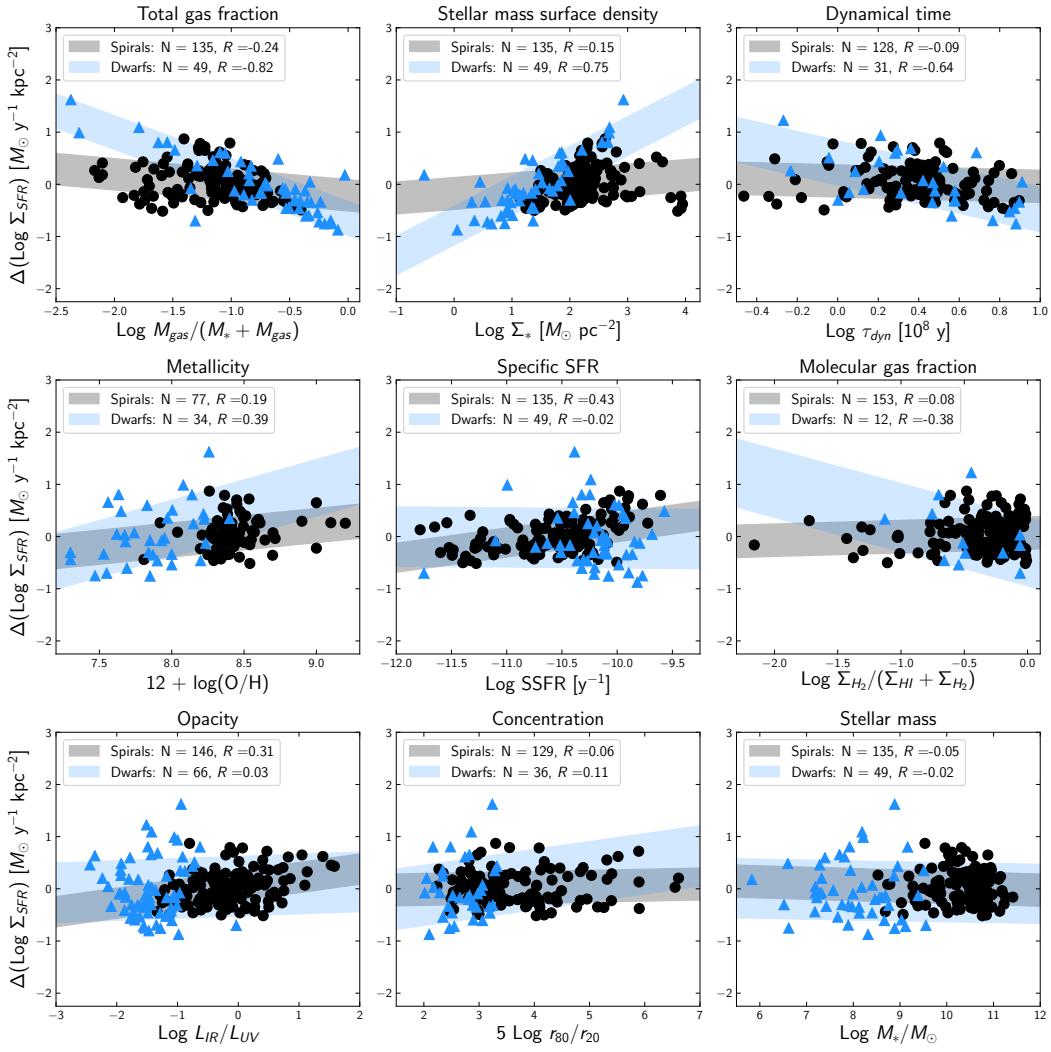

Figure 6.9: The residuals from the star formation law as a function of various physical parameters. Gray (light blue) shaded regions mark the median linear fits and intrinsic dispersions from the linmix MCMC for spiral (dwarf) galaxies, which are marked as black solid points (cyan triangles). Residuals for the dwarf galaxies are computed using just atomic gas, rather than total (atomic + molecular) gas.

well as linmix linear fits to the separate spiral and dwarf samples. Table 6.6 lists the parameters of these linear fits. Since there are so few ($N = 12$) dwarf galaxies with both HI and H_2 measurements, we note that we compute residuals for the dwarf galaxies using only atomic gas (i.e., using Σ_{HI} rather than $\Sigma_{(HI+H_2)}$ in Equation 6.12). This may be an appropriate treatment for dwarf galaxies, which are largely dominated by HI gas.

Both Figure 6.9 and Table 6.6 illustrate that for spiral galaxies (black points), the second-order correlations in the star formation law are weak at best. For example, spiral galaxies show essentially no correlation with molecular gas fraction, with a linear slope consistent with zero slope. The second-order correlations for the spiral galaxies are particularly weak when compared to the second-order correlations for dwarf galaxies. Specific SFR and L_{IR}/L_{UV} are the only parameters for which the second-order correlations for spirals are stronger than the correlations for dwarfs. Spiral galaxies with higher SSFR tend to lie above the fiducial star formation law; this is qualitatively consistent with results from the COLD GASS survey (Saintonge et al. 2011), which found that the molecular gas depletion time for typical star-forming galaxies increases with SSFR. Similarly, galaxies with higher L_{IR}/L_{UV} tend to lie above the star formation law. However, dwarf galaxies show essentially no second-order correlation with SSFR or L_{IR}/L_{UV}.

For most of the parameters, the dwarf galaxies tend to display stronger second-order correlations than spirals. Total gas fraction, stellar mass surface density, and dynamical time are perhaps the strongest examples of this phenomenon. For these parameters, spiral galaxies show only weak correlations between the second-order parameters and residuals ($R = -0.24$ for f_{gas}, $R = 0.15$ for Σ_*, and $R = -0.09$ for τ_{dyn}). Dwarf galaxies, however, show much stronger correlations ($R = 0.82$, $R = 0.75$, and $R = 0.64$, respectively). Furthermore, the linear fits to the dwarf galaxies have steeper slopes than the fits to the spiral galaxies. For example, when plotting the residuals in the star formation law as a function of total gas fraction, the linmix regression method yields a slope of -0.82 ± 0.11 for dwarf galaxies and a smaller slope of -0.20 ± 0.07 for spiral galaxies.

Table 6.6: Linear fits to residuals of star formation law.

	Spiral galaxies			Dwarf galaxies		
Parameter	m	b	σ[a]	m	b	σ[a]
Total gas fraction	$-0.20^{+0.07}_{-0.07}$	$-0.22^{+0.09}_{-0.08}$	$0.30^{+0.02}_{-0.02}$	$-0.82^{+0.09}_{-0.08}$	$-0.66^{+0.08}_{-0.08}$	$0.32^{+0.04}_{-0.03}$
Stellar mass surface density	$0.08^{+0.05}_{-0.05}$	$-0.18^{+0.11}_{-0.11}$	$0.31^{+0.02}_{-0.02}$	$0.57^{+0.07}_{-0.07}$	$-0.80^{+0.11}_{-0.11}$	$0.37^{+0.04}_{-0.04}$
Dynamical time	$-0.098^{+0.099}_{-0.100}$	$0.053^{+0.047}_{-0.045}$	$0.31^{+0.02}_{-0.02}$	$-0.9^{+0.2}_{-0.2}$	$0.41^{+0.12}_{-0.12}$	$0.43^{+0.06}_{-0.05}$
Metallicity	$0.27^{+0.17}_{-0.17}$	$-2.3^{+1.4}_{-1.5}$	$0.33^{+0.03}_{-0.03}$	$0.8^{+0.3}_{-0.3}$	-6^{+3}_{-3}	$0.54^{+0.08}_{-0.07}$
Specific SFR	$0.29^{+0.05}_{-0.05}$	$3.1^{+0.6}_{-0.6}$	$0.28^{+0.02}_{-0.02}$	$-0.02^{+0.18}_{-0.17}$	$-0.3^{+1.8}_{-1.8}$	$0.57^{+0.06}_{-0.06}$
Molecular gas fraction	$0.065^{+0.072}_{-0.073}$	$0.06^{+0.04}_{-0.04}$	$0.31^{+0.02}_{-0.02}$	$-0.7^{+0.6}_{-0.6}$	$-0.30^{+0.34}_{-0.35}$	$0.7^{+0.2}_{-0.1}$
$L_{\rm IR}/L_{\rm UV}$	$0.16^{+0.04}_{-0.04}$	$0.04^{+0.02}_{-0.02}$	$0.29^{+0.02}_{-0.02}$	$0.04^{+0.16}_{-0.16}$	$0.04^{+0.24}_{-0.24}$	$0.57^{+0.06}_{-0.05}$
Concentration	$0.02^{+0.03}_{-0.03}$	$-0.06^{+0.11}_{-0.11}$	$0.31^{+0.02}_{-0.02}$	$0.16^{+0.25}_{-0.25}$	$-0.5^{+0.7}_{-0.7}$	$0.58^{+0.08}_{-0.06}$
Stellar mass	$-0.03^{+0.04}_{-0.05}$	$0.3^{+0.5}_{-0.5}$	$0.31^{+0.02}_{-0.02}$	$-0.013^{+0.096}_{-0.100}$	$0.08^{+0.80}_{-0.78}$	$0.57^{+0.07}_{-0.05}$

[a] As noted in the text, σ is the intrinsic dispersion in the y-direction estimated by the linmix method (Section 6.3.1).

Other parameters, including metallicity and molecular gas fraction, show a similar phenomenon to a lesser extent. While the correlations between these parameters and the star formation law residuals are still weak for spiral galaxies, the correlations are only moderate for dwarf galaxies ($R = 0.39$ for metallicity and $R = 0.38$ for $f_{\rm mol}$). For molecular gas fraction, the small sample ($N = 12$) of dwarf galaxies with observed H_2 makes the correlation spurious. Finally, some parameters—concentration and stellar mass—are weakly correlated with the residuals for both spiral and dwarf galaxies, suggesting that these parameters do not drive any of the scatter in the star formation law.

Which (if any) of these second-order correlations is most physically important? That is, can any of the second-order parameters can explain the most scatter in the star formation law? To more quantitatively assess this, we compare the root-mean-square error (RMSE) of each second-order correlation with the RMSE of the fiducial star formation law (Equation 6.10) for spirals and dwarfs separately. The RMSE of the fiducial star formation law is 0.31 dex for spiral galaxies and 0.55 dex for dwarf galaxies. We compare these to the RMSE of the second-order correlations, which are estimated by convolving the fiducial star formation law with the linear fits to the residual plots listed in Table 6.6.

For example, the linear fit to the relation between metallicity and the residuals is $y = 0.27x - 2.3$ for spiral galaxies, where x is the metallicity $12 + \log[\mathrm{O/H}]$ and $y = \Delta \log \Sigma_{\rm SFR}$, defined in Equation 6.12. Combining these two equations yields the equation of a plane:

$$\log \Sigma_{\rm SFR} = 1.26 \log \Sigma_{(\rm HI+H_2)} + 0.27(12 + \log[\mathrm{O/H}]) - 6.08,$$

for which we can then compute the RMSE in $\log \Sigma_{\rm SFR}$. Repeating this procedure for spiral and dwarf galaxies for each of the parameters, we obtain the RMSEs of the second-order correlations, which are listed in Table 6.7.

Table 6.7 shows that none of the second-order parameters significantly decrease the RMSE for spiral galaxies, implying that the Schmidt law is indeed the most physically relevant star formation scaling law for spiral galaxies. However, nearly all of the second-order correlations decrease the RMSE for dwarf galaxies. In particular, total gas fraction, stellar mass surface density, and dynamical time decrease the RMSE for dwarf galaxies by $\sim 0.1 - 0.2$ dex, suggesting that these parameters may be important in driving star formation in dwarf galaxies. We further consider potential physical interpretations in Section 6.7.

Table 6.7: RMS errors in second-order correlations with star formation law.

Parameter	Spirals RMSE (dex)	Dwarfs RMSE (dex)
Total gas fraction	0.30	0.31
Stellar mass surface density	0.30	0.35
Dynamical time	0.30	0.39
Metallicity	0.32	0.50
Specific SFR	0.27	0.54
Molecular gas fraction	0.31	0.51
$L_{\rm IR}/L_{\rm UV}$	0.29	0.55
Concentration	0.31	0.54
Stellar mass	0.31	0.54
Fiducial SF law	**0.31**	**0.55**

We note that we also tried combining the spiral and dwarf galaxy samples, but the combined sample shows only weak second-order correlations with any physical parameters. None of these correlations significantly decreases the fiducial RMSE.

6.5 Systematic uncertainties

Before considering the implications of our results, we discuss the limitations of our dataset. Although our dataset represents an improvement to the sample size and measurement uncertainties in the K98 dataset, it is still subject to several systematic uncertainties. We consider some of these here.

6.5.1 SFR calibrations

Estimating star formation rates from multiwavelength tracers is subject to several systematic uncertainties. We first consider systematics which could potentially influence the overall form and slope of the star formation law, and then mention the main outstanding uncertainties in the zeropoints of the SFR calibrations and the Schmidt law itself.

As discussed in Section 6.2.3, in this work we use UV-based SFRs and correct the UV fluxes for dust using the $\sim 24m$ infrared flux. The resulting SFR estimates are vastly superior to those presented in K98. The UV fluxes average recent star formation over a much longer period than the Hα fluxes used in K98; as such, they are much less sensitive to IMF variations and are more reliable in systems with very low SFRs such as quiescent dwarf galaxies, where the IMF is not fully populated in O-type stars. In

addition, the use of 24μm fluxes to correct each individual UV measurement for dust attenuation is a major improvement over the statistical estimates applied previously. The reduction in observational uncertainties in SFRs from of order ±0.3 dex to ±0.10 dex is the main reason for the emergence of a well-defined Schmidt power law in these samples, in comparison to the scatter-dominated correlations for normal galaxies seen in K98.

Nevertheless, some uncertainties remain in these UV+IR based SFR measurements. As discussed in Hao et al. (2011) and Boquien et al. (2016), the relative weighting of UV and IR fluxes in the dust attenuation correction is dependent on the age mix in the dust-heating stellar populations, with the weighting coefficient varying by nearly a factor of two between quiescent populations dominated by older stars and the most actively forming starburst galaxies. As discussed in more detail in Paper II, however, the use of the 24μm flux in lieu of the total infrared (TIR) flux mitigates much of this variation, because more active star-forming galaxies have higher 24μm/TIR ratios, largely canceling the deficit in total infrared emission from more evolved stars. This systematic effect is probably comparable in magnitude (up to ±0.1 dex) to random errors due to differences in dust geometry, etc.

Heating of dust by non star-forming stellar populations is another systematic effect that is especially serious in massive, early-type galaxies with very low SFRs. Comparisons of SFRs derived using our simple UV+IR prescriptions with more detailed SFRs estimated from full SED population synthesis fitting show that in such systems, the empirical recipe can overestimate the UV dust attenuation correction and thus the SFRs by factors of two or more (e.g., Boquien et al. 2016; Hunt et al. 2018). This error has the potential to bias the slope of the derived star formation law, because such galaxies tend to have the lowest surface densities of gas and SFRs in the sample (lower left quadrants of Figures 6.3 and 6.4). In order to constrain the magnitude of any such bias for our sample, we replotted the SFR surface densities for the five spiral galaxies in Figure 6.3 with the lowest SFR densities and reddest stellar populations[9], assuming the extreme case of no dust attenuation. Refitting the resulting star formation law steepened the resulting power law slope by 0.04 dex (from $n = 1.41$ to 1.45). Note that this is a worst-case example, but it illustrates the need to carefully consider the dust-corrected SFRs when expanding the dynamic range of the sample to those with the lowest gas densities and SFRs.

It is also worth noting that all SFR calibrations are dependent on metallicity. Kenni-

[9]These galaxies are NGC 4698, NGC 4216, NGC 0404, NGC 1291, and NGC 5101.

cutt and Evans (2012) review the theoretical literature and find that the metallicity dependences are relatively modest for UV and IR fluxes; a factor of ten decrease in metal abundance causes roughly a $\sim 0.07 \pm 0.03$ dex increase in the FUV and IR luminosities for a fixed SFR. The effect is much larger for Hα (i.e., ionizing) fluxes, where the increase can be as much as 0.4 dex over the same range in metallicity. Most of the spiral galaxies in our sample span a relatively small range in abundance (a factor of $3 - 5$ at the extremes), and given the limited information available on abundances for many of the galaxies we have not applied any corrections. The dwarf galaxies are of course more metal-poor on average (typically factors of $3 - 10$, with a few more metal-poor objects). If we conservatively assume that all dwarf galaxies in our sample are indeed a factor of 10 more metal-poor than the spirals, we estimate that their SFRs should increase by ~ 0.07 dex relative to the spirals. This metallicity effect does not decrease the slope of the star formation law for the combined sample of dwarf and spiral galaxies.

In summary, although the new SFRs are not entirely free of systematic uncertainties, none that we are aware of are likely to bias the observed slopes of the Schmidt laws by more than 0.1 dex, comparable to the uncertainties in the fitted slopes themselves. As discussed below, we suspect that biases from uncertainties in the CO-derived molecular gas surface densities are far more important.

We conclude by mentioning sources of systematic error which probably affect all of the SFRs, and thus could bias the zeropoints of the relations. The greatest source of uncertainty by far is the form of the stellar IMF, its slope, upper stellar mass limit, and possible systematic variation with metallicity, cluster mass, or star-formation environment. Discussion of the IMF falls well beyond the scope of this study but always needs to be borne in mind. Likewise, our incomplete understanding of the role of binary stellar evolution and stellar rotation on the luminosities and lifetimes of (especially massive) stars introduce similar global uncertainties into the SFR scales. The general consistency of observed galaxy SEDs with models assuming a Kroupa (2000) or Chabrier (2003) IMF offers some reassurances, but outstanding discrepancies such as the disagreement of SFRs derived from FUV luminosities of galaxies and their resolved color-magnitude diagrams (e.g., McQuinn et al. 2015) serves as a reminder that some systematics may not yet be accounted for in existing SFR calibrations.

6.5.2 Molecular gas densities

We have already discussed the potential effects of applying a metallicity-dependent $X(\mathrm{CO})$ in some detail in Section 6.3.3, particularly focusing on how much Σ_{gas} may change for the separate spiral and dwarf samples. We found that even for spiral galaxies alone, changing from a constant Milky Way value of $X(\mathrm{CO})$ (Equation 6.7) to the metallicity-dependent Bolatto et al. (2013) $X(\mathrm{CO})$ (Equation 6.9) decreases the slope of the total gas star formation law from 1.41 to 1.29. We now consider how much these effects may change the total gas star formation law for the combined dwarf and spiral sample.

We find that changing $X(\mathrm{CO})$ from a constant Milky Way value to the metallicity-dependent Bolatto et al. (2013) prescription again decreases the overall slope of the total gas star formation law from 1.47 ± 0.08 to 1.27 ± 0.08. Note that this 0.2 difference in slopes is a conservative estimate of the effect of a metallicity-dependent $X(\mathrm{CO})$. We assume that dwarf galaxies with observed CO are representative of all dwarf galaxies, when these CO-bright dwarfs are likely to be the most strongly affected by changes in $X(\mathrm{CO})$. The effect of the Bolatto et al. (2013) $X(\mathrm{CO})$ prescription is also less extreme than other prescriptions considered in this paper (see Section 6.3.3). Even this conservative estimate implies that $X(\mathrm{CO})$ produces a systematic effect much larger than those arising from the SFR calibration.

6.5.3 Choice of diameters

The surface densities in the star formation law must be scaled by some area computed from (inclination-corrected) diameters. Nominally, these diameters represent the star-forming regions in galaxy disks, but obtaining truly representative diameters is often difficult.

K98 originally used the optical diameter, defined as the major axis of the B-band 25 mag arcsec^{-2} isophote from the second reference catalog (de Vaucouleurs et al. 1976). Other studies have used different scaling diameters, including: the diameters of UV-defined apertures (Wyder et al. 2009); the Holmberg (1958) size, defined as the B-band 26.5 mag arcsec^{-2} isophote (Roychowdhury et al. 2014); diameters computed from resolved 1.4 GHz radio continuum maps (Liu et al. 2015); and the "near-IR equivalent Holmberg" size, computed using $(B - H)$ and $(B - K)$ colors (López-Sánchez et al. 2018).

In this work, for reasons discussed in Section 6.2.2, we defined the star-forming disk as the region containing ~95% of the Hα flux. Here, we examine the possibility that

this choice of diameters may systematically bias the star formation law. This effect occurs because changing the diameter of an aperture changes the surface density Σ according to the change in flux normalized by the change in area. However, the radial surface brightness profiles of HI are generally flatter and more extended than the radial profiles of UV or CO fluxes (Leroy et al. 2008). As a result, changing the diameter can produce systematically larger changes in Σ_{SFR} and Σ_{H_2} compared to Σ_{HI}. Since the fraction of atomic gas is a function of Σ_{gas}, this can affect the slope of the star formation law.

Here, we demonstrate this effect by considering an extreme case: doubling the diameters for a subset of our galaxies increases the slope of the star formation law by ~0.2 dex. This is a particularly extreme case, especially since our sample is comprised of non-starbursting galaxies, where the star-forming regions are fairly well-defined by our chosen Hα diameters. Nonetheless this example does underscore the importance of choosing appropriate diameters when studying the star formation law. We discuss this effect in further detail in Paper II, where we consider starburst galaxies in which star formation is confined to a region much smaller than the optical disk.

6.6 Comparison with literature

The primary goal of this investigation has been to update and test the main results from the K98 study of the global star formation law, in particular for normal spiral and irregular galaxies. This is not the first reassessment of the star formation law since 1998, and although we cite previous works throughout the previous section, it is appropriate to acknowledge the key results in one place and to emphasize that many of the results presented here mainly confirm previous results by other authors.

The most comprehensive previous study of the integrated star formation law is by Liu et al. (2015). They compiled data on gas and SFR surface densities for 115 normal galaxies and 66 luminous and ultraluminous starburst galaxies. Since the main focus of that paper is on the combined star formation law for normal and starburst galaxies, we defer most of our discussion of this important study to Paper II. However some of their results on normal galaxies can be compared to ours. In particular, Liu et al. (2015) demonstrate the lack of correlation between disk-averaged SFR surface densities and HI surface densities, and a nearly linear slope of the correlation with H_2 surface densities, as presented here in Figure 6.4. They do not fit the slope of the total gas density relation separately for normal galaxies,

but their derived slope $n \sim 1.2$ for the combined sample of normal and starburst galaxies appears to be similar to our value of $n = 1.27 \pm 0.08$ for our combined sample of dwarf and spiral galaxies. An important difference in their study is that they use 1.4 GHz radio continuum maps to estimate the SFRs and (along with 24μm fluxes) to measure the SFRs and disk sizes for their sample. As discussed further in Paper II, the differences in methodology may be able to account for most of the (minor) differences between the results found in that paper and here.

Most papers on the star formation law over the past decade have focused on spatially-resolved measurements of disks, either averaged azimuthally or measured on a point-by-point basis. Although there are significant differences in detail between the results of different studies, depending on the methods used (see Kennicutt and Evans (2012) for a review), most show the same decoupling of the SFR surface density with HI and tight, roughly linear dependence on molecular gas surface density (e.g., Bigiel et al. 2008; Leroy et al. 2008; Schruba et al. 2011). Our new results are in excellent agreement with those results, in marked contrast to K98 which found a stronger correlation in disk-averaged surface densities with HI. It appears that the differences in conclusions were mainly driven by the small sample sizes in K98, a much less diverse sample of galaxies, and a large variation in X(CO) conversion factors in the K98 CO sample. In any case, this apparent discrepancy between disk-averaged and local Schmidt laws seems to have largely disappeared.

Finally we point out that until recently, a turnover or threshold in the star formation law was only seen in spatially-resolved data (e.g., Bigiel et al. 2008; Kennicutt 1989; Martin and Kennicutt 2001; Skillman et al. 1987). In particular, Leroy et al. (2008) performed a thorough analysis of this star formation threshold on local scales by examining radial profiles of the star formation efficiency $\Sigma_{\rm SFR}/\Sigma_{\rm gas}$ as a function of various parameters. On the disk-averaged scale, such a threshold was later observed by Wyder et al. (2009) for the disks of low-surface brightness spiral galaxies. More recently, Filho et al. (2016) and Roychowdhury et al. (2017) have observed a similar threshold for gas-rich dwarf galaxies. Shi et al. (2014) also observed a similar feature for a small set of regions in two metal-poor galaxies. Our new results significantly strengthen the robustness of these results.

6.7 Physical interpretations

Before discussing the potential implications of our results, we emphasize that star formation is an inherently local process. The integrated star formation law averages

over huge local variations, making it much more difficult to relate to physical processes. However, given the stochastic nature of star formation on local scales, we are better equipped to observe the star formation law in a physically meaningful way on disk-averaged scales. It is therefore worth reviewing physical interpretations that may explain our results.

6.7.1 The star formation law for spiral galaxies

We first consider the shape of the star formation law for spiral galaxies. With our updated measurements, we found that spiral galaxies alone obey a tight power law with a slope of $n = 1.41 \pm 0.07$ (assuming a constant value of $X(\mathrm{CO})$), consistent with the oft-cited K98 value of $n = 1.4 \pm 0.15$. Both values of n are conveniently close to $n = 1.5$. This has often been explained by a simplistic argument in which the SFR density scales by the gas density divided by the gravitational free-fall timescale $\tau_{\mathrm{ff}} \propto (G\rho_{\mathrm{gas}})^{-0.5}$:

$$\rho_{\mathrm{SFR}} \propto \frac{\rho_{\mathrm{gas}}}{\tau_{\mathrm{ff}}} \propto \frac{\rho_{\mathrm{gas}}}{(G\rho_{\mathrm{gas}})^{-0.5}} \propto \rho_{\mathrm{gas}}^{1.5}. \tag{6.13}$$

Assuming a constant scale height then yields a Schmidt star formation law with a power law index of $n = 1.5$.

On the other hand, the shape of the star formation law has often been explained by spatially-resolved studies as a result of the multi-phase ISM. The combination of a nearly-linear molecular gas relation and a nearly-vertical atomic gas relation (e.g., Bigiel et al. 2008; Leroy et al. 2013) yields a superlinear slope of $n = 1 - 2$ for the *total* gas star formation law. To the extent that our results agree with these studies, this could also be a viable explanation for our observed star formation law.

6.7.2 Low-density threshold

Other results from our updated investigation of the global star formation law suggest a more complex picture. In particular, a low-Σ_{gas} threshold in the star formation law appears to separate spiral galaxies from dwarf galaxies and low-surface brightness galaxies. This is expected in many theoretical frameworks, which predict different star formation regimes for these galaxies.

For example, this turnover has been observed in the star formation law within radial profiles of disk galaxies (e.g., Kennicutt 1989). Early explanations for this threshold invoked the Toomre-Q criterion for gas stability, which defines some critical density below which gas is stable against collapse, suppressing star formation. The same self-gravitational framework may also explain the threshold using differences in scale

height. In spiral galaxies, the scale height is roughly constant, so that the volumetric densities ρ in Equation 6.13 can be converted to surface densities Σ, leading to a Schmidt power law with index $n \sim 1.5$. However, in dwarf galaxies or flaring disks, the gas scale height might be inversely proportional to $\Sigma_{\rm gas}$. This leads to a Schmidt power law with $n \sim 2$, which is seen in multiple spatially-resolved studies of dwarf irregulars (e.g., Elmegreen and Hunter 2015; Ferguson et al. 1998). We are unable to check these predictions, since we cannot fit a slope in the low-$\Sigma_{\rm gas}$ regime with any certainty given the small sample size and large systematic uncertainties in this regime (Section 6.5). Observational work to account for variations in scale height by studying the volumetric star formation law (i.e., $\rho_{\rm SFR}$ vs. $\rho_{\rm gas}$) is now ongoing (Bacchini et al. 2019, K. Yim, priv. comm.).

More recent studies on local scales have considered another explanation, again suggesting that the low-density threshold may simply result from the multi-phase ISM. In this picture, the low-density turnover is a phase transition below which the ISM becomes predominantly atomic gas, producing a steep, near-vertical star formation law (e.g., Bigiel et al. 2014; Leroy et al. 2008, 2013). Both the gravitational stability and phase transition models may explain our observed low-$\Sigma_{\rm gas}$ threshold.

Various authors have also attempted to find alternative scaling laws that remove the threshold entirely. We find that one of these, the "extended Schmidt law" (Dopita 1985; Roychowdhury et al. 2017; Shi et al. 2011), is indeed a marginally better fit than the conventional Schmidt law for the combined sample of spiral and dwarf galaxies (Section 6.3.5). This law, which sets $\Sigma_{\rm SFR} \propto \Sigma_{\rm gas}\Sigma_*^{0.5}$, may physically arise from stellar feedback regulating star formation (e.g., Orr et al. 2018). In this picture, young massive stars inject pressure into the interstellar medium, so that this feedback pressure is roughly proportional to SFR density. For a system in equilibrium, this pressure must be balanced by hydrostatic pressure. The midplane hydrostatic pressure can be written as a combination of the pressure of gas in the stellar potential (proportional to $\Sigma_{\rm gas}\Sigma_*^{0.5}$) and gas self-gravity (proportional to $\Sigma_{\rm gas}^{1.5}$) (e.g., Blitz and Rosolowsky 2004; Kim et al. 2011; Kim and Ostriker 2015). The stellar potential term $\Sigma_{\rm gas}\Sigma_*^{0.5}$ becomes significant in low-$\Sigma_{\rm gas}$ systems like dwarf galaxies. The extended Schmidt law may therefore better describe low-$\Sigma_{\rm gas}$ galaxies, eliminating the low-density turnover observed in the star formation law.

6.7.3 Second-order correlations

In Section 6.4, we investigated potential second-order correlations in the star formation law. We found that spiral galaxies tended to display weak second-order correlations with other galactic properties. This is somewhat surprising, given that previous works have suggested that parameters like molecular gas fraction and stellar mass surface density should explain many of the features in the star formation law.

On the other hand, the star formation law for dwarf galaxies tended to exhibit stronger second-order correlations with other galactic parameters. To determine which of these correlations could explain the scatter in the star formation law, for each parameter X we compared the RMS error in the $\Sigma_{\rm SFR}$-$\Sigma_{\rm gas}$-X plane to the RMS error in the canonical star formation law. We note that this is not a full multivariate analysis, but it should be sufficient to discover any obvious trends. We found that for dwarf galaxies, the correlations with total gas fraction, stellar mass surface density, and dynamical time most strongly decreased the RMSE in the star formation law (Table 6.7).

The parameter that most significantly decreases the scatter in the star formation law for dwarf galaxies is total gas fraction $f_{\rm gas} = M_{\rm gas}/(M_{\rm gas} + M_*)$. The second-order correlation with $f_{\rm gas}$ suggests that at a given $\Sigma_{\rm gas}$, total gas fraction $f_{\rm gas}$ increases. Both gas mass and stellar mass are measured roughly within the same star forming region, so $f_{\rm gas} \approx \Sigma_{\rm gas}/(\Sigma_{\rm gas} + \Sigma_*)$. This means that at a given $\Sigma_{\rm gas}$, the stellar mass surface density Σ_* increases as $\Sigma_{\rm SFR}$ increases. Indeed, we do see this second-order correlation with Σ_*. Both of these may simply be a restatement of the extended Schmidt law; as discussed in the previous subsection, this may arise from a feedback-regulated model of star formation.

Alternatively, Shi et al. (2011) also point out that the extended Schmidt law may arise from the effects of metallicity. This occurs because Σ_* traces the total metal enrichment in a galaxy, which is roughly correlated with the gas-phase metallicity. We do see a second-order correlation between the residuals of the star formation law and metallicity, but metallicity appears to directly explain less of the scatter in the star formation law than other parameters (cf. Table 6.7).

The correlation with dynamical time suggests that for dwarf galaxies at a given $\Sigma_{\rm gas}$, dynamical time decreases as $\Sigma_{\rm SFR}$ increases. This may imply that global processes are particularly important for star formation in dwarf galaxies, since a shorter $\tau_{\rm dyn}$ implies more rapid global dynamical processes that induce faster SFRs. This picture

of globally-induced star formation could also explain the extended Schmidt law. Since $\tau_{\rm dyn}$ is defined as the orbital timescale at the radius of the star-forming region, it is inversely proportional to the mass interior to this radius. Decreasing the dynamical time therefore increases the mass interior to the star-forming radius; for a given $\Sigma_{\rm gas}$, this increases Σ_*, producing the dependence on Σ_* seen in the extended Schmidt law. However, it is unclear why these global dynamical processes might be more important in dwarf galaxies than in spiral galaxies.

All of these second-order correlations are potentially subject to the systematic uncertainties listed in Section 6.5, as well as uncertainties inherent in our fitting techniques and small sample of dwarf galaxies. As a result, the interpretations offered in this section are merely potential interpretations, and we strongly caution against making conclusive quantitative statements about these second-order correlations.

6.8 Summary

Twenty years after the work of Kennicutt (1998), we have revisited the global star formation law with an improved sample of local star-forming spiral and dwarf galaxies. In general, we find that the commonly-used $n \sim 1.4$ power law from K98 is still a reasonable approximation for non-starbursting galaxies. However, the physics behind the star formation law remain unclear, and we urge the reader to keep in mind that it comes with many caveats. We now summarize our major results here.

1. We have confirmed that spiral galaxies alone obey a tight correlation between gas and star formation rate surface densities (Section 6.3.1):

$$\log \Sigma_{\rm SFR} = 1.41 \log \Sigma_{\rm gas} - 3.74,$$

   where $\Sigma_{\rm gas}$ is the sum of both molecular and atomic hydrogen gas surface densities. We note that starburst galaxies are no longer necessary to define this tight star formation law, as they were in K98.

2. We found that for spiral galaxies, $\Sigma_{\rm SFR}$ is only weakly dependent on HI gas surface density but scales roughly linearly with H_2 gas surface density (Section 6.3.2). This is more consistent with what is seen in spatially-resolved studies of the star formation law.

3. We extended the star formation law to include dwarf galaxies using self-consistent measurement techniques. Although H_2 surface densities are heavily dependent on the X(CO) conversion factor, we found that dwarf galaxies tend

to fall below the star formation law for spirals, producing a turnover in the law at low $\Sigma_{\rm gas}$ (Section 6.3.4).

4. We also considered alternative star formation scaling laws (Section 6.3.5), including the relation between $\Sigma_{\rm SFR}$ and $\Sigma_{\rm gas}/\tau_{\rm dyn}$ (the Silk-Elmegreen relation) and the relation between $\Sigma_{\rm SFR}$ and $\Sigma_{\rm gas}\Sigma_*^{0.5}$ (the extended Schmidt law). We found that while both relations were as strongly correlated as the Schmidt star formation law, the extended Schmidt law removed much of the low-$\Sigma_{\rm gas}$ threshold.

5. We found that much of the scatter in the star formation law is intrinsic, motivating a search for second-order correlations in the star formation law (Section 6.4). We found that there are no significant second-order correlations for spiral galaxies, but that second-order correlations with total gas fraction ($\frac{M_{\rm gas}}{M_{\rm gas}+M_*}$), Σ_*, or $\tau_{\rm dyn}$ may explain much of the scatter in the star formation law for dwarf galaxies.

Again, we note that there are several systematic uncertainties that affect these results, particularly the choice of diameter of the star-forming region and the X(CO) factor (Section 6.5). These uncertainties should be borne in mind when interpreting our results; we offer some potential physical interpretations nonetheless (Section 6.7). We extend this work to revisit local circumnuclear starburst galaxies in Paper II (Kennicutt and de los Reyes 2021). Other future work could more carefully consider the systematic effects discussed in this work, as well as revisit the simple statistical analysis used to determine second-order effects.

6.9 Appendix: Photometry procedure and corrections

6.9.1 UV and IR photometry

This appendix describes the aperture photometry methods we used to obtain UV and IR fluxes for galaxies without available literature data. The photometry procedures are similar to those described in Lee et al. (2011) and Dale et al. (2009) for UV and IR imaging, respectively, of galaxies in the Local Volume Legacy. As discussed in the text, we measured fluxes within elliptical apertures containing ~95% of the Hα flux.

Contaminant removal. We first masked potential contaminants such as foreground stars and background galaxies. We used the `irafstarfind`[10] function from the

[10] `http://photutils.readthedocs.io/en/v0.2/api/photutils.irafstarfind.html`

Python package photutils (now an affiliated package of the Astropy library; see Robitaille et al. 2013) to identify all point sources. For UV images, any sources with $(m_{\rm FUV} - m_{\rm NUV}) > 1$ were masked as foreground Galactic stars. These preliminary masks were then inspected by eye and compared against optical images from the Hubble Legacy Archive and the Sloan Digital Sky Survey. For the Spitzer *MIPS* and AllWISE mid-IR images, we masked obvious diffraction spikes and background galaxies identified in the archival optical images. The masked pixels were linearly interpolated from the surrounding pixels, a negligible correction: the average percent difference between corrected and uncorrected flux was $\sim 0.01\%$ for *GALEX* UV photometry, $\sim 0.11\%$ for mid-IR photometry using AllWISE images, and $\sim 0.28\%$ for mid-IR photometry using Spitzer *MIPS* images.

Background subtraction. Constant backgrounds were already subtracted from the mid-IR Spitzer *MIPS* images during pre-processing. For the *GALEX* UV images and mid-IR images from ALLWISE, the sky background level was calculated using an image completely masked of all objects in the field, including the target galaxy. A circular annulus centered around the location of the target galaxy was divided into 100 equal-area regions. The annulus had a typical inner radius of $2R_{25}$ (except in rare cases where this radius extended outside of the *GALEX* field of view; in these cases, the galaxy's emission often appeared sufficiently compact such that a smaller inner radius of $1.25R_{25}$ could be safely used) and an outer radius 75 arcsec beyond the inner radius. Here R_{25} is the semimajor axis of the B-band 25 mag arcsec^{-2} isophote ($R_{25} = D_{25}/2$). From the equal-area subregions of the annulus, we computed the average sky background and standard deviation per pixel. We subtracted this constant sky background from the contaminant-masked image to produce the final image.

Aperture photometry. We then defined an elliptical aperture with a semimajor axis a given by the diameter of the Hα-defined star-forming region. Both the axis ratio b/a and the position angle θ of the ellipse were determined from RC3. Each aperture was inspected by eye; the final semimajor axes and position angle are listed in Table 6.1. Finally, the photutils Python package `aperture_photometry` was used to sum the intensity units within the elliptical aperture, resulting in the sum $C_{\rm sky-subtracted}$.

For *GALEX* UV images, the intensity units are given by counts/s. Measurement uncertainty (in counts/s) is given by

$$\sigma = \sqrt{(\sqrt{C_{\rm sky-subtracted}})^2 + n(\sigma_{\rm sky})^2}. \tag{6.14}$$

Here, the first term represents the Poisson counting error, while the second term is the uncertainty in sky background; n is the number of pixels within the aperture and σ_{sky} is the measured standard deviation of the sky per pixel. Finally, both $C_{\rm sky-subtracted}$ and σ were then converted to an AB magnitude and error (Oke 1990) according to the *GALEX* prescription:

$$m_{\rm FUV} = -2.5 \times \log_{10}(C_{\rm sky-subtracted}) + 18.82.$$

Following the procedure of Lee et al. (2011), this magnitude was then corrected for Galactic extinction using the following formula:

$$m_{\rm FUV,corrected} = m_{\rm FUV,measured} - A_{\rm FUV}$$

where $A_{\rm FUV} = 7.9E(B-V)$, assuming a total-to-selective extinction ratio of $R_V = 3.1$ (Cardelli et al. 1989). The reddening $E(B-V)$, which is reported in Table 6.1, was given by the dust maps of Schlegel et al. (1998). The only exception is IC 0010, which is located close to the Galactic plane where Schlegel et al. (1998) values become unreliable; for this galaxy, we adopt the independently measured value of $E(B-V) = 0.77 \pm 0.07$ from Richer et al. (2001).

The total UV photometric uncertainty is the sum in quadrature of: the measurement uncertainty (Eq. 6.14), the uncertainty in $E(B-V)$, and the absolute calibration uncertainty in FUV (0.05 mag) or NUV (0.03 mag) for *GALEX* (Hao et al. 2011).

For Spitzer *MIPS* images, which have intensity units of MJy/sr, total photometric uncertainty (in MJy/sr) is given by

$$\sigma = \sqrt{(\sqrt{C_{\rm sky-subtracted}})^2 + (\sigma_{\rm calibration})^2}.$$

Again, the first term represents Poisson counting error. Since the images are already background-subtracted, the second term $\sigma_{\rm calibration}$ is simply the 4% *MIPS* calibration uncertainty at 24 μm (see, e.g., Engelbracht et al. 2007). Using the pixel resolution of 24 μm *MIPS* images (1.5"), $C_{\rm sky-subtracted}$ and σ were converted from MJy/sr to Jy/pixel, then multiplied by the number of pixels within the aperture n to get total aperture flux and uncertainty in Jy.

For AllWISE images, which have intensity units of digital numbers (DN), the 1σ uncertainty in DN is given in the AllWISE Explanatory Supplement as:

$$\sigma = \sqrt{F_{\rm corr}\left(\sum_i^n \sigma_i^2 + \frac{n^2}{n_{\rm annulus}}\sigma_{sky}^2\right)}.$$

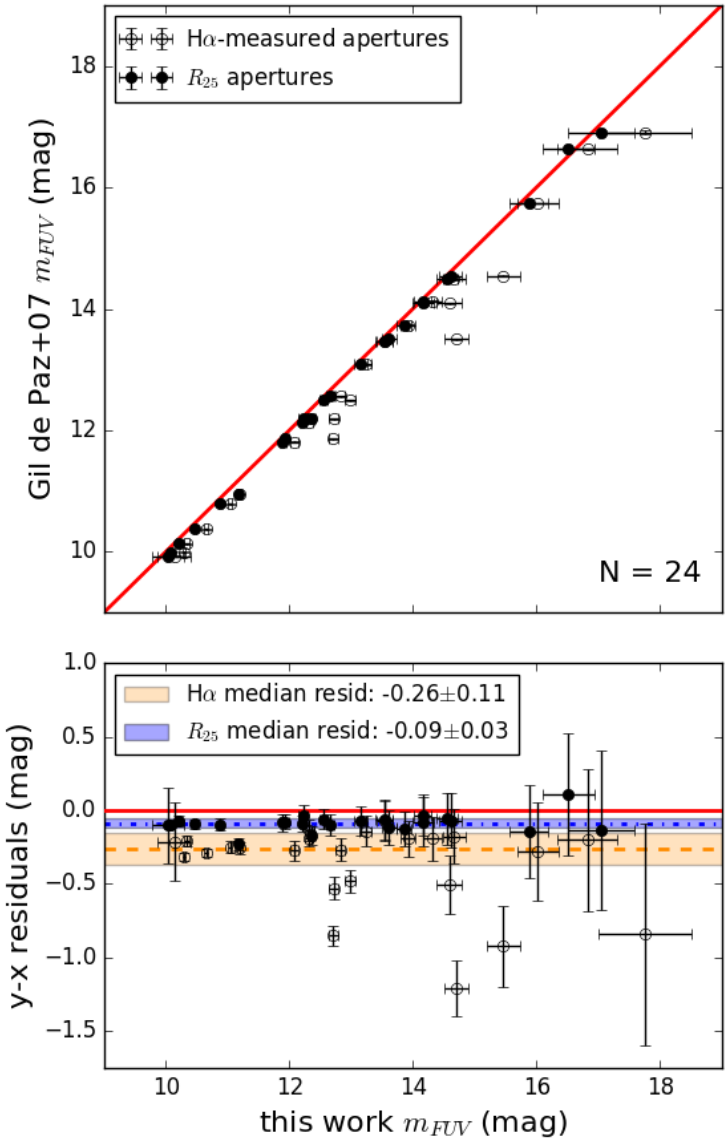

Figure 6.10: Comparison between our measured FUV fluxes and the FUV fluxes reported in Gil de Paz et al. (2007). The empty points denote our measurements using Hα-based apertures, while the filled points denote our measurements using R_{25}-based apertures. (Top) Direct comparison, with the 1-1 line shown in solid red. (Bottom) The $y - x$ residuals, with zero as a solid red line. The median difference between our Hα-aperture (R_{25}-aperture) measurements and the Gil de Paz et al. (2007) fluxes is denoted by a dot-dashed orange (dashed blue) line; the orange (blue) shaded region marks ±1 median absolute deviation.

Here, $F_{\rm corr}$ is the correlated noise correction factor for flux variance, given by $F_{\rm corr} \sim 391.392$ for the 22 μm W4 band. The term $\sum_i^n \sigma_i^2$ is the sum of flux uncertainties (given by the uncertainty map) for all pixels within the aperture. The number of pixels within the source aperture and the number of pixels within the background annulus are denoted by n and $n_{\rm annulus}$, respectively. Since the local galaxies in the sample are largely bright and extended sources, we assumed any confusion noise from faint and unresolved sources is negligible. Finally, both $C_{\rm sky-subtracted}$ and σ could be converted from units of DN to Jy using calibration constants listed in the AllWISE Explanatory Supplement:

$$F\ (\mathrm{Jy}) = (5.2269 \times 10^{-5}) C_{\rm sky-subtracted}$$
$$\sigma_F\ (\mathrm{Jy}) = (5.2269 \times 10^{-5}) \sqrt{(3.4622 \times 10^{-4}) C^2_{\rm sky-subtracted} + \sigma^2}.$$

6.9.2 Photometry systematics and corrections

To ensure that our photometric flux measurements are consistent with existing catalogs, we compared against catalog fluxes.

As Figure 6.10 shows, the FUV fluxes we measured within Hα-defined star forming regions (empty points) were consistently smaller than the catalog fluxes. This discrepancy decreases significantly when the photometry is repeated using apertures with larger semi-major axes determined by R_{25} (filled points). This suggests that the discrepancy is due to systematic differences in aperture size, since most catalogs report estimates of total fluxes rather than aperture fluxes. Figure 6.10 only shows the comparison with Gil de Paz et al. (2007) UV fluxes, but a similar effect occurs for the other UV catalogs.

To account for these systematic effects in the UV, we applied a statistical correction to the catalog FUV fluxes, determined from the median difference between our measured fluxes (using Hα-based apertures) and the fluxes from each catalog. For example, the Gil de Paz et al. (2007) UV fluxes are brighter than our measured fluxes by a median difference of 0.26 ± 0.11 mag; we therefore divided all Gil de Paz et al. (2007) UV fluxes by a corresponding factor of $f_{\rm corr} = 1.27 \pm 0.13$. The dispersion $\sigma_{\rm corr} = 0.13$ was added in quadrature with the photometric uncertainty to produce the final flux uncertainties.

A similar aperture effect occurs with the IR photometric fluxes. Furthermore, the mid-IR fluxes were not all measured at the same wavelengths: Spitzer *MIPS* measures fluxes at 24 μm, while *IRAS* measures fluxes at 25 μm and *WISE* measures 22 μm.

Table 6.8: Aperture correction factors for UV and IR catalogs.

UV catalogs	
Catalog	$f_{\rm corr}$
Gil de Paz et al. (2007)	1.27 ± 0.13
LVL, using IR-matched apertures (Lee et al. 2011)	1.36 ± 0.15
SINGS (Dale et al. 2007)	1.31 ± 0.17
LVL, using "outermost elliptical annulus" apertures (Lee et al. 2011)	1.49 ± 0.29
Bai et al. (2015)	1.14 ± 0.12
Virgo Cluster Survey (Voyer et al. 2014)	0.98 ± 0.07
Herschel Reference Survey (Cortese et al. 2012)	0.94 ± 0.10
IR catalogs	
Catalog	$f_{\rm corr}$
LVL (Dale et al. 2009)	1.08 ± 0.07
SINGS (Dale et al. 2007)	1.07 ± 0.07
Gil de Paz et al. (2007)	1.10 ± 0.20
MIPS LG (Bendo et al. 2012)	1.11 ± 0.08
IRAS BGS (Sanders et al. 2003)	1.19 ± 0.25
AllWISE measurements	1.07 ± 0.08

We therefore compute similar statistical corrections to calibrate all IR catalogs to agree with the fluxes measured from Spitzer *MIPS* images.

Finally, the IR fluxes we measured from AllWISE images were also higher than the fluxes we measured from Spitzer *MIPS* images, although the the same apertures were used for both. This discrepancy may again be due to the effects of different wavelengths (Spitzer *MIPS* at 24 μm, AllWISE at 22 μm). It may also result from different background subtraction techniques. The Spitzer *MIPS* images used for photometry were obtained from the SINGS, LVL, and *MIPS* LG surveys, which each used some form of polynomial fitting to estimate background[11]. For the AllWISE images, on the other hand, only a constant average background value was subtracted. The polynomial fitting used on the *MIPS* images likely produced higher interpolated background values at the locations of the target galaxies, producing the discrepancy between *MIPS* and AllWISE fluxes. Using the median difference between the *MIPS* and AllWISE fluxes, we applied another statistical correction to the AllWISE fluxes to account for this discrepancy.

[11]See SINGS documentation at `http://irsa.ipac.caltech.edu/data/SPITZER/SINGS/doc/sings\_fifth\_delivery\_v2.pdf`, LVL documentation at `http://irsa.ipac.caltech.edu/data/SPITZER/LVL/LVL\_DR5\_v5.pdf`, and *MIPS* LG documentation in Bendo et al. (2012).

The final correction factors for all UV and IR catalogs are listed in Table 6.8. Tables 6.2 and 6.3 list the final aperture-corrected UV and IR fluxes that are used in this work.

6.10 Appendix: References for gas surface densities

We list the references for Table 6.4 here. The numbering scheme largely follows a convention: references 1-21 contain both HI and H_2 data, references 101-157 contain primarily HI data, and references 201-241 contain primarily H_2 data.

1: Young et al. (1996); 2: Young et al. (1995); 3: Dame et al. (1993); 4: Sage (1993); 5: Fisher et al. (2013); 6: Warmels (1985); 7: Wevers et al. (1986); 8: Rhee and van Albada (1996); 9: van der Kruit and Shostak (1984); 10: Broeils and Rhee (1997); 11: van Moorsel (1983); 12: Bosma (1978); 13: Broeils and van Woerden (1994); 14: Mulder et al. (1995); 15: Casertano and van Gorkom (1991); 16: Knapen (1997); 17: van der Kruit and Shostak (1982); 18: Braun et al. (1994); 19: Rogstad et al. (1974); 20: Bosma et al. (1981); 21: Rogstad et al. (1973)

101: Leroy et al. (2008); 102: Corbelli et al. (2010); 103: Chung et al. (2009); 104: Combes et al. (1977); 105: Puche et al. (1991); 106: van der Hulst et al. (2001); 107: van Driel et al. (1988); 108: Nordgren et al. (1998); 109: Jorsater and van Moorsel (1995); 110: Ryder et al. (1996); 111: Kilborn et al. (2005); 112: Taramopoulos et al. (2001); 113: Jore (1997); 114: Verheijen and Sancisi (2001); 115: van der Hulst (1979); 116: Braine et al. (1993a); 117: Warmels (1988); 118: Huchtmeier and Richter (1989); 119: Sancisi et al. (1979); 120: Laine and Gottesman (1998); 121: Liszt and Dickey (1995); 122: Irwin and Seaquist (1991); 123: Swaters et al. (2002); 124: Schwarz (1985); 125: Noordermeer et al. (2005); 126: Stil and Israel (2002); 127: Hunter et al. (2012); 128: Hunter et al. (1999); 129: Bush and Wilcots (2004); 130: Crosthwaite et al. (2001); 131: Thuan et al. (2004); 132: Wilcots and Miller (1998); 133: Lelli et al. (2014); 134: Carignan and Beaulieu (1989); 135: Peters et al. (1994); 136: Ryder et al. (1995); 137: van Zee et al. (1998); 138: Taylor et al. (1995); 139: del Rio et al. (2004); 140: Hunter et al. (1994); 141: Bosma et al. (1980); 142: Meurer et al. (1996); 143: Begum et al. (2008b); 144: de Blok and Walter (2006); 145: van Zee et al. (2001); 146: van Zee et al. (1997); 147: de Blok et al. (1996); 148: Carignan et al. (1988); 149: Begum et al. (2008a); 150: van Zee et al. (1996); 151: Walter et al. (2008); 152: Walter et al. (1997); 153: Teich et al. (2016); 154: Ott et al. (2012); 155: van der Hulst and Huchtmeier (1979); 156: Cote et al. (1991); 157: Shostak (1973)

201: Nieten et al. (2006); 202: Sorai et al. (2000); 203: Hogg et al. (2001); 204: Sandqvist et al. (1988); 205: Bajaja et al. (1995); 206: Li et al. (1993); 207: Solomon and Sage (1988); 208: Braine et al. (1997); 209: Wiklind and Henkel (1989); 210: Leon et al. (1997); 211: Sheth et al. (2000); 212: Stark et al. (1987); 213: Verter (1987); 214: Komugi et al. (2008); 215: Leroy et al. (2013); 216: Leroy et al. (2005); 217: Tacconi et al. (1991); 218: Braine et al. (1993b); 219: Kobulnicky et al. (1995); 220: Boselli et al. (2014); 221: Wiklind and Henkel (1990); 222: Schruba et al. (2012); 223: Hunter et al. (2000); 224: Young et al. (2011); 225: Schruba et al. (2011); 226: Taylor et al. (2015); 227: Warren et al. (2015); 228: Kuno et al. (2007); 229: Thronson Jr. et al. (1989); 230: Leroy et al. (2006); 231: Leroy et al. (2007); 232: Hunt et al. (2015); 233: Sage et al. (1992); 234: Taylor et al. (1998); 235: Cormier et al. (2014); 236: Meier et al. (2002); 237: Israel (2005); 238: Turner et al. (1997); 239: Komugi et al. (2011); 240: Barone et al. (2000); 241: Kepley et al. (2016)

Chapter 7

LOOKING FORWARD

In this thesis, I have presented a number of observational studies examining local dwarf galaxies across a range of spatial scales. With resolved stellar spectroscopy of Local Group dSph galaxies, I have used the abundances of *individual stars* to probe the physics of Type Ia supernovae (Chapters 2 and 3) and to trace the chemical evolution and star formation of a galaxy (Chapter 4). I have used integral field spectroscopy to produce *spatially-resolved maps* of stellar kinematics, which can be used to test galaxy formation scenarios (Chapter 5). Finally, on the largest spatial scales, I have used *global* photometric measurements to probe the galaxy-wide processes that drive star formation (Chapter 6). Although these studies use different observational techniques and address different astrophysical questions, they all illustrate how dwarf galaxies in the nearby universe can be used as "laboratories" to understand stellar and galactic evolution.

In this final chapter, I will summarize my primary results (Section 7.1) and discuss potential next steps for these projects (Section 7.2). I will end with a broader view in Section 7.3 by describing the upcoming and ongoing surveys that have begun to map the local universe in unprecedented detail, which will contribute significantly to our understanding of dwarf galaxies in the local universe.

7.1 Summary

The main results of this thesis are as follows:

1. I have used galactic archaeology to provide unique observational constraints on Type Ia supernovae in dwarf galaxies:

    - Manganese abundances indicate that sub-Chandrasekhar ($\lesssim 1 M_{\odot}$) white dwarf progenitors are the dominant Type Ia supernova channel in Sculptor dSph, although some fraction ($\sim 20\%$) of near-$M_{\rm Ch}$ supernovae (or peculiar Type Iax supernovae) are needed to reproduce the observed manganese yield (Chapter 2; de los Reyes et al. 2020).
    - Dwarf galaxies with extended star formation histories (Leo II, Fornax dSphs) appear to have systematically higher manganese abundances than

galaxies with early bursts of star formation (Sculptor dSph). This suggests that the dominant channel of Type Ia supernovae transitions from sub-$M_{\rm Ch}$ to near-$M_{\rm Ch}$ at later times in a galaxy's chemical evolution (Chapter 2; de los Reyes et al. 2020).

- I have presented a new method for measuring the delay-time distribution of Type Ia supernovae within individual dSph galaxies using stellar abundances. This method indicates that the Type Ia DTD is not universal among dSphs, and that it may be a function of galaxy properties (Chapter 3).

2. I have developed a simple chemical evolution model that uses a wide range of elemental abundances to put precise constraints on the star formation histories of dwarf galaxies. This spectroscopic approach provides a complementary approach to photometric SFH measurements, which may have difficulty resolving age spreads in old and metal-poor stellar populations. I tested this model on Sculptor dSph, showing that this galaxy had a much shorter duration of star formation than previously thought (Chapter 4; de los Reyes et al. 2022).

3. I have led an observational program to measure the spatially-resolved properties of dwarf galaxies in cosmic voids. Preliminary results indicate that void dwarf galaxies appear to be dispersion-supported, suggesting that isolated galaxies with stellar masses $< 10^8\ M_\odot$ form as "puffy" systems rather than disks (Chapter 5).

4. I have remeasured the global star formation law in local non-starbursting galaxies. With updated multi-wavelength measurements, I have shown that spiral galaxies alone define a tight star formation law consistent with the commonly used power-law prescription $\Sigma_{\rm SFR} \propto (\Sigma_{\rm gas})^{1.4}$. Dwarf galaxies, however, tend to fall below this relation, producing a turnover in the star formation law at low $\Sigma_{\rm gas}$. This "turnover" in the law may be physically explained by second-order correlations with other properties (total gas fraction, stellar mass surface density, or dynamical time), suggesting star formation in these dwarf galaxies may be driven by global processes other than the simple gravitational collapse of available gas (Chapter 6; de los Reyes and Kennicutt 2019).

7.2 Next steps

In this section, I discuss some of the potential directions for future work on the research questions addressed in this thesis.

7.2.1 Type Ia supernovae

My measurements of Type Ia manganese yields (Chapter 2) and delay-time distributions (Chapter 3) indicate that the dominant physical channel of Type Ia SNe may depend on the properties of the host galaxy. However, these measurements have so far been limited to only a few dwarf spheroidal galaxies. With additional observations of stellar abundances in the Local Group, the architecture is in place to study Type Ia SNe in a wider range of Local Group dwarf galaxies.

For example, Kirby et al. (2019) and de los Reyes et al. (2020) found indications of a transition from sub-$M_{\rm Ch}$ to near-$M_{\rm Ch}$ over time in dSphs. Additional measurements of manganese abundances in other galaxies would be useful for confirming the existence of such a transition, as well as identifying whether this transition is abrupt or gradual as a function of galaxy properties (like stellar mass or the duration of the SFH). Better understanding this transition would provide additional constraints on theoretical Type Ia models: for instance, an abrupt transition as a function of stellar mass (such that near-$M_{\rm Ch}$ Type Ia SNe only dominate in dSphs above a certain stellar mass) may suggest a minimum mass (or metallicity) below which white dwarfs are unable to accrete mass at the appropriate rates to produce a supernova. A more gradual transition from sub-$M_{\rm Ch}$ to near-$M_{\rm Ch}$ as a function of galaxy stellar mass, on the other hand, may indicate a mass (or metallicity) dependence without a hard cutoff.

Alternatively, sub-$M_{\rm Ch}$ and near-$M_{\rm Ch}$ Type Ia supernovae may have different delay-time distributions; for example, near-$M_{\rm Ch}$ SNe may simply be more delayed than sub-$M_{\rm Ch}$ SNe. While the pilot study in Chapter 3 hints at a potential transition from single- to double-degenerate Type Ia SNe, more precise SFHs and abundance data for more dSphs are needed to confirm this. More data are also needed to determine whether there is a correlation between the mass of the white dwarf progenitor and the number of white dwarfs involved in the explosion—that is, whether the sub-$M_{\rm Ch}$ to near-$M_{\rm Ch}$ transition is related to a transition between single- and double-degenerate channels (if such a transition exists). The existence of such a correlation would provide even more stringent constraints on theoretical Type Ia models.

7.2.2 Galactic chemical evolution

The galactic chemical evolution model discussed in Chapter 4 was originally designed for Local Group dSph galaxies, but may be extended to other types of galaxies in order to address other astrophysical questions.

Ultra-faint dwarf galaxies as a probe of reionization: The reionization of the universe left an indelible imprint on galaxy formation and evolution. Due to their small gravitational potential wells, ultra-faint dwarf galaxies (UFDs) are perhaps the environments most sensitive to reionization. Simulations indicate that reionization could have permanently halted star formation in these low-mass galaxies (e.g., Wheeler et al. 2019); photometric measurements also suggest that the star formation of local UFDs shut down within a short duration ($\sim$ 0.5 Gyr; Brown et al. 2012, 2014), as might be expected from a global event like reionization. However, these UFDs are relatively old and metal-poor, so photometric measurements of their star formation histories have poor time resolution. My galactic chemical evolution model may be able to identify the shape of the UFD SFHs (which may show whether star formation was truncated rapidly, as might be expected from reionization) and the duration of the UFD SFHs (which may place an upper limit on the amount of time between the formation of the first galaxies and reionization—in other words, an upper limit on the redshift of reionization).

Accreted dwarf galaxies and environmental quenching: The halo of stars around the Milky Way contains the shredded remnants of dwarf galaxies that have been accreted onto our galaxy (e.g., Bell et al. 2008). Recent surveys such as Gaia and APOGEE have dramatically increased the number of accreted dwarf galaxies that have been identified in the halo, such as the "Gaia-Enceladus-Sausage" (Belokurov et al. 2018; Helmi et al. 2018) system. The SFHs of these accreted systems can help us understand how environmental effects may quench star formation in satellite galaxies. For example, recent simulations indicate that low-mass satellite galaxies may quench even before their first pericentric passage by a host galaxy, while higher-mass satellites may retain their gas after one or more pericentric passages (Samuel et al. 2022). By measuring the SFHs of accreted dwarf galaxies, my galactic chemical evolution model would help show whether these accreted dwarfs were quenched before, during, or after their merger with the Milky Way, and whether this quenching time was affected by properties like stellar mass.

7.2.3 Void dwarf galaxies

The IFU dataset described in Chapter 5 can be used to measure spatially-resolved properties of void dwarf galaxies other than stellar kinematics. Spatially-resolved gas-phase metallicities, in particular, can be used to test predictions about the evolution of these galaxies.

As discussed in Chapter 5, the low densities of cosmic voids are thought to inhibit galaxy evolution (Goldberg and Vogeley 2004). If this is true, then one might expect to see a difference in the relationship between stellar mass and gas-phase metallicity (the "mass–metallicity relation"; Tremonti et al. 2004) for galaxies inside and outside voids. Since galaxies build up higher gas-phase metallicities as they evolve over time (making the normalization of the mass–metallicity relation a strong function of redshift, e.g., Zahid et al. 2013), dwarf galaxies in voids should have systematically lower metallicities than dwarf galaxies of the same mass in filaments.

Previous studies of the mass-metallicity relation in cosmic voids have been inconclusive. Some studies (Douglass and Vogeley 2017; Douglass et al. 2018; Kreckel et al. 2014; Wegner et al. 2019) have observed no significant differences between these populations, while others (Filho et al. 2015; Kniazev et al. 2018; Pilyugin et al. 2017; Pustilnik et al. 2016, 2011) claim that void dwarfs are more metal-poor than field dwarfs by up to 0.3 dex. These studies all used gas-phase metallicities measured either from long-slit spectra of individual HII regions, or from fiber spectra. Both methods may be subject to significant aperture effects caused by sampling only a fraction of galaxies' full spatial extents (Kewley et al. 2005). My IFU dataset would avoid these aperture effects, since I can obtain integrated gas-phase metallicity across the entire spatial range of a void dwarf galaxy.

My IFU data can also be used to measure spatially-resolved properties within void dwarf galaxies. These can help answer other questions about galaxy evolution: for example, some local (non-void) dwarf galaxies have been shown to have spatial inhomogeneities in metallicity—regions that are particularly metal-poor relative to the rest of the galaxy (Lagos et al. 2018; Sánchez Almeida et al. 2015). These ~ 0.3 dex inhomogeneities have been interpreted as signs of "cold flow" accretion of pristine gas from the cosmic web, but Sánchez Almeida et al. (2015) note that they could also be due to environmental effects like minor mergers or tidally-induced mixing. Disentangling these environmental effects will be much easier in voids, since void dwarf galaxies are significantly more isolated than field galaxies.

7.2.4 Star formation laws

Chapter 6 found that dwarf galaxies (low-metallicity, low-Σ_{gas} systems) may fall below the global star formation law defined by nearby spiral galaxies. It is possible that this discrepancy is related to the formulation of the star formation law itself—Bacchini et al. (2020) have recently found that a star formation law based on *volumetric* densities (rather than surface densities) may be a more physical way to describe star formation in both dwarf and spiral galaxies. However, the sample of local dwarf galaxies with resolved CO measurements (and therefore with reliable measurements of H_2 gas mass) is relatively small. Furthermore, the $X(\mathrm{CO})$ conversion factor is not well-measured for low-metallicity systems like dwarf galaxies, leading to large systematic errors in either volumetric or surface gas density measurements.

Progress in the dwarf galaxy regime therefore requires improvements in tracing H_2 gas—either by improving calibrations of $X(\mathrm{CO})$, especially as a function of metallicity, or by using entirely different observational tracers. In particular, recent work has found that [CII], a dominant cooling line for several phases of the ISM (particularly dense photodissociation regions), may be a more useful tracer of H_2 gas than CO (e.g., Madden et al. 2020). Detailed observations of [CII] can also be used in conjunction with resolved CO maps to re-calibrate $X(\mathrm{CO})$ measurements (e.g., Bigiel et al. 2020). These advances should provide a path forward for future tests of star formation processes in dwarf galaxies.

There are also opportunities to extend the global star formation law to other classes of galaxies. Of particular interest are starburst galaxies, which represent the high-Σ_{gas} and high-Σ_{SFR} regime. Kennicutt and de los Reyes (2021) recently showed that starburst galaxies (luminous and ultra-luminous infrared galaxies) may be systematically offset to higher Σ_{SFR} relative to non-starbursting spiral galaxies, potentially confirming the existence of a "bimodal" star formation law (e.g., Daddi et al. 2010; Genzel et al. 2010). Again, these measurements are also particularly sensitive to systematic uncertainties in the $X(\mathrm{CO})$ conversion factor at high Σ_{gas} (Bolatto et al. 2013). Ongoing work (Kennicutt & de los Reyes, in prep.) will address this by using dust mass as an independent measure of gas mass.

7.3 Upcoming prospects for studying dwarf galaxies in the local universe

In recent years, significant attention in galaxy science has been directed towards our own Milky Way (supported by surveys such as Gaia) and towards high-redshift

galaxies (particularly with the advent of JWST). Dwarf galaxies in the local universe provide a complementary approach to studying galaxy formation and evolution.

Over the next few years, ongoing and upcoming surveys will map out our local universe in unprecedented detail. With the greater spectral and spatial resolutions, deeper surface brightness limits, and larger fields of view afforded by these surveys, the next decade promises to be an exciting era for the low-mass end of galaxy studies. Here I describe some of these surveys, primarily focusing on spectroscopic and IFU surveys, and their potential for advancing dwarf galaxy science.

7.3.1 Subaru PFS

The Subaru Prime Focus Spectrograph (PFS; Takada et al. 2014) is a massively-multiplexed optical and near-infrared spectrograph scheduled to begin taking data in 2023.[1] Capable of simultaneously obtaining 2400 fiber spectra with wavelength range $\Delta\lambda = 380 - 1260$ nm within a 1.3° diameter hexagonal field, PFS will have approximately 100 nights focused on its galactic archaeology program. This program primarily uses the medium-resolution mode of the red arm of PFS, which will aim to obtain spectra of $\sim 10^5$ stars with a spectral resolution of $R = 5000$ over $\Delta\lambda = 710 - 885$ nm. This wavelength range includes CaT and α-element lines, allowing PFS to measure [Fe/H], [α/Fe], and radial velocities for stars in the Milky Way, the M31 halo, and—most relevant to the work in this thesis—Local Group dSphs (dIrrs) down to $V = 21$ mag ($V = 22.5$ mag).

PFS' wide field of view is a particular advantage for studying Local Group dwarf galaxies. Previous samples of elemental abundances in dSphs, including the DEIMOS measurements used throughout this thesis (de los Reyes et al. 2020; Duggan et al. 2018; Kirby et al. 2009, 2010), have been primarily limited to dSphs' innermost regions. As shown in Figure 7.1, PFS will be able to obtain stellar spectra out to the tidal radii of several dSphs.

These large samples of elemental abundances will drastically improve chemical modeling of dSphs—after all, galactic chemical evolution models are only as good as their input data. Specifically, PFS measurements of [Fe/H] and [α/Fe] will help better constrain the downturn in the [α/Fe] vs. [Fe/H] plot caused by the onset of Type Ia supernovae. Improved constraints on the location of this "knee," denoted as $[\mathrm{Fe/H}]_{\mathrm{Ia}}$ in Chapter 2, would directly improve measurements of the timescale of

[1] This date is based on the publicly-released schedule last updated in June 2021, and is subject to change.

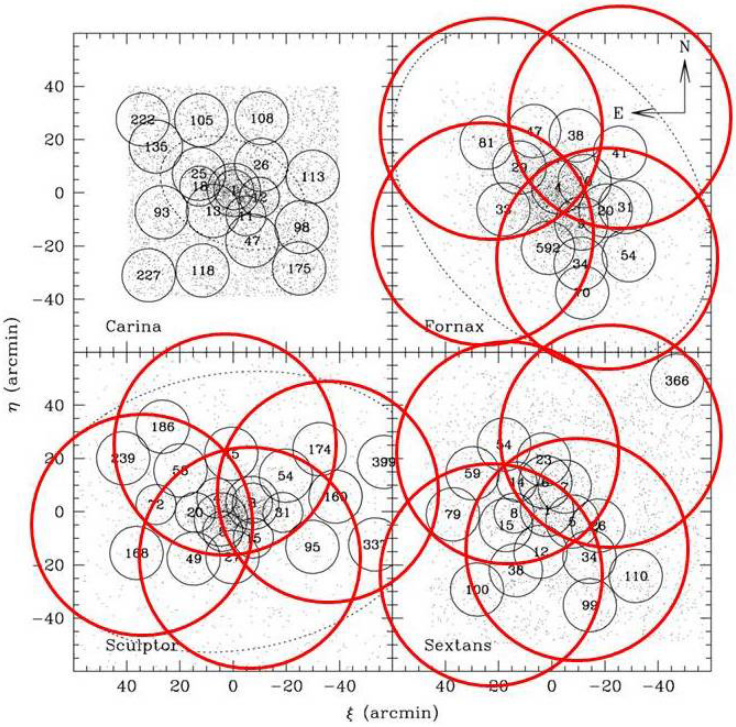

Figure 7.1: Proposed Subaru PFS pointings (red circles) for Fornax, Sculptor and Sextans dSphs. Note that these pointings extend to the tidal radii of these galaxies (dotted lines). Previous measurements were limited to the central parts (black circles, adapted by Walker et al. 2009). Figure used with permission from Takada et al. (2014).

chemical enrichment in dSphs. For example, $[Fe/H]_{Ia}$ is a direct input into the simple calculations of nucleosynthetic yields from Type Ia SNe described in Chapter 2. Abundance patterns of α elements are also key ingredients in full chemical evolution models, like the one described in Chapter 4. The large spatial extent covered by PFS spectra may add another dimension to chemical models: while Chapter 4 uses a simple one-zone model to fit abundances of stars in the innermost region of Sculptor dSph, more detailed models (multi-zone models or chemodynamical simulations) may be needed to fit the abundance patterns of the stellar populations across Sculptor's radial extent.

PFS will also be able to follow up discoveries of new ultra-faint dwarf galaxies by

Gaia and ground-based imaging surveys. Not only will these observations be able to provide spectroscopic confirmation of these new systems, they may also provide chemical abundances—as described in the previous section, chemical models of ultra-faint galaxies may provide a useful probe of the era of reionization. Finally, α abundances in dwarf galaxies can be used to probe the stellar IMF. Because the [α/Fe] "plateau" (at [Fe/H] < $[\mathrm{Fe/H}]_{\mathrm{Ia}}$) is produced by core-collapse supernovae, its value is sensitive to the masses of stars that explode as CCSNe, which is in turn dependent on the IMF. A change in the IMF slope of ~ 1 over the progenitor mass range of $10 - 100\ M_{\odot}$ would lead to a change in the [α/Fe] plateau of ~ 0.3 dex (Wyse et al. 2002), which should be observable with PFS (PFS medium-resolution spectra are expected to produce errors of order ~ 0.2 dex in [Mg/Fe], according to Takada et al. 2014).

7.3.2 Local Volume Mapper

Subaru PFS will focus on measuring stellar abundances in nearby dwarf galaxies, but other instruments will be able to study the other baryonic components of these galaxies. The Local Volume Mapper (LVM; Kollmeier et al. 2017; Konidaris et al. 2020) is an optical IFU designed to target the Milky Way, Small and Large Magellanic Clouds, and—again, most relevant to the work in this thesis—other Local Volume galaxies. In particular, it will be able to map the ISM of galaxies out to a distance of ~ 5 Mpc with a spatial resolution of $20 - 100$ pc.

The LVM's major advantage is its spatial coverage. While fiber-fed spectrographs may cover large fields of view, the actual fiber spectra may only cover a few square degrees; for example, the Subaru PFS galaxy evolution survey will cover a 16 deg^2 field of view (targeting ~ 96000 galaxies out to $z < 1$), but the actual fibers will sample $\lesssim 0.3$ deg^2 of sky. LVM, on the other hand, will cover nearly one full steradian (~ 2500 deg^2) with similar spectral coverage ($\Delta\lambda = 360 - 1000$ nm) and spectral resolution ($R \sim 4000$) as PFS. To accomplish this, it will use an integral field spectrograph design similar to that of the SDSS MaNGA (Bundy et al. 2015), which uses tightly packed bundles of optical fibers.

The goal of the LVM is to map the ISM on spatially-resolved scales across a variety of galactic environments. This will be particularly useful for star formation studies. For example, as discussed in Chapter 6, there are some discrepancies between the global star formation law (i.e., using gas and SFR surface densities integrated over galaxy-wide scales) and the spatially-resolved star formation law on kiloparsec

scales. The LVM will enable direct comparisons between ISM properties—gas-phase kinematics, abundances, and Hα-traced star formation—over a range of spatial scales. Furthermore, the global star formation law for dwarf galaxies have second-order correlations with other galaxy properties (e.g., stellar mass surface density or dynamical time), so LVM measurements will probe the dependence of star formation on the local galactic environment.

The bulk of the LVM survey footprint is focused on the midplane of the Milky Way; other than the LMC and SMC, LVM is not currently expected to target any Local Group dwarf galaxies. However, it may target more distant galaxies in the Local Volume. Such a dataset could be used to map gas-phase kinematics and abundances across dwarf galaxies, similar to the void dwarf galaxy IFU dataset described in Chapter 5. Given LVM's high spatial resolution, these would be particularly useful for directly tracing the mixing of metals produced by massive stars.

7.3.3 SAGA

Many upcoming surveys, including PFS and LVM, focus on galaxies in our local neighborhood. However, the Local Group includes a relatively small sample ($N \sim 40$) of dwarf galaxies—and these dwarf galaxies may not be representative of other $L_\star$ galaxy systems. The ongoing Satellites Around Galactic Analogs (SAGA; Geha et al. 2017) survey aims to test this by identifying 100 Milky Way analogs and their satellites $25 - 40$ Mpc away, down to the luminosity of the Leo I dwarf galaxy ($M_r < -12.3$).

For these Milky Way-like galaxies and their satellites, SAGA has released photometric object catalogs. These photometric measurements have already led to a number of interesting results: for example, SAGA DR2 (Mao et al. 2021) showed that the satellite systems of MW-like galaxies are impressively diverse in their luminosity functions and radial distributions. Low-resolution spectra of the SAGA objects, obtained primarily to measure redshifts, have also been used to measure star formation rates. This has led to the surprising discovery that SAGA satellites appear to be more star-forming than the satellite galaxies in the Local Group—and, indeed, more star-forming than expected from cosmological simulations (Dickey et al. 2021). Whether this discrepancy is real or the result of a selection effect in SAGA (as suggested by, e.g., Font et al. 2022) remains uncertain.

The next step to characterizing these systems is to measure more detailed physical properties of individual satellite galaxies around Milky Way-like galaxies using

high-quality spectroscopy. The SAGA collaboration has already obtained spatially-resolved long-slit spectra of $N \sim 50$ satellites around MW analogs and has plans to obtain an additional ~ 100 spectra over the coming year. These spectra will be invaluable for measuring a number of global and spatially-resolved properties of SAGA satellite galaxies, which could be used to address a number of scientific questions:

- **The relationship between dynamical mass (traced by stellar velocity dispersion σ_v) and stellar mass** probes the connection between dwarf galaxies and their dark matter halos. The observed σ_v-$M_\star$ relation for SAGA satellites would not only be an important test for ΛCDM simulations with baryonic physics (e.g., Garrison-Kimmel et al. 2019), but it would also serve as an empirical calibration for the abundance matching of low-mass halos and galaxies in dark-matter-only simulations (Wechsler and Tinker 2018).

- **The tight correlation between stellar mass and metallicity** (the MZR) is thought to result from metal retention: more massive galaxies have deeper potential wells and are better able to retain heavy elements (Dekel and Silk 1986). Although well-studied at the high-mass end with surveys like SDSS (Tremonti et al. 2004), the MZR for low-mass galaxies—including dwarf satellite galaxies—is poorly constrained due to small sample size. There are some indications that dwarf galaxies lie below the MZR for more massive galaxies, both for gas-phase metallicity (e.g., Lee et al. 2006b) and for stellar metallicity (Leethochawalit et al. 2019; Zhuang et al. 2021). Metallicity measurements of SAGA satellites could confirm the existence of a break in the low-mass end of the MZR and provide clues about its origin.

- **The star formation histories** of SAGA satellites could be used to investigate why these satellites have unexpectedly high current star formation rates relative to the Local Group and cosmological simulations. Is SAGA missing a population of existing galaxies, or is the Local Group (and the simulations, which are frequently tuned to match the Local Group) not representative of $L_\star$ satellite systems? A direct comparison between SFHs of SAGA satellites and SFHs obtained from mock spectra of simulated galaxies could test whether the quenching of star formation in simulations is physical.

7.3.4 DESI

SAGA will provide a statistical sample to test whether the Local Group is representative of other $L_\star$ satellite systems, but such systems are only one kind of environment that dwarf galaxies might live in. The Dark Energy Spectroscopic Instrument (DESI; DESI Collaboration et al. 2016) is one of many massively-multiplexed spectroscopic surveys (e.g., WEAVE and 4MOST; Dalton et al. 2014; de Jong et al. 2014) that will address this by studying a statistical sample of dwarf galaxies across a variety of environments. DESI has 10 identical 500-fiber spectrographs covering a 3° diameter field of view, with spectral properties similar to those of LVM (total wavelength range $\Delta\lambda = 360 - 980$ nm and resolution $R \sim 2000 - 5000$) and excellent ($\sim 70\%$) throughput.

Over the next five years, DESI will obtain spectra of 35 million galaxies and quasars over nearly one-third of the sky (a 14000 deg^2 field). Although many of these galaxies are luminous and high-redshift galaxies, targeted in order to map three-dimensional structure in the universe, DESI will also target a number of low-redshift galaxies. These include an unprecedentedly large sample of several thousand dwarf galaxies with stellar masses $10^{6.5} < M_\odot < 10^9$, for which DESI spectra can be used to measure global properties. This massive sample will vastly improve observational constraints on the low-mass end of galaxy functions—e.g., the galaxy luminosity and stellar mass functions, or the mass-metallicity relation described in the previous subsection. It will also allow us to probe, for the first time, if and how dwarf galaxy properties systematically vary as a function of galaxy environment, fundamentally revolutionizing our understanding of how our Local Group fits into the larger context of dwarf galaxies.

As this thesis has demonstrated, nearby dwarf galaxies are ideal systems for investigating stellar and galaxy evolution on multiple spatial scales. Over the next decade, the groundbreaking capabilities of instruments and surveys like Subaru PFS, the LVM, SAGA, and DESI promise to shed even more light on these fascinating systems. Observational studies of dwarf galaxies have already led to unique insights into a variety of research areas: the physics of Type Ia supernovae, galaxy formation in isolated environments, and star formation on galaxy-wide scales, just to name a few. By advancing our understanding of dwarf galaxies in the local universe, we will be able to address an even wider variety of outstanding astrophysical questions.

BIBLIOGRAPHY

Abazajian, K. N. et al. (2009). "The Seventh Data Release of the Sloan Digital Sky Survey." *ApJS* 182.2, pp. 543–558. DOI: 10.1088/0067-0049/182/2/543.

Abazajian, K. et al. (2005). "The Third Data Release of the Sloan Digital Sky Survey." *AJ* 129.3, pp. 1755–1759. DOI: 10.1086/427544.

Abohalima, A. and A. Frebel (2018). "JINAbase: A Database for Chemical Abundances of Metal-poor Stars." *ApJS* 238.2, p. 36. ISSN: 1538-4365. DOI: 10.3847/1538-4365/aadfe9.

El-Ad, H. and T. Piran (1997). "Voids in the Large-Scale Structure." *ApJ* 491.2, pp. 421–435. DOI: 10.1086/304973.

Aghanim, N. et al. (2020). "Planck 2018 Results: VI. Cosmological Parameters." *A&A* 641, A6. ISSN: 14320746. DOI: 10.1051/0004-6361/201833910.

Ahumada, R. et al. (2020). "The 16th Data Release of the Sloan Digital Sky Surveys: First Release from the APOGEE-2 Southern Survey and Full Release of eBOSS Spectra." *ApJS* 249.1, 3, p. 3. DOI: 10.3847/1538-4365/ab929e.

Akritas, M. G. and M. A. Bershady (1996). "Linear Regression for Astronomical Data with Measurement Errors and Intrinsic Scatter." *ApJ* 470, p. 706. DOI: 10.1086/177901.

Arnett, W. D., J. W. Truran, and S. E. Woosley (1971). "Nucleosynthesis in Supernova Models. II. The ^{12}C Detonation Model." *ApJ* 165, p. 87. ISSN: 0004-637X. DOI: 10.1086/150878.

Asplund, M. et al. (2009). "The Chemical Composition of the Sun." *ARA&A* 47.1, pp. 481–522. DOI: 10.1146/annurev.astro.46.060407.145222.

Bacchini, C. et al. (2019). "Volumetric Star Formation Laws of Disc Galaxies." *A&A* 622, A64, A64. DOI: 10.1051/0004-6361/201834382.

Bacchini, C. et al. (2020). "The Volumetric Star Formation Law for Nearby Galaxies. Extension to Dwarf Galaxies and Low-density Regions." *A&A* 644, A125, A125. DOI: 10.1051/0004-6361/202038962.

El-Badry, K. et al. (2017). "When the Jeans Do Not Fit: How Stellar Feedback Drives Stellar Kinematics and Complicates Dynamical Modeling in Low-mass Galaxies." *ApJ* 835.2, 193, p. 193. DOI: 10.3847/1538-4357/835/2/193.

Bai, Y. et al. (2015). "An Updated Ultraviolet Catalog of GALEX Nearby Galaxies." *ApJS* 220, p. 6. DOI: 10.1088/0067-0049/220/1/6.

Bajaja, E. et al. (1995). "Observations of CO Lines in Southern Spiral Galaxies." *A&AS* 114, p. 147.

Barone, L. et al. (2000). "Molecular Gas in Blue Compact Dwarf Galaxies." *MNRAS* 317, pp. 649–657. DOI: 10.1046/j.1365-8711.2000.03678.x.

Battaglia, G. et al. (2008). "The Kinematic Status and Mass Content of the Sculptor Dwarf Spheroidal Galaxy." *ApJ* 681.1, pp. L13–L16. DOI: 10.1086/590179.

Baumgardt, H. and M. Hilker (2018). "A Catalogue of Masses, Structural Parameters, and Velocity Dispersion Profiles of 112 Milky Way Globular Clusters." *MNRAS* 478.2, pp. 1520–1557. ISSN: 0035-8711. DOI: 10.1093/mnras/sty1057.

Begum, A. et al. (2008a). "FIGGS: Faint Irregular Galaxies GMRT Survey - Overview, Observations and First Results." *MNRAS* 386, pp. 1667–1682. DOI: 10.1111/j.1365-2966.2008.13150.x.

Begum, A. et al. (2008b). "Life in the Last Lane: Star Formation and Chemical Evolution in an Extremely Gas Rich Dwarf." *MNRAS* 383, pp. 809–816. DOI: 10.1111/j.1365-2966.2007.12592.x.

Bell, E. F. et al. (2008). "The Accretion Origin of the Milky Way's Stellar Halo." *ApJ* 680.1, pp. 295–311. DOI: 10.1086/588032.

Belokurov, V. et al. (2018). "Co-formation of the Disc and the Stellar Halo." *MNRAS* 478.1, pp. 611–619. DOI: 10.1093/mnras/sty982.

Bender, R., D. Burstein, and S. M. Faber (1993). "Dynamically Hot Galaxies. II. Global Stellar Populations." *ApJ* 411, p. 153. DOI: 10.1086/172815.

Bendo, G. J., F. Galliano, and S. C. Madden (2012). "MIPS 24-160 μm Photometry for the Herschel-SPIRE Local Galaxies Guaranteed Time Programs." *MNRAS* 423.1, pp. 197–212. DOI: 10.1111/j.1365-2966.2012.20784.x.

Berg, D. A. et al. (2012). "Direct Oxygen Abundances for Low-Luminosity LVL Galaxies." *ApJ* 754.2, p. 98. ISSN: 0004-637X. DOI: 10.1088/0004-637X/754/2/98.

Bergemann, M. and T. Gehren (2008). "NLTE Abundances of Mn in a Sample of Metal-poor Stars." *A&A* 492.3, pp. 823–831. ISSN: 0004-6361. DOI: 10.1051/0004-6361:200810098.

Bergemann, M. et al. (2012). "Non-LTE Line Formation of Fe in Late-type Stars I. Standard Stars with 1D and <3D> Model Atmospheres." *MNRAS* 427.1, pp. 27–49. ISSN: 00358711. DOI: 10.1111/j.1365-2966.2012.21687.x.

Bergemann, M. et al. (2017). "Non-local Thermodynamic Equilibrium Stellar Spectroscopy with 1D and <3D> Models. II. Chemical Properties of the Galactic Metal-poor Disk and the Halo." *ApJ* 847.1, p. 16. ISSN: 1538-4357. DOI: 10.3847/1538-4357/aa88b5.

Bergemann, M. et al. (2019). "Observational Constraints on the Origin of the Elements. I. 3D NLTE Formation of Mn Lines in Late-type Stars." *A&A* 631, A80, A80. DOI: 10.1051/0004-6361/201935811.

Bettinelli, M. et al. (2019). "The Star Formation History of the Sculptor Dwarf Spheroidal Galaxy." *MNRAS* 487.4, pp. 5862–5873. ISSN: 13652966. DOI: 10.1093/mnras/stz1679.

Beygu, B. et al. (2016). "The Void Galaxy Survey: Star Formation Properties." *MNRAS* 458.1, pp. 394–409. DOI: 10.1093/mnras/stw280.

Beygu, B. et al. (2017). "The Void Galaxy Survey: Photometry, Structure and Identity of Void Galaxies." *MNRAS* 464.1, pp. 666–679. DOI: 10.1093/mnras/stw2362.

Bigiel, F., D. Cormier, and T. Schmidt (2014). "The Interstellar Medium and Star Formation in Nearby Galaxies. Ludwig Biermann Award Lecture 2013." *Astronomische Nachrichten* 335.5, pp. 470–485. DOI: 10.1002/asna.201412067.

Bigiel, F. et al. (2008). "The Star Formation Law in Nearby Galaxies on Sub-kpc Scales." *AJ* 136, pp. 2846–2871. DOI: 10.1088/0004-6256/136/6/2846.

Bigiel, F. et al. (2020). "SOFIA/FIFI-LS Full-disk [C II] Mapping and CO-dark Molecular Gas across the Nearby Spiral Galaxy NGC 6946." *ApJ* 903.1, 30, p. 30. DOI: 10.3847/1538-4357/abb677.

Binney, J. (2005). "Rotation and Anisotropy of Galaxies Revisited." *MNRAS* 363.3, pp. 937–942. DOI: 10.1111/j.1365-2966.2005.09495.x.

Blitz, L. and E. Rosolowsky (2004). "The Role of Pressure in Giant Molecular Cloud Formation." *ApJL* 612, pp. L29–L32. DOI: 10.1086/424661.

Bolatto, A. D., M. Wolfire, and A. K. Leroy (2013). "The CO-to-H_2 Conversion Factor." *ARA&A* 51.1, pp. 207–268. ISSN: 0066-4146. DOI: 10.1146/annurev-astro-082812-140944.

Bond, J. R., L. Kofman, and D. Pogosyan (1996). "How Filaments of Galaxies are Woven into the Cosmic Web." *Nature* 380.6575, pp. 603–606. ISSN: 00280836. DOI: 10.1038/380603a0.

Bonifacio, P. et al. (2009). "First Stars XII. Abundances in Extremely Metal-poor Turnoff Stars, and Comparison with the Giants." *A&A* 501.2, pp. 519–530. ISSN: 0004-6361. DOI: 10.1051/0004-6361/200810610.

Boquien, M. et al. (2016). "Towards Universal Hybrid Star Formation Rate Estimators." *A&A* 591, A6. ISSN: 0004-6361. DOI: 10.1051/0004-6361/201527759.

Boselli, A., L. Cortese, and M. Boquien (2014). "Cold Gas Properties of the Herschel Reference Survey. I. ^{12}CO(1-0) and HI Data." *A&A* 564, A65. DOI: 10.1051/0004-6361/201322311.

Bosma, A. (1978). "The Distribution and Kinematics of Neutral Hydrogen in Spiral Galaxies of Various Morphological Types." PhD thesis. Groningen University.

Bosma, A., W. Goss, and R. Allen (1981). "The Giant Spiral Galaxy M101. VI. The Large Scale Radial Velocity Field." *A&A* 93, pp. 106–112.

Bosma, A. et al. (1980). "The Group of Galaxies NGC 2805-2814-2820-Markarian 108." *A&A* 89, pp. 345–352.

Bours, M. C. P., S. Toonen, and G. Nelemans (2013). "Single Degenerate Supernova Type Ia Progenitors. Studying the Influence of Different Mass Retention Efficiencies." *A&A* 552, A24, A24. DOI: 10.1051/0004-6361/201220692.

Braine, J., N. Brouillet, and A. Baudry (1997). "The Anatomy of an Isolated Spiral Galaxy: NGC 4414." *A&A* 318, pp. 19–28.

Braine, J., F. Combes, and W. van Driel (1993a). "NGC 4414: A Flocculent Galaxy with a High Gas Surface Density." *A&A* 280, pp. 451–467.

Braine, J. et al. (1993b). "A CO(1-0) and CO(2-1) Survey of Nearby Spiral Galaxies. I. Data and Observations." *A&AS* 97, pp. 887–936.

Brandt, T. D. et al. (2010). "The Ages of Type Ia Supernova Progenitors." *AJ* 140.3, pp. 804–816. DOI: 10.1088/0004-6256/140/3/804.

Braun, R. et al. (1994). "Counterrotating Gaseous Disks in NGC 4826." *ApJ* 420, pp. 558–569. DOI: 10.1086/173586.

Bravo, E., C. Badenes, and H. Martínez-Rodríguez (2019). "SNR-calibrated Type Ia Supernova Models." *MNRAS* 482.4, pp. 4346–4363. ISSN: 0035-8711. DOI: 10.1093/mnras/sty2951.

Broeils, A. and M.-H. Rhee (1997). "Short 21-cm WSRT Observations of Spiral and Irregular Galaxies. HI Properties." *A&A* 324, pp. 877–887.

Broeils, A. and H. van Woerden (1994). "A Search for Spiral Galaxies with Extended HI Disks." *A&AS* 107, pp. 129–176.

Bromm, V. and N. Yoshida (2011). "The First Galaxies." *ARA&A* 49.1, pp. 373–407. ISSN: 0066-4146. DOI: 10.1146/ANNUREV-ASTRO-081710-102608.

Brown, T. M. et al. (2012). "The Primeval Populations of the Ultra-faint Dwarf Galaxies." *ApJL* 753.1, L21, p. L21. DOI: 10.1088/2041-8205/753/1/L21.

Brown, T. M. et al. (2014). "The Quenching of the Ultra-faint Dwarf Galaxies in the Reionization Era." *ApJ* 796.2, p. 91. ISSN: 15384357. DOI: 10.1088/0004-637X/796/2/91.

Bundy, K. et al. (2015). "Overview of the SDSS-IV MaNGA Survey: Mapping Nearby Galaxies at Apache Point Observatory." *ApJ* 798.1, 7, p. 7. DOI: 10.1088/0004-637X/798/1/7.

Bush, S. and E. Wilcots (2004). "Neutral Hydrogen in the Interacting Magellanic Spirals NGC 4618 and NGC 4625." *AJ* 128, pp. 2789–2796. DOI: 10.1086/425876.

Calura, F. and N. Menci (2009). "Chemical Evolution of Local Galaxies in a Hierarchical Model." *MNRAS* 400.3, pp. 1347–1365. ISSN: 00358711. DOI: 10.1111/j.1365-2966.2009.15440.x.

Cappellari, M. (2008). "Measuring the Inclination and Mass-to-light Ratio of Axisymmetric Galaxies via Anisotropic Jeans Models of Stellar Kinematics." *MNRAS* 390.1, pp. 71–86. DOI: 10.1111/j.1365-2966.2008.13754.x.

– (2017). "Improving the Full Spectrum Fitting Method: Accurate Convolution with Gauss-Hermite Functions." *MNRAS* 466.1, pp. 798–811. DOI: 10.1093/mnras/stw3020.

Cappellari, M. and Y. Copin (2003). "Adaptive Spatial Binning of Integral-field Spectroscopic Data using Voronoi Tessellations." *MNRAS* 342.2, pp. 345–354. DOI: 10.1046/j.1365-8711.2003.06541.x.

Cappellari, M. and E. Emsellem (2004). "Parametric Recovery of Line-of-Sight Velocity Distributions from Absorption-Line Spectra of Galaxies via Penalized Likelihood." *PASP* 116.816, pp. 138–147. DOI: 10.1086/381875.

Carbon, D. F. et al. (1982). "Carbon and Nitrogen Abundances in Giant Stars of the Metal-poor Globular Cluster M92." *ApJS* 49, p. 207. ISSN: 0067-0049. DOI: 10.1086/190796.

Cardelli, J. A., G. C. Clayton, and J. S. Mathis (1989). "The Relationship between Infrared, Optical, and Ultraviolet Extinction." *ApJ* 345, p. 245. DOI: 10.1086/167900.

Carigi, L., X. Hernandez, and G. Gilmore (2002). "Chemical Evolution Models of Local dSph Galaxies." *MNRAS* 334.1, pp. 117–128. DOI: 10.1046/j.1365-8711.2002.05491.x.

Carignan, C. and S. Beaulieu (1989). "Optical and H I Studies of the 'Gas-rich' Dwarf Irregular Galaxy DDO 154." *ApJ* 347, pp. 760–770. DOI: 10.1086/168167.

Carignan, C., R. Sancisi, and T. van Albada (1988). "H I and Mass Distribution in the Dwarf 'Regular' Galaxy UGC 2259." *AJ* 95, pp. 37–44. DOI: 10.1086/114610.

Carnall, A. C. et al. (2019). "How to Measure Galaxy Star Formation Histories. I. Parametric Models." *ApJ* 873.1, p. 44. ISSN: 1538-4357. DOI: 10.3847/1538-4357/ab04a2.

Carretta, E. et al. (2010). "Detailed Abundances of a Large Sample of Giant Stars in M54 and in the Sagittarius Nucleus." *A&A* 520.A95. DOI: 10.1051/0004-6361/201014924.

Carroll, R. J. and D. Ruppert (1996). "The Use and Misuse of Orthogonal Regression in Linear Errors-in-Variables Models." *Am. Stat.* 50.1, pp. 1–6. ISSN: 0003-1305. DOI: 10.1080/00031305.1996.10473533.

Casertano, S. and J. van Gorkom (1991). "Declining Rotation Curves - The End of a Conspiracy?" *AJ* 101, pp. 1231–1241. DOI: 10.1086/115759.

Castelli, F. and R. L. Kurucz (2003). "New Grids of ATLAS9 Model Atmospheres." *IAUS*. Vol. 210. Astronomical Society of the Pacific, A20. URL: adsabs.harvard.edu/abs/2003IAUS..210P.A20C/abstract.

Castrillo, A. et al. (2021). "The Delay Time Distribution of Supernovae from Integral-field Spectroscopy of Nearby Galaxies." *MNRAS* 501.3, p. 3122. ISSN: 0035-8711. DOI: 10.1093/MNRAS/STAA3876.

Cescutti, G. and C. Kobayashi (2017). "Manganese Spread in Ursa Minor as a Proof of Sub-classes of Type Ia Supernovae." *A&A* 607, A23. ISSN: 0004-6361. DOI: 10.1051/0004-6361/201731398.

Cescutti, G. et al. (2006). "The Chemical Evolution of Barium and Europium in the Milky Way." *A&A* 448.2, pp. 557–569. ISSN: 0004-6361. DOI: 10.1051/0004-6361:20053622.

Cescutti, G. et al. (2015). "The Role of Neutron Star Mergers in the Chemical Evolution of the Galactic Halo." *A&A* 577, A139. ISSN: 0004-6361. DOI: 10.1051/0004-6361/201525698.

Chabrier, G. (2003). "Galactic Stellar and Substellar Initial Mass Function." *PASP* 115, pp. 763–795. ISSN: 0004-6280. DOI: 10.1086/376392.

Chai, T. and R. R. Draxler (2014). "Root Mean Square Error (RMSE) or Mean Absolute Error (MAE)? – Arguments Against Avoiding RMSE in the Literature." *Geosci. Model Dev.* 7, pp. 1247–1250. DOI: 10.5194/gmd-7-1247-2014.

Chamulak, D. A. et al. (2008). "The Reduction of the Electron Abundance during the Pre?explosion Simmering in White Dwarf Supernovae." *ApJ* 677.1, pp. 160–168. ISSN: 0004-637X. DOI: 10.1086/528944.

Choi, Y.-Y., D.-H. Han, and S. S. Kim (2010). "Korea Institute for Advanced Study Value-Added Galaxy Catalog." *Journal of Korean Astronomical Society* 43.6, pp. 191–200. DOI: 10.5303/JKAS.2010.43.6.191.

Chung, A. et al. (2009). "VLA Imaging of Virgo Spirals in Atomic Gas (VIVA). I. The Atlas and the H I Properties." *AJ* 138, pp. 1741–1816. DOI: 10.1088/0004-6256/138/6/1741.

Claeys, J. S. W. et al. (2014). "Theoretical Uncertainties of the Type Ia Supernova Rate." *A&A* 563, A83, A83. DOI: 10.1051/0004-6361/201322714.

Combes, F., S. Gottesman, and L. Weliachew (1977). "Aperture Synthesis Study of Neutral Hydrogen in the Galaxy NGC 253." *A&A* 59, pp. 181–187.

Conroy, C. (2013). "Modeling the Panchromatic Spectral Energy Distributions of Galaxies." *ARA&A* 51, pp. 393–455. ISSN: 00664146. DOI: 10.1146/annurev-astro-082812-141017.

Conroy, C. and P. G. Van Dokkum (2012). "The Stellar Initial Mass Function in Early-type Galaxies from Absorption Line Spectroscopy. II. Results." *ApJ* 760.1, p. 71. ISSN: 15384357. DOI: 10.1088/0004-637X/760/1/71.

Cook, D. O. et al. (2014). "Spitzer Local Volume Legacy (LVL) SEDs and Physical Properties." *MNRAS* 445.1, pp. 899–912. ISSN: 0035-8711. DOI: 10.1093/mnras/stu1787.

Cooper, M. C. et al. (2012). "spec2d: DEEP2 DEIMOS Spectral Pipeline." *ASCL*, p. 1203.003.

Corbelli, E. et al. (2010). "A Wide-field H I Mosaic of Messier 31. II. The Disk Warp, Rotation, and the Dark Matter Halo." *A&A* 511, A89. DOI: 10.1051/0004-6361/200913297.

Cormier, D. et al. (2014). "The Molecular Gas Reservoir of 6 Low-metallicity Galaxies from the Herschel Dwarf Galaxy Survey." *A&A* 564, A121. ISSN: 0004-6361. DOI: 10.1051/0004-6361/201322096.

Cortese, L. et al. (2012). "The GALEX view of the Herschel Reference Survey. Ultraviolet Structural Properties of Nearby Galaxies." *A&A* 544, A101. DOI: 10.1051/0004-6361/201219312.

Côté, B. et al. (2017). "The Impact of Modeling Assumptions in Galactic Chemical Evolution Models." *ApJ* 835.2, p. 128. ISSN: 1538-4357. DOI: 10.3847/1538-4357/835/2/128.

Côté, B. et al. (2019). " Neutron Star Mergers Might Not Be the Only Source of r -process Elements in the Milky Way." *ApJ* 875.2, p. 106. ISSN: 1538-4357. DOI: 10.3847/1538-4357/ab10db.

Cote, S., C. Carignan, and R. Sancisi (1991). "A Dark-halo-dominated Galaxy - NGC 5585." *AJ* 102, pp. 904–913. DOI: 10.1086/115922.

Cowan, J. J. et al. (2021). "Origin of the Heaviest Elements: The Rapid Neutron-capture Process." *Reviews of Modern Physics* 93.1, p. 015002. ISSN: 0034-6861. DOI: 10.1103/REVMODPHYS.93.015002.

Cristallo, S. et al. (2011). "Evolution, Nucleosynthesis, and Yields of Low-mass Asymptotic Giant Branch Stars at Different Metallicities. II. The FRUITY Database." *ApJS* 197.2, p. 17. ISSN: 0067-0049. DOI: 10.1088/0067-0049/197/2/17.

Cristallo, S. et al. (2015). "Evolution, Nucleosynthesis and Yields of AGB stars at Different Metallicities (III): Intermediate Mass Models, Revised Low Mass Models and the ph-FRUITY Interface." *ApJS* 219.2, p. 40. DOI: 10.1088/0067-0049/219/2/40.

Crosthwaite, L. et al. (2001). "CO and Neutral Gas in the Disk of the Spiral Galaxy IC 342." *AJ* 122, pp. 797–814. DOI: 10.1086/321148.

Cunha, K. et al. (2010). "Manganese Abundances in the Globular Cluster ω Centauri." *ApJ* 717.1, pp. 333–341. ISSN: 0004-637X. DOI: 10.1088/0004-637X/717/1/333.

Da Costa, G. S. (1984). "The Age(s?) of the Sculptor Dwarf Galaxy." *ApJ* 285, p. 483. ISSN: 0004-637X. DOI: 10.1086/162523.

Daddi, E. et al. (2010). "Different Star Formation Laws for Disks Versus Starbursts at Low and High Redshifts." *ApJL* 714.1, pp. L118–L122. ISSN: 2041-8205. DOI: 10.1088/2041-8205/714/1/L118.

Dale, D. A. et al. (2007). "An Ultraviolet-to-Radio Broadband Spectral Atlas of Nearby Galaxies." *ApJ* 655.2, pp. 863–884. ISSN: 0004-637X. DOI: 10.1086/510362.

Dale, D. A. et al. (2009). "The Spitzer Local Volume Legacy: Survey Description and Infrared Photometry." *ApJ* 703.1, pp. 517–556. DOI: 10.1088/0004-637X/703/1/517.

Dalton, G. et al. (2014). "Project Overview and Update on WEAVE: The Next Generation Wide-field Spectroscopy Facility for the William Herschel Telescope." *Ground-based and Airborne Instrumentation for Astronomy V*. Ed. by S. K. Ramsay, I. S. McLean, and H. Takami. Vol. 9147. Society of Photo-Optical Instrumentation Engineers (SPIE) Conference Series, p. 91470L. DOI: 10.1117/12.2055132.

Dame, T. et al. (1993). "A Complete CO Survey of M31. I. Distribution and Kinematics." *ApJ* 418, p. 730. DOI: 10.1086/173430.

de Jong, R. S. et al. (2014). "4MOST: 4-metre Multi-Object Spectroscopic Telescope." *Ground-based and Airborne Instrumentation for Astronomy V*. Ed. by S. K. Ramsay, I. S. McLean, and H. Takami. Vol. 9147. Society of Photo-Optical Instrumentation Engineers (SPIE) Conference Series, p. 91470M. DOI: 10.1117/12.2055826.

de los Reyes, M. A. C. and R. C. Kennicutt (2019). "Revisiting the Integrated Star Formation Law. I. Non-starbursting Galaxies." *ApJ* 872.1, p. 16. DOI: 10.3847/1538-4357/aafa82.

de los Reyes, M. A. C. et al. (2020). "Manganese Indicates a Transition from Sub- to Near-Chandrasekhar Type Ia Supernovae in Dwarf Galaxies." *ApJ* 891.1, p. 85. DOI: 10.3847/1538-4357/ab736f.

de los Reyes, M. A. C. et al. (2022). "Simultaneous Constraints on the Star Formation History and Nucleosynthesis of Sculptor dSph." *ApJ* 925.1, 66, p. 66. DOI: 10.3847/1538-4357/ac332b.

De Blok, W., S. McGaugh, and J. van der Hulst (1996). "HI Observations of Low Surface Brightness Galaxies: Probing Low-density Galaxies." *MNRAS* 283, pp. 18–54. DOI: 10.1093/mnras/283.1.18.

De Blok, W. and F. Walter (2006). "The Star Formation Threshold in NGC 6822." *AJ* 131, pp. 363–374. DOI: 10.1086/497828.

De Boer, T. J. L. et al. (2012). "The Star Formation and Chemical Evolution History of the Sculptor Dwarf Spheroidal Galaxy." *A&A* 539, A103. ISSN: 0004-6361. DOI: 10.1051/0004-6361/201118378.

De Vaucouleurs, G., A. de Vaucouleurs, and H. G. Corwin (1976). *Second Reference Catalogue of Bright Galaxies. Containing Information on 4,364 Galaxies with References to Papers Published Between 1964 and 1975*. University of Texas Press, pp. 1–396.

De Vaucouleurs, G. et al. (1991). *Third Reference Catalogue of Bright Galaxies*. Springer-Verlag. ISBN: 0387975527.

Dekel, A. and J. Silk (1986). "The Origin of Dwarf Galaxies, Cold Dark Matter, and Biased Galaxy Formation." *ApJ* 303, p. 39. ISSN: 0004-637X. DOI: 10.1086/164050. URL: https://doi.org/10.1086/164050.

Dekel, A. et al. (2009). "Cold Streams in Early Massive Hot Haloes as the Main Mode of Galaxy Formation." *Nature* 457.7228, pp. 451–454. ISSN: 00280836. DOI: 10.1038/nature07648.

Del Rio, M., E. Brinks, and J. Cepa (2004). "High-Resolution H I Observations of the Galaxy NGC 404: A Dwarf S0 with Abundant Interstellar Gas." *AJ* 128, pp. 89–102. DOI: 10.1086/421358.

DESI Collaboration et al. (2016). "The DESI Experiment Part I: Science,Targeting, and Survey Design." *arXiv e-prints*, arXiv:1611.00036, arXiv:1611.00036. arXiv: 1611.00036 [astro-ph.IM].

Desjacques, V., D. Jeong, and F. Schmidt (2018). "Large-scale Galaxy Bias." *Physics Reports* 733, pp. 1–193. DOI: 10.1016/j.physrep.2017.12.002.

Dickey, C. M. et al. (2021). "IQ Collaboratory. II. The Quiescent Fraction of Isolated, Low-mass Galaxies across Simulations and Observations." *ApJ* 915.1, p. 53. ISSN: 0004-637X. DOI: 10.3847/1538-4357/ABC014. URL: https://doi.org/10.3847/1538-4357/ABC014.

Dolphin, A. E. (2002). "Numerical Methods of Star Formation History Measurement and Applications to Seven Dwarf Spheroidals." *MNRAS* 332.1, pp. 91–108. ISSN: 00358711. DOI: 10.1046/j.1365-8711.2002.05271.x.

Domínguez-Gómez, J. et al. (2022). "CO-CAVITY Pilot Survey: Molecular Gas and Star Formation in Void Galaxies." *A&A* 658, A124, A124. DOI: 10.1051/0004-6361/202141888.

Dopita, M. A. (1985). "A Law of Star Formation in Disk Galaxies - Evidence for Self-regulating Feedback." *ApJL* 295, p. L5. ISSN: 0004-637X. DOI: 10.1086/184526.

Dopita, M. A. and S. D. Ryder (1994). "On the Law of Star Formation in Disk Galaxies." *ApJ* 430, p. 163. ISSN: 0004-637X. DOI: 10.1086/174390.

Douglass, K. A. and M. S. Vogeley (2017). "Determining the Large-scale Environmental Dependence of Gas-phase Metallicity in Dwarf Galaxies." *ApJ* 834.2, p. 186. DOI: 10.3847/1538-4357/834/2/186. eprint: 1604.08599.

Douglass, K. A., M. S. Vogeley, and R. Cen (2018). "Influence of the Void Environment on Chemical Abundances in Dwarf Galaxies and Implications for Connecting Star Formation and Halo Mass." *ApJ* 864.2, p. 144. DOI: 10.3847/1538-4357/aad86e.

Draine, B. T. (2003). "Interstellar Dust Grains." *ARA&A* 41, pp. 241–289. ISSN: 0066-4146. DOI: 10.1146/annurev.astro.41.011802.094840.

Drlica-Wagner, A. et al. (2020). "Milky Way Satellite Census. I. The Observational Selection Function for Milky Way Satellites in DES Y3 and Pan-STARRS DR1." *ApJ* 893.1, 47, p. 47. DOI: 10.3847/1538-4357/ab7eb9.

Duggan, G. E. et al. (2018). "Implications of Barium Abundances for the Chemcial Enrichment of Dwarf Galaxies." *ApJ* 869, p. 50.

Einasto, J. et al. (1974). "Missing Mass around Galaxies - Morphological Evidence." *Nature* 252, pp. 111–113. DOI: 10.1038/252111a0.

Eldridge, J. J. et al. (2017). "Binary Population and Spectral Synthesis Version 2.1: Construction, Observational Verification, and New Results." *PASA* 34, e058. ISSN: 1323-3580. DOI: 10.1017/PASA.2017.51.

Elmegreen, B. G. (1997). "Theory of Starbursts in Nuclear Rings." *RMxAC* 6, p. 165. URL: http://adsabs.harvard.edu/abs/1997RMxAC...6..165E.

Elmegreen, B. G. and D. A. Hunter (2015). "A Star Formation Law for Dwarf Irregular Galaxies." *ApJ* 805.2, p. 145. ISSN: 1538-4357. DOI: 10.1088/0004-637X/805/2/145.

Engelbracht, C. W. et al. (2007). "Absolute Calibration and Characterization of the Multiband Imaging Photometer for Spitzer. I. The Stellar Calibrator Sample and the 24 μm Calibration." *PASP* 119.859, pp. 994–1018. DOI: 10.1086/521881.

Escala, I. et al. (2018). "Modelling Chemical Abundance Distributions for Dwarf Galaxies in the Local Group: The Impact of Turbulent Metal Diffusion." *MNRAS* 474.2, pp. 2194–2211. ISSN: 13652966. DOI: 10.1093/mnras/stx2858.

Escala, I. et al. (2019). "Elemental Abundances in M31: Alpha and Iron Element Abundances from Low-resolution Resolved Stellar Spectroscopy in the Stellar Halo." *ApJ* 878, p. 42. DOI: 10.3847/1538-4357/ab1eac.

Eskew, M. R., D. F. Zaritsky, and S. E. Meidt (2012). "Converting from 3.6 and 4.5 Micron Fluxes to Stellar Mass." *AJ* 143.6, p. 139. ISSN: 0004-6256. DOI: 10.1088/0004-6256/143/6/139.

Faber, S. M. et al. (2003). "The DEIMOS Spectrograph for the Keck II Telescope: Integration and Testing." *2003SPIE 4841*. Ed. by M. Iye and A. F. M. Moorwood. Vol. 4841, p. 1657. DOI: 10.1117/12.460346.

Fabian, A. C. (2012). "Observational Evidence of Active Galactic Nuclei Feedback." *ARA&A* 50, pp. 455–489. ISSN: 00664146. DOI: 10.1146/annurev-astro-081811-125521.

Falcón-Barroso, J. et al. (2011). "An Updated MILES Stellar Library and Stellar Population Models." *A&A* 532, A95, A95. DOI: 10.1051/0004-6361/201116842.

Fall, S. M. and G. Efstathiou (1980). "Formation and Rotation of Disc Galaxies with Haloes." *MNRAS* 193, pp. 189–206. DOI: 10.1093/mnras/193.2.189.

Feltzing, S., M. Fohlman, and T. Bensby (2007). "Manganese Trends in a Sample of Thin and Thick Disk Stars." *A&A* 467.2, pp. 665–677. ISSN: 0004-6361. DOI: 10.1051/0004-6361:20065797.

Fenner, Y. et al. (2006). "Cosmological Implications of Dwarf Spheroidal Chemical Evolution." *ApJ* 646.1, pp. 184–191. DOI: 10.1086/504893.

Ferguson, A. et al. (1998). "Discovery of Recent Star Formation in the Extreme Outer Regions of Disk Galaxies." *ApJL* 506, pp. L19–L22. DOI: 10.1086/311626.

Ferré-Mateu, A. et al. (2021). "Low-mass Compact Elliptical Galaxies: Spatially Resolved Stellar Populations and Kinematics with the Keck Cosmic Web Imager." *MNRAS* 503.4, pp. 5455–5472. DOI: 10.1093/mnras/stab805.

Fielding, D., E. Quataert, and D. Martizzi (2018). "Clustered Supernovae Drive Powerful Galactic Winds after Superbubble Breakout." *MNRAS* 481.3, pp. 3325–3347. ISSN: 13652966. DOI: 10.1093/mnras/sty2466.

Filho, M. E. et al. (2015). "Extremely Metal-Poor Galaxies: The Environment." *ApJ* 802.2, p. 82. DOI: 10.1088/0004-637X/802/2/82. eprint: 1501.06709.

Filho, M. E. et al. (2016). "The Kennicutt-Schmidt Relation in Extremely Metal-Poor Dwarf Galaxies." *ApJ* 820.2, p. 109. ISSN: 1538-4357. DOI: 10.3847/0004-637X/820/2/109.

Fink, M. et al. (2014). "Three-dimensional Pure Deflagration Models with Nucleosynthesis and Synthetic Observables for Type Ia Supernovae." *MNRAS* 438.2, pp. 1762–1783. ISSN: 0035-8711. DOI: 10.1093/mnras/stt2315.

Fisher, D. et al. (2013). "The Molecular Gas Density in Galaxy Centers and how it Connects to Bulges." *ApJ* 764, p. 174. DOI: 10.1088/0004-637X/764/2/174.

Florez, J. et al. (2021). "Void Galaxies Follow a Distinct Evolutionary Path in the Environmental COntext Catalog." *ApJ* 906.2, 97, p. 97. DOI: 10.3847/1538-4357/abca9f.

Font, A. S. et al. (2022). "Quenching of Satellite Galaxies of Milky Way Analogues: Reconciling Theory and Observations." *MNRAS* 511.1, pp. 1544–1556. DOI: 10.1093/mnras/stac183.

Foreman-Mackey, D. et al. (2013). "emcee: The MCMC Hammer." *PASP* 125.925, pp. 306–312. ISSN: 00046280. DOI: 10.1086/670067.

Frebel, A. et al. (2010). "Linking Dwarf Galaxies to Halo Building Blocks with the Most Metal-poor Star in Sculptor." *Nature* 464.7285, pp. 72–75. ISSN: 0028-0836. DOI: 10.1038/NATURE08772.

Gao, Y. and P. M. Solomon (2004). "The Star Formation Rate and Dense Molecular Gas in Galaxies." *ApJ* 606.1, pp. 271–290. ISSN: 0004-637X. DOI: 10.1086/382999.

Gardner, J. P. et al. (2006). "The James Webb Space Telescope." *SSRv* 123.4, pp. 485–606. DOI: 10.1007/s11214-006-8315-7.

Garrison-Kimmel, S. et al. (2019). "The Local Group on FIRE: Dwarf Galaxy Populations across a Suite of Hydrodynamic Simulations." *MNRAS* 487.1, pp. 1380–1399. ISSN: 0035-8711. DOI: 10.1093/MNRAS/STZ1317. URL: https://doi.org/10.1093/MNRAS/STZ1317.

Geha, M. et al. (2017). "The SAGA Survey. I. Satellite Galaxy Populations around Eight Milky Way Analogs." *ApJ* 847.1, 4, p. 4. DOI: 10.3847/1538-4357/aa8626.

Genzel, R. et al. (2010). "A Study of the Gas-Star Formation Relation Over Cosmic Time." *MNRAS* 407.4, pp. 2091–2108. ISSN: 00358711. DOI: 10.1111/j.1365-2966.2010.16969.x.

Giammichele, N., P. Bergeron, and P. Dufour (2012). "Know Your Neighborhood: A Detailed Model Atmosphere Analysis of Nearby White Dwarfs." *ApJS* 199.2, p. 29. ISSN: 0067-0049. DOI: 10.1088/0067-0049/199/2/29.

Gil de Paz, A. et al. (2007). "The GALEX Ultraviolet Atlas of Nearby Galaxies." *ApJS* 173.2, pp. 185–255. ISSN: 0067-0049. DOI: 10.1086/516636.

Gilmore, G. and R. F. G. Wyse (1991). "Chemical Evolution with Bursts of Star Formation - Element Ratios in Dwarf Galaxies." *ApJ* 367, p. L55. ISSN: 0004-637X. DOI: 10.1086/185930.

Glover, S. C. O. and M. .-.-M. Mac Low (2010). "On the Relationship Between Molecular Hydrogen and Carbon Monoxide Abundances in Molecular Clouds." *MNRAS* 412, pp. 337–350. ISSN: 0035-8711. DOI: 10.1111/j.1365-2966.2010.17907.x.

Goddard, Q. E., R. C. Kennicutt, and E. V. Ryan-Weber (2010). "On the Nature of Star Formation at Large Galactic Radii." *MNRAS* 405, pp. 2791–2809. ISSN: 0035-8711. DOI: 10.1111/j.1365-2966.2010.16661.x.

Goldberg, D. M. and M. S. Vogeley (2004). "Simulating Voids." *ApJ* 605.1, pp. 1–6. ISSN: 0004-637X. DOI: 10.1086/382143.

Graur, O. et al. (2011). "Supernovae in the Subaru Deep Field: The Rate and Delay-time Distribution of Type Ia Supernovae out to Redshift 2." *MNRAS* 417.2, pp. 916–940. DOI: 10.1111/j.1365-2966.2011.19287.x.

Grcevich, J. and M. E. Putman (2009). "HI in Local Group Dwarf Galaxies and Stripping by the Galactic Halo." *ApJ* 696, pp. 385–395. DOI: 10.1088/0004-637X/696/1/385.

Greggio, L. (2005). "The Rates of Type Ia Supernovae. I. Analytical Formulations." *A&A* 441.3, p. 1055. ISSN: 0004-6361. DOI: 10.1051/0004-6361:20052926.

Griffith, E. J. et al. (2021). "The Impact of Black Hole Formation on Population-averaged Supernova Yields." *ApJ* 921.1, 73, p. 73. DOI: 10.3847/1538-4357/ac1bac.

Grogin, N. A. and M. J. Geller (1999). "An Imaging and Spectroscopic Survey of Galaxies within Prominent Nearby Voids. I. The Sample and Luminosity Distribution." *AJ* 118.6, pp. 2561–2580. ISSN: 00046256. DOI: 10.1086/301126. URL: doi.org/10.1086/301126.

– (2000). "An Imaging and Spectroscopic Survey of Galaxies within Prominent Nearby Voids. II. Morphologies, Star Formation, and Faint Companions." *AJ* 119.1, pp. 32–43. ISSN: 00046256. DOI: 10.1086/301179.

Gustafsson, B. et al. (1975). "A Grid of Model Atmospheres for Metal-deficient Giant Stars." *A&A* 42, pp. 407–432.

Gustafsson, B. et al. (2003). "A Grid of Model Atmospheres for Cool Stars." *Stellar Atmosphere Modeling*. Ed. by I. Hubeny, D. Mihalas, and K. Werner. Vol. 288. Astronomical Society of the Pacific Conference Series, p. 331.

Gustafsson, B. et al. (2008). "A Grid of MARCS Model Atmospheres for Late-type Stars. I. Methods and General Properties." *A&A* 486.3, pp. 951–970. DOI: 10.1051/0004-6361:200809724.

Hao, C.-N. et al. (2011). "Dust-Corrected Star Formation Rates of Galaxies. II. Combinations of Ultraviolet and Infrared Tracers." *ApJ* 741.124, p. 22. DOI: 10.1088/0004-637X/741/2/124.

Harris, W. E. (1996). "A Catalog of Parameters for Globular Clusters in the Milky Way." *AJ* 112, p. 1487. ISSN: 00046256. DOI: 10.1086/118116.

Helmi, A. et al. (2018). "The Merger that Led to the Formation of the Milky Way's Inner Stellar Halo and Thick Disk." *Nature* 563.7729, pp. 85–88. DOI: 10.1038/s41586-018-0625-x.

Hernandez, X., G. Gilmore, and D. Valls-Gabaud (2000). "Non-parametric Star Formation Histories for 5 Dwarf Spheroidal Galaxies of the Local Group." *MNRAS* 317.4, pp. 831–842. DOI: 10.1046/j.1365-8711.2000.03809.x.

Hill, V. et al. (2019). "VLT/FLAMES High-resolution Chemical Abundances in Sculptor: A Textbook Dwarf Spheroidal Galaxy." *A&A* 626, p. 15. ISSN: 14320746. DOI: 10.1051/0004-6361/201833950.

Hirai, Y. et al. (2017). "Early Chemo-dynamical Evolution of Dwarf Galaxies Deduced from Enrichment of r-process Elements." *MNRAS* 466.2, pp. 2474–2487. ISSN: 13652966. DOI: 10.1093/mnras/stw3342.

Hogg, D. W., J. Bovy, and D. Lang (2010). "Data Analysis Recipes: Fitting a Model to Data."

Hogg, D. et al. (2001). "Hot and Cold Gas in Early-Type Spirals: NGC 3623, NGC 2775, and NGC 1291." *AJ* 121, pp. 1336–1357. DOI: 10.1086/319400.

Holmberg, E. (1958). "A Photographic Photometry of Extragalactic Nebulae." *MeLuS* 136, p. 1. URL: http://adsabs.harvard.edu/abs/1958MeLuS.136....1H.

Homma, H. et al. (2015). "A New Chemical Evolution Model for Dwarf Spheroidal Galaxies Based on Observed Long Star Formation Histories." *ApJ* 799.2, p. 230. ISSN: 15384357. DOI: 10.1088/0004-637X/799/2/230.

Hoyle, F. and M. S. Vogeley (2002). "Voids in the Point Source Catalogue Survey and the Updated Zwicky Catalog." *ApJ* 566.2, pp. 641–651. DOI: 10.1086/338340.

Huchtmeier, W. and O.-G. Richter (1989). *A General Catalog of HI Observations of Galaxies. The Reference Catalog*. Springer-Verlag New York, p. 350.

Hunt, L. K. et al. (2018). "Comprehensive Comparison of Models for Spectral Energy Distributions from 0.1 micron to 1 mm of Nearby Star-forming Galaxies." *A&A* 621, A51. DOI: 10.1051/0004-6361/201834212.

Hunt, L. et al. (2015). "Molecular Depletion Times and the CO-to-H_2 Conversion Factor in Metal-poor Galaxies." *A&A* 583, A114. DOI: 10.1051/0004-6361/201526553.

Hunter, D., H. van Woerden, and J. Gallagher III (1994). "Neutral Hydrogen and Optical Properties of Three Amorphous Galaxies." *ApJS* 91, pp. 79–110. DOI: 10.1086/191938.

Hunter, D., H. van Woerden, and J. Gallagher (1999). "Neutral Hydrogen and Star Formation in the Irregular Galaxy NGC 4449." *AJ* 118, pp. 2184–2210. DOI: 10.1086/301096.

Hunter, D., C. Walker, and E. Wilcots (2000). "Observations of Cold and Warm CO in the Irregular Galaxy NGC 4449." *AJ* 119, pp. 668–680. DOI: 10.1086/301225.

Hunter, D. et al. (2012). "Little Things." *AJ* 144, p. 134. DOI: 10.1088/0004-6256/144/5/134.

Husemann, B. et al. (2013). "CALIFA, the Calar Alto Legacy Integral Field Area Survey. II. First Public Data Release." *A&A* 549, A87, A87. DOI: 10.1051/0004-6361/201220582.

Iben, I. and A. V. Tutukov (1984). "Supernovae of Type I as End Products of the Evolution of Binaries with Components of Moderate Initial Mass (M Not Greater than about 9 Solar Masses)." *ApJS* 54, p. 335. ISSN: 0067-0049. DOI: 10.1086/190932.

Illingworth, G. (1977). "Rotation (?) in 13 Elliptical Galaxies." *ApJL* 218, pp. L43–L47. DOI: 10.1086/182572.

Irwin, J. and E. Seaquist (1991). "The Neutral Hydrogen Distribution of NGC 3079." *ApJ* 371, pp. 111–130. DOI: 10.1086/169875.

Israel, F. (2005). "Molecular Gas in Compact Galaxies." *A&A* 438, pp. 855–866. DOI: 10.1051/0004-6361:20042237.

Iwamoto, K. et al. (1999). "Nucleosynthesis in Chandrasekhar Mass Models for Type Ia Supernovae and Constraints on Progenitor Systems and Burning-Front Propagation." *ApJS* 125.2, pp. 439–462. ISSN: 0067-0049. DOI: 10.1086/313278.

Ji, A. P. et al. (2016). "Complete Element Abundances of Nine Stars in the r-process Galaxy Reticulum II." *ApJ* 830.2, p. 93. ISSN: 0004-637X. DOI: 10.3847/0004-637X/830/2/93.

Johnson, C. I. and C. A. Pilachowski (2010). "Chemical Abundances for 855 Giants in the Globular Cluster Omega Centauri (NGC 5139)." *ApJ* 722.2, pp. 1373–1410. ISSN: 15384357. DOI: 10.1088/0004-637X/722/2/1373.

Jones, E., T. Oliphant, P. Peterson, et al. (2001–). *SciPy: Open Source Scientific Tools for Python*. URL: http://www.scipy.org/.

Jore, K. (1997). "The Kinematics and Dynamics of SA Galaxies." PhD thesis. Cornell University.

Jorsater, S. and G. van Moorsel (1995). "High Resolution Neutral Hydrogen Observations of the Barred Spiral Galaxy NGC 1365." *AJ* 110, p. 2037. DOI: 10.1086/117668.

Karakas, A. I. and M. Lugaro (2016). "Stellar Yields from Metal-Rich Asymptotic Giant Branch Models." *ApJ* 825.1, p. 26. ISSN: 0004-637X. DOI: 10.3847/0004-637x/825/1/26.

Karakas, A. I. et al. (2018). "Heavy-element Yields and Abundances of Asymptotic Giant Branch Models with a Small Magellanic Cloud Metallicity." *MNRAS* 477.1, pp. 421–437. ISSN: 13652966. DOI: 10.1093/mnras/sty625.

Kauffmann, G. et al. (2003). "Stellar Masses and Star Formation Histories for 10^5 Galaxies from the Sloan Digital Sky Survey." *MNRAS* 341.1, pp. 33–53. DOI: 10.1046/j.1365-8711.2003.06291.x.

Kawata, D. et al. (2006). "Origin of Two Distinct Populations in Dwarf Spheroidal Galaxies." *ApJ* 641.2, pp. 785–794. DOI: 10.1086/500633.

Kazantzidis, S. et al. (2011). "On the Efficiency of the Tidal Stirring Mechanism for the Origin of Dwarf Spheroidals: Dependence on the Orbital and Structural Parameters of the Progenitor Disky Dwarfs." *ApJ* 726.2, 98, p. 98. DOI: 10.1088/0004-637X/726/2/98.

Kazantzidis, S. et al. (2017). "The Effects of Ram-pressure Stripping and Supernova Winds on the Tidal Stirring of Disky Dwarfs: Enhanced Transformation into Dwarf Spheroidals." *ApJL* 836.1, L13, p. L13. DOI: 10.3847/2041-8213/aa5b8f.

Kelly, B. C. (2007). "Some Aspects of Measurement Error in Linear Regression of Astronomical Data." *ApJ* 665.2, pp. 1489–1506. DOI: 10.1086/519947.

Kennicutt Robert C., J. and M. A. C. de los Reyes (2021). "Revisiting the Integrated Star Formation Law. II. Starbursts and the Combined Global Schmidt Law." *ApJ* 908.1, 61, p. 61. DOI: 10.3847/1538-4357/abd3a2.

Kennicutt, R. C. (1989). "The Star Formation Law in Galactic Disks." *ApJ* 344, p. 685. ISSN: 0004-637X. DOI: 10.1086/167834.

– (1998). "The Global Schmidt Law in Star-forming Galaxies." *ApJ* 498, pp. 541–552. ISSN: 0004-637X. DOI: 10.1086/305588.

Kennicutt, R. C. and N. J. Evans (2012). "Star Formation in the Milky Way and Nearby Galaxies." *ARA&A* 50.1, pp. 531–608. ISSN: 0066-4146. DOI: 10.1146/annurev-astro-081811-125610.

Kennicutt, R. C. et al. (2007). "Star Formation in NGC 5194 (M51a). II. The Spatially Resolved Star Formation Law." *ApJ* 671.1, pp. 333–348. ISSN: 0004-637X. DOI: 10.1086/522300.

Kennicutt, R. C. et al. (2008). "An Hα Imaging Survey of Galaxies in the Local 11 Mpc Volume." *ApJS* 178.2, pp. 247–279. ISSN: 0067-0049. DOI: 10.1086/590058.

Kent, S. M. (1985). "CCD Surface Photometry of Field Galaxies. II. Bulge/Disk Decompositions." *ApJS* 59, pp. 115–159.

Kepley, A. et al. (2016). "The Molecular Clouds Fueling A 1/5 Solar Metallicity Starburst." *ApJ* 828, p. 50. DOI: 10.3847/0004-637X/828/1/50.

Kewley, L. J., R. A. Jansen, and M. J. Geller (2005). "Aperture Effects on Star Formation Rate, Metallicity, and Reddening." *PASP* 117.829, pp. 227–244. ISSN: 0004-6280. DOI: 10.1086/428303. eprint: 0501229 (astro-ph).

Khokhlov, A. (1991). "Delayed Detonation Model for Type Ia Supernovae." *A&A* 245.1, pp. 114–128.

Kilborn, V. et al. (2005). "A Wide-field HI Study of the NGC 1566 Group." *MNRAS* 356, pp. 77–88. DOI: 10.1111/j.1365-2966.2004.08450.x.

Kim, C.-G., W.-T. Kim, and E. C. Ostriker (2011). "Regulation of Star Formation Rates in Multiphase Galactic Disks: Numerical Tests of the Thermal/Dynamical Equilibrium Model." *ApJ* 743.1, p. 25. ISSN: 0004-637X. DOI: 10.1088/0004-637X/743/1/25.

Kim, C.-G. and E. C. Ostriker (2015). "Vertical Equilibrium, Energetics, and Star Formation Rates in Magnetized Galactic Disks Regulated by Momentum Feedback from Supernovae." *ApJ* 815.1, p. 67. ISSN: 0004-637X. DOI: 10.1088/0004-637X/815/1/67.

Kirby, E. N. et al. (2009). "Multi-Element Abundance Measurements from Medium-Resolution Spectra. I. The Sculptor Dwarf Spheroidal Galaxy." *ApJ* 705, pp. 328–346. ISSN: 0004-637X. DOI: 10.1088/0004-637X/705/1/328.

Kirby, E. N. et al. (2010). "Multi-Element Abundance Measurements from Medium-Resolution Spectra. II. Catalog of Stars in Milky Way Dwarf Satellite Galaxies." *ApJS* 191.2, pp. 352–375. ISSN: 00670049. DOI: 10.1088/0067-0049/191/2/352.

Kirby, E. N. et al. (2011). "Multi-Element Abundance Measurements from Medium-Resolution Spectra. IV. Alpha Element Distributions in Milky Way Dwarf Satellite Galaxies." *ApJ* 727.2, p. 79. DOI: 10.1088/0004-637X/727/2/79.

Kirby, E. N. et al. (2013). "The Universal Stellar Mass-Stellar Metallicity Relation for Dwarf Galaxies." *ApJ* 779.2, p. 102. ISSN: 15384357. DOI: 10.1088/0004-637X/779/2/102.

Kirby, E. N. et al. (2014). "The Dynamics of Isolated Local Group Galaxies." *MNRAS* 439.1, pp. 1015–1027. DOI: 10.1093/mnras/stu025.

Kirby, E. N. et al. (2015). "Carbon in Red Giants in Globular Clusters and Dwarf Spheroidal Galaxies." *ApJ* 801.2, p. 125. ISSN: 1538-4357. DOI: 10.1088/0004-637X/801/2/125.

Kirby, E. N. et al. (2016). "Lithium-rich Giants in Globular Clusters." *ApJ* 819.2, p. 135. ISSN: 1538-4357. DOI: 10.3847/0004-637X/819/2/135.

Kirby, E. N. et al. (2017). "Chemistry and Kinematics of the Late-forming Dwarf Irregular Galaxies Leo A, Aquarius, and Sagittarius DIG." *ApJ* 834.1, 9, p. 9. DOI: 10.3847/1538-4357/834/1/9.

Kirby, E. N. et al. (2018). "Catalog of Chromium, Cobalt, and Nickel Abundances in Globular Clusters and Dwarf Galaxies." *ApJSupplement Series* 237.1, p. 18. ISSN: 1538-4365. DOI: 10.3847/1538-4365/aac952.

Kirby, E. N. et al. (2019). "Evidence for Sub-Chandrasekhar Type Ia Supernovae from Stellar Abundances in Dwarf Galaxies." *ApJ* 881.1, p. 45. ISSN: 1538-4357. DOI: 10.3847/1538-4357/ab2c02.

Knapen, J. (1997). "Atomic Hydrogen in the Spiral Galaxy NGC 3631." *MNRAS* 286, pp. 403–414. DOI: 10.1093/mnras/286.2.403.

Kniazev, A. Y., E. S. Egorova, and S. A. Pustilnik (2018). "Study of Galaxies in the Eridanus Void. Sample and Oxygen Abundances." *MNRAS* 479.3, pp. 3842–3857. ISSN: 0035-8711. DOI: 10.1093/mnras/sty1704.

Kobayashi, C., S.-C. Leung, and K. Nomoto (2020). "New Type Ia Supernova Yields and the Manganese and Nickel Problems in the Milky Way and Dwarf Spheroidal Galaxies." *ApJ* 895.2, p. 138. ISSN: 0004-637X. DOI: 10.3847/1538-4357/AB8E44.

Kobayashi, C. and K. Nomoto (2009). "The Role of Type Ia Supernovae in Chemical Evolution. I. Lifetime of Type Ia Supernovae and Metallicity effect." *ApJ* 707.2, pp. 1466–1484. ISSN: 0004-637X. DOI: 10.1088/0004-637X/707/2/1466.

Kobayashi, C., K. Nomoto, and I. Hachisu (2015). "Subclasses of Type Ia Supernovae as the Origin of [α/Fe] Ratios in Dwarf Spheroidal Galaxies." *ApJL* 804.1, p. L24. ISSN: 20418213. DOI: 10.1088/2041-8205/804/1/L24.

Kobayashi, C. et al. (2006). "Galactic Chemical Evolution: Carbon through Zinc." *ApJ* 653.2, pp. 1145–1171. ISSN: 0004-637X. DOI: 10.1086/508914.

Kobulnicky, H. et al. (1995). "Aperture Synthesis Observations of Molecular and Atomic Gas in the Wolf- Rayet Starburst Galaxy." *AJ* 110, p. 116. DOI: 10.1086/117500.

Kollmeier, J. A. et al. (2017). "SDSS-V: Pioneering Panoptic Spectroscopy." *arXiv e-prints*, arXiv:1711.03234, arXiv:1711.03234. arXiv: 1711.03234 [astro-ph.GA].

Komugi, S. et al. (2008). "Molecular Gas Distribution in Barred and Nonbarred Galaxies along the Hubble Sequence." *ApJS* 178, pp. 225–246. DOI: 10.1086/590469.

Komugi, S. et al. (2011). "Deep CO Observations and the CO-to-H$_{2}$ Conversion Factor in DDO 154, a L ow Metallicity Dwarf Irregular Galax." *PASJ* 63, pp. L1–L5. DOI: 10.1093/pasj/63.1.L1.

Konidaris, N. P. et al. (2020). "SDSS-V Local Volume Mapper Instrument: Overview and Status." *Society of Photo-Optical Instrumentation Engineers (SPIE) Conference Series*. Vol. 11447, p. 1144718. DOI: 10.1117/12.2557565.

Kramida, A. et al. (2014). *NIST Atomic Spectra Database (ver. 5.2)*. Online. URL: physics.nist.gov/asd.

Kreckel, K. et al. (2012). "The Void Galaxy Survey: Optical Properties and HI Morphology and Kinematics." *AJ* 1, p. 16. ISSN: 0004-6256. DOI: 10.1088/0004-6256/144/1/16.

Kreckel, K. et al. (2014). "The Metallicity of Void Dwarf Galaxies." *ApJ* 798.1, p. L15. ISSN: 2041-8213. DOI: 10.1088/2041-8205/798/1/L15.

Kromer, M. et al. (2015). "Deflagrations in Hybrid CONe White Dwarfs: A Route to Explain the Faint Type Iax Supernova 2008ha." *MNRAS* 450.3, pp. 3045–3053. ISSN: 0035-8711. DOI: 10.1093/mnras/stv886.

Kroupa, P., C. A. Tout, and G. Gilmore (1993). "The Distribution of Low-mass Stars in the Galactic Disc." *MNRAS* 262.3, pp. 545–587. ISSN: 0035-8711. DOI: 10.1093/mnras/262.3.545.

Kroupa, P. (2000). "On the Variation of the Initial Mass Function." *MNRAS* 322, pp. 231–246. ISSN: 0035-8711. DOI: 10.1046/j.1365-8711.2001.04022.x.

Kruijssen, J. M. D. et al. (2019). "The Formation and Assembly History of the Milky Way Revealed by its Globular Cluster Population." *MNRAS* 486.3, pp. 3180–3202. DOI: 10.1093/mnras/sty1609.

Krumholz, M. R., A. Dekel, and C. F. Mckee (2012). "A Universal, Local Star Formation Law in Galactic Clouds, Nearby Galaxies, High-Redshift Disks, and Starbursts." *ApJ* 745.16pp, p. 69. ISSN: 0004-637X. DOI: 10.1088/0004-637X/745/1/69.

Kuno, N. et al. (2007). "Nobeyama CO Atlas of Nearby Spiral Galaxies: Distribution of Molecular Gas in Barred and Nonbarred Spiral Galaxies." *PASJ* 59, pp. 117–166. DOI: 10.1093/pasj/59.1.117.

Kurucz, R. (1993). "ATLAS9 Stellar Atmosphere Programs and 2 km/s grid." *ATLAS9 Stellar Atmos. Programs 2 km/s grid. Kurucz CD-ROM No. 13. Cambridge* 13. URL: adsabs.harvard.edu/abs/1993KurCD..13.....K.

Lagos, P. et al. (2018). "Detecting Metal-poor Gas Accretion in the Star-forming Dwarf Galaxies UM 461 and Mrk 600." *MNRAS* 477.1, pp. 392–411. DOI: 10.1093/mnras/sty601.

Laine, S. and S. Gottesman (1998). "Neutral Hydrogen Gas Distribution and Kinematics in NGC 7479." *MNRAS* 297, pp. 1041–1051. DOI: 10.1046/j.1365-8711.1998.01513.x.

Lanfranchi, G. A. and F. Matteucci (2003). "Chemical Evolution of Dwarf Spheroidal and Blue Compact Galaxies." *MNRAS* 345.1, pp. 71–85. DOI: 10.1046/j.1365-8711.2003.06919.x.

– (2004). "The Predicted Metallicity Distribution of Stars in Dwarf Spheroidal Galaxies." *MNRAS* 351.4, pp. 1338–1348. DOI: 10.1111/j.1365-2966.2004.07877.x.

Lardo, C. et al. (2013). "The Double RGB in M 2: C, N, Sr and Ba Abundances." *MNRAS* 433.3, pp. 1941–1950. DOI: 10.1093/mnras/stt854.

Larson, R. B. (1972). "Infall of Matter in Galaxies." *Nature* 236.5340, pp. 21–23. ISSN: 00280836. DOI: 10.1038/236021a0.

– (1974). "Effects of Supernovae on the Early Evolution of Galaxies." *MNRAS* 169.2, pp. 229–245. ISSN: 0035-8711. DOI: 10.1093/mnras/169.2.229.

Law, D. R. et al. (2016). "The Data Reduction Pipeline for the SDSS-IV MaNGA IFU Galaxy Survey." *AJ* 152.4, 83, p. 83. DOI: 10.3847/0004-6256/152/4/83.

Leaman, R. et al. (2012). "The Resolved Structure and Dynamics of an Isolated Dwarf Galaxy: A VLT and Keck Spectroscopic Survey of WLM." *ApJ* 750.1, 33, p. 33. DOI: 10.1088/0004-637X/750/1/33.

Lee, H. et al. (2006a). "On Extending the Mass-Metallicity Relation of Galaxies by 2.5 Decades in Stellar Mass." *ApJ* 647, pp. 970–983. DOI: 10.1086/505573.

– (2006b). "On Extending the Mass-Metallicity Relation of Galaxies by 2.5 Decades in Stellar Mass." *ApJ* 647.2, pp. 970–983. ISSN: 0004-637X. DOI: 10.1086/505573. URL: https://doi.org/10.1086/505573.

Lee, J. C. et al. (2009). "Comparison of Hα and UV Star Formation Rates in the Local Volume: Systematic Discrepancies for Dwarf Galaxies." *ApJ* 706.1, pp. 599–613. ISSN: 0004-637X. DOI: 10.1088/0004-637X/706/1/599.

Lee, J. C. et al. (2011). "A GALEX Ultraviolet Imaging Survey of Galaxies in the Local Volume." *ApJS* 192.1, p. 6. ISSN: 0067-0049. DOI: 10.1088/0067-0049/192/1/6.

Leethochawalit, N. et al. (2019). "Evolution of the Stellar Mass-Metallicity Relation. II. Constraints on Galactic Outflows from the Mg Abundances of Quiescent Galaxies." *ApJ* 885.2, p. 100. ISSN: 0004-637X. DOI: 10.3847/1538-4357/AB4809.

Leja, J. et al. (2019). "How to Measure Galaxy Star Formation Histories. II. Non-parametric Models." *ApJ* 876.1. DOI: 10.3847/1538-4357/ab133c.

Lelli, F., M. Verheijen, and F. Fraternali (2014). "Dynamics of Starbursting Dwarf Galaxies. III. A H I Study of 18 Nearby Objects." *A&A* 566, A71. DOI: 10.1051/0004-6361/201322657.

Leon, S., F. Combes, and T. K. Menon (1997). "Molecular Gas in Galaxies of Hickson Compact Groups." *A&A* 330, pp. 37–56. ISSN: 0004-6361.

Leonard, D. C. (2007). "Constraining the Type Ia Supernova Progenitor: The Search for Hydrogen in Nebular Spectra." *ApJ* 670.2, pp. 1275–1282. DOI: 10.1086/522367.

Leroy, A. K. et al. (2006). "Molecular Gas in the Low-Metallicity, Star-forming Dwarf IC 10." *ApJ* 643, pp. 825–843. DOI: 10.1086/503024.

Leroy, A. K. et al. (2007). "The Low CO Content of the Extremely Metal-poor Galaxy I Zw 18." *ApJ* 663, pp. 990–994. DOI: 10.1086/518501.

Leroy, A. K. et al. (2008). "The Star Formation Efficiency in Nearby Galaxies: Measuring Where Gas Forms Stars Effectively." *AJ* 136, pp. 2782–2845. DOI: 10.1088/0004-6256/136/6/2782.

Leroy, A. K. et al. (2012). "Estimating the Star Formation Rate at 1kpc Scales in Nearby Galaxies." *AJ* 144.1, p. 3. DOI: 10.1088/0004-6256/144/1/3.

Leroy, A. K. et al. (2013). "Molecular Gas and Star Formation in Nearby Disk Galaxies." *AJ* 146, p. 19. DOI: 10.1088/0004-6256/146/2/19.

Leroy, A. et al. (2005). "The Molecular Interstellar Medium of Dwarf Galaxies on Kiloparsec Scales: A New Survey for CO in Northern, IRAS-detected Dwarf Galaxies." *ApJ* 625, pp. 763–784. DOI: 10.1086/429578.

Lesaffre, P. et al. (2006). "The C Flash and the Ignition Conditions of Type Ia Supernovae." *MNRAS* 368.1, pp. 187–195. ISSN: 0035-8711. DOI: 10.1111/j.1365-2966.2006.10068.x.

Letarte, B. et al. (2010). "A High Resolution VLT/FLAMES Study of Individual Stars in the Centre of the Fornax Dwarf Spheroidal Galaxy." *A&A* 523, A17. ISSN: 0004-6361. DOI: 10.1051/0004-6361/200913413.

Leung, S.-C. and K. Nomoto (2018). "Explosive Nucleosynthesis in Near-Chandrasekhar-mass White Dwarf Models for Type Ia Supernovae: Dependence on Model Parameters." *ApJ* 861.2, p. 143. ISSN: 1538-4357. DOI: 10.3847/1538-4357/aac2df.

– (2020). "Explosive Nucleosynthesis in Sub-Chandrasekhar Mass White Dwarf Models for Type Ia Supernovae: Dependence on Model Parameters." *ApJ* 888.2, p. 80. DOI: 10.3847/1538-4357/ab5c1f.

Li, H. et al. (2014). "Estimating R-Process Yields from Abundances of the Metal-Poor Stars." *PASP* 126.940, pp. 544–552. DOI: 10.1086/677201.

Li, J., E. Seaquist, and L. Sage (1993). "Molecular Gas in the Early-type Starburst Galaxy NGC 3928." *ApJL* 411, pp. L71–L74. DOI: 10.1086/186915.

Limongi, M. and A. Chieffi (2018). "Presupernova Evolution and Explosive Nucleosynthesis of Rotating Massive Stars in the Metallicity Range -3 < [Fe/H] < 0." *ApJS* 237.1, p. 13. ISSN: 23318422. DOI: 10.3847/1538-4365/aacb24.

Lin, D. N. C. and S. M. Faber (1983). "Some Implications of Nonluminous Matter in Dwarf Spheroidal Galaxies." *ApJ* 266, p. L21. ISSN: 0004-637X. DOI: 10.1086/183971.

Liszt, H. and J. Dickey (1995). "HI Emission from the Seyfert Galaxies NGC 4051 and NGC 6814." *AJ* 110, p. 998. DOI: 10.1086/117579.

Liu, G. et al. (2011). "The Super-Linear Slope of the Spatially Resolved Star Formation Law in NGC 3521 and NGC 5194 (M51a)." *ApJ* 735.1, p. 63. ISSN: 0004-637X. DOI: 10.1088/0004-637X/735/1/63.

Liu, L., Y. Gao, and T. R. Greve (2015). "The Global Star Formation Laws of Galaxies from a Radio Continuum Perspective." *ApJ* 805.1, p. 31. ISSN: 1538-4357. DOI: 10.1088/0004-637X/805/1/31.

Livne, E. (1990). "Successive Detonations in Accreting White Dwarfs as an Alternative Mechanism for Type I Supernovae." *ApJ* 354, p. L53. ISSN: 0004-637X. DOI: 10.1086/185721.

López-Sánchez, Á. R. et al. (2018). "The Disc-averaged Star Formation Relation for Local Volume Dwarf Galaxies." *MNRAS* 480.1, pp. 210–222. ISSN: 0035-8711. DOI: 10.1093/mnras/sty1272.

Lugaro, M. et al. (2012). "The s process in Asymptotic Giant Branch Stars of Low Metallicity and the Composition of Carbon-enhanced Metal-poor Stars." *ApJ* 747.1, p. 2. DOI: 10.1088/0004-637X/747/1/2.

Lundqvist, P. et al. (2013). "Hydrogen and Helium in the Spectra of Type Ia Supernovae." *MNRAS* 435.1, pp. 329–345. DOI: 10.1093/mnras/stt1303.

Lynden-Bell, D. (1975). "The Chemical Evolution of Galaxies." *Vistas in Astronomy* 19.3, pp. 299–316. ISSN: 00836656. DOI: 10.1016/0083-6656(75)90005-7.

Madden, S. C. et al. (2020). "Tracing the Total Molecular Gas in Galaxies: [CII] and the CO-dark Gas." *A&A* 643, A141, A141. DOI: 10.1051/0004-6361/202038860.

Magris C., G. et al. (2015). "On the Recovery of Galaxy Properties from SED Fitting Solutions." *PASP* 127.947, pp. 16–30. ISSN: 00046280. DOI: 10.1086/679742.

Majewski, S. R. et al. (2017). "The Apache Point Observatory Galactic Evolution Experiment (APOGEE)." *AJ* 154.3, p. 94. ISSN: 1538-3881. DOI: 10.3847/1538-3881/aa784d.

Mannucci, F., M. Della Valle, and N. Panagia (2005). "Two Populations of Progenitors for Type Ia SNe?" *MNRAS* 370.2, pp. 773–783. DOI: 10.1111/j.1365-2966.2006.10501.x.

Mao, Y.-Y. et al. (2021). "The SAGA Survey. II. Building a Statistical Sample of Satellite Systems around Milky Way-like Galaxies." *ApJ* 907.2, 85, p. 85. DOI: 10.3847/1538-4357/abce58.

Maoz, D. and F. Mannucci (2012). "Type Ia Supernova Rates and the Progenitor Problem: A review." *PASA* 29.4, pp. 447–465. ISSN: 13233580. DOI: 10.1071/AS11052.

Maoz, D. and C. Badenes (2010). "The Supernova Rate and Delay Time Distribution in the Magellanic Clouds." *MNRAS* 407.2, pp. 1314–1327. DOI: 10.1111/j.1365-2966.2010.16988.x.

Maoz, D. and O. Graur (2017). "Star Formation, Supernovae, Iron, and α: Consistent Cosmic and Galactic Histories." *ApJ* 848.1, 25, p. 25. DOI: 10.3847/1538-4357/aa8b6e.

Maoz, D., F. Mannucci, and T. D. Brandt (2012). "The Delay-time Distribution of Type Ia Supernovae from Sloan II." *MNRAS* 426.4, pp. 3282–3294. ISSN: 00358711. DOI: 10.1111/j.1365-2966.2012.21871.x.

Maoz, D., F. Mannucci, and G. Nelemans (2014). "Observational Clues to the Progenitors of Type Ia Supernovae." *ARA&A* 52.1, pp. 107–170. ISSN: 0066-4146. DOI: 10.1146/annurev-astro-082812-141031.

Maoz, D., K. Sharon, and A. Gal-Yam (2010). "The Supernova Delay Time Distribution in Galaxy Clusters and Implications for Type-Ia Progenitors and Metal Enrichment." *ApJ* 722.2, pp. 1879–1894. ISSN: 15384357. DOI: 10.1088/0004-637X/722/2/1879.

Maoz, D. et al. (2011). "Nearby Supernova Rates from the Lick Observatory Supernova Search - IV. A Recovery Method for the Delay-time Distribution." *MNRAS* 412.3, pp. 1508–1521. DOI: 10.1111/j.1365-2966.2010.16808.x.

Marcolini, A. et al. (2006). "Star Formation Feedback and Metal Enrichment by SN Ia and SN II in Dwarf Spheroidal Galaxies: The Case of Draco." *MNRAS* 371.2, pp. 643–658. DOI: 10.1111/j.1365-2966.2006.10671.x.

Marcolini, A. et al. (2008). "The Chemical Evolution of Dwarf Spheroidal Galaxies: Dissecting the Inner Regions and their Stellar Populations." *MNRAS* 386.4, pp. 2173–2180. DOI: 10.1111/j.1365-2966.2008.13175.x.

Margutti, R. et al. (2012). "Inverse Compton X-ray emission from supernovae with compact progenitors: Application to SN2011fe." *ApJ* 751.2, p. 134. ISSN: 0004-637X. DOI: 10.1088/0004-637X/751/2/134. URL: doi.org/10.1088/0004-637X/751/2/134.

Marigo, P. and L. Girardi (2007). "Evolution of Asymptotic Giant Branch Stars I. Updated Synthetic TP-AGB Models and Their Basic Calibration." *A&A* 469.1, pp. 239–263. ISSN: 00046361. DOI: 10.1051/0004-6361:20066772.

Martin, C. L. and R. C. Kennicutt (2001). "Star Formation Thresholds in Galactic Disks." *ApJ* 555, pp. 301–321. DOI: 10.1086/321452.

Martin, D. C. et al. (2005). "The Galaxy Evolution Explorer: A Space Ultraviolet Survey Mission." *ApJL* 619.1, pp. L1–L6. DOI: 10.1086/426387.

Martínez-Rodríguez, H. et al. (2016). "Neutronization During Carbon Simmering in Type Ia Supernova Progenitors." *ApJ* 825.1, p. 57. ISSN: 1538-4357. DOI: 10.3847/0004-637X/825/1/57.

Mashonkina, L. et al. (2019). "Influence of Inelastic Collisions with Hydrogen Atoms on the Non-local Thermodynamic Equilibrium Line Formation for Fe i and Fe II in the 1D Model Atmospheres of Late-type Stars." *A&A* 631. ISSN: 14320746. DOI: 10.1051/0004-6361/201935753.

Massari, D. et al. (2014). "Chemical and Kinematical Properties of Galactic Bulge Stars Surrounding the Stellar System Terzan 5." *ApJ* 791.2. DOI: 10.1088/0004-637X/791/2/101.

Mathews, W. G. and J. C. Baker (1971). "Galactic Winds." *ApJ* 170, p. 241. ISSN: 0004-637X. DOI: 10.1086/151208.

Matteucci, F. (2012). *Chemical Evolution of Galaxies*. Astronomy and Astrophysics Library. Berlin, Heidelberg: Springer Berlin Heidelberg.

Matteucci, F. et al. (2014). "Europium Production: Neutron Star Mergers Versus Core-collapse Supernovae." *MNRAS* 438.3, pp. 2177–2185. ISSN: 00358711. DOI: 10.1093/mnras/stt2350.

Mayer, L. et al. (2001). "Tidal Stirring and the Origin of Dwarf Spheroidals in the Local Group." *ApJL* 547.2, pp. L123–L127. DOI: 10.1086/318898.

McConnachie, A. W. (2012). "The Observed Properties of Dwarf Galaxies in and around the Local Group." *The Astronomical Journal* 144, p. 4. DOI: 10.1088/0004-6256/144/1/4.

McConnachie, A. W. et al. (2016). "Science-based Requirements and Operations Development for the Maunakea Spectroscopic Explorer." *Proceedings of the SPIE*. Vol. 9906. SPIE. ISBN: 9781510601918. DOI: 10.1117/12.2232967.

McConnachie, A. W. et al. (2021). "Solo Dwarfs - III. Exploring the Orbital Origins of Isolated Local Group Galaxies with Gaia Data Release 2." *MNRAS* 501.2, pp. 2363–2377. DOI: 10.1093/mnras/staa3740.

McQuinn, K. B. W. et al. (2015). "Calibrating UV Star Formation Rates for Dwarf Galaxies from STARBIRDS." *ApJ* 808.2, p. 109. ISSN: 1538-4357. DOI: 10.1088/0004-637X/808/2/109.

McWilliam, A. et al. (2018). "Evidence for a Sub-Chandrasekhar-mass Type Ia Supernova in the Ursa Minor Dwarf Galaxy." *ApJ* 857.2, p. 97. ISSN: 1538-4357. DOI: 10.3847/1538-4357/aab772.

Meier, D., J. Turner, and S. Beck (2002). "Molecular Gas and the Young Starburst in NGC 5253 Revisited." *AJ* 124, pp. 877–885. DOI: 10.1086/341752.

Mennekens, N. et al. (2010). "The Delay-time Distribution of Type Ia Supernovae: A Comparison Between Theory and Observation." *A&A* 515, A89, A89. DOI: 10.1051/0004-6361/201014115.

Meurer, G. et al. (1996). "NGC 2915.II.A Dark Spiral Galaxy With a Blue Compact Dwarf Core." *AJ* 111, p. 1551. DOI: 10.1086/117895.

Momose, R. et al. (2013). "Star Formation on Subkiloparsec Scale Triggered by Non-Linear Processes in Nearby Spiral Galaxies." *ApJL* 772.1, p. L13. ISSN: 2041-8205. DOI: 10.1088/2041-8205/772/1/L13.

Monkiewicz, J. et al. (1999). "The Age of the Sculptor Dwarf Spheroidal Galaxy from Imaging with WFPC2." *PASP* 111.765, pp. 1392–1397. ISSN: 0004-6280. DOI: 10.1086/316447.

Moran, E. C. et al. (2014). "Black Holes At the Centers of Nearby Dwarf Galaxies." *AJ* 148.6, 136, p. 136. DOI: 10.1088/0004-6256/148/6/136.

Morokuma-Matsui, K. and K. Muraoka (2017). "Kennicutt-Schmidt Relation Variety and Star-forming Cloud Fraction." *ApJ* 837.2, p. 137. ISSN: 1538-4357. DOI: 10.3847/1538-4357/aa6115.

Morrissey, P. et al. (2005). "The On-Orbit Performance of the Galaxy Evolution Explorer." *ApJL* 619.1, pp. L7–L10. DOI: 10.1086/424734.

Morrissey, P. et al. (2007). "The Calibration and Data Products of GALEX." *ApJS* 173.2, pp. 682–697. DOI: 10.1086/520512.

Morrissey, P. et al. (2018). "The Keck Cosmic Web Imager Integral Field Spectrograph." *ApJ* 864.1, 93, p. 93. DOI: 10.3847/1538-4357/aad597.

Moustakas, J. and R. C. Kennicutt (2006). "An Integrated Spectrophotometric Survey of Nearby Star-Forming Galaxies." *ApJS* 164, pp. 81–98. ISSN: 0067-0049. DOI: 10.1086/500971.

Moustakas, J. et al. (2010). "Optical Spectroscopy and Nebular Oxygen Abundances of the Spitzer/SINGS Galaxies." *ApJS* 190.2, pp. 233–266. DOI: 10.1088/0067-0049/190/2/233.

Mulder, P., W. van Driel, and J. Braine (1995). "Distribution and Motions of H I and H_2 in the Peculiar Spiral Galaxy NGC 3310." *A&A* 300, p. 687.

Muñoz-Mateos, J. C. et al. (2013). "The Impact of Bars on Disk Breaks as Probed by S4G Imaging." *ApJ* 771. ISSN: 0004-637X. DOI: 10.1088/0004-637X/771/1/59.

Murphy, E. J. et al. (2011). "Calibrating Extinction-free Star Formation Rate Diagnostics with 33 GHz Free-free Emission in NGC 6946." *ApJ* 737, p. 67. DOI: 10.1088/0004-637X/737/2/67.

Narayanan, D. et al. (2012). "A General Model for the CO-H_2 Conversion Factor in Galaxies with Applications to the Star Formation Law." *MNRAS* 421.4, pp. 3127–3146. ISSN: 00358711. DOI: 10.1111/j.1365-2966.2012.20536.x.

Nelemans, G., S. Toonen, and M. Bours (2013). "Theoretical Delay Time Distributions." *Binary Paths to Type Ia Supernovae Explosions*. Ed. by R. Di Stefano, M. Orio, and M. Moe. Vol. 281, pp. 225–231. DOI: 10.1017/S1743921312015098.

Neugebauer, G. et al. (1984). "The Infrared Astronomical Satellite (IRAS) mission." *ApJL* 278, p. L1. ISSN: 0004-637X. DOI: 10.1086/184209.

Newman, J. A. et al. (2013). "The DEEP2 Galaxy Redshift Survey: Design, Observations, Data Reduction, and Redshifts." *ApJS* 208.1, p. 5. ISSN: 0067-0049. DOI: 10.1088/0067-0049/208/1/5.

Nieten, C. et al. (2006). "Molecular Gas in the Andromeda Galaxy." *A&A* 453, pp. 459–475. DOI: 10.1051/0004-6361:20035672.

Nomoto, K. (1982). "Accreting White Dwarf Models for Type 1 Supernovae. II. Off-center Detonation Supernovae." *ApJ* 257, p. 780. ISSN: 0004-637X. DOI: 10.1086/160031.

Nomoto, K., C. Kobayashi, and N. Tominaga (2013). "Nucleosynthesis in Stars and the Chemical Enrichment of Galaxies." *ARA&A* 51, pp. 457–509. ISSN: 00664146. DOI: 10.1146/annurev-astro-082812-140956.

Nomoto, K. et al. (2006). "Nucleosynthesis Yields of Core-collapse Supernovae and Hypernovae, and Galactic Chemical Evolution." *Nuclear Physics A* 777, pp. 424–458. ISSN: 03759474. DOI: 10.1016/j.nuclphysa.2006.05.008.

Noordermeer, E. et al. (2005). "The Westerbork HI Survey of Spiral and Irregular Galaxies. III. HI Observations of Early-type Disk Galaxies." *A&A* 442, pp. 137–157. DOI: 10.1051/0004-6361:20053172.

Nordgren, T. et al. (1998). "Very Wide Galaxy Pairs of the Northern and Southern Sky." *ApJS* 115, pp. 43–57. DOI: 10.1086/313078.

North, P. et al. (2012). "Manganese in Dwarf Spheroidal Galaxies." *A&A* 541, A45, A45. DOI: 10.1051/0004-6361/201118636.

Nuñez, E. H., E. N. Kirby, and C. C. Steidel (2022). "Empirical Constraints on Core-collapse Supernova Yields Using Very Metal-poor Damped Lyα Absorbers." *ApJ* 927.1, 64, p. 64. DOI: 10.3847/1538-4357/ac470e.

Oke, J. B. (1990). "Faint Spectrophotometric Standard Stars." *AJ* 99, p. 1621. DOI: 10.1086/115444.

Orr, M. E. et al. (2018). "What FIREs Up Star Formation: The Emergence of the Kennicutt-Schmidt Law from Feedback." *MNRAS* 478.3, p. 3653. ISSN: 0035-8711. DOI: 10.1093/mnras/sty1241.

O'Sullivan, D. and Y. Chen (2020). "CWITools: A Python3 Data Analysis Pipeline for the Cosmic Web Imager Instruments." *arXiv e-prints*, arXiv:2011.05444, arXiv:2011.05444.

Ott, J. et al. (2012). "VLA-ANGST: A High-resolution H I Survey of Nearby Dwarf Galaxies." *AJ* 144, p. 123. DOI: 10.1088/0004-6256/144/4/123.

Padovani, P. and F. Matteucci (1993). "Stellar Mass Loss in Elliptical Galaxies and the Fueling of Active Galactic Nuclei." *ApJ* 416, p. 26. ISSN: 0004-637X. DOI: 10.1086/173212.

Pagel, B. E. J. (2006). *Nucleosynthesis and Chemical Evolution of Galaxies*. 2nd. Cambridge, UK: Cambridge University Press.

Palla, M. (2021). "The Effects of Different Type Ia SN Yields on Milky Way Chemical Evolution." *MNRAS* 503.3, pp. 3216–3231.

Pan, D. C. et al. (2012). "Cosmic Voids in Sloan Digital Sky Survey Data Release 7." *MNRAS* 421.2, pp. 926–934. DOI: 10.1111/j.1365-2966.2011.20197.x.

Pancino, E. et al. (2011). "The Subgiant Branch of ω Centauri Seen Through High-resolution Spectroscopy." *A&A* 527, A18. ISSN: 0004-6361. DOI: 10.1051/0004-6361/201016024.

Pandey, K. and C. West (2021). "Galactic Isotopic Decomposition for the Sculptor Dwarf Spheroidal Galaxy."

Penny, S. J. et al. (2015). "Galaxy And Mass Assembly (GAMA): The Bright Void Galaxy Population in the Optical and Mid-IR." *MNRAS* 453.4, pp. 3519–3539. DOI: 10.1093/mnras/stv1926.

Pérez-Torres, M. A. et al. (2014). "Constraints on the Progenitor System and the Environs of SN 2014J from Deep Radio Observations." *ApJ* 792.1, p. 38. ISSN: 1538-4357. DOI: 10.1088/0004-637X/792/1/38.

Perlmutter, S. et al. (1999). "Measurements of Ω and Λ from 42 High-Redshift Supernovae." *ApJ* 517.2, pp. 565–586. DOI: 10.1086/307221.

Peters, W. et al. (1994). "HI Aperture Synthesis of the Southern Barred Spiral NGC1313." *MNRAS* 269, p. 1025. DOI: 10.1093/mnras/269.4.1025.

Phillips, M. M. (1993). "The Absolute Magnitudes of Type IA Supernovae." *ApJ* 413, p. L105. ISSN: 0004-637X. DOI: 10.1086/186970.

Pilyugin, L. S. et al. (2017). "On the Influence of the Environment on Galactic Chemical Abundances." *MNRAS* 465.2, p. 1358. DOI: 10.1093/mnras/stw2831. eprint: 1611.02502.

Pilyugin, L. S. and T. X. Thuan (2005). "Oxygen Abundance Determination in H ii Regions: The Strong Line Intensities - Abundance Calibration Revisited." *ApJ* 631.1, pp. 231–243. ISSN: 0004-637X. DOI: 10.1086/432408.

Piro, A. L. and L. Bildsten (2008). "Neutronization During Type Ia Supernova Simmering." *ApJ* 673.2, pp. 1009–1013. ISSN: 0004-637X. DOI: 10.1086/524189.

Placco, V. M. et al. (2014). "Carbon-Enhanced Metal-Poor Star Frequencies in the Galaxy: Corrections for the Effect of Evolutionary Status on Carbon Abundances." *ApJ* 797.1, p. 21. DOI: 10.1088/0004-637X/797/1/21.

Puche, D., C. Carignan, and J. van Gorkom (1991). "H I Studies of the Sculptor Group Galaxies. V. NGC 253." *AJ* 101, pp. 456–464. DOI: 10.1086/115696.

Pustilnik, S. A., Y. A. Perepelitsyna, and A. Y. Kniazev (2016). "Study of Galaxies in the Lynx-Cancer Void. VII. New Oxygen Abundances." *MNRAS* 463.1, pp. 670–683. ISSN: 0035-8711. DOI: 10.1093/mnras/stw2039.

Pustilnik, S. A., A. L. Tepliakova, and A. Y. Kniazev (2011). "Study of Galaxies in the Lynx-Cancer Void. II. Element Abundances." *Astrophys. Bull.* 66.3, pp. 255–292. ISSN: 19903413. DOI: 10.1134/S1990341311030011. eprint: 1108.4850.

Pustilnik, S. A., A. L. Tepliakova, and D. I. Makarov (2019). "Void Galaxies in the Nearby Universe. I. Sample Description." *MNRAS* 482.4, pp. 4329–4345. DOI: 10.1093/mnras/sty2947.

Putman, M. E. et al. (2021). "The Gas Content and Stripping of Local Group Dwarf Galaxies." *ApJ* 913.1, p. 53. ISSN: 0004-637X. DOI: 10.3847/1538-4357/ABE391.

Querejeta, M. et al. (2015). "The Spitzer Survey of Stellar Structure in Galaxies (S^4G): Precise Stellar Mass Distributions from Automated Dust Correction at 3.6 microns." *ApJS* 219, p. 5. ISSN: 0067-0049. DOI: 10.1088/0067-0049/219/1/5.

Recchi, S., F. Matteucci, and A. D'Ercole (2001). "Dynamical and Chemical Evolution of Gas-rich Dwarf Galaxies." *MNRAS* 322.4, pp. 800–820. ISSN: 00358711. DOI: 10.1046/j.1365-8711.2001.04189.x.

Reimers, D. (1975). *Circumstellar Envelopes and Mass Loss of Red Giant Stars.* New York: Springer-Verlag New York.

Reines, A. E., J. E. Greene, and M. Geha (2013). "Dwarf Galaxies with Optical Signatures of Active Massive Black Holes." *ApJ* 775.2, 116, p. 116. DOI: 10.1088/0004-637X/775/2/116.

Reines, A. E. et al. (2020). "A New Sample of (Wandering) Massive Black Holes in Dwarf Galaxies from High-resolution Radio Observations." *ApJ* 888, p. 36. DOI: 10.3847/1538-4357/ab4999.

Revaz, Y. and P. Jablonka (2012). "The Dynamical and Chemical Evolution of Dwarf Spheroidal Galaxies with GEAR." *A&A* 538, p. 82. ISSN: 00046361. DOI: 10.1051/0004-6361/201117402.

Revaz, Y. et al. (2016). "Computational Issues in Chemo-dynamical Modelling of the Formation and Evolution of Galaxies." *A&A* 588, p. 21. ISSN: 14320746. DOI: 10.1051/0004-6361/201526438.

Revaz, Y. et al. (2009). "The Dynamical and Chemical Evolution of Dwarf Spheroidal Galaxies." *A&A* 501.1, pp. 189–206. DOI: 10.1051/0004-6361/200911734.

Rhee, M.-H. and T. van Albada (1996). "Short WSRT HI Observations of Spiral Galaxies." *A&AS* 115, pp. 407–437.

Richer, M. G. et al. (2001). "IC 10: More Evidence That It Is a Blue Compact Dwarf." *A&A* 370.1, pp. 34–42. ISSN: 0004-6361. DOI: 10.1051/0004-6361:20010206.

Rieke, G. H. et al. (2004). "The Multiband Imaging Photometer for Spitzer (MIPS)." *ApJS* 154.1, pp. 25–29. DOI: 10.1086/422717.

Riess, A. G. et al. (1998). "Observational Evidence from Supernovae for an Accelerating Universe and a Cosmological Constant." *AJ* 116.3, pp. 1009–1038. DOI: 10.1086/300499.

Robitaille, T. P. et al. (2013). "Astropy: A Community Python Package for Astronomy." *A&A* 558.558, A33. ISSN: 0004-6361. DOI: 10.1051/0004-6361/201322068.

Rogstad, D., I. Lockhart, and M. Wright (1974). "Aperture-synthesis Observations of H I in the Galaxy M83." *ApJ* 193, pp. 309–319. DOI: 10.1086/153164.

Rogstad, D., G. Shostak, and A. Rots (1973). "Aperture Synthesis Study of Neutral Hydrogen in the Galaxies NGC 6946 and IC 342." *A&A* 22, pp. 111–119.

Romano, D. and E. Starkenburg (2013). "Chemical Evolution of Local Group Dwarf Galaxies in a Cosmological Context. I. A New Modelling Approach and its Application to the Sculptor Dwarf Spheroidal Galaxy." *MNRAS* 434.1, pp. 471–487. ISSN: 00358711. DOI: 10.1093/mnras/stt1033.

Rosales-Ortega, F. F., S. Arribas, and L. Colina (2012). "Integrated Spectra Extraction Based on Signal-to-noise Optimization Using Integral Field Spectroscopy." *A&A* 539, A73, A73. DOI: 10.1051/0004-6361/201117774.

Rosswog, S. et al. (2018). "The First Direct Double Neutron Star Merger Detection: Implications for Cosmic Nucleosynthesis." *A&A* 615, A132. ISSN: 0004-6361. DOI: 10.1051/0004-6361/201732117.

Roychowdhury, S., J. N. Chengalur, and Y. Shi (2017). "Extended Schmidt Law Holds for Faint Dwarf Irregular Galaxies." *A&A* 608, A24. ISSN: 0004-6361. DOI: 10.1051/0004-6361/201731083.

Roychowdhury, S. et al. (2014). "The Relation Between Atomic Gas and Star Formation Rate Densities in Faint Dwarf Irregular Galaxies." *MNRAS* 445.2, pp. 1392–1402. ISSN: 0035-8711. DOI: 10.1093/mnras/stu1814.

Ruiter, A. J. et al. (2011). "Delay Times and Rates for Type Ia Supernovae and Thermonuclear Explosions from Double-detonation Sub-Chandarsekhar Mass Models." *MNRAS* 417.1, pp. 408–419. ISSN: 00358711. DOI: 10.1111/j.1365-2966.2011.19276.x.

Ruiter, A. J., K. Belczynski, and C. Fryer (2009). "Rates and Delay Times of Type Ia Supernovae." *ApJ* 699.2, pp. 2026–2036. DOI: 10.1088/0004-637X/699/2/2026.

Ryder, S. et al. (1995). "A New Optical and H I Study of the Nearby Galaxy NGC 1313." *AJ* 109, pp. 1592–1607. DOI: 10.1086/117388.

Ryder, S. et al. (1996). "Neutral Hydrogen in the Ringed Barred Galaxies NGC 1433 and NGC 6300." *ApJ* 460, p. 665. DOI: 10.1086/177000.

Sage, L. (1993). "Molecular Gas in Nearby Galaxies. II. The Data." *A&AS* 100, pp. 537–569.

Sage, L. et al. (1992). "Star Formation and Molecular Clouds in Blue Compact Galaxies." *A&A* 265, pp. 19–31.

Saintonge, A. et al. (2011). "COLD GASS, an IRAM Legacy Survey of Molecular Gas in Massive Galaxies. II. The Non-universality of the Molecular Gas Depletion Time-scale." *MNRAS* 415.1, pp. 61–76. ISSN: 00358711. DOI: 10.1111/j.1365-2966.2011.18823.x.

Salpeter, E. E. (1955). "The Luminosity Function and Stellar Evolution." *ApJ* 121, p. 161. ISSN: 0004-637X. DOI: 10.1086/145971.

Samuel, J. et al. (2022). "Extinguishing the FIRE: Environmental Quenching of Satellite Galaxies Around Milky Way-mass Hosts in Simulations." *arXiv e-prints*, arXiv:2203.07385, arXiv:2203.07385. arXiv: 2203.07385 [astro-ph.GA].

Sánchez Almeida, J. et al. (2015). "Localized Starbursts in Dwarf Galaxies Produced by the Impact of Low-metallicity Cosmic Gas Clouds." *ApJL* 810.2, L15, p. L15. DOI: 10.1088/2041-8205/810/2/L15.

Sánchez, S. F. et al. (2016). "Pipe3D, a Pipeline to Analyze Integral Field Spectroscopy Data: I. New Fitting Philosophy of FIT3D." *RMxAA* 52, pp. 21–53.

Sánchez-Blázquez, P. et al. (2006). "Medium-resolution Isaac Newton Telescope Library of Empirical Spectra." *MNRAS* 371.2, pp. 703–718. DOI: 10.1111/j.1365-2966.2006.10699.x.

Sánchez-Janssen, R., J. Méndez-Abreu, and J. A. L. Aguerri (2010). "Thin Discs, Thick Dwarfs and the Effects of Stellar Feedback." *MNRAS* 406.1, pp. L65–L69. DOI: 10.1111/j.1745-3933.2010.00883.x.

Sancisi, R., R. Allen, and W. Sullivan III (1979). "Neutral Hydrogen Observations of the Barred Spiral Galaxy NGC 5383." *A&A* 78, pp. 217–225.

Sanders, D. B. et al. (2003). "The IRAS Revised Bright Galaxy Sample (RBGS)." *AJ* 126.4, pp. 1607–1664. DOI: 10.1086/376841.

Sandqvist, A., T. Elfhag, and S. Jorsater (1988). "CO and Dust in the Barred Spiral Galaxy NGC 1365." *A&A* 201, pp. 223–231.

Sartori, L. F. et al. (2015). "The Search for Active Black Holes in Nearby Low-mass Galaxies Using Optical and Mid-IR Data." *MNRAS* 454.4, pp. 3722–3742. DOI: 10.1093/mnras/stv2238.

Savino, A. et al. (2018). "MORGOTH: Incorporating Horizontal Branch Modelling into Star Formation History Determinations." *MNRAS* 480.2, pp. 1587–1598. ISSN: 0035-8711. DOI: 10.1093/mnras/sty1954.

Schlafly, E. F. and D. P. Finkbeiner (2011). "Measuring Reddening with Sloan Digital Sky Survey Stellar Spectra and Recalibrating SFD." *ApJ* 737.2, 103, p. 103. DOI: 10.1088/0004-637X/737/2/103.

Schlegel, D. J., D. P. Finkbeiner, and M. Davis (1998). "Maps of Dust Infrared Emission for Use in Estimation of Reddening and Cosmic Microwave Background Radiation Foregrounds." *ApJ* 500.2, pp. 525–553. DOI: 10.1086/305772.

Schmidt, M. (1959). "The Rate of Star Formation." *ApJ* 129, p. 243. ISSN: 0004-637X. DOI: 10.1086/146614.

– (1963). "The Rate of Star Formation. II. The Rate of Formation of Stars of Different Mass." *ApJ* 137, p. 758. ISSN: 0004-637X. DOI: 10.1086/147553.

Schombert, J. M. (2006). "On the Structural Differences between Disk and Dwarf Galaxies." *AJ* 131.1, pp. 296–303. DOI: 10.1086/497964.

Schruba, A. et al. (2011). "A Molecular Star Formation Law in the Atomic Gas Dominated Regime in Nearby Galaxies." *AJ* 142.2, p. 37. ISSN: 0004-6256. DOI: 10.1088/0004-6256/142/2/37.

Schruba, A. et al. (2012). "Low CO Luminosities in Dwarf Galaxies." *AJ* 143.6, p. 138. DOI: 10.1088/0004-6256/143/6/138.

Schwarz, U. (1985). "H I Synthesis Observations of the Peculiar Galaxy NGC 3718 and Its Companion NGC 3729." *A&A* 142, pp. 273–288.

Seitenzahl, I. R., S. Taubenberger, and S. A. Sim (2009). "Late-time Supernova Light Curves: The Effect of Internal Conversion and Auger Electrons." *MNRAS* 400.1, pp. 531–535. ISSN: 00358711. DOI: 10.1111/j.1365-2966.2009.15478.x.

Seitenzahl, I. R. et al. (2013a). "Solar Abundance of Manganese: A Case for Near Chandrasekhar-mass Type Ia Supernova Progenitors." *A&A* 559, p. L5. ISSN: 0004-6361. DOI: 10.1051/0004-6361/201322599.

Seitenzahl, I. R. et al. (2013b). "Three-dimensional Delayed-detonation Models with Nucleosynthesis for Type Ia Supernovae." *MNRAS* 429.2, pp. 1156–1172. ISSN: 0035-8711. DOI: 10.1093/mnras/sts402.

Seitenzahl, I. R. et al. (2015). "5.9-keV Mn K-shell X-ray Luminosity from the Decay of 55Fe in Type Ia Supernova Models." *MNRAS* 447.2, pp. 1484–1490. ISSN: 1365-2966. DOI: 10.1093/mnras/stu2537.

Seitenzahl, I. R. and D. M. Townsley (2017). "Nucleosynthesis in Thermonuclear Supernovae." *Handbook of Supernovae*. Ed. by A. Alsabti and P. Murdin. Springer, Cham, p. 1955. DOI: 10.1007/978-3-319-21846-5{_}87.

Seitenzahl, I. R. et al. (2016). "Three-dimensional Simulations of Gravitationally Confined Detonations Compared to Observations of SN 1991T." *A&A* 592, A57. ISSN: 0004-6361. DOI: 10.1051/0004-6361/201527251.

Shapley, H. (1938). "A Stellar System of a New Type." *Harvard College Observatory Bulletin* 908, pp. 1–11.

Shappee, B. J. et al. (2018). "Strong Evidence against a Non-degenerate Companion in SN 2012cg." *ApJ* 855.1, 6, p. 6. DOI: 10.3847/1538-4357/aaa1e9.

Shappee, B. J. et al. (2013). "No Stripped Hydrogen in the Nebular Spectra of Nearby Type Ia Supernova 2011fe." *ApJL* 762.1, L5, p. L5. DOI: 10.1088/2041-8205/762/1/L5.

Shen, K. J. and L. Bildsten (2007). "Thermally Stable Nuclear Burning on Accreting White Dwarfs." *ApJ* 660.2, pp. 1444–1450. ISSN: 0004-637X. DOI: 10.1086/513457.

Shen, K. J. et al. (2018a). "Sub-Chandrasekhar-mass White Dwarf Detonations Revisited." *AJ* 854.1, p. 52. ISSN: 1538-4357. DOI: 10.3847/1538-4357/aaa8de.

Shen, K. J. et al. (2018b). "Three Hypervelocity White Dwarfs in Gaia DR2: Evidence for Dynamically Driven Double-degenerate Double-detonation Type Ia Supernovae." *ApJ* 865.1, p. 15. ISSN: 1538-4357. DOI: 10.3847/1538-4357/aad55b.

Sheth, K. et al. (2010). "The Spitzer Survey of Stellar Structure in Galaxies (S^4G)." *PASP* 122, p. 1397. ISSN: 0004-6280. DOI: 10.1086/657638.

Sheth, K. et al. (2000). "Molecular Gas, Dust, and Star Formation in the Barred Spiral NGC 5383." *ApJ* 532, pp. 221–237. DOI: 10.1086/308530.

Shetrone, M. et al. (2003). "VLT/UVES Abundances in Four Nearby Dwarf Spheroidal Galaxies: I. Nucleosynthesis and Abundance Ratios." *AJ* 125.2, pp. 684–706. ISSN: 00046256. DOI: 10.1086/345966.

Shi, Y. et al. (2011). "Extended Schmidt Law: Role Of Existing Stars In Current Star Formation." *ApJ* 733.2, p. 87. ISSN: 0004-637X. DOI: 10.1088/0004-637X/733/2/87.

Shi, Y. et al. (2014). "Inefficient Star Formation in Extremely Metal Poor Galaxies." *Nature* 514.7522, pp. 335–338. ISSN: 0028-0836. DOI: 10.1038/nature13820.

Shibata, M. and K. Hotokezaka (2019). "Merger and Mass Ejection of Neutron Star Binaries." *ARNPS* 69, pp. 41–64. DOI: 10.1146/annurev-nucl-101918-023625.

Shimasaku, K. et al. (2001). "Statistical Properties of Bright Galaxies in the SDSS Photometric System." *AJ* 122, pp. 1238–1250. DOI: 10.1086/322094.

Shostak, G. (1973). "Aperture Synthesis Stady of Neutral Hydrogen in NGC 2403 and NGC 4236. II. Discussion." *A&A* 24, p. 411.

Siegel, D. M., J. Barnes, and B. D. Metzger (2019). "Collapsars as a Major Source of r-process Elements." *Nature* 569 (7755), pp. 241–244. DOI: 10.1038/s41586-019-1136-0.

Silk, J. (1997). "Feedback, Disk Self-regulation and Galaxy Formation." *ApJ* 481, pp. 703–709. ISSN: 0004-637X. DOI: 10.1086/304073.

Simmerer, J. et al. (2004). "The Rise of the s-process in the Galaxy." *ApJ* 617.2, pp. 1091–1114. ISSN: 0004-637X. DOI: 10.1086/424504.

Simon, J. D. and M. Geha (2007). "The Kinematics of the Ultra-Faint Milky Way Satellites: Solving the Missing Satellite Problem." *ApJ* 670.1, pp. 313–331. ISSN: 0004-637X. DOI: 10.1086/521816.

Simonetti, P. et al. (2019). "A New Delay Time Distribution for Merging Neutron Stars Tested Against Galactic and Cosmic Data." *MNRAS* 486.2, pp. 2896–2909. ISSN: 13652966. DOI: 10.1093/mnras/stz991.

Skillman, E. D. et al. (1987). "Neutral Hydrogen Observations of Four Dwarf Irregular Galaxies in the Virgo Cluster." *A&A* 185, pp. 61–76.

Skúladóttir, Á. et al. (2019). "Neutron-capture Elements in Dwarf Galaxies. I. Chemical Clocks and the Short Timescale of the r-process." *A&A* 631, A171. ISSN: 0004-6361. DOI: 10.1051/0004-6361/201936125.

Smith, D. and C. Hayward (2015). "Deriving Star Formation Histories from Photometry Using Energy Balance Spectral Energy Distribution Modelling." *MNRAS* 453.2, pp. 1597–1607. ISSN: 13652966. DOI: 10.1093/mnras/stv1727.

Smith, G. H. and M. M. Briley (2006). "CN Abundance Inhomogeneities in the Globular Cluster Messier 13 (NGC 6205): Results Based on Merged Data Sets from the Literature." *PASP* 118.843, pp. 740–753. ISSN: 0004-6280. DOI: 10.1086/503610.

Sneden, C., J. J. Cowan, and R. Gallino (2008). "Neutron-capture Elements in the Early Galaxy." *ARA&A* 46, p. 241. ISSN: 0066-4146. DOI: 10.1146/ANNUREV.ASTRO.46.060407.145207.

Sneden, C. et al. (1997). "Star-To-Star Abundance Variations Among Bright Giants in the Metal-Poor Globular Cluster M15." *AJ* 114, p. 1964. ISSN: 00046256. DOI: 10.1086/118618.

Sneden, C. et al. (2016). "Iron-group Abundances in the Metal-poor Main-sequence Turnoff Star HD 84937." *ApJ* 817.1, p. 53. ISSN: 1538-4357. DOI: 10.3847/0004-637X/817/1/53.

Sneden, C. et al. (2012). "MOOG: LTE Line Analysis and Spectrum Synthesis." *Astrophys. Source Code Libr.* P. 1202.009. URL: adsabs.harvard.edu/abs/2012ascl.soft02009S.

Sobeck, J. S. et al. (2006). "Manganese Abundances in Cluster and Field Stars." *AJ* 131.6, pp. 2949–2958. ISSN: 0004-6256. DOI: 10.1086/503106.

Solomon, P. and L. Sage (1988). "Star-formation Rates, Molecular Clouds, and the Origin of the Far-infrared Luminosity of Isolated and Interacting Galaxies." *ApJ* 334, pp. 613–625. DOI: 10.1086/166865.

Sorai, K. et al. (2000). "Distribution and Kinematics of Molecular Gas in Barred Spiral Galaxies. II. NGC 253." *PASJ* 52, pp. 785–802. DOI: 10.1093/pasj/52.5.785.

Spekkens, K. et al. (2014). "The Dearth of Neutral Hydrogen in Galactic Dwarf Spheroidal Galaxies." *ApJ* 795.5pp, p. 5. DOI: 10.1088/2041-8205/795/1/L5.

Spite, M. (1967). "Étude de l'étoile χ Draconis." *Annales d'Astrophysique* 30, p. 211.

Stanway, E. R. and J. J. Eldridge (2018). "Re-evaluating Old Stellar Populations." *MNRAS* 479.1, pp. 75–93. ISSN: 0035-8711. DOI: 10.1093/MNRAS/STY1353.

Stark, A., B. Elmegreen, and D. Chance (1987). "Molecules in Galaxies. V - CO Observations of Flocculent and Grand-design Spirals." *ApJ* 322, pp. 64–73. DOI: 10.1086/165703.

Stil, J. and F. Israel (2002). "Neutral hydrogen in dwarf galaxies. I. The spatial distribution of HI." *A&A* 389, pp. 29–41. DOI: 10.1051/0004-6361:20020352.

Straniero, O., R. Gallino, and S. Cristallo (2006). "s process in Low-mass Asymptotic Giant Branch Stars." *NuPhA* 777, pp. 311–339. ISSN: 0375-9474. DOI: 10.1016/j.nuclphysa.2005.01.011.

Suntzeff, N. B. (1981). "Carbon and Nitrogen Abundances in the Giant Stars of the Globular Clusters M3 and M13." *ApJS* 47, p. 1. ISSN: 0067-0049. DOI: 10.1086/190750.

Swaters, R. et al. (2002). "The Westerbork HI Survey of Spiral and Irregular Galaxies. I. HI Imaging of Late-type Dwarf Galaxies." *A&A* 390, pp. 829–861. DOI: 10.1051/0004-6361:20011755.

Tacconi, L. et al. (1991). "CO Observations of Southern S0 Galaxies." *A&A* 252, pp. 541–549.

Takada, M. et al. (2014). "Extragalactic Science, Cosmology, and Galactic Archaeology with the Subaru Prime Focus Spectrograph." *PASJ* 66.1, R1, R1. DOI: 10.1093/pasj/pst019.

Tamura, N. et al. (2018). "Prime Focus Spectrograph (PFS) for the Subaru Telescope: Ongoing Integration and Future Plans." *Proceedings of the SPIE*. Vol. 10702. SPIE, p. 48. ISBN: 9781510619579. DOI: 10.1117/12.2311871.

Taramopoulos, A., H. Payne, and F. Briggs (2001). "HI Observations of the Starburst Galaxy NGC 2146." *A&A* 365, pp. 360–369. DOI: 10.1051/0004-6361:20000143.

Taylor, C., H. Kobulnicky, and E. Skillman (1998). "CO Emission in Low-Luminosity, H I-rich Galaxies." *AJ* 116, pp. 2746–2756. DOI: 10.1086/300655.

Taylor, C., G. Petitpas, and M. del Rio (2015). "High-resolution Observations of Molecular Gas in the Early-type Dwarf Galaxy NGC 404." *AJ* 149, p. 187. DOI: 10.1088/0004-6256/149/6/187.

Taylor, C. et al. (1995). "An H i/Optical Atlas of H II Galaxies and Their Companions." *ApJS* 99, p. 427. DOI: 10.1086/192193.

Taylor, W. D. et al. (2018). "Rising MOONS: An Update on the VLT's Next Multi-object Spectrograph as it Begins to Grow." *Proceedings of the SPIE*. Vol. 10702. SPIE-Intl Soc Optical Eng, p. 52. ISBN: 9781510619579. DOI: 10.1117/12.2313403.

Teich, Y. G. et al. (2016). "SHIELD: Comparing Gas and Star Formation in Low-mass Galaxies." *ApJ* 832.1, p. 85. ISSN: 1538-4357. DOI: 10.3847/0004-637X/832/1/85.

Teyssier, M., K. V. Johnston, and M. Kuhlen (2012). "Identifying Local Group Field Galaxies that Have Interacted with the Milky Way." *MNRAS* 426.3, pp. 1808–1818. DOI: 10.1111/j.1365-2966.2012.21793.x.

Thilker, D. A. et al. (2007). "A Search for Extended Ultraviolet Disk (XUV?Disk) Galaxies in the Local Universe." *ApJS* 173.2, pp. 538–571. ISSN: 0067-0049. DOI: 10.1086/523853.

Thronson Jr., H. et al. (1989). "Molecular Gas, the Interstellar Medium, and Star Formation in S0 and SA Galaxies." *ApJ* 344, pp. 747–762. DOI: 10.1086/167839.

Thuan, T., J. Hibbard, and F. Lévrier (2004). "The H I Kinematics and Distribution of Four Blue Compact Dwarf Galaxies." *AJ* 128, pp. 617–643. DOI: 10.1086/422431.

Tinsley, B. M. (1979). "Stellar Lifetimes and Abundance Ratios in Chemical Evolution." *ApJ* 229, p. 1046. ISSN: 0004-637X. DOI: 10.1086/157039.

Tinsley, B. M. and R. B. Larson (1979). "Stellar Population Explosions in Proto-elliptical Galaxies." *MNRAS* 186.3, pp. 503–517. ISSN: 0035-8711. DOI: 10.1093/mnras/186.3.503.

Tinsley, B. M. (1968). "Evolution of the Stars and Gas in Galaxies." *ApJ* 151, p. 547. ISSN: 0004-637X. DOI: 10.1086/149455.

Tollerud, E. J. et al. (2016). "HST Imaging of the Local Volume Dwarf Galaxies Pisces A and B: Prototypes for Local Group Dwarfs." *ApJ* 827.2, 89, p. 89. DOI: 10.3847/0004-637X/827/2/89.

Tolstoy, E., V. Hill, and M. Tosi (2009). "Star-Formation Histories, Abundances, and Kinematics of Dwarf Galaxies in the Local Group." *ARA&A* 47.1, pp. 371–425. ISSN: 00664146. DOI: 10.1146/annurev-astro-082708-101650.

Tolstoy, E. et al. (2006). "The Dwarf Galaxy Abundances and Radial-velocities Team (DART) Large Programme - A Close Look at Nearby Galaxies." *Msngr* 123, p. 33. ISSN: 0722-6691.

Tremblay, P.-E. et al. (2016). "The Field White Dwarf Mass Distribution." *MNRAS* 461.2, pp. 2100–2114. ISSN: 0035-8711. DOI: 10.1093/mnras/stw1447.

Tremonti, C. A. et al. (2004). "The Origin of the Mass-Metallicity Relation: Insights from 53,000 Star-forming Galaxies in the Sloan Digital Sky Survey." *ApJ* 613.2, pp. 898–913. ISSN: 0004-637X. DOI: 10.1086/423264.

Tully, R. B. and P. Fouque (1985). "The Extragalactic Distance Scale. I. Corrections to Fundamental Observables." *ApJS* 58, p. 67. DOI: 10.1086/191029.

Turner, J., S. Beck, and R. Hurt (1997). "A CO Map of the Dwarf Starburst Galaxy NGC 5253." *ApJL* 474, pp. L11–L14. DOI: 10.1086/310412.

Ural, U. et al. (2015). "An Inefficient Dwarf: Chemical Abundances and the Evolution of the Ursa Minor Dwarf Spheroidal Galaxy." *MNRAS* 449.1, pp. 761–770. ISSN: 13652966. DOI: 10.1093/mnras/stv294.

van der Hulst, J. (1979). "The Kinematics and Distribution of Neutral Hydrogen in the Interacting Galaxy Pair NGC 4038/39." *A&A* 71, pp. 131–140.

van der Hulst, J. and W. Huchtmeier (1979). "The Peculiar Scd Galaxy NGC 5475 - The Distribution and Kinematics of the Neutral Hydrogen." *A&A* 78, pp. 82–86.

van der Hulst, J., T. van Albada, and R. Sancisi (2001). "The Westerbork HI Survey of Irregular and Spiral Galaxies, WHISP." *Gas Galaxy Evol.* Ed. by J. Hibbard, M. Rupen, and J. van Gorkom. Vol. 240. Astronomical Society of the Pacific Conference Series, p. 451.

Van der Kruit, P. and G. Shostak (1982). "Studies of Nearly Face-on Spiral Galaxies. I. The Velocity Dispersion of the H I Gas in NGC 3938." *A&A* 105, pp. 351–358.

– (1984). "Studies of Nearly Face-on Spiral Galaxies. III. H I Synthesis Observations of NGC 1058 and the Mass Distribution in Galactic Disks." *A&A* 134, pp. 258–267.

van Driel, W., A. Rots, and H. van Woerden (1988). "Distribution and Motions of Atomic Hydrogen in Lenticular Galaxies. VII. The S0a-Sa Galaxies NGC 1291, NGC 5101 and IC 5267." *A&A* 204, pp. 39–60.

van Moorsel, G. (1983). "Neutral Hydrogen Observations of Double Spiral Galaxies. III NGC 3504/3512, NGC 4085/4088, IC 65/UGC 622, NGC 797/801. IV NGC 4618/4625, NGC 4016/4017, NGC 3725/UGC 6528, UGC 725/728, NGC 2336/IC 467." *A&AS* 54, pp. 1–37.

van Zee, L., J. Salzer, and E. Skillman (2001). "Kinematic Constraints on Evolutionary Scenarios for Blue Compact Dwarf Galaxies. I. Neutral Gas Dynamics." *AJ* 122, pp. 121–139. DOI: 10.1086/321108.

van Zee, L., E. Skillman, and J. Salzer (1998). "Neutral Gas Distributions and Kinematics of Five Blue Compact Dwarf Galaxies." *AJ* 116, pp. 1186–1204. DOI: 10.1086/300510.

van Zee, L. et al. (1996). "Evolutionary Studies of the Low Metallicity Dwarf Irregular Galaxy UGCA 20." *AJ* 112, p. 129. DOI: 10.1086/117994.

– (1997). "A Comparative Study of Star Formation Thresholds in Gas-Rich Low Surface Brightness Dwarf Galaxies." *AJ* 113, pp. 1618–1637. DOI: 10.1086/118379.

Vassiliadis, E. et al. (1993). "Evolution of Low- and Intermediate-Mass Stars to the End of the Asymptotic Giant Branch with Mass Loss." *ApJ* 413, p. 641. ISSN: 0004-637X. DOI: 10.1086/173033.

Verheijen, M. and R. Sancisi (2001). "The Ursa Major Cluster of Galaxies. IV. HI Synthesis Observations." *A&A* 370, pp. 765–867. DOI: 10.1051/0004-6361:20010090.

Verter, F. (1987). "Systematic Properties of CO Emission from Galaxies. I. Luminosity Function." *ApJS* 65, pp. 555–580. DOI: 10.1086/191236.

Vincenzo, F. et al. (2019). "The Fall of a Giant. Chemical Evolution of Enceladus, alias the Gaia Sausage." *MNRAS* 487.1, pp. L47–L52. ISSN: 0035-8711. DOI: 10.1093/mnrasl/slz070.

Vincenzo, F. et al. (2014). "Chemical Evolution of Classical and Ultra-faint Dwarf Spheroidal Galaxies." *MNRAS* 441.4, pp. 2815–2830. ISSN: 13652966. DOI: 10.1093/mnras/stu710.

Vincenzo, F. et al. (2016). "Lighting Up Stars in Chemical Evolution Models: The CMD of Sculptor." *MNRAS* 460.2, p. 2238. ISSN: 0035-8711. DOI: 10.1093/mnras/stw1145.

Voyer, E. N. et al. (2014). "The GALEX Ultraviolet Virgo Cluster Survey (GUViCS) III. The Ultraviolet Source Catalogs." *A&A* 569, A124. ISSN: 0004-6361. DOI: 10.1051/0004-6361/201322511.

Walcher, J. et al. (2011). "Fitting the Integrated Spectral Energy Distributions of Galaxies." *Astrophys. & Space Sci.* 331, pp. 1–51. ISSN: 1572946X. DOI: 10.1007/s10509-010-0458-z.

Walker, M. G. et al. (2009). "A Universal Mass Profile for Dwarf Spheroidal Galaxies?" *ApJ* 704.2, pp. 1274–1287. DOI: 10.1088/0004-637X/704/2/1274.

Walter, F. et al. (1997). "A Dynamical Analysis of the HII Galaxy II Zwicky 33 and Its Low Surface Brightness Companion." *AJ* 113, pp. 2031–2045. DOI: 10.1086/118415.

Walter, F. et al. (2008). "THINGS: The H I Nearby Galaxy Survey." *AJ* 136, pp. 2563–2647. DOI: 10.1088/0004-6256/136/6/2563.

Wang, B. and Z. Han (2012). "Progenitors of Type Ia Supernovae." *New Astronomy Reviews* 56.4, pp. 122–141. DOI: 10.1016/j.newar.2012.04.001.

Warmels, R. H. (1985). PhD thesis. Univ. Groningen.

– (1988). "The H I Properties of Spiral Galaxies in the Virgo cluster. IV. Westerbork Observations of 12 Field Galaxies." *A&AS* 73, pp. 453–470.

Warren, S. et al. (2015). "CARMA CO Observations of Three Extremely Metal-poor, Star-forming Galaxies." *ApJ* 814, p. 30. DOI: 10.1088/0004-637X/814/1/30.

Webbink, R. F. (1984). "Double White Dwarfs as Progenitors of R Coronae Borealis Stars and Type I Supernovae." *ApJ* 277, p. 355. DOI: 10.1086/161701.

Wechsler, R. H. and J. L. Tinker (2018). "The Connection Between Galaxies and Their Dark Matter Halos." *ARA&A* 56, pp. 435–487. ISSN: 0066-4146. DOI: 10.1146/ANNUREV-ASTRO-081817-051756.

Wegner, G. A. et al. (2019). "Metal Abundances and Star Formation Rates of Emission-line Galaxies in and around the Boötes Void." *ApJ* 883.1, p. 29. ISSN: 1538-4357. DOI: 10.3847/1538-4357/ab3a3c. eprint: 1908.07539.

Wehmeyer, B., M. Pignatari, and F.-K. Thielemann (2015). "Galactic Evolution of Rapid Neutron Capture Process Abundances: The Inhomogeneous Approach." *MNRAS* 452.2, p. 1970. ISSN: 0035-8711. DOI: 10.1093/MNRAS/STV1352.

Weisz, D. R. et al. (2014). "The Star Formation Histories of Local Group Dwarf Galaxies I. Hubble Space Telescope / Wide Field Planetary Camera 2 Observations." *ApJ* 789.2, p. 147. ISSN: 0004-637X. DOI: 10.1088/0004-637X/789/2/147.

Westfall, K. B. et al. (2019). "The Data Analysis Pipeline for the SDSS-IV MaNGA IFU Galaxy Survey: Overview." *AJ* 158.6, 231, p. 231. DOI: 10.3847/1538-3881/ab44a2.

Wevers, B., P. van der Kruit, and R. Allen (1986). "The Palomar-Westerbork Survey of Northern Spiral Galaxies." *A&AS* 66, pp. 505–662.

Wheeler, C. et al. (2017). "The No-spin Zone: Rotation Versus Dispersion Support in Observed and Simulated Dwarf Galaxies." *MNRAS* 465, pp. 2420–2431. DOI: 10.1093/mnras/stw2583.

Wheeler, C. et al. (2019). "Be It Therefore Resolved: Cosmological Simulations of Dwarf Galaxies with 30 Solar Mass Resolution." *MNRAS* 490.3, pp. 4447–4463. DOI: 10.1093/mnras/stz2887.

White, S. D. M. and M. J. Rees (1978). "Core Condensation in Heavy Halos: A Two-stage Theory for Galaxy Formation and Clustering." *MNRAS* 183, pp. 341–358. DOI: 10.1093/mnras/183.3.341.

White, S. D. M. and C. S. Frenk (1991). "Galaxy Formation Through Hierarchical Clustering." *ApJ* 379, p. 52. ISSN: 0004-637X. DOI: 10.1086/170483.

Wiklind, T. and C. Henkel (1989). "The Molecular Cloud Content of Early Type Galaxies. I. Detections and global properties." *A&A* 225, pp. 1–11.

– (1990). "The Molecular Cloud Content of Early Type Galaxies. II. A Molecular Ring in NGC 404." *A&A* 227, pp. 394–406.

Wilcots, E. and B. Miller (1998). "The Kinematics and Distribution of H I in IC 10." *AJ* 116, pp. 2363–2394. DOI: 10.1086/300595.

Wiseman, P. et al. (2021). "Rates and Delay Times of Type Ia Supernovae in the Dark Energy Survey." *MNRAS* 506.3, pp. 3330–3348. ISSN: 0035-8711. DOI: 10.1093/MNRAS/STAB1943.

Woo, J., S. Courteau, and A. Dekel (2008). "Scaling Relations and the Fundamental Line of the Local Group Dwarf Galaxies." *MNRAS* 390.4, pp. 1453–1469. ISSN: 00358711. DOI: 10.1111/j.1365-2966.2008.13770.x.

Woosley, S. E. and D. Kasen (2011). "Sub-Chandrasekhar Mass Models for Supernovae." *ApJ* 734.1, p. 38. ISSN: 0004-637X. DOI: 10.1088/0004-637X/734/1/38.

Woosley, S. E., R. E. Taam, and T. A. Weaver (1986). "Models for Type I Supernova. I. Detonations in White Dwarfs." *ApJ* 301, p. 601. ISSN: 0004-637X. DOI: 10.1086/163926.

Wright, E. L. et al. (2010). "The Wide-field Infrared Survey Explorer (WISE): Mission Description and Initial On-orbit Performance." *AJ* 140.6, p. 1868. ISSN: 0004-6256. DOI: 10.1088/0004-6256/140/6/1868.

Wyder, T. K. et al. (2009). "The Star Formation Law At Low Surface Density." *ApJ* 696.2, pp. 1834–1853. ISSN: 0004-637X. DOI: 10.1088/0004-637X/696/2/1834.

Wyse, R. F. G. et al. (2002). "Faint Stars in the Ursa Minor Dwarf Spheroidal Galaxy: implications for the Low-mass Stellar Initial Mass Function at High Redshift." *New Astronomy* 7.7, pp. 395–433. DOI: 10.1016/S1384-1076(02)00156-2.

Yamaguchi, H. et al. (2015). "A Chandrasekhar Mass Progenitor for the Type Ia Supernova Remnant 3C 397 from The Enhanced Abundances of Nickel and Manganese." *ApJ* 801.2, p. L31. ISSN: 2041-8213. DOI: 10.1088/2041-8205/801/2/L31.

Yong, D. et al. (2014). "Iron and Neutron-capture Element Abundance Variations in the Globular Cluster M2 (NGC 7089)." *MNRAS* 441.4, pp. 3396–3416. ISSN: 1365-2966. DOI: 10.1093/mnras/stu806.

Young, J. et al. (1995). "The FCRAO Extragalactic CO Survey. I. The Data." *ApJS* 98, p. 219. DOI: 10.1086/192159.

Young, J. et al. (1996). "The Global Rate and Efficiency of Star Formation in Spiral Galaxies as a Function of Morphology and Environment." *AJ* 112, p. 1903. DOI: 10.1086/118152.

Young, L. et al. (2011). "The ATLAS^{3D} Project - IV. The Molecular Gas Content of Early-type Galaxies." *MNRAS* 414, pp. 940–967. DOI: 10.1111/j.1365-2966.2011.18561.x.

Yungelson, L. R. (2010). "Evolution of the Number of Accreting White Dwarfs with Shell Nuclear Burning and the SNe Ia Rate." *Astronomy Letters* 36.11, pp. 780–787. DOI: 10.1134/S1063773710110034.

Zahid, H. J. et al. (2013). "The Chemical Evolution of Star-Forming Galaxies Over the Last 11 Billion Years." *AJ* 771.2, p. L19. DOI: 10.1088/2041-8205/771/2/L19. eprint: 1303.5987.

Zhuang, Z. et al. (2021). "NGC 147 Corroborates the Break in the Stellar Mass-Stellar Metallicity Relation for Galaxies." *ApJ* 920.1, 63, p. 63. DOI: 10.3847/1538-4357/ac1340.